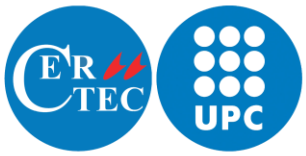

UNIVERSITAT POLITÈCNICA DE CATALUNYA
BARCELONATECH
Centre d'Estudis del Risc Tecnològic

Validation of CFD codes for risk analysis of accidental hydrocarbon fires

Ph.D. Thesis

Borja Rengel Darnaculleta

Ph.D. Advisors:

Dra. Elsa Pastor Ferrer

Dra. Eulàlia Planas Cuchi

Thesis submitted in partial fulfilment of the requirements for the degree of Doctor of Philosophy.

Programa de Doctorat en Enginyeria de Processos Químics

Barcelona 2019

This thesis has been developed at the Centre d'Estudis del Risc Tecnològic, CERTEC. The research was partially funded by the Spanish Ministry of Economy and Competitiveness (project CTM2014-57448-R, co-financed with FEDER funds).

All I know is that I know nothing

Socrates

For Alba.

AGRAÏMENTS

En primer lloc, m'agradaria agrair a l'Eulàlia i a l'Elsa haver-me donat la oportunitat de fer el doctorat a la ciutat on vaig créixer. Mil gràcies per ajudar-me en tot moment i haver confiat en mi per dur a terme aquesta tesi. Hi ha hagut moments durs, però al final ens em sortit. Sense vosaltres això no hagués estat possible.

Agrair també els consells i recomanacions d'en Joaquim Casal. Un gran home, no per l'edat que té, sinó per ser com és i saber tot el que sap, que no és poc. Els *afterworks* no serien el mateix sense ell. Sens dubte, un pilar fonamental d'aquesta etapa al CERTEC.

Així mateix, als meus companys de doctorat per tots els moments compartits. Us desitjo la millor de les sorts a cadascú de vosaltres. En especial a Christian Mata, qui ha omplert d'alegria la sala cada dia.

Un más que especial reconocimiento a Adriana Palacios, quien me 'adoptó' en tierras mexicanas. Siempre recordaré las conversaciones diarias buscando ese pasito más en la investigación. Jamás te podré acabar de agradecer cuanto disfruté y aprendí trabajando contigo. Me llevo conmigo una parte de México.

A tots els amics que m'han fet companyia aquests anys. La millor etapa de la meva vida, on m'emporto amics de veritat allà on vagi.

A la família, per què no tot és felicitat i alegria. Cal aprendre a acceptar les realitats de la vida i gaudir del que ens envolta. Els moments viscuts són inesborrables, i perduraran en el temps.

A Alba, la persona que me guía en esta vida. Sin ti, no habría llegado hasta aquí. Por suerte, lo mejor aún está por llegar.

RESUM

Les fuites accidentals d'hidrocarburs inflamables en indústries de processos químics poden desencadenar greus riscos: explosions, incendis i dispersions de núvols de vapor tòxics. Les explosions i les dispersions de gasos poden ferir a persones en un radi de danys més gran; tanmateix, els incendis són els esdeveniments accidentals més habituals que poden causar conseqüències catastròfiques en termes de pèrdues de vida i de propietats.

En aquest marc, la predicció dels efectes dels incendis pot contribuir significativament a identificar les mesures necessàries per eliminar o mitigar les conseqüències dels accidents en entorns de processos. Els mètodes semi-empírics poden proporcionar estimacions ràpides de la geometria de la flama així com del flux de calor rebut a una distància determinada de l'origen de l'incendi. A partir d'aquesta informació, es poden implementar sistemes de protecció actius i mesures de disseny inherents (és a dir, distàncies de seguretat entre equips) per evitar grans accidents d'incendis. No obstant, aquestes es basen en dades empíriques i no cobreixen les característiques generals del desenvolupaments dels incendis.

El modelatge de dinàmica de fluids computacionals (CFD) pot proporcionar una visió més detallada dels efectes dels incendis ja que tenen en compte la complexitat addicional dels escenaris, com ara geometries i condicions límits diferents, i poden representar diferents mides d'incendis: des de petita fins a gran escala. No obstant, les simulacions CFD requereixen dades d'entrada detallades, coneixements experts sobre el fenomen simulat i sobre els models físics implementats, i exigeixen elevats recursos computacionals. L'ús del modelat CFD per a l'anàlisi del risc tecnològic encara és incipient, i per tant, es necessiten exercicis de validació abans de fomentar la seva aplicació en casos reals.

Aquesta tesi està dirigida principalment a avaluar les capacitats predictives de diferents codis CFD (FDS, FLACS-Fire i FireFOAM) alhora de predir els efectes perillosos dels incendis de bassa i de dolls de foc. Concretament, de bassa a gran escala amb dièsel i gasolina (d'1.5 fins a 6 m de diàmetre), dolls de foc verticals sònics amb propà (de 0.09 fins a 0.34 $kg \cdot s^{-1}$ amb diàmetres d'orificis compresos entre 10 i 25.5 mm), dolls de foc verticals subsònics amb metà a diferents pressions atmosfèriques (des de 0.6 fins a 1 bar amb un diàmetre d'orifici de 3 mm), i dolls de foc verticals i horitzontals subsònics amb propà (de 0.007 fins a 0.11 $kg \cdot s^{-1}$ amb diàmetres d'orifici compresos entre 12.75 i 43.1 mm) s'han simulat amb les

diferents eines CFD. La prescripció de la velocitat de combustió proporciona prediccions precises dels efectes dels incendis de bassal quan la mida de la cel·la és de 0.2 m com a màxim. D'altra banda, la mida de la cel·la per a simulacions de dolls de foc sònics i subsònics s'ha de determinar tenint en compte un diàmetre característic de l'incendi de 16 i 12, respectivament. Es recomana un número mínim de 400 angles sòlids per obtenir estimacions precises dels fluxos tèrmics.

A partir de les nombroses simulacions computacionals realitzades es desenvolupament directrius de bones pràctiques (BPG) per determinar un codi com a 'vàlid' o no, i per proporcionar orientació sobre els paràmetres de modelatge més adequats quan es realitzen simulacions CFD d'incendis accidentals d'hidrocarburs. La utilitat del les BPG es demostra mitjançant un cas d'estudi d'una granja d'emmagatzematge d'hidrocarburs situada al Port de Barcelona. Es troben grans sobreestimacions dels valors del fluxos de calor mitjançant correlacions semi-empíriques. Per tant, es recomana la utilització d'eines CFD per realitzar FHA detallats en indústries químiques i de processos.

La tesi s'organitza de la manera següent: el Capítol 1 introdueix els diferents tipus d'incendis d'hidrocarburs que es poden produir en instal·lacions industrial i descriu els diferents mètodes de modelatge per determinar els efectes d'aquests; el Capítol 2 presenta les dades experimentals considerades per a l'anàlisi de validació de les eines CFD; el Capítol 3 descriu les eines de simulació d'incendis CFD utilitzades; el Capítol 4 detalla els resultats d'incendis de bassal obtinguts amb les eines CFD; el Capítol 5 descriu els resultats de les simulacions CFD dels dolls de foc verticals i horitzontals amb propà i metà; el Capítol 6 recull les BPG sobre el modelat CFD d'incendis accidentals d'hidrocarburs en entorns oberts; el Capítol 7 mostra un cas d'estudi sobre l'ús del modelat CFD per avaluar els perills d'incendi; i el Capítol 8 presenta les principals conclusions obtingudes a la tesi.

ABSTRACT

Accidental releases of flammable hydrocarbons in chemical process industries can trigger severe hazards: explosions, fires, and dispersion of toxic vapour clouds. Explosions and toxic releases may injure people within a large damage radius; however, fires are the most common accidental events that may lead to catastrophic consequences in terms of life and property losses.

Within this framework, the prediction of the related-fire effects may significantly contribute to identify measures needed to eliminate or mitigate the consequences of accidents in processing environments. Semi-empirical methods can provide rapid estimations of the flame-geometry descriptors as well as estimations of the heat flux received at a given distance from the fire origin. Based on that information, active protection systems and inherent safer design measures (i.e. safety distances between equipment) can be determined to prevent major fire accidents. Nevertheless, these are based on empirical and statistical data, and do not cover the overall characteristics of the fire behaviour.

Computational Fluid Dynamics (CFD) modelling can provide more detailed insights of the related fire effects considering additional complexity, such as different geometries and alternative boundary conditions, and representing different fire sizes: from small to large scale fires. Nevertheless, CFD requires detailed input data, expert knowledge on the phenomenon simulated and on the physical models implemented, and demands high computational resources. The use of CFD modelling for technological risk analysis is still incipient, so detailed validation exercises are needed before their use in real applications.

This thesis is mainly aimed at assessing the predictive capabilities of different CFD codes (FDS, FLACS-Fire and FireFOAM) when predicting the hazardous effects of hydrocarbon pool fires and jet fires. Specifically, large-scale pool fires of diesel and gasoline (from 1.5 to 6 m-diameter), vertical sonic jet fires of propane (from 0.09 to 0.34 $kg \cdot s^{-1}$ with orifice diameters of from 10 to 25.5 mm), vertical subsonic jet fires of methane in normal- and sub- atmospheric pressures (from 0.6 to 1 bar with an orifice diameter of 3 mm), and vertical and horizontal subsonic jet fires of propane (from 0.007 to 0.11 $kg \cdot s^{-1}$ with orifice diameters of from 12.75 to 43.1 mm-diameter) are modelled with the different CFD modelling codes. Prescribing burning rates provide accurate predictions of the pool fire effects with maximum cell sizes of 0.2 m. On the other hand, the cell sizes of sonic and subsonic jet fires

should be determined by considering a fire characteristic diameter of 16 and 12, respectively. A minimum number of 400 solid angles is recommended to obtain accurate estimations of the thermal flux.

Based on the numerous computational simulations performed, Best Practice Guidelines (BPG) are developed to determine a code as 'valid' or not, and to provide guidance on the most suitable modelling settings when performing CFD simulations of accidental hydrocarbon fires. The BPG usefulness is proved through a case study of an oil storage farm located in the Port of Barcelona. Large over-estimations of the heat flux values are found with semi-empirical correlations and thus, the safety measures required would be very conservative and costly. Therefore, CFD modelling is recommended method to perform detailed FHA in chemical and process industries.

The thesis is organized as follows: Chapter 1 introduces the different types of hydrocarbon fires that can occur in industrial facilities and describes the different modelling methods to estimate the related-fire effects; Chapter 2 presents the experimental data considered for CFD validation analysis; Chapter 3 describes the CFD fire codes used; Chapter 4 details the CFD modelling results of large-scale pool fires; Chapter 5 describes the simulations of methane and propane jet fires at different release and flow conditions; Chapter 6 gathers BPG in CFD modelling of accidental hydrocarbon fires in open environments; Chapter 7 reports a case study on the use of CFD modelling to assess the fire hazards in an oil storage farm; and Chapter 8 presents the main conclusions of this thesis.

CONTENTS

LIST OF FIGURES

LIST OF TABLES

a	pixel area (m^2)
A	area (m^2)
c	sound velocity of the fuel ($m \cdot s^{-1}$)
c_p	specific heat ($kJ \cdot kg^{-1} \cdot K^{-1}$)
C	model constant (-)
d	separation distance (m)
D	diameter (m)
D^*	characteristic fire diameter
E	surface emissive power ($kW \cdot s^{-2}$)
g	gravitational acceleration ($m \cdot s^{-2}$)
G	total irradiance ($kW \cdot s^{-2}$)
h	height of reference (m)
h_c	canopy height (m)
H	total height (m)
I	segmented image (-)
I_b	black body radiation intensity ($kW \cdot s^{-2}$)
k	turbulent kinetic energy ($m^2 \cdot s^{-2}$)
K	Von Kármán constant (0.41)
L	length (m)
$\dot{m}$	mass flow rate ($kg \cdot s^{-1}$)
$\dot{m}''$	mass flow rate per unit area ($kg \cdot m^{-2} \cdot s^{-1}$)
M	molecular weight of the fuel ($kg \cdot kmol^{-1}$)
M_a	Mach number (-)
n	number of measures (-)
N	total number of images (-)
O_2	oxygen (-)
p	altitude exponent (-)
P	pressure (atm)

$\dot{q}_r''$	radiative heat flux (kW·s^{-2})
$\dot{Q}$	heat release rate (kW)
R	universal gas constant (kJ·kmol^{-1}·K^{-1})
Re	Reynolds number (-)
Re_L	Reynolds number based on D_{or} and S_L (-)
s	stoichiometric ratio (-)
S	lift-off distance (m)
S_L	laminar burning velocity (m·s^{-1})
T	temperature (K)
u	velocity (m·s^{-1})
U^*	dimensionless flow number for choked and unchoked flows (-)
x	variable (-)
Y	mass fraction (-)

Greek

α	diffusivity (m^2·s^{-1})
γ	isentropic ratio (-)
Δ	LES filter size (m)
Δh_c	heat of combustion (kJ·kg^{-1})
δ_x	cell size (m)
ε	emissivity/dissipation rate (m^2/s^3)
η	ground roughness (-)
κ	Planck absorption coefficient (m^{-1})
μ_t	turbulent viscosity (kg·m^{-1}·s^{-1})
ν	kinematic viscosity (m^2·s^{-1})
ρ	density (kg·m^{-3})
σ	Stefan-Boltzmann constant ($5.67 \cdot 10^{-11}$ kJ·m^{-2}·s^{-1}·K^{-4})
τ	atmospheric transmissivity (-)
τ_{mix}	mixing time scale (s)
$\varphi_{F,t}$	view factor (-)
χ	reacting fractions of fine structures (-)

χ_r	radiative fraction (-)
ψ	similarity function (-)
Ω	tilt angle (º)
$\dot{\omega}'''$	chemical reaction rate ($kg \cdot m^{-3} \cdot s^{-1}$)

Subscripts

a	advection
c	chemical species
d	diffusion
eff	effective
eq	equivalent
f	fuel
F	flame
g	buoyant acceleration
H	horizontal
i	stagnation
i, j	coordinates
m	measured
or	orifice
θ	friction
p	predicted
r	threshold
ref	reference
R	radial
T	thermocouples
V	vertical
w	wind
∞	ambient

Abbreviation

AHJ	Authorities Having Jurisdiction
ARE	average relative error
BPG	best practice guideline

CFD	Computational Fluid Dynamics
CFM	conversion factor model
DOM	discrete ordinate method
DTM	discrete transfer method
EDC	eddy dissipation concept
EIA	U.S. Energy Information Administration
FB	fractional bias
FHA	fire hazard assessment
GUI	graphical user interface
LES	Large Eddy Simulations
MAE	mean absolute error
MFC	mean forcing concept
MG	geometric mean bias
MO	Monin-Obukhov
MRE	maximum relative error
NED	normalized Euclidean distance
NMSE	normalized mean square error
OECD	Organization for Economic Cooperation and Development
PBD	performance-based design
PC	performance criteria
PL	power law
RANS	Reynolds averaged Navier-Stokes
RMSE	root mean square error
SF	slice file
SGS	sub-grid scale
VG	geometric mean variance

CHAPTER 1

INTRODUCTION

Hydrocarbon fuels are involved in most of the major fire accidents occurring in industrial facilities, which may lead to catastrophic consequences in terms of life and property losses. In this regard, the prediction of the related-fire effects is essential to design effective protection measures to mitigate the fire impact. This chapter briefly introduces the reader to the different types of hydrocarbon fires that could occur in chemical and process plants (Section 1.1) and describes the different modelling techniques able to estimate the hazardous fire effects (Section 1.2). Based on findings from a wide literature survey of previous CFD modelling studies involving hydrocarbon fires, the main objectives of this thesis are proposed (Section 1.3). Finally, Section 1.4 describes the structure of this thesis.

1.1. Accidental hydrocarbon fires in industries

1.1.1. Hydrocarbon fuels

The U.S. Energy Information Administration (EIA) reported in 2016 that the industrial sector consumed about the 54% of the world's total delivered energy for multiple purposes (U.S. Energy Information Administration (EIA), 2016). The diversity and the amount of fuels consumed vary notably between countries according to their economic activities and technological developments. Those countries outside of the Organization for Economic Cooperation and Development (OECD) register the highest consumption growth by an average of 1.5%/year from 2012 to 2040, while those belonging to the OECD register a consumption growth of 0.5%/year (Figure 1.1). Globally, the energy consumed worldwide in the industrial sector is estimated to increase by an average of 1.2%/year until 2040.

Among the different available energy sources, it is observed that hydrocarbons are and will be the most used in the near future. One of the main advantages of these fuels is their high calorific values, responsible of the release of tremendous amounts of energy. Also, the earth's reservoirs containing hydrocarbons are easily found, hence facilitating its extraction and transportation to industrial sites. As a result, the process to produce energy from hydrocarbon fuels is cheaper and more cost-effective than with other non-conventional forms of energy, such as

renewables. Nevertheless, the amount of hydrocarbon fuels on earth is limited, and it is well acknowledged that the solid particles released from soot and smoke into the ambient can considerably damage the environment and human health.

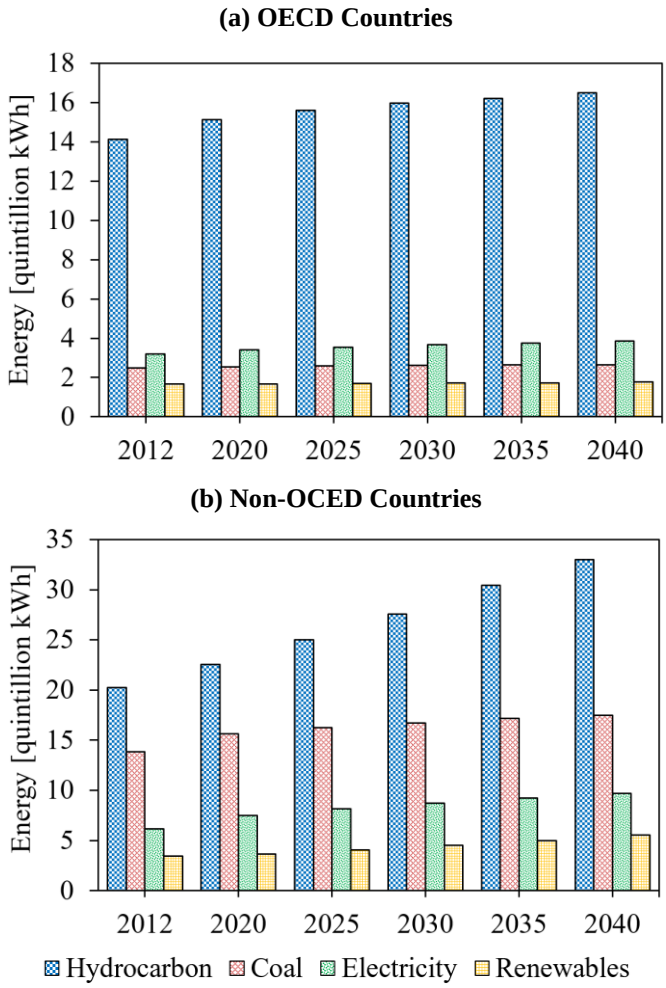

Figure 1.1. Worldwide energy consumption in the industrial sector for a) OECD countries and b) non-OECD countries (U.S. Energy Information Administration (EIA), 2016).

1.1.2. Hydrocarbon fires

Accidental releases of flammable hydrocarbons in chemical and process industries can lead to hazardous events: explosions, fires and dispersion of toxic vapour clouds (Khan and Abbasi, 1999). Explosions and toxic releases may injure people within a larger damage radius. However, fires are the most common events (41.5%) as reported from a MHIDAS (Major Hazard Incident Data Service) survey involving 6,099 accidents (Palazzi and Fabiano, 2012).

Depending on the fuel properties and their state, different types of fires can be originated from a loss of containment (Casal, 2017). For example, spills of liquid fuels may lead to pool fires when finding an ignition source (Figure 1.2). Otherwise, if the liquid evaporates before ignition or a gas is released through a leak, a flammable vapour cloud may be originated and dispersed in the ambient. If the cloud reaches an ignition source, a flash fire may occur, which can travel back to the spill source (Rew et al., 1998). When a pipe is broken, when a hole forms in a tank, when gas leaks from a flange, or when a safety valve is opened, a high-velocity leak of gas, or two-phase flow can be immediately ignited creating a jet fire or a flare (Gómez-Mares et al., 2009). The dynamics of jet fires are dominated by the initial jet momentum, while buoyancy controls liquid pool fires (Palacios et al., 2008).

Pool fires are characterized by buoyancy-driven turbulent flames taking place on a horizontal pool of liquid fuel. The pool mainly receives heat from the flames by convection and radiation, hence allowing the vaporisation of the fuel. In particular, the pool diameter, D, has been recognised as the most important feature governing the mass evaporation rate and thus, the pool fire (Steinhaus et al., 2007). Accordingly, pool fires can be classified as small-scale pool fires (D < 0.1 m), medium-scale pool fires (0.1 m ≤ D ≤ 1 m) and large-scale pool fires (D > 1 m) (Trouvé, 2008). The former are dominated by a laminar flow and a convective thermal feedback from the flame to the pool surface, whereas large-scale pool fires, which commonly occur in industrial accidents, are subjected to turbulent flows and radiant thermal feedback (Koylu and Faeth, 1992). Medium-scale pool fires represent a transitional stage between small and large pools. In addition, hydrocarbon pool fires release considerable amounts of soot that affect the overall thermal heat transfer (Casal, 2017). In the case of small-scale pool fires, soot particles are accumulated in the lower fire region (fuel rich), while these are accumulated in the upper fire region (fuel lean) for large-scale pools.

In the case of jet fires, the mass flow rate, $\dot{m}$, which depends on the orifice size and the exit pressure, governs the jet fire dynamics. A well-recognized classification criterion is given as follows: small-scale (0.03 - 0.3 kg/s); medium-scale (0.3 - 3 kg/s); large-scale (3 - 30 kg/s); and major failure (> 30 kg/s) (Lowesmith et al., 2007). Depending on the exit velocity of the gas released through the orifice, u_{or}, two possible flow regimes can be found: sonic and subsonic flows. Sonic jet fires are the most common accidents involving gas fuel leaks in industries (Casal et al., 2012).

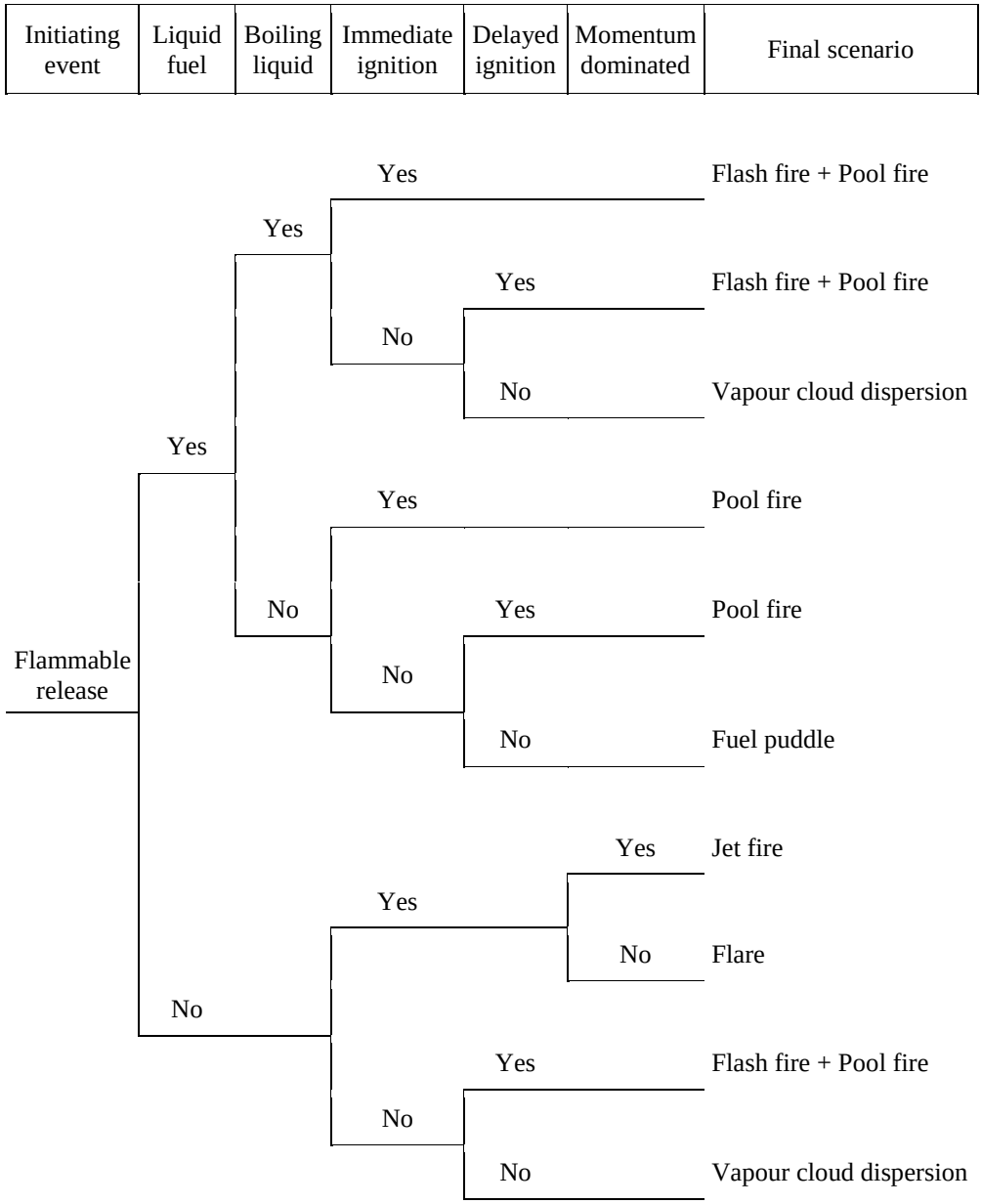

Figure 1.2. Event tree of accidental hydrocarbon fires. Adapted from (Beyler, 2016).

1.1.3. Hazards and consequences of accidental hydrocarbon fires

Among the possible fires occurring in process plants, pool fires were reported as the most common scenarios (66% of the cases), followed by flash fires (29%) and jet fires (5%) (Planas-Cuchi et al., 1997). The primary effects of accidental hydrocarbon fires are flames engulfment and thermal radiation, that can in turn

affect the equipment and personnel of the plant within a very short period of time (Pula et al., 2005).

Jet fires are less frequent and smaller than other accidental fires; however, a sudden ignition of an accidental release of pressurized fuel can involve high risk regarding industry personnel and the installation itself (Lowesmith et al., 2007). Apart from the high radiative heat fluxe emitted, the probability of flame impingement on the surrounding equipment may trigger an escalation of the incident, known as domino effect, hence leading to additional fires and explosions. Particularly, an escalation of the incident normally occurs in the 50% of jet fire accidents with further inventory loss and structural collapse (Gómez-Mares et al., 2008; Masum et al., 2015). Also, an escalation of the flash fire accident occurs in the 33% of the cases (Villafañe et al., 2011). Either way, flash fires are still poorly understood, being this partly due to experimental difficulties when controlling the gas release conditions in real tests.

The consequences derived from accidental hydrocarbon fires can be catastrophic in terms of economic costs, number of injuries and deaths. Figure 1.3 shows the statistical data of fire accidents in industrial facilities registered from 1917 to 2011 classified per continent (Mihailidou et al., 2012). As it can be seen, the number of hydrocarbon fires registered is greater in facilities from developed countries, whereas the number of deaths, injuries and costs per accident are considerably less than in developing ones. South and Central America, featured with the minor number of accidents, are the most affected regions, probably because of deficient preventive measures and lack of emergency planning. In contrast, Europe has the lowest number of injuries and deaths per accident; the reason behind this is the stronger regulations applied in European countries.

Within this framework, fire hazard assessments (FHA) are needed to identify the required measures to eliminate or mitigate the consequences of fire accidents in processing environments (Health and Safety Executive, 2006). Essentially, FHA provides information on the flame-geometry descriptors needed to estimate the likelihood of flame impingement on plant equipment, as well as estimations of the heat flux received at a given distance from the fire origin (Casal et al., 2012). Based on that information, active protection systems and inherently safer design measures (i.e. safety distances) can be determined to prevent major fire accidents and the occurrence of domino effect, especially in compact arrangements, such as those found in certain process plants and offshore oil platforms. Two main modelling approaches can be used to perform FHA studies: semi-empirical correlations and Computational Fluid Dynamics (CFD) simulations. Both modelling methods are described in detail in the following section.

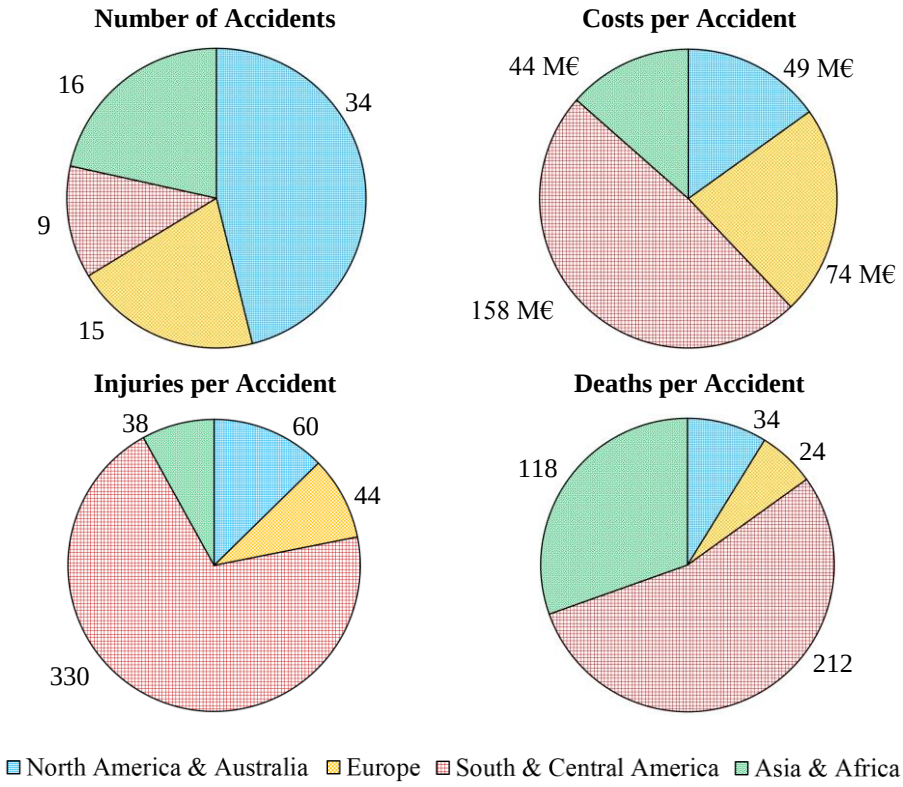

Figure 1.3. Number of major hydrocarbon fire accidents reported in industrial facilities from 1917 to 2011 (Mihailidou et al., 2012).

1.2. Modelling approaches in FHA

1.2.1. Semi-empirical correlations

During the last decades, semi-empirical correlations were developed from specific sets of well-defined experiments to predict the harmful effects of hydrocarbon fires (Cowley and Johnson, 1992). On one side, some of these were conceived to estimate the flame-geometry descriptors of jet fires (Costa et al., 2004; Gómez-Mares et al., 2009; Gore, 1986; Hu et al., 2015, 2014; L. Hu et al., 2013; L. H. Hu et al., 2013; Kiran and Mishra, 2007; McCaffrey, 1989; Palacios et al., 2012, 2008; Palacios and Casal, 2011; Rokke et al., 1994; Santos and Costa, 2005; Sonju and Hustad, 1984; Sugawa and Sakai, 1995; T., 1984) and pool fires (Heskestad, 1999; Lam and Weckman, 2015; Mangialavori and Rubino, 1992; Moorhouse, 1982; Muñoz et al., 2004; Pritchard and Binding, 1992) (Figure 1.4). The flame length, L_F, is defined as the distance from the base of the fire to the tip of the visible flame, whereas the flame height, H_F, is the orthogonal distance from the base of the fuel source to the tip of the visible flame. The flame area, A_F, represents the surface

covered by the visible flames where the combustion reaction occurs and the mean equivalent diameter, D_{eq}, indicates the mean width of the flame. In the occurrence of jet fires, the lift-off distance, S_F, concerns the flameless distance between the nozzle orifice and the base of the flame. Also, in the presence of wind, the flames can be inclined due to the wind forces creating a tilt angle, Ω_F, between the total flame height and the flame length. More detailed information about the available semi-empirical correlations describing the flames shape of jet fires and pool fires can be found in Appendix A.

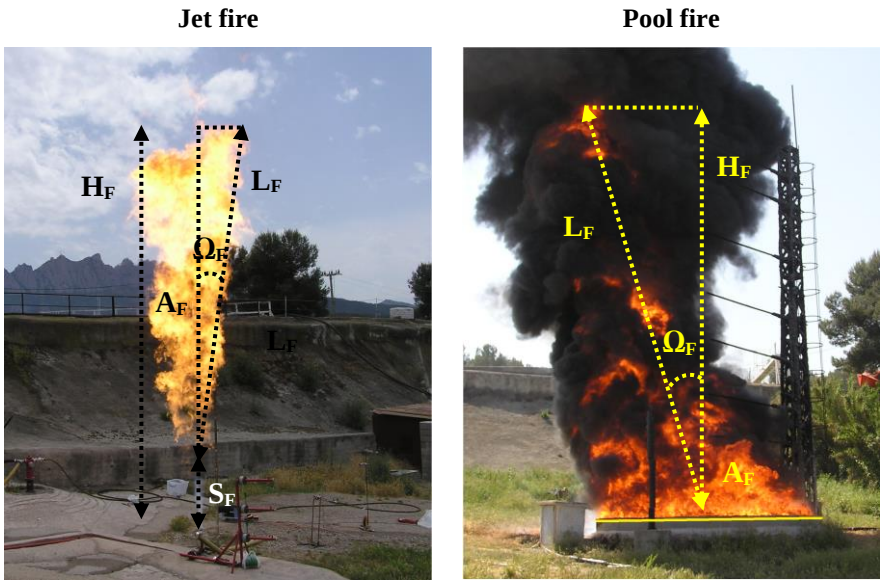

Figure 1.4. Main geometrical parameters describing jet fires (left) and pool fires (right).

On the other side, the thermal flux properties of jet fires (Brzustowski and Sommer, 1973; McCaffrey, 1981; Tan, 1967) and pool fires (Koseki, 1989; Muñoz et al., 2007; Shen et al., 2018) were reported for authors in different ways. Some of them measured the radiative fraction, χ_r, which is referred to the amount of energy that is transferred by radiation in a fire. The greater the fire diameter, the lower the radiative fractions as a result of the higher amount of soot particles that block the radiation emitted from the luminous flame to the outside (Beyler, 2016). Based on the radiative fraction, the heat flux received at a given distance from the fire origin, $\dot{q}_r''$, can be calculated by using the point source model (Drysdale, 2011):

$$\dot{q}_r'' = \frac{\chi_r \dot{Q}}{4\pi {d_R}^2} \tag{1.1}$$

where d_R is the distance from the flame centre to the target location and $\dot{Q}$ is the heat release rate of the fire.

Radiative data is also reported in terms of surface emissive power, E, which represents the radiative heat flux at the flame surface:

$$E = \sigma \varepsilon {T_F}^4 \quad (1.2)$$

where σ is the Stefan-Boltzmann constant ($5.67 \cdot 10^{-11}$ kJ/m^2·s·K^4), T_F is the flame temperature and ε represents the emissivity. Then, by determining the view factor between the target and the flame, $\varphi_{F,t}$, and the atmospheric transmissivity, τ, the radiant heat flux can be calculated with the solid flame model (Mudan, 1984):

$$\dot{q}_r'' = E \varphi_{F,t} \tau \quad (1.3)$$

Semi-empirical correlations can be rapidly applied to provide estimations of the flame shape and the thermal flux of hydrocarbon fires. Nevertheless, the results found are only valuable if the fire scenarios studied are identical to the experimental tests from which the equations were developed. Given the constantly changing processes performed in industrial plants affecting the configuration of the facility, the fuel inventory and the location of the ignition sources, the use of this type of correlations can be notably restricted to a few number of fire scenarios (Azzi and Rogstadkjenet, 2016). Therefore, alternative modelling approaches, such as Computational Fluid Dynamics (CFD) modelling, should be used to estimate the harmful effects of hydrocarbon fires for a wide range of complex scenarios.

1.2.2. Computational Fluid Dynamics

CFD is an emerging modelling technique that can help assessing the fire hazards in industries. CFD fire simulations are able to consider complex distributions of the equipment, different inventory and type of fuels, remote location of possible ignition sources and diverse environmental conditions (i.e. wind, ambient temperature and humidity). Also, a large set of variables can be calculated at any location within the computational domain according to the user's interests. Therefore, this technique can provide a deeper understanding of the fire behaviour and the subsequent harmful effects.

CFD simulations require detailed input data, expert knowledge of the sub-models solved within the codes and usually demand high computational resources. Table 1.1 summarizes the main CFD fire codes developed by different research institutes, organizations and private companies during the last years. As it is shown, the availability of codes may differ depending on the developer's interests. For example, there are commercial codes such as Fluent and CFX that require costly licences to be used, while others such as FDS or FireFOAM are open-source tools freely available. On the other hand, there are 'private' codes developed for the internal use of some organizations.

Table 1.1. Main CFD codes used for fire simulations.

CFD Code	Reference	Source	Developer
FDS	(McGrattan et al., 2017)	Open	NIST
FireFOAM	(Greenshields, 2017)	Open	FM Global & CFD Direct
Fluent	(*ANSYS FLUENT User's Guide*, 2017)	Commercial	ANSYS
CFX	(*ANSYS CFX-Pre User's Guide*, 2017)	Commercial	ANSYS
VULCAN	(DesJardin et al., 2000)	Open	NASA LaRC
CAFE-3D	(Suo-anttila et al., 2005)	Private	Sandia National Laboratories
Isis-3D	(Greiner and Suo-Anttila, 2004)	Private	Sandia National Laboratories
ISIS	(IRSN, 2018)	Open	IRSN
Code_Saturne	(EDF R&D, 2018)	Open	EDF Energy
Kameleon FireEx	(Magnussen et al., 2000)	Commercial	ComputIT
PHOENICS	(Ludwing and Mortimore, 2013)	Commercial	CHAM
FLACS-Fire	(Gexcon AS, 2017)	Commercial	Gexcon AS
ARCHES	(Guilkey et al., 2009)	Open	University of Utah
GENMIX	(Spalding, 2013)	Commercial	CHAM
JASMINE	(Ciambelli et al., 2006)	Commercial	BRE - Fire Research Station
SOFIE	(Pierce and Moss, 2007)	Commercial	BRE - Fire Research Station
FLEXSIM	(Osenbroch, 2006)	Commercial	DNV-GL
SOLVENT	(Nilsen and Log, 2009)	Commercial	Parsion Brinckherhoff's Tunnel Ventilation Division & Innovative Research, Inc.

1.2.3. Validation analysis

Validation of numerical codes, which consists in a comparison process between experimental and predicted data, is a necessary first step before their use in real applications. Through validation exercises, the appropriateness of the governing equations to represent the physical phenomena of interest can be determined and the uncertainties generated either in the conceptual modelling or during the

computational design phase can be highlighted (Mok et al., 2004). In consequence, validation analysis allows the model amelioration from the disparities reached and increases the accuracy of predictions (McGrattan and Miles, 2016).

There exist two types of comparison methods often used to assess the predictions performance of CFD tools: qualitative scatter plots and quantitative statistical methods. The first method graphically illustrates the level of agreement reached between predictions and measurements. This comparison method can rapidly bring an idea about the accuracy of the results obtained with the CFD tools. Figure 1.5 shows a qualitative scatter plot that compares the emissive power of large-scale pool fires predicted in FDS with those measured in real experiments. The presented graph was previously published in (Rengel et al., 2018). The solid diagonal line indicates perfect agreement between predictions and measurements, while dotted lines and long-dashed lines represent the ± 25% and ± 50% prediction error, respectively, with regard to the measurement. So, the closer to the solid diagonal line, the more accurate the predictions are. When possible, graphs include also vertical and horizontal bars to represent the standard deviation of the simulation results and the experiments, respectively.

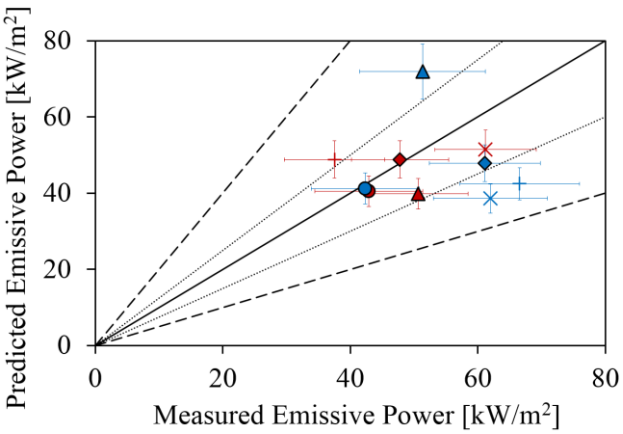

Figure 1.5. Example of a qualitative scatter plot comparing the emissive power predicted of different fire scenarios against the experimental measurements (Rengel et al., 2018).

Moreover, quantitative statistical methods are complementarily used to evaluate both the computational uncertainties and the agreement reached over time (Oberkampf and Barone, 2006). Table 1.2 summarizes some of the quantitative methods often used in CFD validation analysis.

The ARE cannot adequately determine the model accuracy due to the strong smoothing nature of the integration operator, while the MRE could bring more valuable information in particular cases where large errors at some points are found. On the other hand, the absolute error methods ($RMSE$, MAE and NED) indicate how far a value is from an original measurement. The $RMSE$ was found

more suitable to quantify a model performance than the MAE, as it avoids the use of mean values (Chai et al., 2014). Similarly, the NED gives an overview of the code capabilities by considering the differences between computational results and measurements during all the fire duration.

Table 1.2. Quantitative comparison methods applicable to CFD codes validation analysis. $\bar{x}_m$ and $\bar{x}_p$ are the mean experimental and predicted values, respectively; x_m and x_p are single experimental and predicted values for each time step, respectively; and n is the number of measures.

Ref.	Method	Formulae
(Oberkampf and Barone, 2006)	Average relative error (ARE)	$ARE = \frac{1}{n}\sum_{i=1}^{n}\left\|\frac{x_m - x_p}{x_p}\right\|$
	Maximum relative error (MRE)	$MRE = \left\|\frac{\bar{x}_m - \bar{x}_p}{\bar{x}_p}\right\|$
(Rew and Deaves, 1995)	Fractional bias (FB)	$FB = \frac{1}{n}\sum_{i=1}^{n} 2\frac{x_m - x_p}{x_m + x_p}$
	Normalized mean square error ($NMSE$)	$NMSE = \frac{1}{n}\sum_{i=1}^{n}\frac{(x_m - x_p)^2}{x_m x_p}$
(Audouin et al., 2011)	Normalized Euclidean distance (NED)	$NED = \sqrt{\frac{\sum_{i=1}^{n}(x_m - x_p)^2}{\sum_{i=1}^{n}(x_p)^2}}$
(Chai et al., 2014)	Root mean square error ($RMSE$)	$RMSE = \sqrt{\frac{\sum_{i=1}^{n}(x_m - x_p)^2}{n}}$
	Mean absolute error (MAE)	$MAE = \frac{\left\|\bar{x}_m - \bar{x}_p\right\|}{n}$
(Rigas and Sklavounos, 2005)	Geometric mean bias (MG)	$MG = exp\left[\frac{1}{n}\sum_{i=1}^{n} ln\left(\frac{x_m}{x_p}\right)\right]$
	Geometric mean variance (VG)	$VG = exp\left[\frac{1}{n}\sum_{i=1}^{n} ln\left(\frac{x_m}{x_p}\right)^2\right]$

The use of statistical performance measures (FB, MG, VG and $NMSE$) were recommended to evaluate the predictions of CFD codes (Hanna et al., 2004; Rew

and Deaves, 1995). A perfect model would have a MG and VG value of 1 and a FB and NMSE value of 0. In the case of the FB, negative results indicate that the values have been over-estimated, while positive ones note that the values have been under-estimated. NMSE is a measure of the scatter that reflects the fit of the estimations to data. In general, when performing any model evaluation exercise, multiple quantitative approaches must be applied as there is not a single measure that is universally applicable to all conditions.

1.2.4. Literature review of CFD modelling of hydrocarbon fires

During the last decades, CFD modelling has been used in the field of fire risk analysis due to the need for an in-depth understanding of the phenomena associated to hydrocarbon fires in industrial facilities. The present literature survey is aimed at reflecting the state of the art of CFD modelling when assessing this type of fires. For that purpose, articles in peer-reviewed journals and congress communications from the 90's until nowadays containing CFD simulation studies of hydrocarbon pool fires, jet fires and flash fires in open environments have been considered. The complete list of surveyed works is tabulated in Appendix B.

Among the simulations analysed, pool fires (55%) were the main scenarios modelled, followed by jet fires (40%) and flash fires (5%) (Figure 1.6). The limited quantity of flash fires modelled might be due to the reduced number of experiments available and the significant difficulties in obtaining reliable results given the large distances involved in these types of accidents (hundreds of meters); another reason could be the fact that flash fires have a negligible effect on equipment (except for the case of floating roof tanks) and its risk is usually estimated by applying a few simplifying assumptions. In contrast, jet fires and pool fires have been much more simulated mainly due to the great number of experimental tests performed under different configurations. This fact allows detailed comparisons between simulation results and experimental measurements. Also, the high number of accidents caused by these type of fires may have increased the interest in performing such simulations for a better understanding on their consequences.

Figure 1.7 classifies the works considered as a function of the fire sizes, the fuels modelled, the CFD codes used and the variables of interest measured. As observed, most pool fires were modelled as large-scale (84%), while jet fires were simulated equally at different scales: small-scale (22%), medium-scale (36%) and large-scale (34%). Most of the simulations performed involved large and medium-scale fires, especially pool fires, as these represent the worst-case scenarios occurring in facilities. Otherwise, small fires were barely modelled due to their minor impact in comparison with medium and large-scale fires. Nevertheless, these can represent the initiating event of the domino effect and thus, the predictive

capabilities of CFD codes have not been widely studied when assessing the hazards and consequences derived from small-scale hydrocarbon fires.

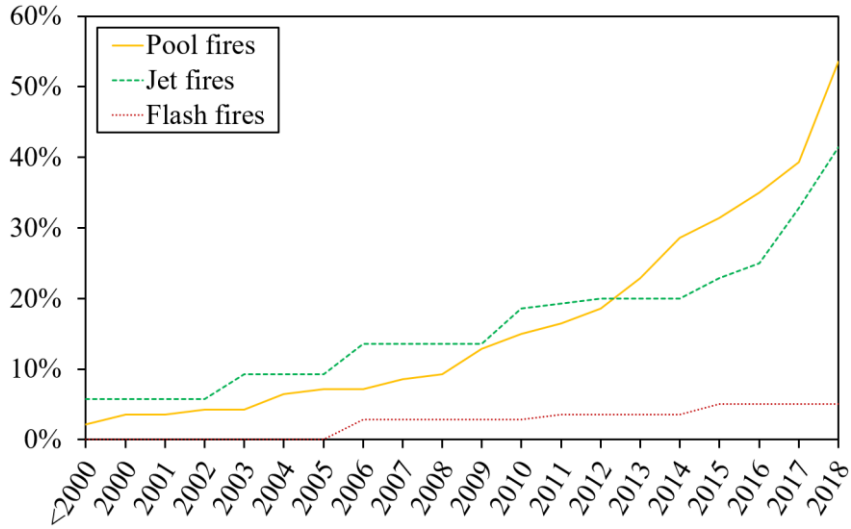

Figure 1.6. Accumulated frequency of the different published works involving CFD simulations of hydrocarbon fires.

Concerning the substances involved, it is noted that heavy hydrocarbon combustibles, such as gasoline (32%) and diesel (17%), were the main fuels used to run pool fires simulations. Indeed, these are fuels associated to many industrial activities and applications such as transport, storage, paintings, coatings and energy sources for engine devices. On the other hand, jet and flash fires were only simulated with methane and propane, as these are well-investigated gas fuels commonly found in the industry. In particular, methane was the fuel used in the 81% and in the 71% of the scenarios involving jet fires and flash fires, respectively.

The main variables of interest measured were flame temperature, radiative heat flux received at a certain distance from the fire origin and flame-geometry descriptors (height, length, area and tilted angle). These are of special interest to determine the safety separation distances and to examine the flame impingement in adjacent structures (Ray et al., 2014). Particularly, two different approaches were used to measure the heat flux and the flame temperature: (i) monitor points to determine their evolutions at specific locations; and (ii) 2D slice files to register their results within a rectangular array of grid points. On the other hand, four different approximations were performed to determine the flame-geometry descriptors: image analysis, mixture fraction calculation, boundary flame temperature and semi-empirical methods (Sedano et al., 2017). Image analysis consists on measuring the point's locations at which the products of combustion had the highest mass fractions around the flame. Mixture fraction calculation

estimates the average mixture fraction along the centreline axis of the flame. Then, the geometrical parameters are determined depending on the stoichiometric value of the burning fuel. Boundary flame temperature calculates the flame shape by applying a threshold temperature that differentiates the flame region from the background. Semi-empirical methods predict the geometry of the flame based on empirical correlations that directly depend on the heat release rate and the fire diameter. Certain fire features were practically neglected by most authors (for example, surface emissive power and soot formation). Indeed, one of the key problems is that fire modelling techniques are still under development and thus, some fire characteristics and effects are difficult to be accurately obtained.

Most of the simulations were intended to validate the modelling tools by using experimental data. In particular, a large number of authors preferred to validate a code under various scenarios (fuel and/or fire size) instead of analysing different tools under a single scenario. Nevertheless, a validation of multiple CFD tools under just one fire scenario might highlight the advantages and disadvantages of these in terms of computational times and results accuracy. Similarly, no comparisons between CFD codes and semi-empirical methods were found. Therefore, more research in this field is still required in order to determine the most appropriate technique (i.e. CFD code and/or semi-empirical method) as a function of a given fire scenario, the variables of interest and the available time computational resources.

A reasonably good agreement was generally declared when comparing simulations with experiments, with slight under-predictions of the heat flux at larger distances. Nevertheless, the accuracy of the CFD outcomes cannot be totally guaranteed, as qualitative comparisons were done in the 67% of the validation exercises performed. Thus, it is recommended to carry out quantitative comparisons to recognize whether a CFD code is able to simulate accidental hydrocarbon fires.

In addition, the mesh resolution still remains a concern as most authors simulate fire scenarios within random computational domains under one mesh configuration based on previous published works or according to the characteristic fire diameter and cell size ratio (Sally and Kassawara, 2007). Even if the chosen mesh could be the most appropriate for the scenario investigated, different cell sizes should be tested (from coarse to fine) to avoid possible errors caused by the cell size. Also, most published works barely provide the reader with the details of the computational domain set-up, which could affect the fire development calculations.

Based on the main findings and suggestions noted in the present review, it is deduced that the development and implementation of Best Practice Guidelines (BPG) in CFD modelling of accidental hydrocarbon fires would be of high interest to the fire community. These may contribute to properly perform further CFD

validation analysis and to provide guidance in performing real fire simulations, hence increasing the reliability of simulation outcomes.

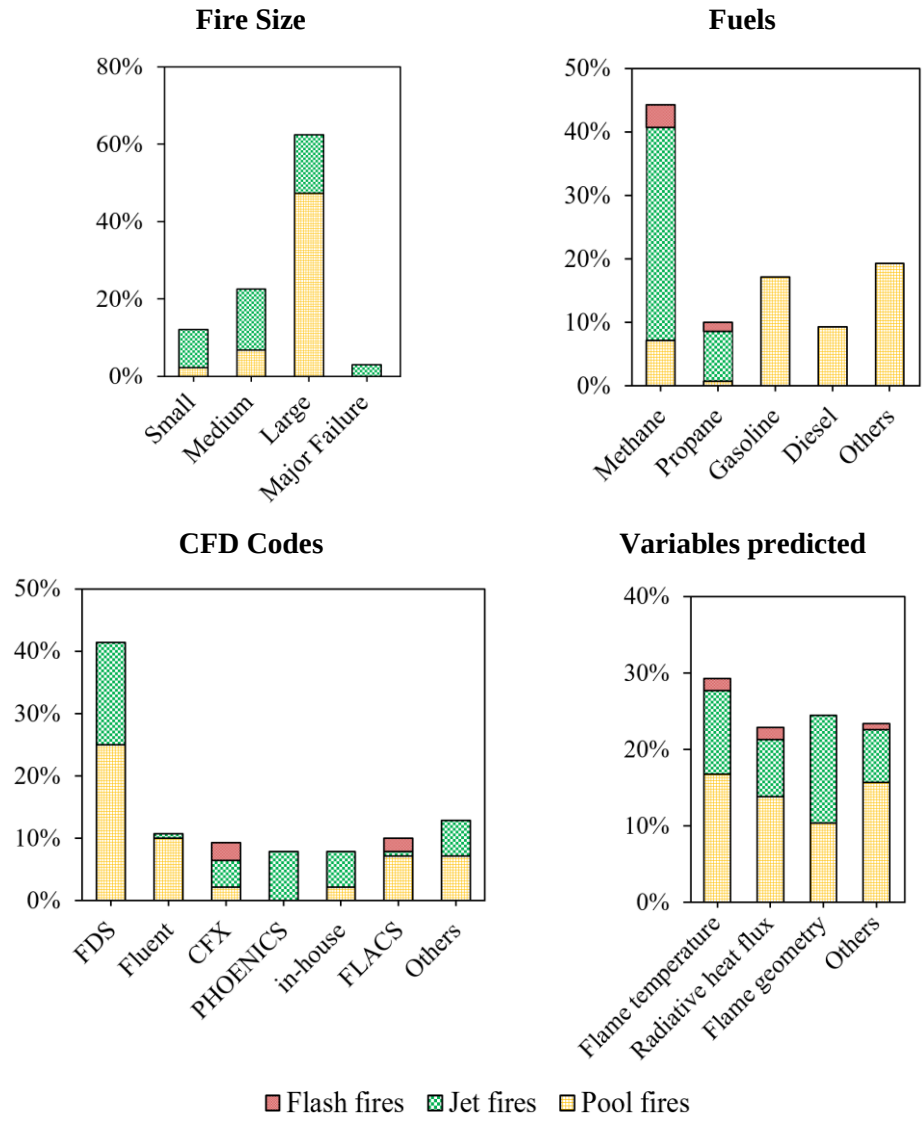

Figure 1.7. Main features of the pool, jet and flash fires simulated: a) sizes represented, b) fuels modelled, c) CFD tools used and d) variables of interest measured.

Although a significant effort has been made to improve the knowledge concerning the fire-related phenomena of hydrocarbon fires by means of CFD modelling, there is still a long way to go, as this literature review has shown. In general, fires in open environments have been poorly evaluated with CFD codes, as there is a considerable lack of data regarding the most suitable modelling parameters and comparison methods. Therefore, further CFD validation works should be carried

out, especially in complex fire scenarios, due to the need to perform more reliable risk analysis in chemical industries and thus, to provide safer plants.

1.3. Thesis objectives

Considering the expected growth on the use of hydrocarbon fuels in the industrial sector, the severe consequences triggered by accidental hydrocarbon fires and the stated limitations of semi-empirical methods, there is an essential need to promote the use of CFD modelling to estimate the hazardous effects of industrial fires. In this context, the main goal of this thesis is to assess the predictive capabilities of three CFD modelling tools (FDS, FireFOAM and FLACS-Fire) to estimate the effects derived from accidental hydrocarbon fires in open environments. To address the main goal defined, the following specific objectives are proposed:

- Determine the most appropriate numerical settings of CFD codes to obtain reasonable estimations of the fire scenarios examined.

- Establish a comparison between CFD codes and determine the most appropriate one to predict the related-fire effects according to the hydrocarbon fire accident of interest.

- Develop best practice guidelines in CFD modelling of hydrocarbon fire accidents in open environments to be used in real applications.

- Examine the applicability of CFD codes for their implementation on fire emergency prevention and management.

1.4. Thesis structure

This thesis is structured as follows:

Chapter 2 describes the experimental data considered for CFD validation analysis. There is a brief description of the experimental set-up for both pool and jet fires, and the main characteristics of our dataset.

Chapter 3 describes the CFD fire codes used in the thesis providing detailed information on the mathematical correlations implemented at hand to solve the different phenomenon (i.e. turbulence, combustion, radiation, etc.).

Chapter 4 details the CFD modelling results of large-scale pool fires of gasoline and diesel under different wind conditions, and Chapter 5 describes the simulations of methane and propane jet fires at different release and flow conditions: subsonic/sonic and vertical/horizontal.

Chapter 6 gathers best practice guidelines in CFD modelling of accidental hydrocarbon fires in open environments based on the main findings of previous

chapters. Firstly, a standard methodology developed for carrying out CFD validation analysis of this type of fire accidents is proposed. Secondly, recommendations on the most appropriate numerical parameters are provided.

Chapter 7 reports a case study showing the use of CFD modelling to assess the fire hazards in an oil storage farm. For that purpose, computational simulations are performed based on the best practice guidelines suggested. Finally, Chapter 8 presents the main conclusions of this thesis.

CHAPTER 2
EXPERIMENTAL DATA

In this thesis no experimental work has been performed, but experimental data from several sources have been used to assess the predictive capabilities of different CFD fire codes. This chapter includes a brief description of the experimental set-up and the data available of different hydrocarbon fire tests: (i) large-scale liquid pool fires of gasoline and diesel (Section 2.1.), (ii) vertical sonic jet fires of propane (Section 2.2.), (iii) vertical subsonic jet fires of methane in normal- and sub- atmospheric pressures (Section 2.3.) and (iv) horizontal and vertical subsonic jet fires of methane (Section 2.4.).

The experimental measurements used in this thesis are summarized in Appendix C. These have been obtained during the steady state of the fire, which coincides with fully developed flames. The data are mainly related with hazardous fire effects (i.e. flame-geometry descriptors, flame temperature, emissive power and radiative heat flux) and when possible, these are expressed in dimensionless quantities to allow further comparison with other fire experiments.

2.1. Large-scale pool fires

2.1.1. Experimental set-up

A series of outdoor large-scale pool fire tests carried out under different conditions are used in this thesis (Ferrero et al., 2007, 2006; Muñoz et al., 2007, 2004). As shown in Table 2.1, pool fire experiments involved gasoline and diesel as fuel, lying on top of a thin layer of water in five concentric circular pools made of reinforced concrete, of 1.5 m, 3 m, 4 m, 5 m and 6 m-diameter.

Different measuring devices were used to record the main variables of interest. The weather conditions were obtained by using a meteorological station located at 10 m height, which provided the ambient temperature, $\bar{T}_{\infty}$, the wind velocity, $\bar{u}_{w}$, and the wind direction. A set of five K-type thermocouples (3 mm-diameter) were located in the pool centreline axis to measure the flame temperatures at different heights over the fuel layer: 2.84 m (TB1), 3.96 m (TB2), 5.53 m (TB3), 6.96 m (TB4) and 11.01 m (TB5). A wide-angle radiometer, whose axial and radial

distance to the pool origin varied according to the experiments performed, was located opposite to the wind direction to measure the irradiance received at a certain distance. Particularly, in some experiments the radial distance was three times the pool diameter (3D) while in others was five times the pool diameter (5D). The burning rates of pool fires were measured through a system of communicating vessels connected to an electronic balance that measured the amount of combustible loss (Chatris et al., 2001).

Table 2.1. Main features of the large-scale pool fire experiments of diesel and gasoline used in this thesis. Data sources come from (Ferrero et al., 2007, 2006; Muñoz et al., 2007, 2004).

Experiment	Fuel	D (m)	$\overline{u}_w$ (m·s^{-1})	$\overline{T}_\infty$ (ºC)	Radiometer distance (m)	
					Axial	*Radial*
22_D15	Diesel	1.5	1.33	22	1.5	7.5
21_G15	Gasoline	1.5	0.44	20	1.5	7.5
01_D3	Diesel	3.0	2.39	12	0.1	9.0
17_G3	Gasoline	3.0	1.14	14	1.5	9.0
04_D3	Diesel	3.0	0.00	16	0.1	15.0
03_G3	Gasoline	3.0	0.00	13	0.1	15.0
14_D4	Diesel	4.0	0.43	20	0.1	12.0
13_G4	Gasoline	4.0	0.52	19	0.1	12.0
10_D5	Diesel	5.0	1.02	16	1.0	15.0
08_G5	Gasoline	5.0	0.00	19	0.1	15.0
07_D6	Diesel	6.0	1.10	19	0.1	18.0
06_G6	Gasoline	6.0	0.00	18	0.1	18.0

Apart from the 03_G3 and 04_D3 pool fires, the rest of the experiments were filmed with a VHS camera that registered the visible images of the fire (Figure 2.1a) and with a thermographic IR camera that recorded the apparent temperature distribution of the flame (Figure 2.1b). Both cameras were placed together perpendicular to the predominant wind direction, at different distances from the fire origin depending on the pool diameter to record the complete structure of the flames.

2.1.2. IR image segmentation process

For each test, the recorded IR images corresponding to the stationary state of the fire were lately treated with an in-house MATLAB algorithm (Mata et al., 2018). The main goal of this software developed is to differentiate the flame region from

the smoke plume, hence allowing the determination of the mean flame height, $\bar{H}_F$, and the mean flame area, $\bar{A}_F$. To achieve this objective, the IR images were exported and stored in an appropriate format within a private project file. These contained the temperature matrix for each instant of time, the matrix size and the camera parameters. Then, segmentation was performed using a normalized threshold temperature, T_r (Figure 2.1c). This is intended to separate the flame region from the background for each IR image by comparing the temperature at each pixel element, $T_{i,j}$, with the defined threshold temperature:

$$I(i,j) = \begin{cases} 1, if\ T_{i,j} \geq T_r \\ 0, if\ T_{i,j} < T_r \end{cases} \quad (2.1)$$

where $I(i,j)$ is the segmented image, 1 indicates that the pixel is within the flame region and 0 means that the pixel element belongs to the background of the image. In particular, a threshold temperature of 600 K was applied to segment the IR images of pool fires (Audouin et al., 1995; Cox and Chitty, 1980).

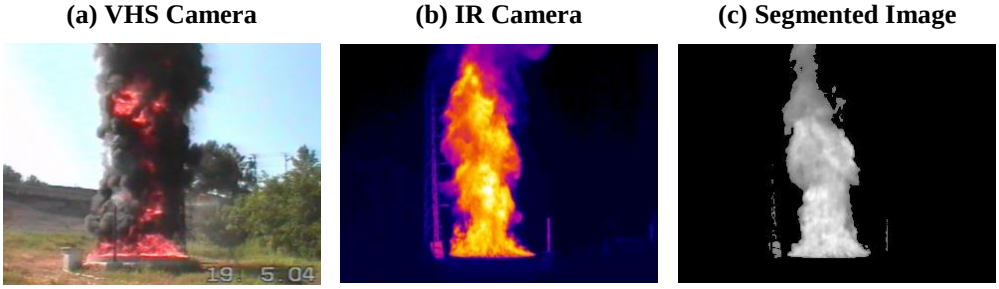

Figure 2.1. Example of video images recorded during the stationary state of the 06_G6 pool fire by means of a) a VHS camera, b) a IR camera and c) the corresponding segmentation process applied.

Given the temperatures distribution of the segmented flame images, we calculated the surface emissive power at each pixel, $E_{i,j}$:

$$E_{i,j} = \varepsilon \sigma T_{i,j}^4 \quad (2.2)$$

where i and j indicate the position of the pixel in the IR image. As hydrocarbon pool fires become optically thick at diameters of ~ 3 m (Planas-Cuchi et al., 2003), the following emissivity values were adopted according to the pools sizes: 0.95 for diameters of 1.5 m, 0.98 for 3 m, and 1 for diameters equal or higher than 4 m. Then, the time averaged surface emissive power of a pixel element during the steady state, $\bar{E}_{i,j}$, can be calculated by:

$$\bar{E}_{i,j} = \frac{\sum_1^N E_{i,j}}{N} \quad (2.3)$$

where N represents total number of images in the thermographic sequence. Finally, the mean surface emissive power of the whole flame, $\bar{E}$, is written as:

$$\bar{E} = \frac{\sum_i \sum_j \bar{E}_{i,j} a_{i,j}}{\sum_i \sum_j a_{i,j}} \tag{2.4}$$

where $a_{i,j}$ is the area of a pixel in the infrared image.

2.1.3. Data available

Data obtained during the experiments include: flame temperatures and emissivity, heat fluxes captured by the radiometers, fuel mass loss rates and flame geometry (height and area). Figure 2.2 depicts the mean flame temperature as a function of the dimensionless thermocouples heights, H_T/D. Three diesel pool fire experiments with different diameters (22_D15, 01_D3 and 10_D5) registered similar low temperatures along the centerline axis (~40 ºC). In those cases, the lateral winds significantly tilted the flames and thus, the centerline thermocouples were not in contact with the flames. Other diesel pool fires under the presence of wind (i.e. 14_D4 and 07_D6) achieved higher temperatures along the axis, while the highest ones were reached in the absence of wind (i.e. 04_D3). Consequently, it is highlighted that wind significantly affects the mean centerline temperatures of diesel pool fires as flames may be tilted depending on the pool diameter and the wind velocity (Figure 2.3). In addition, it might be inferred that for each pool diameter there is a characteristic wind speed that inclines its flame, hence modifying its height and area: the larger the pool diameter, the higher the characteristic wind speed should be to overcome the buoyancy-driven forces of the pool fire.

Gasoline pool fires commonly reached greater centerline flame temperatures than diesel pool fires under similar boundary conditions. For example, 3 m-diameter pool fires in the absence of wind achieved mean maximum temperatures of 900 ºC and 750 ºC when involving gasoline and diesel, respectively. Significant temperature fluctuations are observed in some pool fire experiments (i.e. 04_D3, 07_D6, 06_G6, 13_G4) when $H_T/D \leq 2$, which may be due to possible measuring errors induced by the type of thermocouples used and the experimental conditions. This fact may lead to disagreements between the temperatures predicted in CFD codes and those registered in the tests.

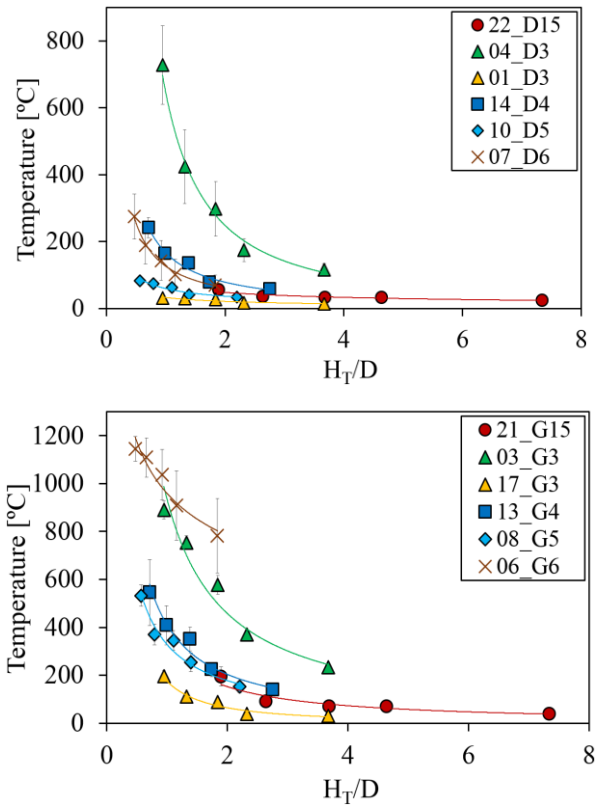

Figure 2.2. Mean values of flame temperature registered by the thermocouples as a function of their dimensionless height above the liquid fuel for large-scale pool fires of diesel (up) and gasoline (down). Vertical error bars indicate the standard deviation of the measurements.

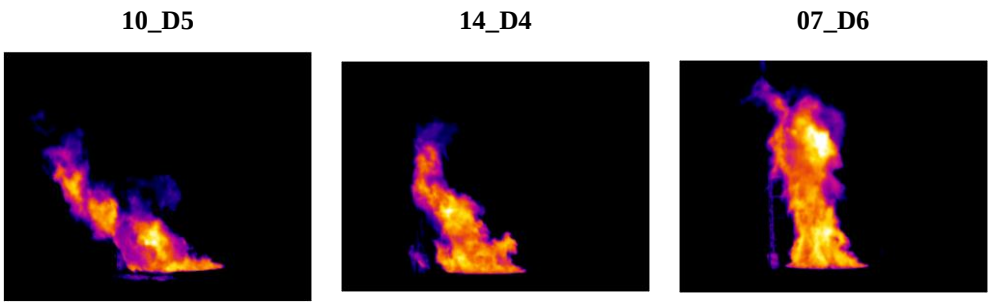

Figure 2.3. IR images belonging to one instant of time during the steady state of different pool fire experiments that reveal flame tilting.

Figure 2.4 shows the mean mass loss rate obtained for gasoline and diesel pool fires as a function of the pool diameter (up) and wind velocity (down). As observed, the amount of mass loss increases as the pool diameter or the wind velocity increases for both fuels. In addition, higher values are found for gasoline compared to diesel pool fires, with negligible deviations among the mean values.

The burning rate data can be used as input variables within the CFD codes to reasonably estimate other variables of interest (i.e. flame temperature, radiative heat flux, emissive power and geometrical features of the flame). Otherwise, mass loss rates may be predicted in computational codes by solving advanced pyrolysis sub-models. Nevertheless, modelling errors may be derived given its high dependency on the pool diameter and the wind velocity.

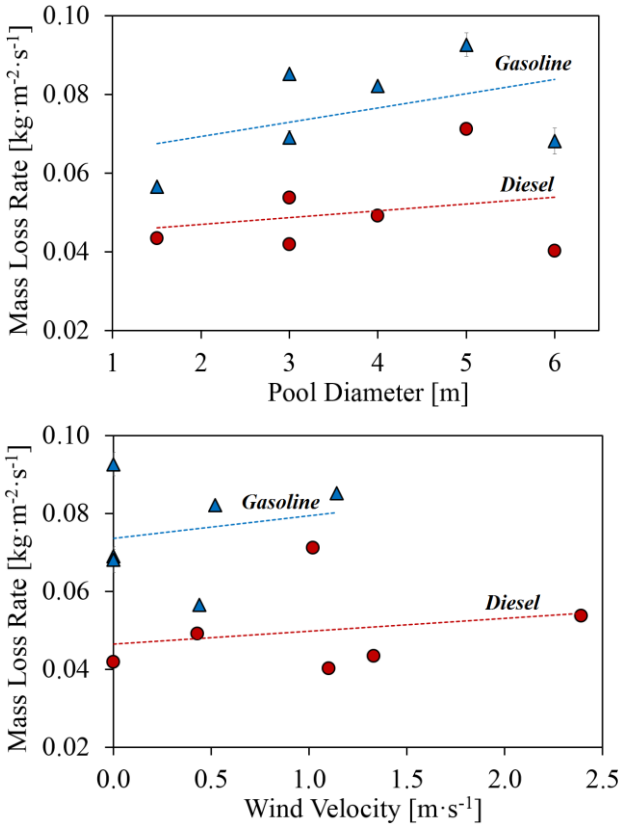

Figure 2.4. Mean values of mass loss rate as a function of the pool diameter (up) and the wind velocity (down) for large-scale pool fires of diesel and gasoline.

Figure 2.5 depicts the mean heat fluxes received by the wide-angle radiometer located at 5D m from the fire origin. As seen, steady values are generally registered regardless of the pool diameter, which may be due to the smoke blockage effect. The soot particles released in the fire plume retain the heat flux emitted by the flames. The occurrence of this phenomenon highlights the importance of prescribing reliable soot yield values for both fuels in CFD codes to obtain reasonable heat flux estimations. On the other hand, the wind considerably affects the radiative heat transfer in large-scale pool fires: the greater the wind velocity, the greater the heat fluxes registered. This occurs as a result of the tilt effect under significant wind speeds, which shorten the separation distance between flames and

the wide-angle radiometer. Therefore, the wind velocity profile must be well defined in CFD codes to increase the agreement reached between simulation results and experimental data in windy pool fire scenarios.

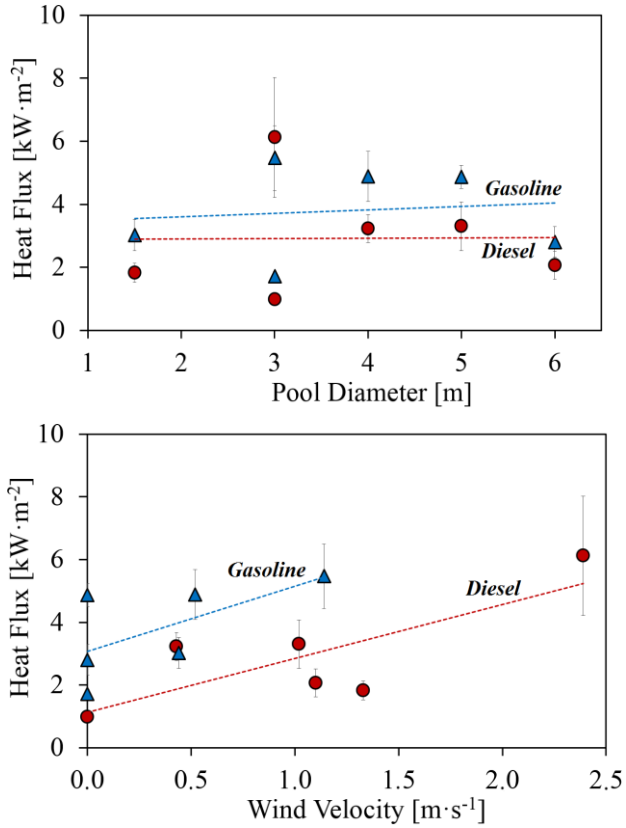

Figure 2.5. Mean values of heat flux received at a 5D m distance from the fire origin obtained as a function of the pool diameter (up) and the wind velocity (down) for large-scale pool fires of diesel and gasoline. Vertical error bars indicate the standard deviation of the measurements.

Figure 2.6 shows the mean dimensionless flame height determined through the IR image segmentation process for diesel and gasoline pool fires as a function of the pool diameter (up) and wind velocity (down). Regardless of the pool diameter and wind velocity, constant flame heights are generally found with greater mean values in gasoline pool fires. In contrast, the mean dimensionless values of flame area (Figure 2.7) and surface emissive power (Figure 2.8) noticeably varied as the diameter of the pool or the wind velocity increased in both liquid fuels. The large amount of smoke generated and the possible changes in wind direction and velocity could have affected the reliability of the image segmentation process by temperature difference criteria. Multiple IR cameras differently located could have allowed a more precise determination of the geometrical features of the flames and thus, of the surface emissive power. In addition, it is worth noting that significant

deviations of the mean flame height, mean flame area and mean emissive power are found all over the pool diameters and wind velocities experimented. In consequence, certain lack of agreement may be found when compared with simulation results.

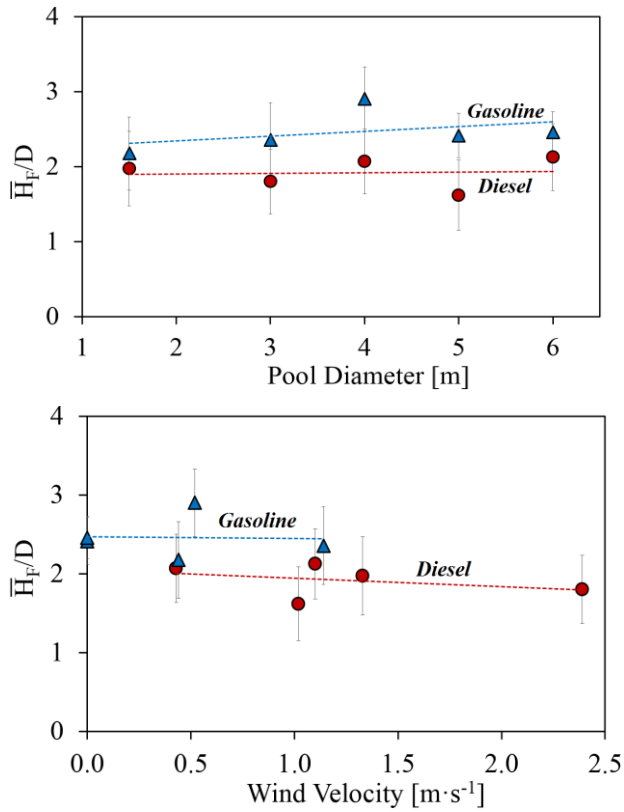

Figure 2.6. Mean dimensionless values of flame height obtained as a function of the pool diameter (up) and the wind velocity (down) for large-scale pool fires of diesel and gasoline. Vertical error bars indicate the standard deviation of the measurements.

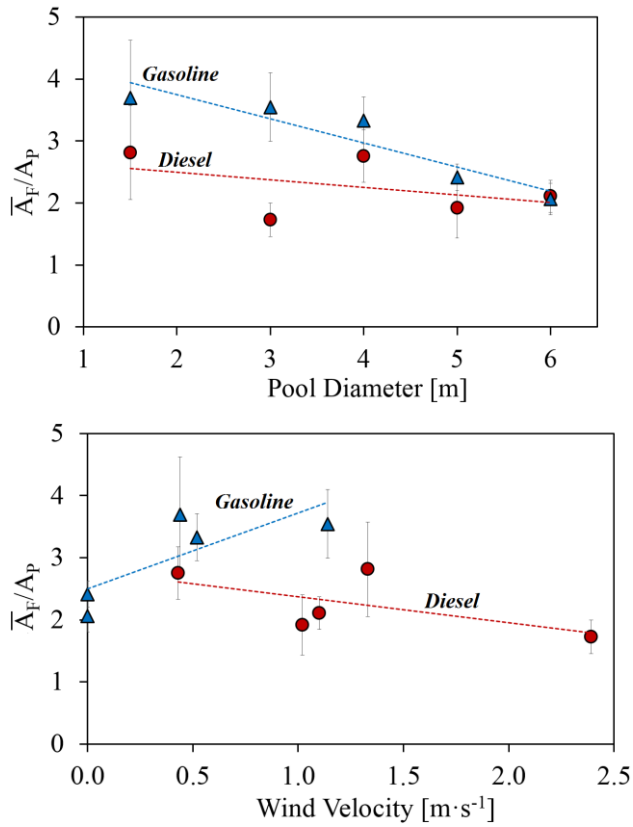

Figure 2.7. Mean dimensionless values of flame area obtained as a function of the pool diameter (up) and the wind velocity (down) for large-scale pool fires of diesel and gasoline. Vertical error bars indicate the standard deviation of the measurements.

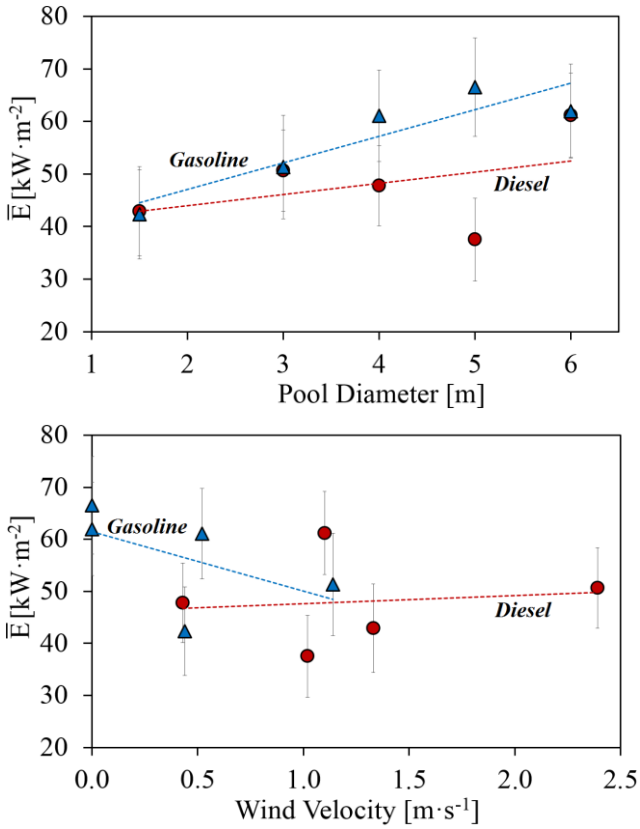

Figure 2.8. Mean values of surface emissive power obtained as a function of the pool diameter (up) and the wind velocity (down) for large-scale pool fires of diesel and gasoline. Vertical error bars indicate the standard deviation of the measurements.

2.2. Vertical sonic jet fires of propane

2.2.1. Experimental set-up

Vertical sonic jet fire tests of propane carried out in an open environment are also considered in this thesis for CFD validation analysis (Gómez-Mares et al., 2010, 2009; Palacios et al., 2012, 2008; Palacios and Casal, 2011). Table 2.2 shows the main conditions at which the jet fire experiments were undertaken. The first figure corresponds to the diameter of the jet orifice in mm, D_{or}, and the second figure the mean mass flow rate of the gas through the exit orifice in kg/s, $\dot{m}_{or}$.

A wide-angle radiometer was located at 5 m distance from the fire origin and 1 m above the exit orifice to record the radiative heat flux. Also, a B-type uncoated thermocouple (0.35 mm-diameter) was located 3.2 m above the gas exit orifice to register the centreline flame axis temperature. The mean ambient temperatures, $\bar{T}_{\infty}$, for the different jet fire experiments were recorded using a meteorological

station located at 10 m height, while the wind velocities, u_w, were accounted for some cases. The mean Reynolds number, $\overline{Re}$, was calculated based on the nozzle diameter, the mean gas exit velocity, the gas density and dynamic viscosity of propane.

Moreover, jet fires were filmed using a VHS camera that registered visible images of the fires (Figure 2.9a) and a thermographic IR camera that recorded the apparent temperature distribution of the flames (Figure 2.9b). The IR image segmentation process undertaken was done as described in Section 2.1.2 for large-scale pool fires. The only difference is that the threshold temperature defined to segment sonic jet fires was of 800 K instead of 600 K, as suggested in different works (Bradley et al., 2016; Gómez-Mares et al., 2009; Palacios et al., 2012; Palacios and Casal, 2011). Figure 2.9c shows a segmented image of G25.5_0.34 jet fire scenario corresponding to one instant of time during the steady state of the fire.

Table 2.2. Main features of the vertical sonic jet fire experiments of propane used in this thesis. Data sources come from (Gómez-Mares et al., 2010, 2009; Palacios et al., 2012, 2008; Palacios and Casal, 2011).

Experiment	D_{or} (mm)	$\dot{m}_{or}$ (kg·s^{-1})	$\overline{u}_w$ (m·s^{-1})	$\overline{T}_\infty$ (ºC)	$\overline{Re}$
D10_0.09	10	0.09	n.a	20	$2.1 \cdot 10^6$
D12.75_0.13	12.75	0.13	1.02	27	$2.7 \cdot 10^6$
D15_0.18	15	0.18	n.a	21	$3.1 \cdot 10^6$
D20_0.27	20	0.27	1.55	22	$4.2 \cdot 10^6$
D25.5_0.34	25.5	0.34	n.a	24	$5.3 \cdot 10^6$

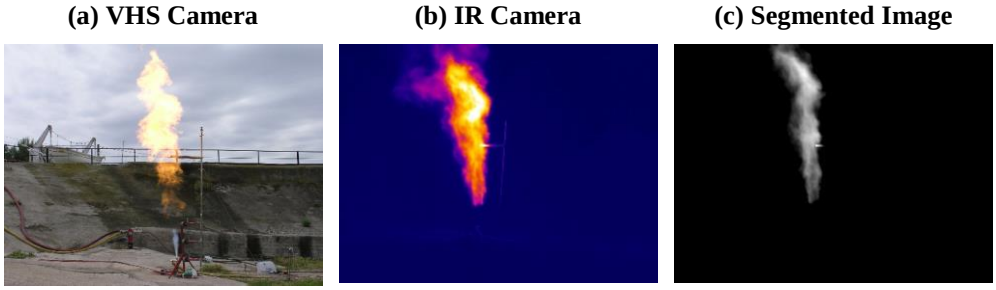

Figure 2.9. Example of video images recorded during the stationary state of the G25.5_0.34 sonic vertical jet fire by means of a) a VHS camera, b) a IR camera and c) the corresponding segmentation process applied.

2.2.2. Data available

Data obtained during the experiments include flame temperature, heat flux captured by the radiometers and flame-geometry descriptors (height and area).

Figure 2.10 shows the mean flame temperature (up) and heat flux (down) obtained as a function of the Reynolds number. Regardless of the experimental sonic jet conditions, the mean flame temperature oscillated between 1100 and 1600 ºC. The type of thermocouple used and the possible inclination of the flames resulting from high wind velocities may have originated these temperature differences. On the other hand, the measured heat fluxes slightly increase as the Reynolds number became greater. The notorious standard deviations found in the D15_0.18 may lead to some disagreements when compared against CFD predictions.

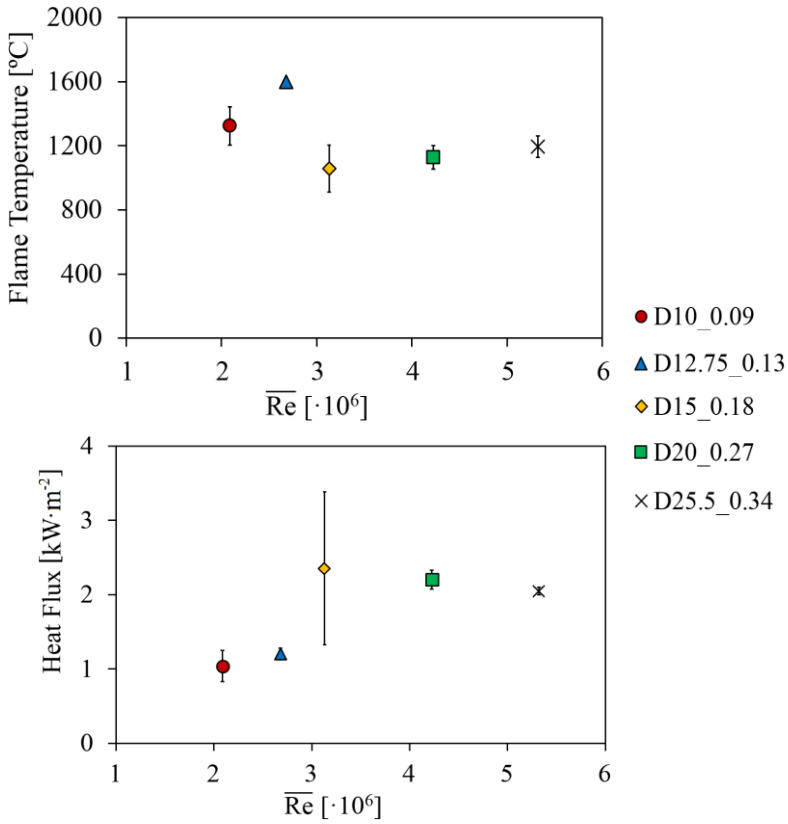

Figure 2.10. Mean values of flame temperature registered by the thermocouple (up) and heat fluxes by the radiometer (down) as a function of the Reynolds number for vertical sonic jet fires of propane. Vertical error bars indicate the standard deviation of the measurements.

Figure 2.11 shows mean dimensionless values of flame height (up) (which include the lift-off distances) and flame area (down) determined through the IR segmentation process. The mean heights of the flames were almost constant despite the unknown wind conditions at which the sonic jet fires were exposed. The lowest mean dimensionless flame height ($\overline{H}_F/D_{or} \sim 300$) is found when $\overline{Re} > 3 \cdot 10^6$, while the rest are maintained around $\overline{H}_F/D_{or} \sim 450$. In contrast, the non-dimensional flame areas constantly decrease as the Reynolds number

increases. This fact remarks that sonic jet flames become thinner and shorter as the Re increases.

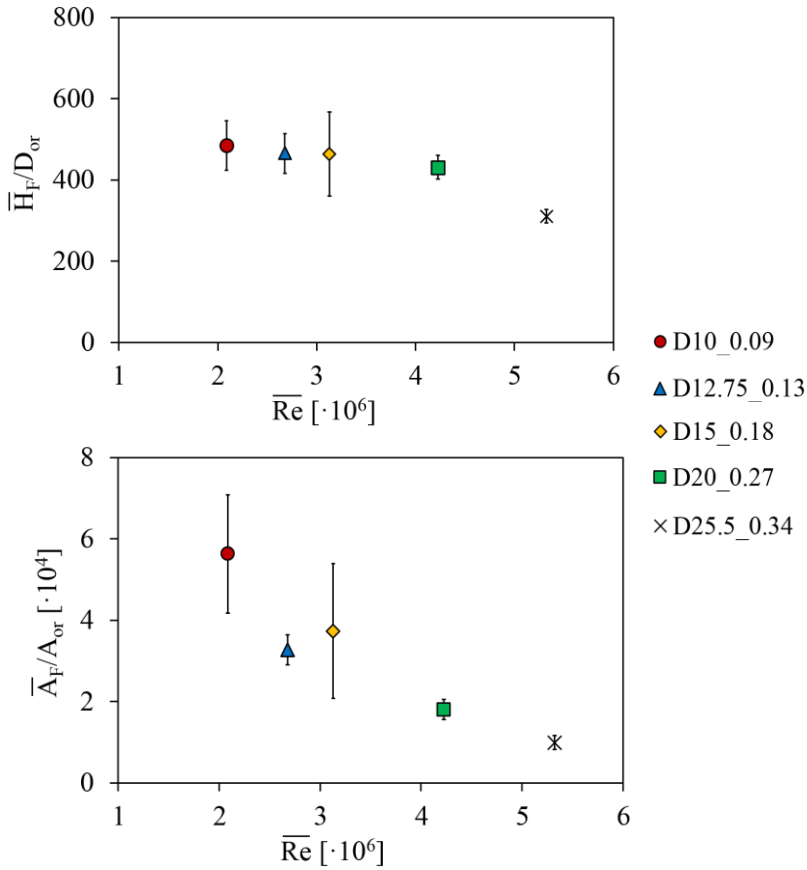

Figure 2.11. Mean dimensionless values of flame height (up) and flame area (down) obtained as a function of the Reynolds number for the vertical sonic jet fires of propane. Vertical error bars indicate the standard deviation of the measurements.

2.3. Vertical subsonic jet fires of methane in normal- and sub- atmospheric pressures

2.3.1. Experimental set-up

A series of vertical subsonic jet fire tests of methane in normal- and sub-atmospheric pressures performed in Hefei (China) are also used in this thesis (Rengel et al., 2019). Table 2.3 shows the five different atmospheric pressures, P_∞, and jet fire conditions examined during the experiments: 0.6 atm, 0.7 atm, 0.8 atm, 0.9 atm and 1.0 atm. As the ambient pressure decrease, other parameters affecting the jet fires development also decrease: the effective amount of oxygen in air, $O_{2,eff}$, the fuel density, ρ_f, the mass flow rate of the gas released through the

orifice, $\dot{m}_{or}$, and the mean Reynolds number, $\overline{Re}$. Each test began when the pressure inside the chamber was stable for a period of about 5 min after pumping fresh air into the low pressure chamber to replace previous air. The duration of each experimental test was 2 min.

Table 2.3. Main features of the vertical jet fire experiments of methane in normal- and sub-atmospheric pressures used in this thesis. Data source come from (Rengel et al., 2019).

Experiment	P_∞ (atm)	$O_{2,eff}$	ρ_f (kg·m^{-3})	$\dot{m}_{or}$ (kg·s^{-1})	$\overline{Re}$
1	0.6	0.12	0.39	$6.7 \cdot 10^{-5}$	$2.6 \cdot 10^{3}$
2	0.7	0.14	0.46	$7.8 \cdot 10^{-5}$	$3.0 \cdot 10^{3}$
3	0.8	0.16	0.52	$8.9 \cdot 10^{-5}$	$3.5 \cdot 10^{3}$
4	0.9	0.18	0.59	$1.0 \cdot 10^{-4}$	$3.9 \cdot 10^{3}$
5	1.0	0.21	0.66	$1.1 \cdot 10^{-4}$	$4.3 \cdot 10^{3}$

2.3.2. Video image segmentation process

A charged-coupled device (CCD) digital camera of sensor size 8.5 mm and an image size of 320 x 240 pixel was used to film the jet fire experiments. The recording frequency was 25 Hz. For each video footage, a video image segmentation process was performed to discriminate the flame region from the background and determine the flame-geometry descriptors of the jet fire experiments. Figure 2.12 shows the main steps followed to segment the images with the Interactive Segmentation Tool® (McGuinness and O'Connor, 2010). First, the frames belonging to the steady state of the fires were individually extracted and imported into the software (Step 1). Then, for each image, a red continuous line was manually drawn to define the flame contour, which could be clearly distinguished through the colourful shapes (Step 2).

Thereupon, an outer contour was also drawn within the background of the image in a yellow continuous line to facilitate the colour distinction between the flame and the rest of the picture (Step 3). Automatically, the Binary Partition Trees algorithm (Adamek, 2006) was applied to segment the image and save it as a binary file (Step 4). After that, the ImageJ® software (Ferreira and Rasband, 2012) was used to convert the binary files created into spreadsheet documents containing a binary matrix where 0 corresponds to background regions and 1 to flame regions. Based on the exit orifice diameter and the dimensions of the imported image, the flame-geometry descriptors were determined for the complete set of segmented images.

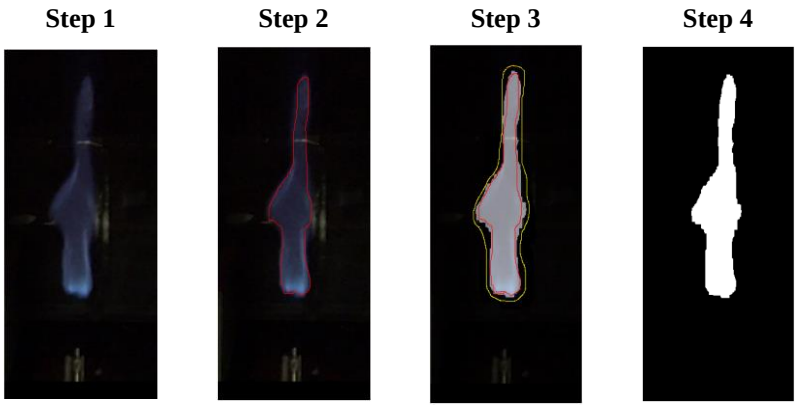

Figure 2.12. Instant captures of a test (atmospheric pressure = 0.7 atm) in the steady state. The four steps followed during the image segmentation process are depicted. Red line depicts the manually drawn flame contour. Yellow line depicts the outer contour.

2.3.3. Data available

Figure 2.13 shows instant captures of the original and segmented images during the stationary state of the different jet fire tests. As it can be seen, the shapes and the colours of the jet flames significantly varied according to the ambient pressure. This may be due to the effective amount of oxygen available, which altered the soot formation rate and the chemical reaction rate (Joo et al., 2013; Lee et al., 2000). At 1.0 atm, there was sufficient oxygen present near the base of the flame to support the reaction of combustion from the nozzle orifice. As the axial distance from the orifice increased, the flame turned to be more yellow and luminous, indicating the oxidation of the soot particles as a result of an incomplete combustion process (Flower and Bowman, 1988). At lower pressures, there was no formation of soot given the lower amount of oxygen particles present in air, hence creating a blue and smaller flame. Indeed, reduced atmospheres lead to premixed flames due to the lower concentration of oxygen molecules, which requires a better fuel/air mixing process to allow the reaction of combustion.

Data related to the geometrical features of the methane jet flames was obtained during the experiments. Figure 2.14 shows the mean dimensionless values of lift-off distance, flame length and equivalent diameter obtained from the image segmentation process as a function of the Reynolds number.

The mean lift-off distances varied according to the ambient pressure: the lower the atmospheric pressure, the larger the flameless distances. This occurred due to the high amount of fuel released downstream the orifice that required a significant amount of oxygen molecules, which were not present at reduced pressures. As the methane gas was diluted into the ambient air, its concentration decreased until the fuel-oxidizer mixture was within the flammability limits. A similar tendency on

the lift-off behaviour was found in the methane jet fire experiments performed by Zeng et al. [20], who examined laminar flames released from 3 mm-diameter nozzles and ambient pressures ranged from 0.5 atm to 1.0 atm.

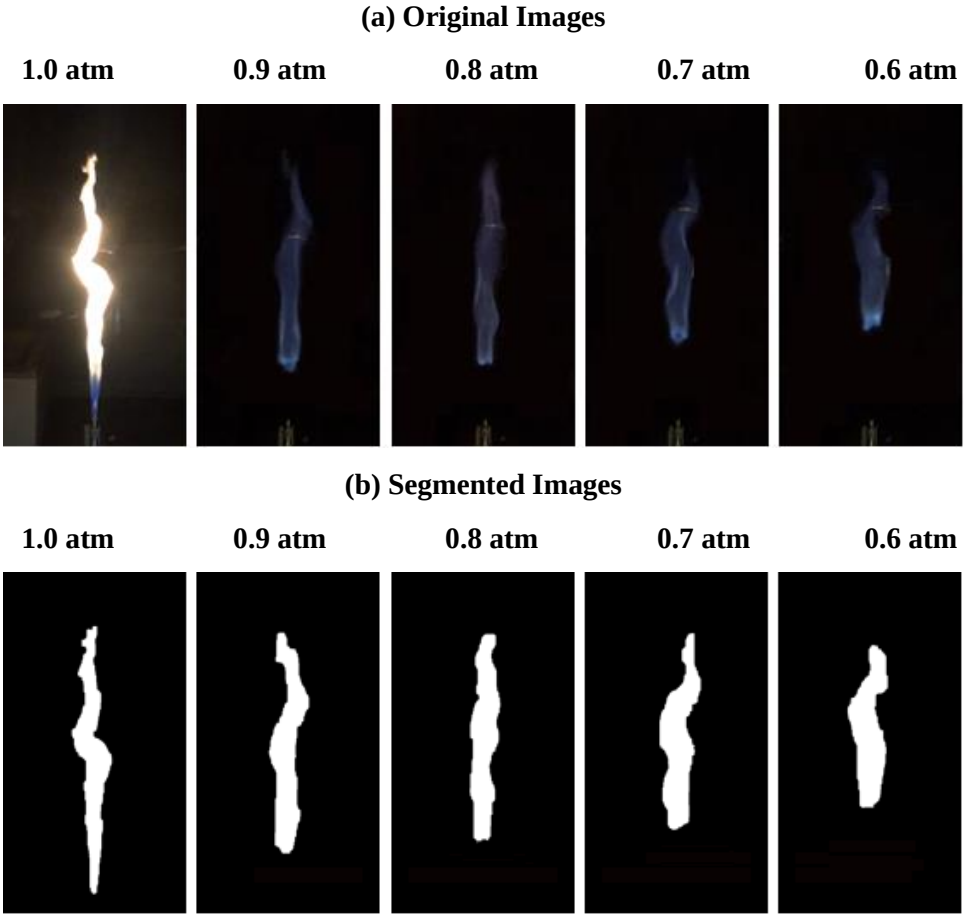

Figure 2.13. Instant captures of (a) original and (b) segmented images obtained during the stationary state of the vertical jet fire experiments of methane in normal- and sub- atmospheric pressures.

The mean flame lengths increased with the Reynolds number, whereas the equivalent diameter remained approximately steady with slight variations. Thus, vertical jet flames of methane became thinner as the ambient pressure decreased. Given the opposite behaviour of the lift-off distance and the radiant flame length, the flame length remained steady regardless the ambient pressure. Therefore, the flames always achieve the same length from the exit orifice and occupy the same area. These values were found to be $\bar{H}_F = 200D_{or}$ and $\bar{A}_F = 3000A_{or}$ (Figure 2.15).

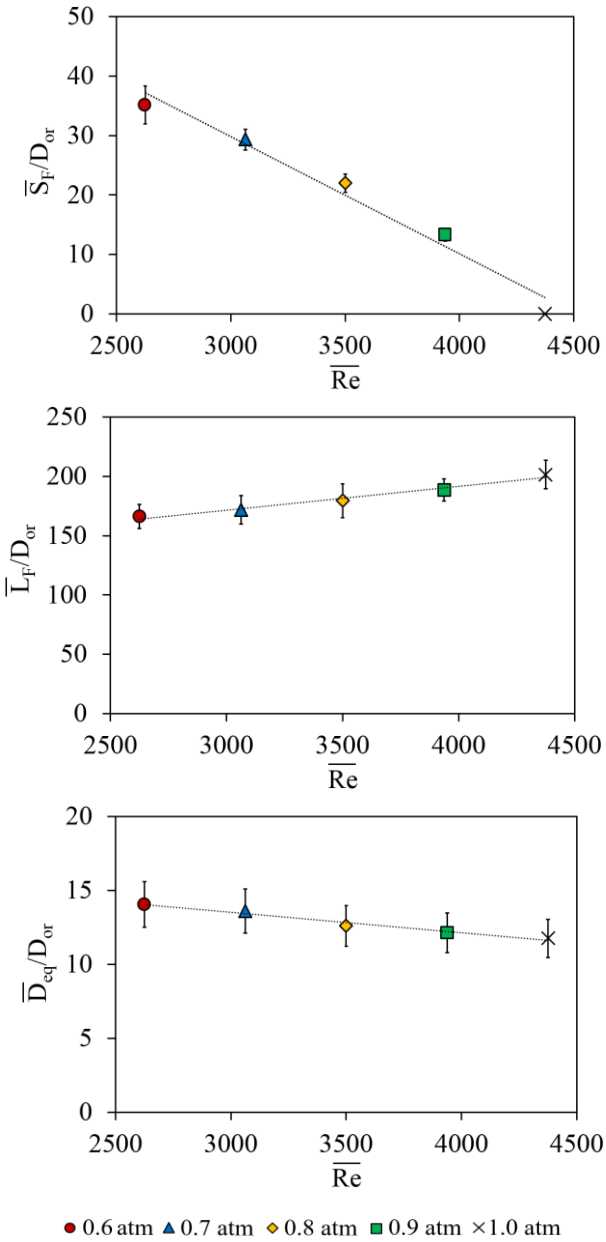

Figure 2.14. Mean dimensionless values of lift-off distance, flame length and equivalent diameter obtained as a function of the Reynolds number for the vertical subsonic jet fire experiments of methane in normal- and sub- atmospheric pressures. Vertical error bars indicate the standard deviation of the measurements.

It is worth noting that sooty flames, such as those occurring at 1 atm, are featured with lower temperatures since the radiative fraction is higher than at sub-atmospheric pressures (Hu et al., 2014, 2013). In addition, jet flames at 1 atm are larger and closer to the nozzle orifice than at reduced atmospheres. Consequently,

in terms of geometrical characteristics, jet flames pose a more hazardous situations at 1 atm than at reduced pressure given the greater possibility of flame impingement in adjacent equipment. However, higher thermal fluxes are expected to be emitted in sub-atmospheric pressures.

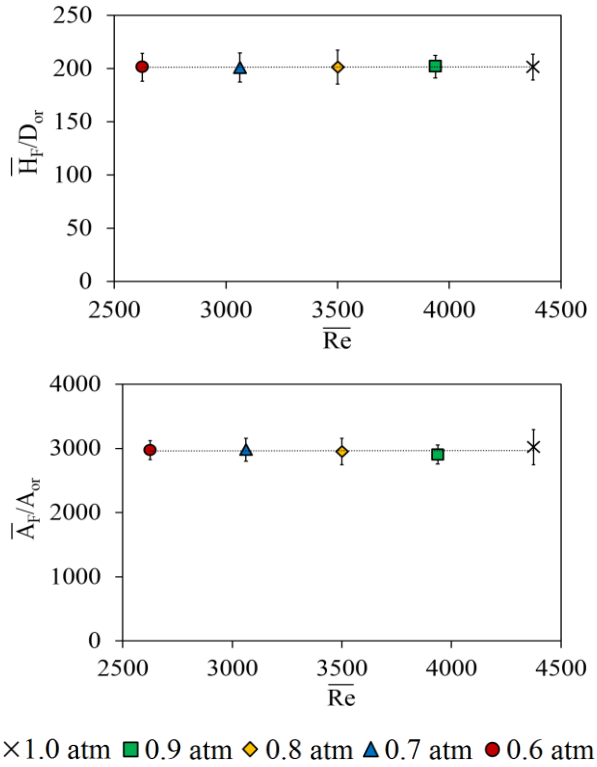

Figure 2.15. Mean dimensionless values of flame length and flame area as a function of the Reynolds number for the vertical subsonic jet fire experiments of methane in normal- and sub-atmospheric pressures. Vertical error bars indicate the standard deviation of the measurements.

2.4. Vertical and horizontal subsonic jet fires of propane

2.4.1. Experimental set-up

Vertical and horizontal subsonic jet fire tests of propane carried out in an open environment are considered in this thesis. The data shown and the measuring devices used can be found in the original reports: (Gopalaswami et al., 2016; Laboureur et al., 2016; Zhang et al., 2015) for horizontal jet fires and (Palacios et al., 2012, 2008) for vertical ones. Table 2.4 summarizes the experimental conditions of the horizontal and vertical jet fire tests. The first figure indicates the jet orientations (i.e. 'V' for vertical ones and 'H' for horizontal ones) followed by the diameter of the nozzle orifice in mm and the second figure indicates the mean

mass flow rate of the gas in kg/s. For this dataset there are no standard deviations reported among the mean values found.

Table 2.4. Main features of the horizontal (Gopalaswami et al., 2016; Laboureur et al., 2016; Zhang et al., 2015) and vertical (Palacios et al., 2012, 2008) subsonic jet fire experiments of propane used in this thesis.

Orientation	Experiment	D_{or} (mm)	$\dot{m}_{or}$ (kg·s^{-1})	$\overline{u}_w$ (m·s^{-1})	$\overline{T}_\infty$ (ºC)	$\overline{Re}$
Vertical	V12.75_0.007	12.75	0.007	0.88	28.8	$6.9 \cdot 10^4$
	V12.75_0.016	12.75	0.016	0.88	28.8	$1.7 \cdot 10^5$
	V20_0.020	20	0.020	1.80	25.0	$1.4 \cdot 10^5$
	V43.1_0.066	43.1	0.066	1.0	25.0	$2.6 \cdot 10^5$
	V43.1_0.142	43.1	0.142	1.0	25.0	$5.7 \cdot 10^5$
Horizontal	H19.05_0.015	19.05	0.015	2.2	30,85	$5.3 \cdot 10^4$
	H19.05_0.016	19.05	0.016	2.2	29.85	$5.6 \cdot 10^4$
	H19.05_0.025	19.05	0.025	2.2	29.85	$8.8 \cdot 10^4$
	H19.05_0.040	19.05	0.040	2.2	29.85	$1.4 \cdot 10^5$
	H19.05_0.042	19.05	0.042	2.2	21.85	$1.4 \cdot 10^5$

Different measuring devices were set-up to register the main variables of interest. A meteorological station was used to measure the ambient temperature and the wind speed. In the case of horizontal jet fires, the wind and the exit orifice were aligned in the same direction. An IR camera located perpendicular to the wind direction was used to register the temperature evolution of the fire tests, from which the mean geometrical parameters of the jet flames were determined: flame length, flame area and lift-off distance. In addition, the surface emissive power was calculated based on the IR camera recordings. A detailed description of the post-processing methods applied can be found in the original reports.

2.4.2. Data available

Figure 2.16 shows the mean dimensionless values of the experimental measurements regarding lift-off distance, flame length and flame area found as a function of the Reynolds number for horizontal (blue) and vertical (red) subsonic jet fires of propane.

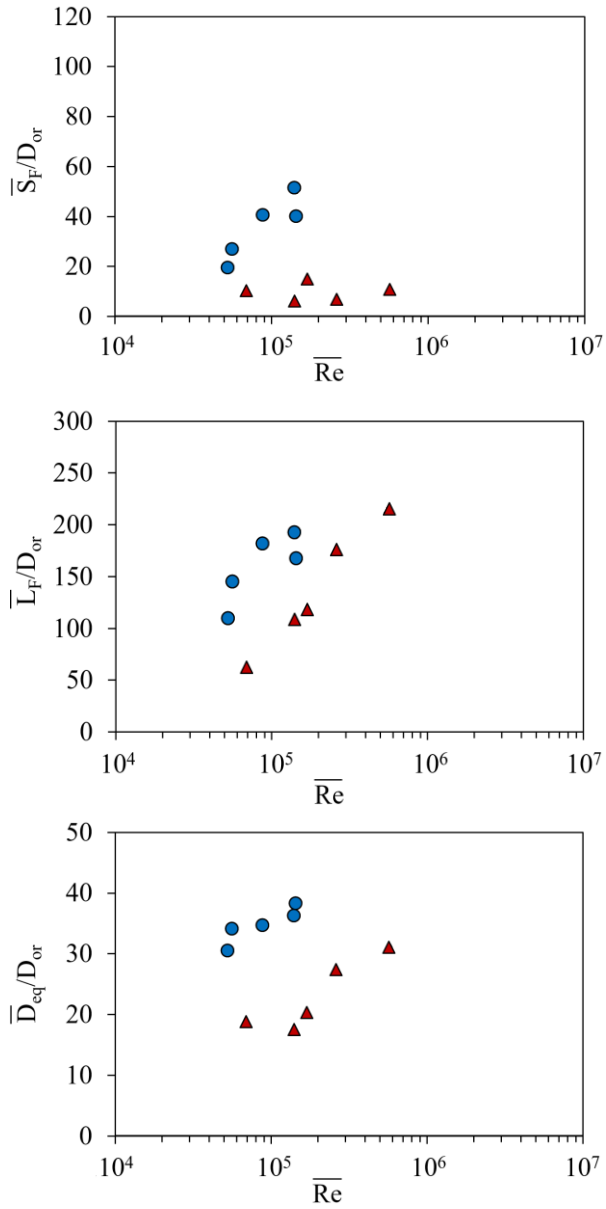

Figure 2.16. Mean dimensionless values of lift-off distance, flame length and equivalent diameter obtained as a function of the Reynolds number for horizontal (○) and vertical (△) subsonic jet fires of propane.

The lift-off distance varied according to the jet fires orientation. In the case of horizontal releases, the lift-off distance considerably increased as the Reynolds numbers became greater. On the other hand, the flameless regions between the exit orifice and the flame base barely varied for vertical flames. In consequence, vertical flames are closer to the equipment surrounding the exit orifice than

horizontal ones. The mean flame lengths increased as a function of the Reynolds number for both types of jet releases, with greater values under horizontal jet flames than vertical ones for a given Reynolds number. Similarly, greater mean equivalent diameters are found in horizontal jet flames than in vertical ones. In particular, slight variations of the equivalent diameters are found in horizontal releases, while these became greater as the Reynolds number increased for vertical jet flames. Therefore, horizontal jet flames are longer and wider than vertical ones possibly due to the influence of the gravitational acceleration on the combustion process, which slows down the vertical velocity of the gas upward the nozzle. As a result of longer and wider flames, horizontal jets are featured with greater flame areas than vertical ones for similar Reynolds numbers (Figure 2.17). In addition, Reynolds numbers lower than 10^6 lead to surface emissive powers ranged between 20 kW/m^2 and 80 kW/m^2 for both types of jet releases.

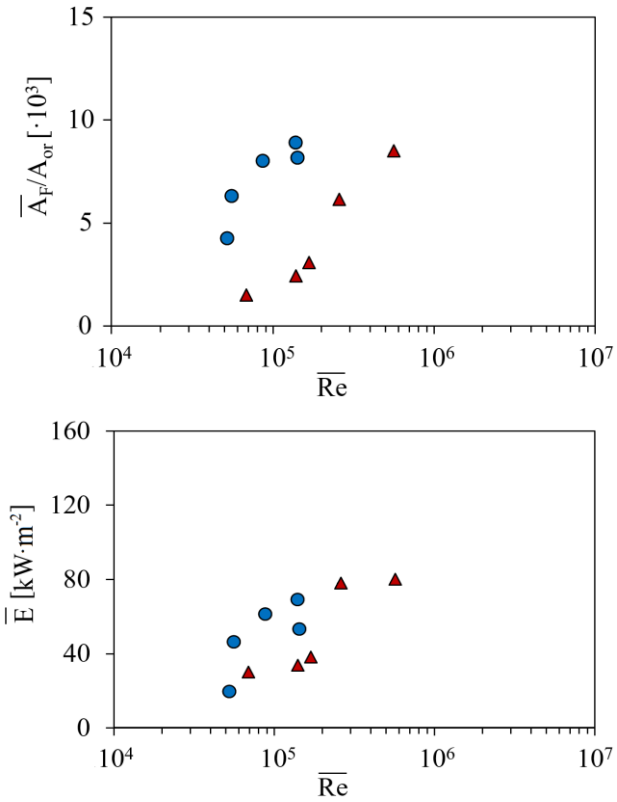

Figure 2.17. Mean values of dimensionless flame area (up) and surface emissive power (down) obtained as a function of the Reynolds number for horizontal (○) and vertical (△) subsonic jet fires of propane.

CHAPTER 3
COMPUTATIONAL FLUID DYNAMICS

The predictive capabilities of three Computational Fluid Dynamics (CFD) codes have been assessed in this thesis: Fire Dynamics Simulator v6.7 (FDS), the fire solver of OpenFOAM v6.0 (FireFOAM 2.2.x) and Flame Accelerator Simulator Fire v10.7 (FLACS-Fire). In particular, FDS and FLACS-Fire are used for modelling large-scale pool fires (Chapter 4), while FDS, FireFOAM and FLACS-Fire are used for modelling jet fires (Chapter 5). Firstly, this chapter individually introduces the codes used to perform validation analysis (Section 3.1) and describes the sub-models solved in each of them to predict the fire development (Section 3.2). Then, the definition of the mesh resolution within the computational domain (Section 3.3) and the measuring techniques applied to estimate the main variables of interest are described in detail (Section 3.4). Next, the qualitative and quantitative methods used to evaluate the predictions found are summarized (Section 3.5). Unless indicated otherwise, the default numerical settings of the CFD codes used, which are described in the present chapter, are the ones used to perform the hydrocarbon fire simulations in this thesis.

3.1. Fire codes

FDS v6.7 is an open source code developed by the National Institute of Standards and Technology (NIST) that numerically solves a form of the Navier-Stokes equations appropriate for low-speed, thermally-driven flow, with an emphasis on smoke and heat transport from fires. FireFOAM 2.2.x is another open-source code developed between CFD Direct and FM Global, based on a set of object-oriented toolboxes written in C++. FLACS-Fire v10.7 is a commercial CFD code developed by Gexcon AS, especially built for quantitative risk assessment applications related to fire hazards in the process industry. The CFD fire codes used consider the low Mach number formulation of the Navier-Stokes equations to reduce the number of equations solved ($M_a \leq 0.3$), hence improving the numerical stability and reducing the computational times.

The numerical model in FDS uses a 2nd order explicit Runge-Kutta scheme. The spatial derivatives are estimated with 2nd order finite differences on a rectangular

grid, with scalar and velocity quantities assigned to the cell center and cell faces, respectively. On the other hand, the equations are advanced in time using a 1st order implicit Euler scheme in FireFOAM, while the convective terms are 2nd order centrally differenced. All quantities are assigned to the cell centres with velocities linearly interpolated to the cell faces. The stability criteria in the explicit schemes applied is regulated through the Courant-Friedrichs-Lewy (CFL) condition, which places a restriction on the time step to maintain physically realizable conditions. In both codes, a CFL default value of 0.8 was defined to avoid a fluid element to traverse more than one cell within a time step hence keeping the implicit temporal and spatial filters consistent in LES turbulence model.

FLACS-Fire uses a 2nd order central difference scheme for resolving diffusive fluxes and a 2nd order so-called *kappa* scheme to resolve the convective fluxes. This last is a hybrid scheme, which does weighting between 2nd order upwind and 2nd order central difference, with delimiters for some equations. The time stepping scheme relies on the CFL numbers based on the speed of sound (CFLC) and flow velocity (CFLV). As recommended in the user's guide, a CFLC of 20 and a CFLV of 2 were set-up for the fire simulations.

3.2. Sub-models solved

The proposed fire codes solve the fundamental conservation equations governing fluid dynamics, coupled with additional sub-models (i.e. turbulence, combustion, radiation and wind) to describe the processes occurring during a fire.

3.2.1. Turbulence

Due to the high-turbulent flows occurring in accidental fires, the exact solution of the governing equations is beyond the capabilities of the most powerful computers. Alternatively, turbulent structures are modelled in a sub-grid scale stress (SGS) that accounts for the important small-scale processes, hence neglecting some of the very small effects derived from turbulent flows. The resolved scales are commonly obtained by introducing the SGS turbulent viscosity, μ_t, on the stress tensor parameter, τ_{ij}, to filter out the unresolvable small scales of turbulence.

Numerous turbulence sub-models have been developed to determine the value of the turbulent viscosity, which arises as a key parameter that governs the turbulence phenomenon on CFD fire simulations. One of the least expensive is used in the FLACS-Fire, the Reynolds Averaged Navier-Stokes (RANS) (Jones and Launder, 1972), which essentially solves the Navier-Stokes equations for the mean flow variables. The $k-\varepsilon$ two-equation eddy viscosity model is used to closure the RANS equations:

$$\mu_t = \rho C_\mu \frac{k^2}{\varepsilon} \tag{3.1}$$

where k is the turbulent kinetic energy, ε is the dissipation rate and C_μ is a model constant experimentally determined with a value of 0.09 (Launder and Spalding, 1974). On the other hand, FDS and FireFOAM use the Large Eddy Simulations (LES) equations, which is very similar to that of RANS with subtle differences in the interpretation of the decomposition of the primitive variables. LES emphasizes spatial filtering by considering the structures smaller than the grid cell size, while RANS emphasizes temporal averaging. In addition, LES does not require additional equations, hence rendering a more realistic-looking flow field than the time-averaged RANS model. However, it is more computational expensive and more grid sensitive; non-reliable results can be obtained if there are not enough cells to describe the flow field (McGrattan and Miles, 2016). Both codes use different LES closure methods. Particularly, FireFOAM uses by default one of the simplest ones, the Smagorinsky model (Smagorinsky, 1963):

$$\mu_t = \rho (C_s \Delta)^2 |S| \tag{3.2}$$

where C_s is a model constant with a value of 0.2 (Lilly, 1967), S is the strain rate tensor and Δ is the LES filter size (i.e. cubic root of the cell volume). The model generally over-predicts the turbulent viscosity in near-wall regions, hence rendering the model unsuitable for certain transitional flows. In order to correct the shortcomings derived from the Smagorinsky model, FDS solves by default the Deardoff turbulence model (Deardorff, 1980). Instead of solving the strain rate tensor, the model mainly depends on the SGS turbulent kinetic energy, k_{sgs}:

$$\mu_t = \rho C_d \Delta \sqrt{k_{sgs}} \tag{3.3}$$

where C_d is a model constant with a value of 0.1 (Pope, 2012).

3.2.2. Combustion

The gas phase combustion refers to the reaction of fuel vapour and oxygen and the associated entrainment of air into the fire plume. FDS, FireFOAM and FLACS-Fire calculate the chemical reaction rate, $\dot{\omega}'''$, between the fuel and the oxidizer via the Eddy Dissipation Concept (Magnussen and Hjertager, 1977):

$$\dot{\omega}''' = \frac{\rho}{\tau_{mix}} min\left(Y_f, \frac{Y_{O_2}}{s}\right) \tag{3.4}$$

where Y_f and Y_{O_2} are the mass fractions of the fuel and the oxygen, respectively, s is the oxygen-fuel mass stoichiometric ratio and τ_{mix} is the mixing time scales. The approach uses the simple chemistry by assuming the 'mixed is burnt'

statement for computational cost reasons. Therefore, the reaction of fuel species and air occurs immediately when fuel and air are available in a cell.

This is an appropriate model when the detailed kinetics of the fuel are not important and when the products of combustion released are known from experimental data (McGrattan and Miles, 2016). The chemistry is simplified into the calculation of mixing time scales, τ_{mix}, which dictate the necessary time to carry out the mixture between the fuel and the oxidizer (Maragkos and Merci, 2017). The main difference between codes using the EDC approach lies on the way they deal with the mixing time scales. In particular, FDS uses a detailed reaction time scale model based on the fastest physical process of the local state of the flow field:

$$\tau_{mix} = max\left[\tau_c, min\left(\tau_d, \tau_a, \tau_g\right)\right] \tag{3.5}$$

where τ_c represents the mixing time scale for chemical species, τ_d for diffusion, τ_a for advection and τ_g for buoyant acceleration. As a result, the total mixing scale solved in FDS can be expressed as:

$$\tau_{mix} = max\left[10^{-4}, min\left(\frac{\Delta^2}{\alpha}, \frac{0.4\Delta}{\sqrt{\left(\frac{2}{3}\right)k_{sgs}}}, \sqrt{\frac{2\Delta}{g}}\right)\right] \tag{3.6}$$

where α is the thermal diffusivity. On the other hand, FireFOAM solves by default a simplified mixing time scale expressed as:

$$\tau_{mix} = C_{EDC}\frac{\varepsilon_{sgs}}{k_{sgs}} \tag{3.7}$$

where $C_{EDC} = 4$ is a model constant (Maragkos et al., 2017) and $\varepsilon_{sgs} = 1.048{k_{sgs}}^{3/2}\Delta^{-1}$ is the sub-grid scale dissipation rate (Fureby et al., 1997). Therefore, the resulting mixing time scale becomes:

$$\tau_{mix} = 4.192\frac{{k_{sgs}}^{1/2}}{\Delta} \tag{3.8}$$

Otherwise, the mixing time scales in FLACS-Fire is resolved as follows:

$$\tau_{mix} = \frac{2.433\left(\frac{\varepsilon}{\nu}\right)^{1/2}\gamma^3\chi}{1-\gamma^3\chi} \tag{3.9}$$

where ν the kinematic viscosity, χ the reacting fractions of fine structures and γ the isentropic ratio determined as:

$$\gamma = min\left(0.8{,}2.13\left(\frac{\nu\varepsilon}{k}\right)^{1/4}\right) \tag{3.10}$$

The formation of soot significantly affects the heat transfer process during the gas-phase combustion due to its capacity to absorb/emit part of the radiative energy of the flame. There exists some detailed models intended to calculate the formation and growth of soot from large fires; however, these require some form of adjustment to provide reasonable predictions. Because of that, the simplified Conversion Factor Model (CFM) is used in the CFD codes to reduce the derived uncertainties of complex soot models and the computational times. The CFM model directly converts a certain fraction of the fuel carbon to soot. To that end, a soot yield value is prescribed in computational simulations, which depends on the fuel used.

3.2.3. Radiation

There are two main models used in CFD fire modelling to solve the radiation transport equation (RTE): the discrete ordinate method (DOM) (Fiveland, 1984) and the discrete transfer method (DTM) (Shah, 1979). The DOM model is used by default in FDS and FireFOAM simulations and the DTM in FLACS-Fire. Both approaches are based on a refined spatial discretization of the RTE through a finite number of solid angles. The calculation of the radiation source term is based on the distance travelled for the rays fired from the surface elements.

The discretization can lead to a non-uniform distribution of the radiative flux for targets far away from the fire plume. This error, which is known as "ray effect", can be lessened by the inclusion of more solid angles. This, in turn, increases the computational cost of the radiation solution proportionally to the number of angles defined. Thus, the radiation phenomenon poses a significant challenge in CFD simulations since it has to be a proper balance between accuracy and computational times. In the simulations proposed, 100 solid angles are defined by default to solve the radiative heat transfer within the computational domains. It was found adequate to provide distributions of the radiant heat flux emitted of fires (Chatterjee et al., 2015). The DOM model uses a complex ray tracing algorithm as follows:

$$\dot{q}_r{}'' = \kappa(4I_b - G) \tag{3.11}$$

where G is the total irradiance, κ is the Planck absorption coefficient and I_b is the black body radiation intensity:

$$I_b = \sigma T^4 \tag{3.12}$$

where is σ is the Stefan-Boltzmann constant. Although FDS and FireFOAM use the DOM model, there exist subtle differences between their applications. FDS

incorporates a correction factor for the I_b estimation, C_r, that is dynamically calculated and is aimed to improve the results accuracy as recommended by the code developers. Differently, the DTM approach used in FLACS-Fire simulations is based on the solution of the radiative heat transfer equation along specified directions:

$$\dot{q}_r{}'' = (1-\varepsilon)G + \varepsilon\sigma T^4 \tag{3.13}$$

Even though the DTM model is theoretically acceptable for fires simulations, it may become computationally expensive.

3.2.4. Wind

Some of the hydrocarbon fire experiments described in Chapter 2 were performed under the presence of wind. In this sense, the wind effect affecting the fire development must be represented in computational simulations. For that purpose, there exist different wind sub-models able to reproduce wind velocities in a given computational domain. For example, FLACS-Fire solves by default the Monin-Obukhov (MO) similarity model (Monin and Obukhov, 1959), which is able to determine the buoyancy effects on the atmospheric boundary layer as follows:

$$u_w \begin{cases} \dfrac{u_\theta}{K}\left[\ln\left(\dfrac{h-h_c+\eta}{\eta}\right) - \psi\left(\dfrac{h}{L}\right)\right] & if\ \eta > 0 \\ u_{ref} & if\ \eta = 0 \end{cases} \tag{3.14}$$

where u_w is the wind velocity at a height h, u_{ref} is the wind velocity measured in the experiments, $\eta = 0.03$ is the ground roughness for open grass terrains (Möller, 1973), $K = 0.41$ is the Von Kármán constant, h_c is the canopy height, which refers to the height above the ground where the vegetation and buildings are located, ψ is a similarity function that is dynamically determined, $L = 100$ is the Obukhov length for stable conditions and u_θ is the velocity friction defined as:

$$u_\theta = \frac{K u_{ref}}{\ln\left(\dfrac{h_{ref}-h_c+\eta}{\eta}\right) - \psi(h_{ref})} \tag{3.15}$$

where h_{ref} is the reference height. It is worth noting that the MO approach can be also used in FDS. Nevertheless, the atmospheric wind conditions are modelled by default in FDS and FireFOAM through the Power Law (PL) wind profile. This approach essentially creates a 'wall of wind' where an entire side of the computational domain is turned into a giant fan blowing air laterally:

$$u_w = u_{ref}\left(\frac{h}{\eta}\right)^p \tag{3.16}$$

where p is the altitude exponent, commonly defined with a value of 0.6, which is a function of the roughness length and the thermal stability of the planetary boundary layer. In addition, there is another available wind model in FDS, which is the so-called Mean Forcing Concept (MFC), that simply consists on adding a forcing term to the momentum equation to represent the wind force throughout the domain in a given direction:

$$\frac{\partial u_i}{\partial t} + \cdots = \frac{u_i(h,t)}{\tau_{ij}} \tag{3.17}$$

3.3. Mesh resolution

The size of the cells probably represents the most important numerical parameter user-defined in CFD simulations. The grid sizes coupled with the numerical methods significantly influence the accuracy of the results and the computational simulation times: the thinner the cell size, the better the computational resolution and the greater the simulation time (Miralles et al., 2014). Therefore, it is necessary to provide a good balance between high grid resolution and reasonable computational costs.

The selection of suitable cell sizes mostly depends on the fire regime. In the case of hydrocarbon accidental fires occurring in industry plants, two main regimes can be identified: (i) one for buoyancy-dominated flames that merges large-scale pool fires and subsonic jet fires and (ii) one for momentum-dominated flames involving sonic and supersonic jet fires. For simulations involving buoyant and subsonic fires, the non-dimensional expression D^*/δ_x is recommended to measure how well the fluid flows in buoyant and subsonic fire regimes (Lin et al., 2010):

$$D^* = \left(\frac{\dot{Q}}{\rho_\infty c_p T_\infty \sqrt{g}}\right)^{(2/5)} \tag{3.18}$$

where D^* is the characteristic diameter of the fire, δ_x is the cell size, $\dot{Q}$ is the heat release rate of the fire, ρ_∞ is the ambient air density, c_p is the specific heat, T_∞ is the ambient temperature and g is the gravitational acceleration. The D^*/δ_x expression can be seen as the number of grid cells spanning the characteristic diameter of the fire, whose values should be ranged between 4 (coarse cell size) and 16 (thin cell size) for being solved adequately (Sally and Kassawara, 2007).

On the other hand, different regimes can be found depending on the nature of the jet fire. Based on a vast data bank covering 880 sets of flame height measurements, Bradley et al. (Bradley et al., 2016) identified the flow regimes of jet flames as a function of the dimensionless flow number for choked and unchoked flow, U^*:

$$U^* = \left(\frac{u_f}{S_L}\right) {Re_L}^{-0.4} \left(\frac{P_i}{P_\infty}\right) \tag{3.19}$$

where u_f is the gas velocity, S_L is the laminar burning velocity, $Re_L = D_{or}S_L/\nu$ is the Reynolds number based on D_{or} and S_L and P_i and P_∞ are the stagnation and ambient pressures, respectively. They noted that buoyant and turbulent subsonic regimes are featured with $U^* < 10$, whereas sonic and supersonic flames with $U^* > 80$. Between both, there is the transition regime from buoyant to momentum-dominated fires. In this sense, the Eq. 3.21 can be applied to subsonic jet fires and those in the early transition regime. Differently, under momentum-dominated flows ($U^* > 80$), the D^*/δ_x correlation is no longer applied and alternative techniques must be used according to the modeller's needs. When possible, sensitivity analysis is recommended to find out the most suitable cell size for the fire scenario of interest.

The domain modelled in FDS and FireFOAM can be divided in multiple meshes contained in different CPU cores. This fact speeds up the computational time and can be of high interest when high resolution is required to simulate complex obstructions. The amount and location of the meshes considered can vary according to the modeller's interests. In contrast, FLACS-Fire simulations are run in one only grid that fills the entire volume under a single CPU core. Given the nature of the experiments, the computational boundaries of the simulations are opened to the outside to allow the external flow to enter and to leave the domain. The *Nozzle* formulation is used in FLACS-Fire simulations, while *Open* vents are applied in FDS and FireFOAM.

The computational domains in the whole codes used are composed by rectangular and isotropic grid cells that varied according to the simulated tests. Round geometries are drawn in FLACS-Fire to represent nozzle orifices and pool bases, while squared ones are drawn in FDS and FireFOAM. FLACS-Fire also incorporates the porosity concept, from which the code is able to estimate the fraction of the area or volume accessible for a fluid to flow: 0 means that the volume is completely blocked and 1 that the volume is completely open.

3.4. Simulation outputs

When performing a CFD validation analysis, experimental data must be compared against simulation results to assess the predictive capabilities of the code. To that end, the parameters measured during the fire tests, which are commonly related to the hazardous fire effects (i.e. temperature, heat flux, emissive power and flame geometry), must be numerically calculated. The following measuring techniques have been applied for the CFD codes used in this thesis. It is pointed out that the whole computational measurements have been registered each 0.50 s.

The temperatures and radiative heat fluxes received at a certain distance from the fire origin are determined through virtual sensors located and oriented as described in the experimental set-up within the computational domain. The flame-geometry descriptors are calculated by means of a slice file (SF) positioned on the centreline axis of the fire, parallel to the wind direction to register the temperatures evolutions. Different post-processors are used to convert the slice files into spreadsheets containing the mean temperatures registered at each cell of the domain simulated: fds2ascii for FDS, ParaView v5.4 for FireFOAM and Flowvis v5 for FLACS-Fire. Then, a normalized threshold temperature, T_r, is applied to perform a segmentation process intended to discriminate the flame region, $I(i,j)$, from the background by comparing the temperature at each pixel element, $T_{i,j}$, with the defined threshold temperature:

$$I(i,j) = \begin{cases} 1, if\ T_{i,j} \geq T_r \\ 0, if\ T_{i,j} < T_r \end{cases} \tag{3.20}$$

where 1 indicates that the pixel is within the flame region and 0 means that the pixel element belongs to the background of the image. This segmentation process, which is based on temperature difference criteria, is identical to the one used for the IR images obtained from the experiments (Section 2.1.2). Pixels with apparent temperatures ≥ 600 K are considered as flames for pool fires and subsonic jet fires (Audouin et al., 1995; Cox and Chitty, 1980), whereas temperatures ≥ 800 K are considered as flames for sonic jet fires (Palacios et al., 2012; Palacios and Casal, 2011). Figure 3.1 depicts the location of the SF within the computational domain and exemplifies the post-processing methodology undertaken to determine the flames shape.

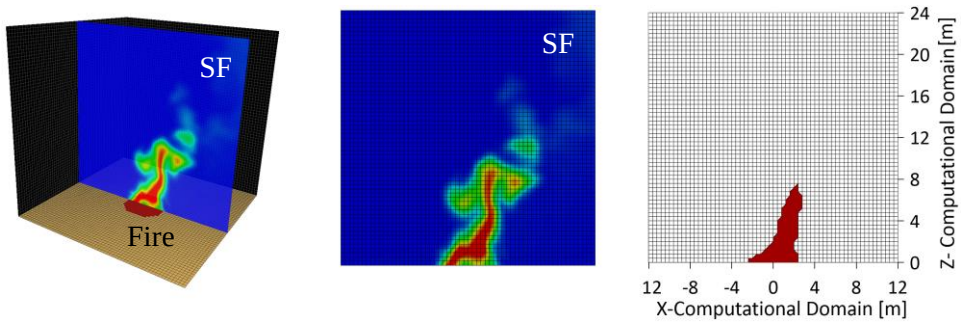

Figure 3.1. Example of a pool fire scenario simulated in FDS: (left) perspective view of the fire; (centre) front view of the temperatures distribution registered in the SF; and (right) flame contour determined by applying the appropriate threshold temperature.

Moreover, the surface emissive power, E, is also obtained in certain fire simulations. To that end, an additional wide-angle radiometer (RD_SEP) is perpendicularly located to the predominant wind direction facing the fire flames (Figure 3.2).

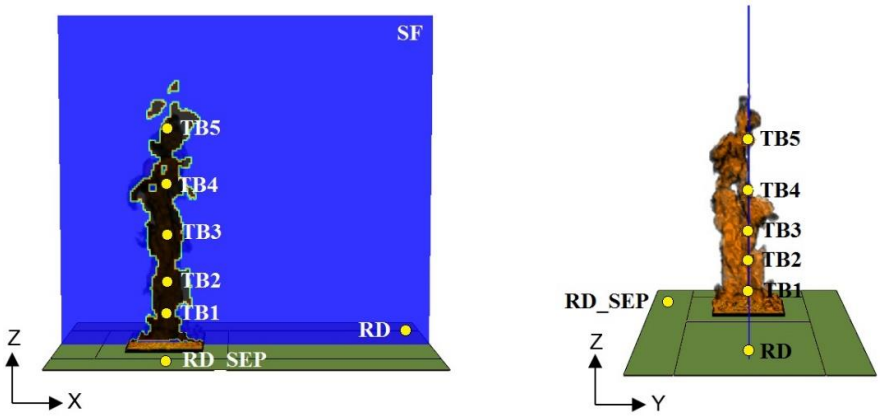

Figure 3.2. Example of a pool fire scenario simulated revealing the location of the RD_SEP defined to calculate the surface emissive power. Data source from (Rengel et al., 2018).

Based on the heat fluxes received by the radiometer and assuming an atmospheric transmissivity of 1, the emissive power of the flames can be calculated as (Mudan, 1984):

$$E = \frac{\dot{q}_r{}''}{\varphi_{F,t}\tau} \tag{3.21}$$

where $\varphi_{F,t}$ represents the view factor between the flame and the radiometer obtained as:

$$\varphi_{F,R} = \sqrt{{\varphi_V}^2 + {\varphi_H}^2} \tag{3.22}$$

where φ_V and φ_H are the vertical and horizontal view factors. Both can be estimated as follows (Mishra, 2010):

$$\varphi_V = \frac{1}{\pi S}\tan^{-1}\left(\frac{h}{\sqrt{S^2-1}}\right) - \frac{h}{\pi S}\tan^{-1}\sqrt{\frac{S^2-1}{S^2+1}} + \frac{Ah}{\pi S\sqrt{A^2-1}}\tan^{-1}\sqrt{\frac{(A+1)(S-1)}{(A-1)(S+1)}} \tag{3.23}$$

$$\varphi_H = \frac{(B-1/S)}{\pi\sqrt{B^2-1}}\tan^{-1}\sqrt{\frac{(B+1)(S-1)}{(B-1)(S+1)}} - \frac{(A-1/S)}{\pi\sqrt{A^2-1}}\tan^{-1}\sqrt{\frac{(A+1)(S-1)}{(A-1)(S+1)}} \tag{3.24}$$

where S, h, B and A are model constants calculated as:

$$S = \frac{2d_R}{D} \tag{3.25}$$

$$h = \frac{2L_F}{D} \tag{3.26}$$

$$A = \frac{h^2 + S^2 + 1}{2S} \tag{3.27}$$

$$B = \frac{1 + S^2}{2S} \tag{3.28}$$

where d_R is the radial distance between the radiometer and the centre of the flame.

3.5. Assessment of the predictions

Qualitative and quantitative comparisons between simulation results and experimental measurements have been carried out to assess the result's accuracy obtained with the CFD codes. In a first instance, scatter plots are performed to graphically illustrate the level of agreement. These represent the mean values of the variables estimated, which are obtained by averaging the simulation results over 30 s during the steady state. Solid diagonal lines indicate perfect agreement between simulated and experimental values, while dotted and long-dashed lines represent the ± 25% and ± 50% prediction error with regard to the measurements, respectively. All graphs include vertical and horizontal bars that represent the standard deviation of the simulation results and the experiments, respectively.

Complementarily, the FB and $NMSE$ methods are determined to quantitatively assess the code's performance (Rew and Deaves, 1995):

$$FB = \frac{1}{n}\sum_{i=1}^{n} 2\frac{x_m - x_p}{x_m + x_p} \tag{3.29}$$

$$NMSE = \frac{1}{n}\sum_{i=1}^{n} \frac{\left(x_m - x_p\right)^2}{x_m x_p} \tag{3.30}$$

where x_m and x_p are the single experimental and predicted values for each time step, respectively; and n is the number of measures. The following performance criteria is adopted to dictate a code as 'valid': the random scatter is within a factor of 2 of the mean ($NMSE \leq 0.5$) and the mean bias is within ± 30% of the mean ($-0.3 \leq FB \leq 0.3$) (Hanna et al., 2004). More details on the both types of assessment techniques can be found in Section 1.2.3.

CHAPTER 4

CFD MODELLING OF LARGE-SCALE POOL FIRES

This chapter includes the investigation of the predictive capabilities of FDS and FLACS-Fire codes when modelling large-scale hydrocarbon pool fires ($D \geq 1$ m). A preliminary sensitivity analysis of the cell size and the computational domain is firstly carried out in both codes to assess their influence on the outcomes obtained (Section 4.1.). Later on, the complete set of large-scale pool fires is simulated by considering the most appropriate modelling features previously found (Section 4.2. and Section 4.3.). Given the notable differences between the mathematical methods applied to solve the CFD sub-models, this study is not aimed at directly comparing both codes (i.e. using identical sub-models choices). The present CFD analysis is intended to reveal the potential of each software separately by applying the most appropriate modelling options for each tool. Based on a qualitative and a quantitative assessment of the predictions found (i.e. flame temperature, burning rate, heat flux, flame length, flame surface and surface emissive power), the main strengths and weaknesses of FDS and FLACS-Fire are identified. The work presented in this chapter have been presented in the *2nd SFPE Europe Fire Safety Engineering Conference & Expo* and in the *10th World Congress of Chemical Engineering* as well as published in the paper entitled *A priori validation of CFD modelling of hydrocarbon pool fires* at Journal of Loss Prevention in the Process Industries (Rengel et al., 2018).

4.1. Analysis of cell size and computational domain

Model predictions are highly sensitive to uncertainties in input data, to the level of rigour used in modelling the relevant physics and chemistry of the fire and to the accuracy of numerical treatment (Hasofer, 2009). Input data are defined as provided from the experiments, whereas the sub-models solved and the numerical schemes are commonly defined by the code developers. Therefore, there are many modelling parameters affecting the estimations reached that cannot be modified. Chapter 3 provides more details about the mathematical equations solved and the constants considered by default in CFD fire codes.

Nevertheless, there are some user-defined parameters that may have a significant impact on the simulation outcomes. For example, the cell sizes defined in CFD simulations have a direct influence on the turbulent viscosity solved under the LES approach, μ_t, and the mixing scale times solved in the EDC combustion model, τ_{mix}. Similarly, the computational domain, which is often defined according to the obstacles dimensions and their locations, may affect the amount of air entrained and mixed with the combustible gases. Also, it must be large enough to simulate the entire flame shape and its effects.

As previously discussed, both parameters may greatly affect the predicted fire development and its related hazardous effects. Consequently, it is essential to determine the most precise cell sizes and computational domains prior to perform simulations aimed to assess the effects of large-scale pool fires. To that end, a preliminary sensitivity analysis is proposed, which consists on running numerous CFD fire simulations under different cell sizes and computational domains. The results obtained are qualitatively compared against experimental data to determine the most appropriate ones: the closer the agreement reached, the more suitable the modelling conditions defined.

Firstly, there is a short description of the fire scenarios used and the modelling settings applied in FDS and FLACS-Fire. Then, the mesh size is firstly evaluated given its greater influence on the predicted results, especially in the turbulence and combustion sub-models. Based on the most suitable cell size results, five cubic computational domains are then assessed.

4.1.1. Fire scenarios and modelling settings

Table 4.1 gathers data regarding the gasoline and diesel pool fires of 3 and 6 m-diameter at 0 and 3 m/s wind speeds considered for sensitivity analysis. In the first column, the first figure corresponds to the diameter of the pool in meters followed by the liquid fuel (i.e. 'G' for gasoline and 'D' for diesel) and the second one indicates if there is a presence of wind in the fire scenario (i.e. 0 for windless scenarios and 1 for windy scenarios).

The mean flame height obtained in the experimental tests, $\overline{H}_F$, are compared against those determined in FDS and FLACS-Fire through a 2D temperature slice file. For all the simulations performed, an ambient temperature of 293 K is defined, a soot fraction of 0.12 kg/kg is considered for the reaction of combustion for both fuels (Kent and Honnery, 1987) and the burning rates are prescribed according to the experimental data. Simulations are run for 60 s to achieve long-duration steady states of the fires in an Intel® Xeon® E5 2.20 GHz with 256 GB RAM. Table 4.2 summarizes the sub-models solved in both codes for the analysis of the cell size and the computational domain. More details about the mathematical correlations and models constants applied can be found in Section 3.2.

Table 4.1. Pool fire scenarios considered for assessing the cell size and computational domain influence in FDS and FLACS-Fire simulations.

Fire Scenarios	D (m)	Fuel	$\bar{u}_w$ (m·s^{-1})	$\dot{m}$ (kg·s^{-1})	$\bar{H}_F$ (m)
3G_W0	3	C_6H_{14}	0	0.51	6.58
3G_W1	3	C_6H_{14}	1.5	0.60	6.50
3D_W0	3	$C_{12}H_{26}$	0	0.30	5.65
3D_W1	3	$C_{12}H_{26}$	1.5	0.40	5.57
6G_W0	6	C_6H_{14}	0	1.92	11.74
6G_W1	6	C_6H_{14}	3	2.09	11.64
6D_W0	6	$C_{12}H_{26}$	0	1.30	10.44
6D_W1	6	$C_{12}H_{26}$	3	1.50	10.33

Table 4.2. CFD sub-models solved in FDS and FLACS-Fire simulations for the preliminary sensitivity analysis.

CFD Sub-models	FDS	FLACS-Fire
Turbulence	**LES** $\mu_t = \rho C_d \Delta \sqrt{k_{sgs}}$	**RANS** $\mu_t = \rho C_\mu \frac{k^2}{\varepsilon}$
Combustion	**EDC** $\tau_{mix} = max[\tau_c, min(\tau_d, \tau_a, \tau_g)]$	**EDC** $\tau_{mix} = \frac{2.433\left(\frac{\varepsilon}{\nu}\right)^{1/2}\gamma^3\chi}{1-\gamma^3\chi}$
Radiation	**DOM** $\dot{q}_r'' = \kappa(4I_b - G)$ $I_b = C_r\sigma T^4$	**DTM** $\dot{q}_r'' = (1-\varepsilon)G + \varepsilon\sigma T^4$
Wind	**PL** $u_w = u_{ref}\left(\frac{h}{\eta}\right)^p$	**MO** $u_w = \frac{u_\theta}{K}\left[\ln\left(\frac{h-h_c+\eta}{\eta}\right) - \psi\left(\frac{h}{L}\right)\right]$

4.1.2. Cell size

The 3G_W0 and 6G_W0 are the scenarios modelled for the cell size assessment because there is no presence of wind affecting the fire behaviours. Also, the noted scenarios are the ones where the highest flame heights were found 3 and 6 m-diameter. The computational domains set-up were of 3D (Length) x 3D (Width) x 8D (Height) to predict the entire shape of the flames. Figure 4.1 depicts the mean flame heights obtained in FDS and FLACS-Fire for the two fire scenarios based

on the D^*/δ_x recommended values (see Section 3.3). Black dotted lines indicate the experimental flame height of each fire scenario.

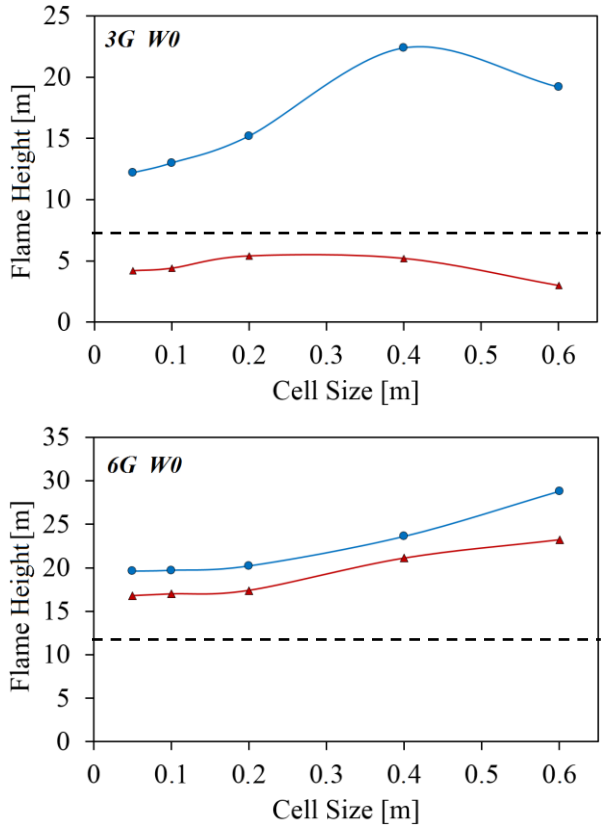

Figure 4.1. Mean flame height evolutions of the 3G_W0 (up) and 6G_W0 (down) fire scenarios obtained in (▲) FDS and (●) FLACS-Fire under different cell sizes.

As it can be observed, similar mean flame height are found in FLACS-Fire under cells ranged from 0.05 to 0.2 m and in FDS from 0.05 to 0.4 m. Regardless of the fire scenario assessed, significant over-predictions are found in FLACS-Fire: the greater the cell size, the more notable the over-estimation achieved. On the other hand, under/over estimations are found in FDS for 3 and 6 m-diameter scenarios, respectively, with less noticeable variations among the cell sizes tested. In general, the thinner the cell size, the better the agreement reached in FDS simulations. According to these results, it is noted that the maximum cell size able to reasonably predict the mean experimental flame height in both CFD codes should be of 0.2 m.

4.1.3. Computational domain

Five different cubic computational domains have been used in this analysis, with the cube side changing as a function of the pool diameter: 3D, 4D, 6D, 8D and

10D. Figure 4.2 and Figure 4.3 show the mean flame height obtained for pool fires of 3 m and 6 m-diameter, respectively, simulated in both CFD codes by considering a uniform mesh composed by cells of 0.2 m. The diagonal straight line indicates the height of the computational domain, while the dotted one represents the maximum experimental flame height, which corresponds to the windless gasoline pool fires.

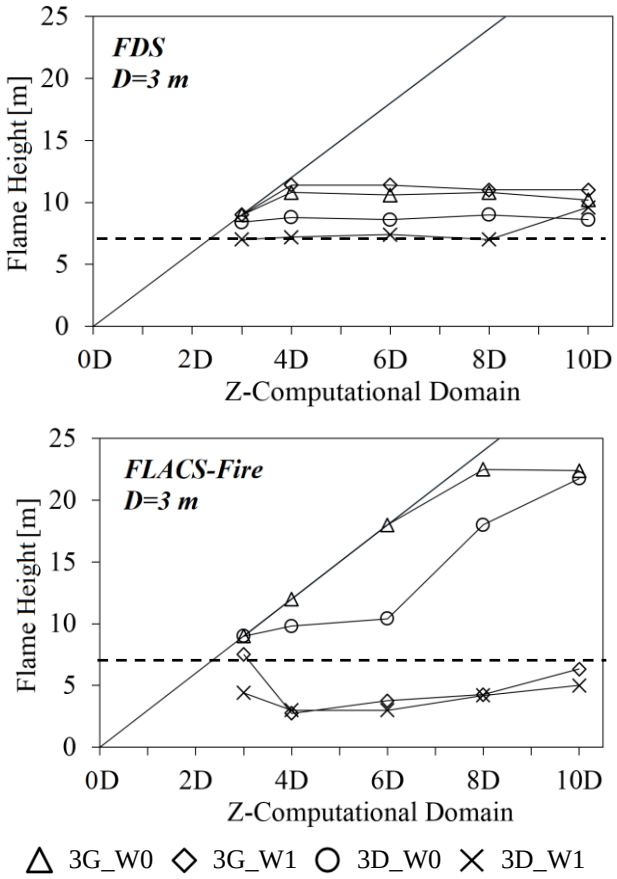

Figure 4.2. Mean flame heights obtained for the 3 m-diameter pool fire scenarios simulated in FDS (up) and FLACS-Fire (down) under different computational domains.

As it can be seen, windless pool fire simulations commonly reached the maximum computational heights under the 3D domain in both fire codes. Nevertheless, for greater domains, the predictions found in FDS barely varied regardless of the fire scenarios modelled. Therefore, it is noted that the domain defined in FDS had a negligible influence on the simulation results. On the other hand, noticeable variations on the mean flame heights are found in FLACS-Fire as the domain varied, especially in the windless fire scenarios. In particular, pool flames achieved the top of the computational domain under the 3D, 4D and 6D cases. Because of

that, larger domain heights should be defined in FLACS-Fire to represent the whole flame surface.

Both CFD codes tended to over-estimate the experimental flame heights in most pool fire simulations in the absence of wind. The greatest differences between predictions and experiments are achieved in FLACS-Fire. In contrast, under-estimations are often found in both CFD codes in the presence of wind, especially under 6 m-diameter pool fires. This is mainly due to the lateral wind forces that inclines the flames, hence leading to shorter flames than in windless fire scenarios.

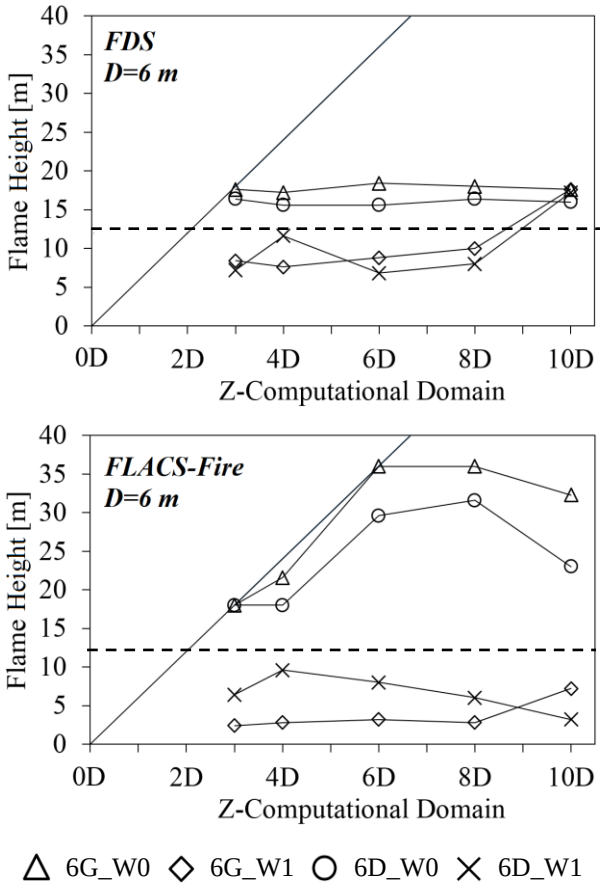

Figure 4.3. Mean flame heights obtained for the 6 m-diameter pool fire scenarios simulated in FDS (up) and FLACS-Fire (down) under different computational domains.

Table 4.3 shows the absolute differences of the mean flame heights predicted as a function of computational domains. These have only been reported when the whole flame surface is contained within the domains compared. The lowest absolute differences between domains corresponds to FDS (~1.35 m), while the highest ones correspond to FLACS-Fire (~2.65 m). Consequently, it is demonstrated that FDS arises as the least affected code by the domain dimensions,

whereas FLACS-Fire results are strongly influenced. Particularly, the smallest deviations of the flame height obtained in FDS (~0.60 m) are found when simulated between 4D and 8D domains. In contrast, noticeable absolute differences are obtained in FLACS-Fire despite the domains modelled.

Table 4.3. Absolute differences of the mean flame heights predicted between computational domains as a function of the fire scenarios simulated and the CFD code used.

Fire Scenarios	CFD Code	3D-4D	4D-6D	6D-8D	8D-10D
3D_W0	FDS	0.40	0.20	0.40	0.40
	FLACS	n.a.	0.60	7.60	4.00
3D_W1	FDS	0.20	0.20	0.40	2.60
	FLACS	1.40	0.00	1.20	0.80
3G_W0	FDS	n.a.	-0.20	0.20	0.60
	FLACS	n.a.	n.a.	n.a.	0.20
3G_W1	FDS	n.a.	n.a.	0.40	0.00
	FLACS	4.80	1.00	0.40	2.20
6D_W0	FDS	0.80	0.00	0.80	0.40
	FLACS	n.a.	11.60	2.00	8.60
6D_W1	FDS	4.40	-2.20	1.20	9.20
	FLACS	3.20	-1.60	2.00	2.80
6G_W0	FDS	0.40	1.20	0.40	0.40
	FLACS	n.a.	n.a.	n.a.	3.80
6G_W1	FDS	0.80	0.80	1.20	7.60
	FLACS	0.40	0.40	0.40	4.40

The computational time arises as another key factor when determining the most suitable domain. Table 4.4 shows the mean time required to simulate a second per CPU-core according to the number of cells defined. As expected, the smaller the domain modelled, the lower the time required to complete simulations. Given the large flame height obtained, the prediction's deviations between domains and the computational time, the 8D domain is the minimum recommended for both codes to simulate large-scale pool fires in open environments. Greater domains may be modelled with no impact on the simulation results; however, computational times would significantly increase.

Eventually, the domain width (X and Y axis) may be diminished to reduce the number of cells and thus, the computational times. Figure 4.4 and Figure 4.5 show

the mean flame height obtained for windless pool fires of 3 m and 6 m-diameter, respectively, simulated in both CFD codes as a function of the width modelled. The computational height is of 8D according to previous recommendation.

Table 4.4. Mean time required to simulate a second per CPU-core according to the number of cells modelled. Time is expressed in minutes.

Computational Domain (per axis)	Nº of Cells	Time in FDS	Time in FLACS
3D	91,125	0.93 ± 0.25	4.25 ± 1.93
4D	216,000	1.37 ± 0.50	7.62 ± 3.37
6D	729,000	20.58 ± 6.76	25.70 ± 2.73
8D	1,728,000	56.47 ± 8.28	53.76 ± 2.29
10D	3,375,000	162.96 ± 8.17	167.89 ± 23.77

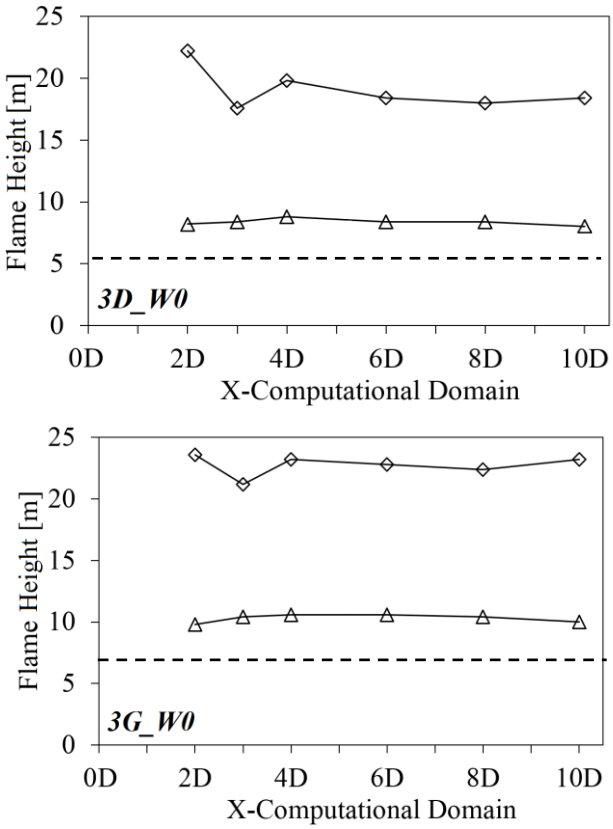

Figure 4.4. Mean flame height obtained for the 3 m-diameter windless pool fire scenarios of diesel (up) and gasoline (down) simulated in (△) FDS and (◇) FLACS-Fire under different X-computational domains.

As it can be observed, the computational width had a negligible influence as the results obtained slightly varied in FDS (± 0.54 m) and FLACS-Fire (± 1.62 m). Therefore, cubic domains are not necessary if there are no other objects or geometrical restrictions that must be included within the volume modelled.

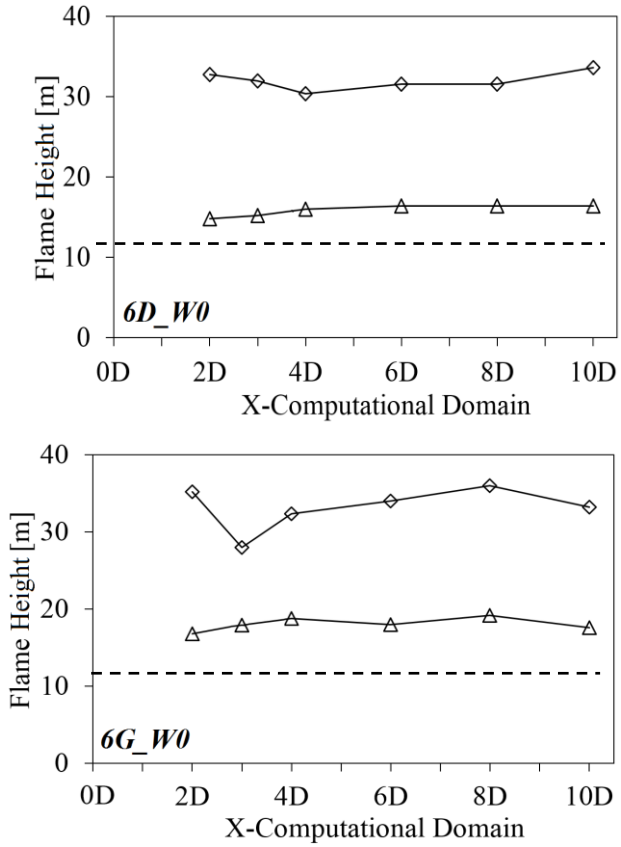

Figure 4.5. Mean flame height obtained for the 6 m-diameter windless pool fire scenarios of diesel (up) and gasoline (down) simulated in (△) FDS and (◇) FLACS-Fire under different X-computational domains.

4.2. *A priori* validation analysis

In general, there are two types of CFD validation analysis techniques: *a posteriori* or open simulations (Jahn et al., 2011) and *a priori* or blind simulations (Torero et al., 2009). In *a posteriori* simulations, the user has complete access to the experimental data (i.e. fuel source, ventilation conditions, mass loss rate, etc.). Modelling parameters can be modified if necessary to improve the agreement reached between simulation results and measurements. *A posteriori* simulations were shown to satisfactorily reproduce the general fire behaviour in previous works (Jahn et al., 2008; Lazaro et al., 2008). In contrast, in *a priori* simulations

the user has no information about the experimental results and has access only to a brief description of the initial scenario conditions. Consequently, the user is responsible for developing appropriate modelling assumptions in order to obtain reasonable predictions of the fire scenario of interest.

Furthermore, blind simulations are commonly performed in fire hazard assessment studies, where the modeller has to estimate the consequences of the possible fire scenarios (Fu et al., 2016). Consequently, *a priori* validation analysis is necessary to assess the predictive capabilities of CFD codes and to quantify the uncertainties that can be reached. This section presents *a priori* CFD simulations performed in FLACS-Fire and FDS aimed at reproducing large-scale pool fire experiments of diesel and gasoline. More details about the experimental data can be found in Section 2.1.

4.2.1. Numerical modelling

In *a priori* simulations, the fuel mass loss rate is unknown and thus, it should be estimated by means of the fuel evaporation models implemented in the CFD codes. Prior to the liquid ignition, the evaporation process of fuel should generate a certain volume of flammable gases over the liquid fuel layer. In FLACS-Fire, the evaporation rate of the liquid fuel is determined through a heat transfer balance dominated by the heat from the flame, the sun and the substrate. In order to accelerate the formation of the combustible gas cloud downstream the pool, a ground temperature of 490 K and 341 K is set-up for diesel and gasoline pools, respectively. These values correspond to the boiling temperatures of each compound at which their vapour pressures are equal to the atmospheric pressure, hence changing their states from liquid to gas. Higher temperature values have not been proposed to avoid possible numerical instabilities. After a while, a heat source is settled just above the liquid surface to allow the ignition of the combustible gases released.

The liquid evaporation rate in FDS is calculated as a function of the temperature of the liquid and the fuel vapour pressure, as presented by Sikanen and Hostikka (Sikanen and Hostikka, 2016). Regardless of the fuel layer depth, the liquid is treated as a thermally-thick solid to consider the heat conduction within the pool. The evaporation model directly allows the flame ignition of gasoline pools due to vapour pressure of the compound. On the other hand, a static particle at 800 K remained during a short period of time above the diesel pools to heat the liquid fuel, hence allowing the evaporation and ignition of the flammable gases. Table 4.5 summarizes the thermal properties of both liquid fuels (diesel (Sikanen and Hostikka, 2017) and gasoline (Sudheer, 2013)) used for solving the reaction of combustion in FDS.

The sub-models solved and constants applied are those described in Table 4.2. According to the previous cell size analysis, a uniform cell size of 0.2 m is defined for the whole set of simulations run in FLACS-Fire. Similarly, a cell size of 0.2 m is also defined for FDS simulations; however, smaller ones of 0.05 m and 0.10 m are located near the liquid pool region to improve the accuracy of the evaporation rate as proposed by Sikanen and Hostikka (Sikanen and Hostikka, 2016). Multiple meshes are used in FDS to speed up the computational calculations. The amount and location of the meshes considered in the fire scenarios simulated varied according to the fire experiment simulated and the boundary conditions. The computational domains set-up in both codes were of 4D (L) x 4D (W) x 8D (H) to predict the entire shape of the flames. In previous experiments, it was found that the steady state of gasoline and diesel fires are approximately achieved 50 and 100 s after the ignition occurs, respectively (Muñoz et al., 2004). Because of that, numerical simulations are set to run for 150 s to achieve long-duration steady state in both CFD codes (> 30 s).

Table 4.5. Thermal properties of the pool liquid fuels required to solve the fuel evaporation and the reaction of combustion in FDS.

Parameter	Units	Diesel	Gasoline
Density	$kg \cdot m^{-3}$	749	750
Specific heat	$kJ \cdot kg^{-1} \cdot K^{-1}$	2.4	2.06
Conductivity	$W \cdot m^{-1} \cdot K^{-1}$	0.18	0.11
Absorption coefficient	m^{-1}	300	200
Heat of reaction	$MJ \cdot kg^{-1}$	42.0	44.4
Boiling temperature	ºC	215.8	68
Soot yield	$kg \cdot kg^{-1}$	0.12	0.12
Carbon monoxide yield	$kg \cdot kg^{-1}$	0.012	0.010

Simulation measurements include flame temperatures at different heights above the liquid fuel, radiative heat flux and surface emissive power of the flames, fuel mass loss rate and the geometrical features of the flames (height and area,. In particular, the emissive power was obtained through an additional wide-angle radiometer located at 4.5 m from the fire base and 0.5 above the ground facing the flames perpendicular to the predominant wind direction.

4.2.2. Assessment of the predictions

Table 4.6 summarizes the FB and $NMSE$ statistical values determined for the variables predicted in the different fire scenarios. Italic blue values indicate that the measurement is within the performance criteria.

Flame temperature

The predicted flame temperatures are obtained by averaging the mean values registered on the different thermocouples set-up for each fire simulation. As it can be seen in Figure 4.6, notable discrepancies are found between simulation results and experimental data. In particular, the mean flame temperatures meet the performance criteria in the 8% of the simulations performed in both CFD codes. This significant lack of agreement reached may be partly due to certain measuring errors derived during the tests. The thermocouples used were of 3 mm-diameter and thus, thinner thermocouples would have probably led to more accurate temperature results.

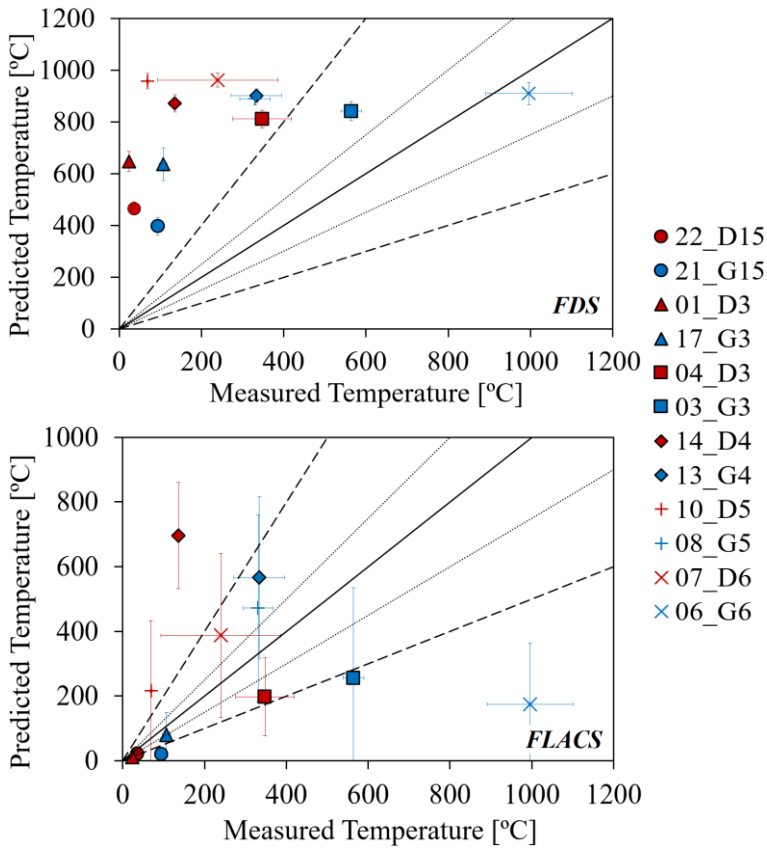

Figure 4.6. Mean temperatures obtained for the large-scale pool fires simulated in FDS (up) and FLACS-Fire (down).

Table 4.6. FB and NMSE measurements of the main variables of interest obtained in FDS and FLACS-fire for the large-scale pool fires simulated. Italic blue values indicate that the measurement is within the performance criteria established.

Fire Scenarios	Statistical Measurements	T_F		$\dot{m}''$		$\dot{q}_r''$		H_F		A_F		E	
		FDS	FLACS	FDS	FLACS	FDS	FLACS	FDS	FLACS	FDS	FLACS	FDS	FLACS
22_D15	*FB*	-1.71	0.49	*-0.30*	-0.46	1.30	1.35	-0.47	-1.32	*0.25*	1.60	*0.06*	0.91
	NMSE	10.9	0.26	*0.15*	0.22	3.36	3.45	0.24	3.10	*0.06*	6.99	*0.00*	1.05
21_G15	*FB*	-1.23	1.28	*-0.26*	0.85	1.20	1.59	-0.78	-1.28	*-0.25*	*0.08*	*0.03*	0.68
	NMSE	2.65	2.9	*0.07*	0.88	2.63	6.98	0.73	2.77	*0.06*	*0.01*	*0.00*	0.53
17_G3	*FB*	-1.42	0.45	*-0.13*	*-0.25*	1.05	-0.87	*-0.23*	-0.69	0.76	1.44	-0.33	-0.37
	NMSE	4.18	0.57	*0.02*	*0.06*	1.67	1.30	*0.05*	0.54	0.67	4.36	0.12	0.14
04_D3	*FB*	-0.81	0.63	-0.52	*-0.04*	1.90	*0.28*	n.a.	n.a.	n.a.	n.a.	n.a.	n.a.
	NMSE	0.87	1.41	0.29	*0.00*	49.2	*0.30*	n.a.	n.a.	n.a.	n.a.	n.a.	n.a.
03_G3	*FB*	-0.39	1.00	-0.32	-0.44	1.76	*0.24*	n.a.	n.a.	n.a.	n.a.	n.a.	n.a.
	NMSE	0.16	5.02	0.11	0.20	17.7	*0.25*	n.a.	n.a.	n.a.	n.a.	n.a.	n.a.
01_D3	*FB*	-1.86	0.65	-0.53	-0.84	0.69	1.81	*-0.04*	-1.00	*0.16*	*0.23*	*0.24*	-0.50
	NMSE	25.6	0.47	0.31	0.86	0.71	18.6	*0.00*	1.32	*0.03*	*0.05*	*0.06*	0.27
14_D4	*FB*	-1.46	-1.32	*-0.23*	*0.13*	1.61	1.39	*-0.23*	-0.63	0.76	1.87	*-0.02*	*0.02*
	NMSE	4.66	3.43	*0.06*	*0.02*	10.2	4.89	*0.05*	0.44	0.67	27.86	*0.00*	*0.00*
13_G4	*FB*	-0.93	*-0.28*	*-0.15*	*-0.30*	1.59	1.08	*-0.27*	-0.43	*0.17*	-0.53	*0.24*	0.68
	NMSE	1.17	*0.48*	*0.02*	*0.09*	8.52	3.75	*0.07*	0.19	*0.03*	0.30	*0.06*	0.52

Table 4.6. Cont.

Fire Scenarios	Statistical Measurements	T_F		$\dot{m}''$		$\dot{q}_r''$		H_F		A_F		E	
		FDS	FLACS	FDS	FLACS	FDS	FLACS	FDS	FLACS	FDS	FLACS	FDS	FLACS
10_D5	FB	-1.73	-0.58	*0.02*	-0.55	1.68	-1.06	-0.36	-0.96	0.72	*-0.19*	*-0.26*	0.90
	$NMSE$	12.0	1.73	*0.00*	0.33	11.6	3.58	0.14	1.20	0.60	*0.03*	*0.07*	1.01
08_G5	FB	-0.92	-0.13	*0.18*	-0.52	1.77	1.22	-0.45	-0.62	*0.08*	-1.00	0.44	1.12
	$NMSE$	1.10	1.09	*0.04*	0.29	22.6	3.45	0.21	0.43	*0.01*	1.33	0.21	1.83
07_D6	FB	-1.24	-0.64	*-0.28*	*-0.30*	1.74	-0.74	*-0.21*	-0.61	0.63	*0.22*	*0.17*	*0.18*
	$NMSE$	3.56	1.81	*0.08*	*0.09*	15.3	0.83	*0.05*	0.41	0.44	*0.05*	*0.03*	*0.03*
06_G6	FB	*0.09*	1.48	*-0.24*	1.39	1.75	1.54	*-0.22*	-0.42	*0.27*	*-0.24*	0.46	-0.39
	$NMSE$	*0.02*	15.5	*0.06*	3.72	19.4	6.06	*0.05*	0.18	*0.08*	*0.06*	0.23	0.16

In the case of FDS, the wind profile modelled may have also affected the predictions found. Most of the mean flame temperatures are notably over-estimated, which can be due to the low impact of the wind forces. Figure 4.7 shows instant captures of the flame contours belonging to the diesel pool fires of 1.5 and 3 m-diameter (i.e. 22_D15 and 17_G3) in the presence of wind obtained by means of the IR camera and the slice files defined in FDS. These images reveal that the modelled flames are less tilted than in reality and thus, these remain in permanent contact with the thermocouples, hence leading to greater temperature values than the measured ones.

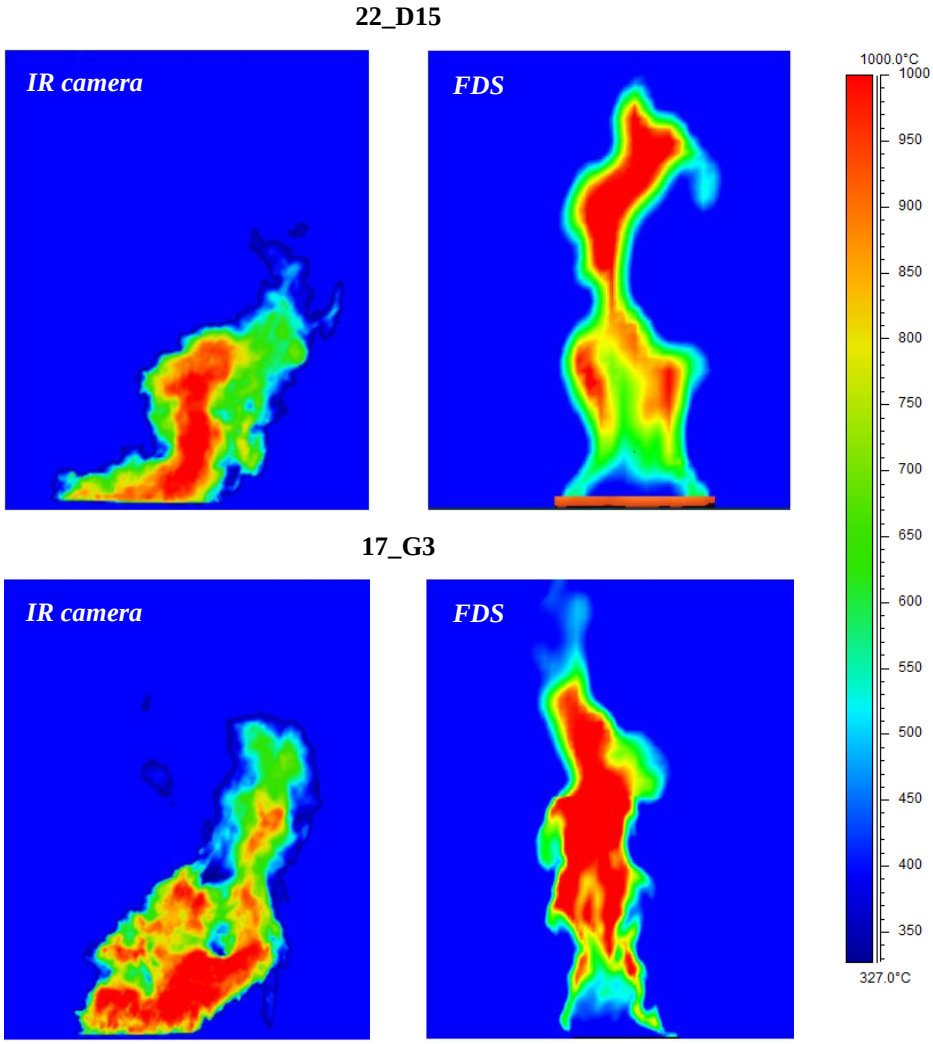

Figure 4.7. Instant captures of the flame contours belonging to the 22_D15 (up) and 17_G3 (down) pool fire scenarios obtained by means of the IR images (left) and the slice files defined in FDS (right).

On the other hand, FLACS-Fire randomly under/over-estimates the registered mean flame temperatures. For example, these are always under-predicted for pool fires of 3 m-diameter, while over-predictions are reached when simulating 4 and 5 m-diameter pool fires. In addition, it is remarked that the standard deviation of the flame temperatures is more noticeable in FLACS-Fire than in FDS throughout the fire scenarios simulated. This fact indicates that more stable flames are modelled in FDS, whereas those estimated in FLACS-Fire are featured with high puffing frequencies.

Burning rate

Regardless of the fuels involved and the boundary conditions modelled, the agreement between the burning rate simulated and measured mostly depend on the pool diameter in both CFD codes (Figure 4.8). More accurate mean burning rate is obtained in FDS as the pools diameter increase: 1.5 and 3 m-diameter pool fires have an over-estimation error slightly higher than 25%, whereas the rest of the fires modelled are identified with an estimation error lower than 25%. Specifically, 5 m-diameter pool fires show perfect agreement with measurements. These comply within the performance criteria in the 75% of the cases, which highlights the appropriateness of the assumptions solved within the fuel evaporation model implemented and the thin cell size defined in this region.

In contrast, lower accuracy is found as the pool diameter increases in FLACS-Fire: 1.5 and 3 m-diameter pool fires reached the highest mean burning rate agreements. Therefore, as the pool's size increase in FLACS-Fire simulations, the radiative heat from the flame considerably accelerates the liquid evaporation rate, hence releasing a greater amount of vapour fuel than what was observed in the experiments. In particular, the 42% of the pool fire simulations are in accordance with performance criteria.

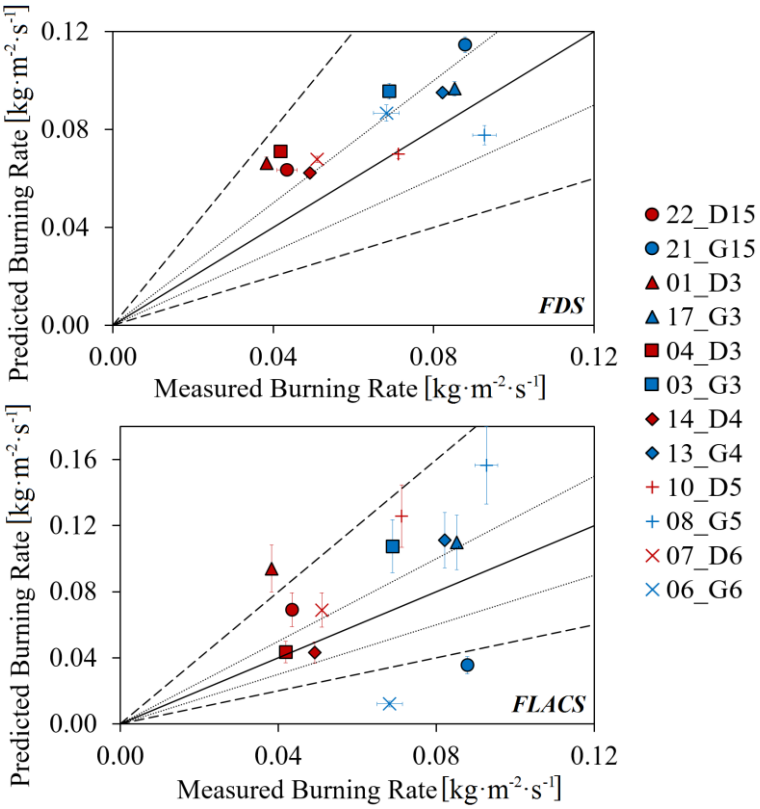

Figure 4.8. Mean burning rates obtained for the large-scale pool fires simulated in FDS (up) and FLACS-Fire (down).

Flame height

As it can be seen in Figure 4.9, both CFD codes over-estimate the mean dimensionless flame height. Particularly, FDS is able to reasonably predict the flame height measured, where the 60% of the pool fires simulated agree with the established performance criteria. However, more noticeable over-predictions are found in FLACS-Fire, especially when modelling 1.5 m-diameter pools and fire scenarios with wind velocities greater than 1 m/s (01_D3 and 10_D5). Consequently, none of the pool fires modelled in FLACS-Fire meet the defined criteria. As occurred in FDS simulations, the modelled flames in FLACS-Fire are less tilted than in the experiments. Different constant values for the MO wind approach, such as the canopy height, h_c, and the ground roughness, η, may have led to more accurate results.

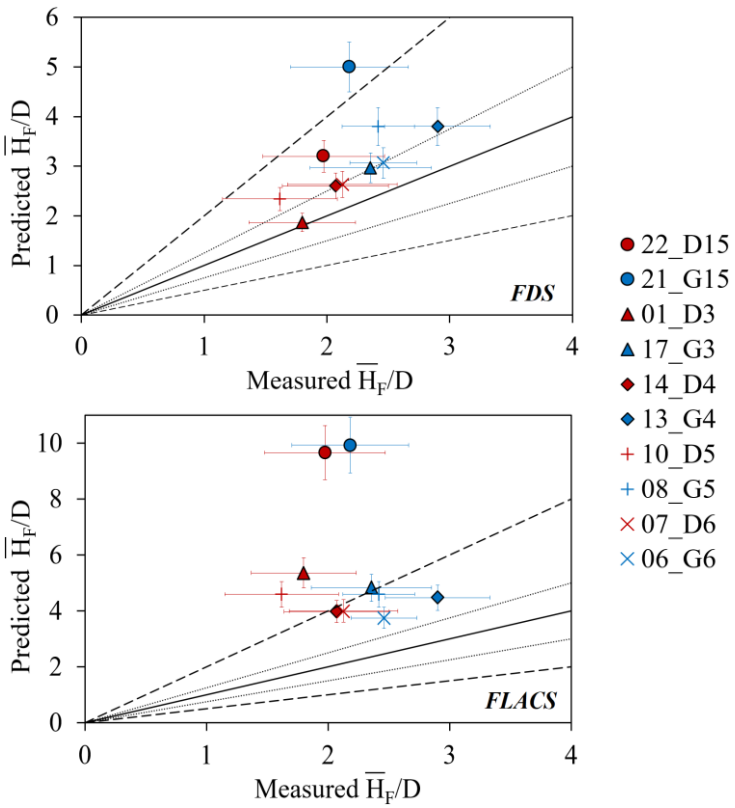

Figure 4.9. Mean dimensionless flame height obtained for the large-scale pool fires simulated in FDS (up) and FLACS-Fire (down).

Flame area

Figure 4.10 depicts the mean dimensionless flame areas estimated in both codes, which correspond to the surfaces projected on the centreline axis plane of the pool fires with temperatures greater than 600 K. Good qualitative agreement is often found in FDS with slightly under-predictions. In particular, the 60% of the flame areas analysed in FDS agree with the quantitative criteria defined. The non-complying simulations are those concerning pool fires of 4 m, 5 m and 6 m-diameter under wind speeds higher than 0.75 m/s. Based on the flame geometry predictions (areas and heights), it is noted that FDS commonly reproduces longer and thinner pool flames than those observed in the tests.

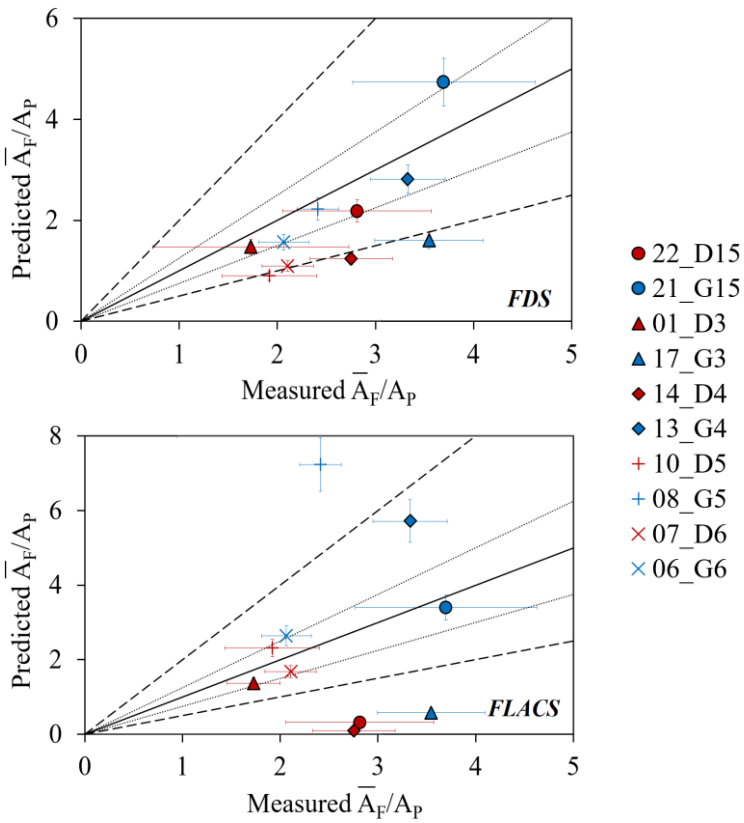

Figure 4.10. Mean dimensionless flame area obtained for the large-scale pool fires simulated in FDS (up) and FLACS-Fire (down).

On the other hand, the 50% of the simulations performed in FLACS-Fire meet the performance criteria and thus, more precise estimations of the flame-geometry descriptors are generally obtained in FDS. Apart from the wind profile modelled, which considerably affects the predicted pool flame shapes, other modelling settings may be also responsible for this lack of agreement found in FLACS-Fire. For example, the fact of averaging the flow motion in the RANS turbulence model, or the simplified mixing scale times adopted in the EDC combustion model, may also result important when estimating the flame-geometry descriptors of large-scale pool fires.

Heat flux

The heat flux is significantly under-estimated in both CFD codes (Figure 4.11), which may be probably due to the negligible impact of the wind velocity on the modelled flames. Given the insignificant inclination of the flames, the separation distances between the fire and the wide-angle radiometer are greater than those observed in the experiments and thus, lower heat flux values are received by the

virtual radiometers. In addition, the default number of solid angles considered may also have affected the heat flux estimations.

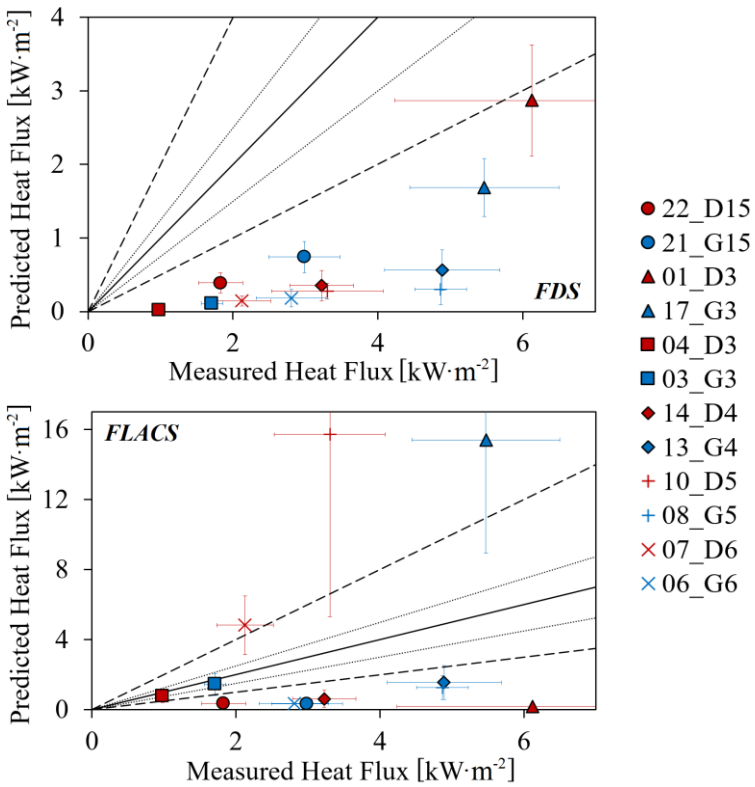

Figure 4.11. Mean radiative heat flux obtained for the large-scale pool fires simulated in FDS (up) and FLACS-Fire (down).

Despite the general disagreements reached, better heat flux estimations are found in FLACS-Fire than in FDS, especially in the case of the 3 m-diameter windless pool fires (04_D3 and 03_G3), whose heat fluxes are reasonably well predicted. In particular, only the 17% of the simulation results agree within the performance criteria in FLACS-Fire. Therefore, the DTM radiation model, which is the one used in FLACS-Fire, seems to provide more reliable results than the DOM approach.

Surface emissive power

The mean surface emissive power obtained in FDS reasonably agrees with the experimental data (Figure 4.12). In particular, the estimations are in accordance with the performance criteria in the 70% of the cases. On the other hand, less well predictions of the emissive powers are found in FLACS-Fire as only the 20% of the cases agree with the criteria. Windless gasoline pool fires modelled in FDS lead to erroneous predictions as they often estimate higher flame temperatures than

expected, while the low agreement found in FLACS-Fire may be due to the erroneous flame height predictions.

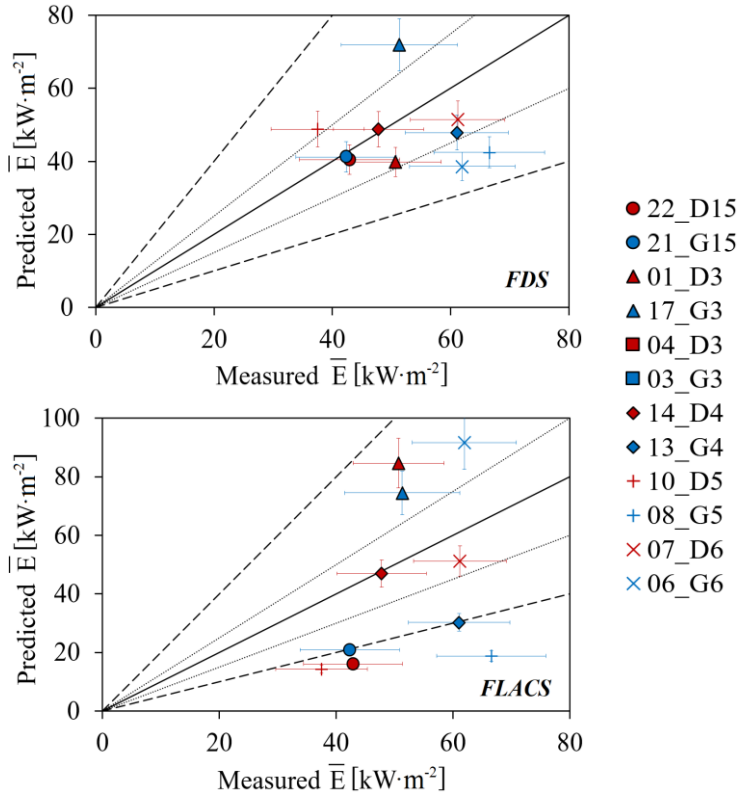

Figure 4.12. Mean surface emissive power obtained for the large-scale pool fires simulated in FDS (up) and FLACS-Fire (down).

4.3. *A posteriori* sensitivity analysis

As observed in previous section, numerous discrepancies between simulations results and measurements were often reached in both CFD codes. The disagreements became particularly noticeable when determining the flame temperatures and the heat fluxes received at a certain distance from the pool origin. Consequently, this lack of agreement restricts the use of the CFD codes examined to a limited number of fire scenarios.

In order to extend the use of FDS and FLACS-Fire to multiple scenarios involving large-scale pool fires, *a posteriori* sensitivity analysis is proposed. This study is mainly intended to reveal the most appropriate modelling settings able to deliver accurate estimations of the variables of interest. For that purpose, the present analysis is focused on quantitatively assessing the influence of different modelling hypothesis than those used in the *a priori* validation analysis. In particular,

different wind sub-models, fuel evaporation approaches and number of solid angles are evaluated to study its influence on the results accuracy. The cell sizes and the computational domains considered are the same as in the previous analysis.

4.3.1. Wind

The wind velocity arose as one of the most important modelling features affecting the development of buoyancy-dominated fires in open environments. The Monin-Obukhov approach is the only wind sub-model available in FLACS-Fire; however, different methods can be used in FDS to determine the wind influence: (i) the power law wind profile (PL), which was used in *a priori* simulations, (ii) an approximation Monin-Obukhov similarity theory (MO) and (iii) the mean forcing concept (MFC), which simply consists on adding a forcing term to the momentum equation to represent the wind force throughout the computational domain in a given direction. More details on the wind sub-models can be found in Section 3.2.4.

Table 4.7 gathers the quantitative performance measures of the flame temperatures and heat fluxes obtained in windy fire scenarios simulated in FDS under the MO and MFC approaches. As it can be seen, both wind sub-models commonly provide more accurate results than the PL previously applied in both variables. In particular, the 50% of the flame temperatures and the 40% heat fluxes estimated with the MFC method are in agreement with the experimental data. On the other hand, none of the flame temperature obtained with the MO approach are in accordance with the performance criteria. Predicted flame temperature these largely over-estimate the values recorded with the centreline axis thermocouples set-up. Nevertheless, the 50% of the heat flux obtained in windy fire scenarios under the MO approach are in agreement with measurements. So, considering the reasonable flame temperature and heat flux estimations found, the MFC approach is noted as the most appropriate one to simulate windy fire scenarios in FDS.

Table 4.7. FB and NMSE measurements of the flame temperature and heat flux obtained in FDS under different wind sub-models. Italic blue values indicate that the measurement is within the performance criteria established. The symbols ✓and ✗ indicate that the results are more and less accurate than those obtained in the a priori validation analysis, respectively.

Fire Scenarios	Statistical Measurements	T_F		$\dot{q}_r''$	
		MFC	MO	MFC	MO
22_D15	*FB*	*0.14* ✓	-1.31 ✓	-0.50 ✓	*0.14* ✓
	NMSE	*0.02* ✓	3.15 ✓	0.34 ✓	*0.26* ✓
21_G15	*FB*	-0.85 ✓	-0.97 ✓	*0.22* ✓	*-0.05* ✓
	NMSE	0.98 ✓	1.67 ✓	*0.14* ✓	*0.13* ✓
17_G3	*FB*	*0.27* ✓	1.23 ✓	-0.98 ✓	*0.05* ✓
	NMSE	*0.09* ✓	2.93 ✓	1.35 ✓	*0.09* ✓
01_D3	*FB*	*0.00* ✓	-1.22 ✓	*-0.30* ✓	*-0.22* ✓
	NMSE	*0.00* ✓	2.66 ✓	*0.25* ✓	*0.22* ✓
14_D4	*FB*	-1.02 ✓	-1.34 ✓	0.95 ✓	1.79 ✗
	NMSE	1.46 ✓	3.50 ✓	1.38 ✓	21.54 ✗
13_G4	*FB*	*-0.17* ✓	-0.56 ✓	0.76 ✓	0.50 ✓
	NMSE	*0.07* ✓	0.40 ✓	0.81 ✓	0.57 ✓
10_D5	*FB*	-0.93 ✓	-1.70 ✓	*-0.12* ✓	1.05 ✓
	NMSE	1.14 ✓	10.39 ✓	*0.12* ✓	2.51 ✓
07_D6	*FB*	*0.05* ✓	-1.23 ✓	*0.08* ✓	1.11 ✓
	NMSE	*0.24* ✓	3.49 ✓	*0.09* ✓	3.51 ✓

4.3.2. Fuel evaporation

Rather than determining the fuel evaporation rate by means of a heat transfer balance (FLACS-Fire), or by means of a one-dimensional heat transfer model (FDS), it can be prescribed in both CFD codes as the mass of fuel entering into the domain through a horizontal vent. Table 4.8 shows the *FB* and *NMSE* measurements of the flame temperatures and heat fluxes obtained in FDS and FLACS-Fire when the mass loss rates are prescribed according to the experimental data. The PL wind model is used in the FDS simulations to observe the differences in predicting and prescribing the fuel evaporation rate.

Table 4.8. FB and NMSE measurements of the flame temperature and heat flux obtained when prescribing the mass loss rates in FDS and FLACS. Italic blue values indicate that the measurement is within the performance criteria established. The symbols ✓ and ✗ indicate that the results are more and less accurate than those obtained in the a priori validation analysis, respectively.

Fire Scenarios	Statistical Measurements	T_F		$\dot{q}_r''$	
		FDS	FLACS	FDS	FLACS
22_D15	*FB*	-1.43 ✓	0.38 ✓	1.15 ✓	1.21 ✓
	NMSE	7.52 ✓	*0.19* ✓	3.02 ✓	3.41 ✓
21_G15	*FB*	-1.32 ✗	0.37 ✓	1.38 ✗	0.35 ✗
	NMSE	3.25 ✗	*0.17* ✓	4.22 ✗	*0.16* ✓
17_G3	*FB*	-1.51 ✗	1.31 ✗	0.77 ✓	-1.24 ✗
	NMSE	5.37 ✗	3.04 ✗	0.83 ✓	2.78 ✗
04_D3	*FB*	-0.66 ✓	1.38 ✗	1.83 ✓	-0.77 ✓
	NMSE	0.56 ✓	0.73 ✓	9.26 ✓	0.71 ✓
03_G3	*FB*	*-0.30* ✓	*0.21* ✓	1.15 ✓	*0.08* ✓
	NMSE	*0.10* ✓	*0.05* ✓	8.72 ✓	*0.01* ✓
01_D3	*FB*	1.76 ✓	0.64 ✓	1.46 ✗	0.90 ✓
	NMSE	20.8 ✓	*0.46* ✓	5.28 ✗	1.22 ✓
14_D4	*FB*	-1.37 ✓	-1.12 ✓	1.33 ✓	*0.29* ✓
	NMSE	3.55 ✓	2.05 ✓	4.06 ✓	*0.13* ✓
13_G4	*FB*	-0.89 ✓	1.51 ✗	1.53 ✓	*0.26* ✓
	NMSE	1.03 ✓	5.60 ✗	6.75 ✓	*0.16* ✓
10_D5	*FB*	-1.61 ✓	0.45 ✓	1.13 ✓	-1.38 ✗
	NMSE	7.53 ✓	0.65 ✓	3.37 ✓	3.87 ✗
08_G5	*FB*	-0.99 ✗	1.31 ✓	1.66 ✓	1.68 ✗
	NMSE	1.34 ✗	3.03 ✓	11.10 ✓	9.79 ✗
07_D6	*FB*	-1.09 ✓	1.48 ✗	1.58 ✓	-1.29 ✗
	NMSE	2.70 ✓	6.77 ✗	11.07 ✓	3.03 ✗
06_G6	*FB*	*0.06* ✓	*0.16* ✓	1.46 ✓	*-0.30* ✓
	NMSE	*0.01* ✓	*0.04* ✓	5.87 ✓	*0.15* ✓

In general, a better agreement of the variables predicted is found in both CFD codes when prescribing evaporation rates. In the case of the flame temperature, the agreement reached increases by 75% in both tools. Regarding the heat flux predictions, the increase is of 83% in FDS and of 58% in FLACS-Fire. Although more accurate predictions have been obtained, only the 10% and the 37.5% of the variables predicted are still in accordance with the performance criteria in FDS and FLACS-Fire, respectively.

4.3.3. Number of solid angles

Increasing the number of solid angles, which directly affects the RTE equation, may contribute to improve the accuracy of the heat flux estimations. In this sense, gasoline pool fires are modelled under different number of solid angles to figure out the most suitable option at reasonable computational time: 100, 200, 300 and 400. As gathered in Table 4.9, the agreement reached completely varies depending on the CFD code used, the pool size and the wind conditions. For example, windy fire scenarios of 1.5 and 3 m-diameter simulated in FDS match with the measurements under 200 solid angles or more, whereas windless fire scenarios or pool fires with greater diameters require at least 400 solid angles. These differences may be due to the higher radial distances originated as a result of longer flame heights and greater flame areas. Conversely, good agreement is achieved for the wide range of solid angles examined in the windless 3-m diameter pool fires in both CFD codes. In the absence of wind, the radiative heat transfer can be accurately predicted under 100 solid angles. Nevertheless, for the rest of simulated pool fires, the minimum number of rays recommended is of 300 in FLACS-Fire and of 400 in FDS to reasonably estimate the radiative heat fluxes.

Table 4.9. FB and NMSE measurements of the heat flux predicted in FDS and FLACS-Fire under different number of solid angles. Italic blue values indicate that the measurement is within the performance criteria established.

Fire Scenarios	Statistical Measurements	100		200		300		400	
		FDS	FLACS	FDS	FLACS	FDS	FLACS	FDS	FLACS
21_G15	*FB*	1.20	1.59	*0.21*	0.83	*0.07*	*0.23*	*-0.20*	*0.19*
	NMSE	2.00	2.00	*0.11*	0.83	*0.05*	*0.43*	*0.07*	*0.39*
17_G3	*FB*	1.05	-0.87	*0.18*	-0.75	*0.11*	*-0.27*	*0.00*	*-0.22*
	NMSE	1.67	1.30	*0.10*	0.65	*0.06*	*0.36*	*0.07*	*0.35*
03_G3	*FB*	1.76	*0.24*	1.02	*0.07*	1.01	*-0.10*	*0.25*	*-0.20*
	NMSE	2.00	*0.25*	2.00	*0.00*	1.67	*0.01*	*0.11*	*0.04*
13_G4	*FB*	1.59	1.08	0.86	1.08	0.35	0.47	*0.29*	*0.30*
	NMSE	2.00	2.00	1.05	1.66	*0.44*	*0.35*	*0.40*	*0.09*

Table 4.9. Cont.

Fire Scenarios	Statistical Measurements	100		200		300		400	
		FDS	FLACS	FDS	FLACS	FDS	FLACS	FDS	FLACS
08_G5	FB	1.77	1.22	1.11	1.01	0.78	0.37	*0.15*	*0.28*
	$NMSE$	2.00	2.00	2.00	1.35	2.00	*0.24*	*0.40*	*0.15*
06_G6	FB	1.75	1.54	1.28	0.80	0.84	*0.29*	*0.28*	*0.28*
	$NMSE$	2.00	2.00	2.00	0.76	0.98	*0.08*	*0.29*	*0.08*

4.4. Concluding remarks

The predictive capabilities of FDS and FLACS-Fire were examined when determining the related-fire effects of unconfined large-scale pool fires of different sizes: 1.5, 3, 4, 5 and 6 m-diameter. First, a preliminary sensitivity analysis of the cell size and the computational domain was performed. It was found that the maximum cell size able to reasonably predict the mean experimental flame height in both CFD codes should be of 0.2 m. Also, a minimum domain height of 8D was recommended to simulated heavy hydrocarbon buoyant plumes, while the domain width had a negligible impact on both CFD codes.

When performing *a priori* CFD simulations, the modelled flames were usually higher and less tilted than in the experiments. Consequently, numerous discrepancies were found when comparing flame temperatures and heat flux in both tools. On the other hand, accurate burning rates were commonly found in FDS, while less accurate ones were obtained in FLACS-Fire as the diameter increased. Additionally, reasonable predictions of the flame shapes and the surface emissive powers were found, with more accurate values in FDS than in FLACS-Fire.

Moreover, *a posteriori* sensitivity analysis of the fuel evaporation rate, the wind sub-models and the number of solid angles was performed in both CFD codes. The aim of this study was to find out the most suitable modelling settings different to those implemented in the *a priori* validation analysis. Predictions of the flame temperatures and heat fluxes were more accurate when prescribing the mass loss rate of the pool fires in both codes. Similarly, the wind sub-models applied in FDS notably improved the simulation results found. Particularly, the MO wind approach was revealed as the most accurate one. Also, a higher number of solid angles improved the heat flux estimations. The minimum number of rays recommended was of 300 for FLACS-Fire and of 400 for FDS to reasonably estimate the radiative heat fluxes.

CHAPTER 5

CFD MODELLING OF JET FIRES

In this section, the predictive capabilities of CFD codes when modelling different types of hydrocarbon jet fires are investigated. Given the possible jet fire scenarios occurring in industrial facilities, a considerable number of computational simulations have been performed involving different jet release orientations and flow conditions. Firstly, the expanded regions of vertical sonic propane jet fires are modelled with FDS, FireFOAM and FLACS-Fire to estimate the flame temperature, the emitted heat flux and the flame shape (Section 5.1). To that end, the pseudo-diameter approach is used to convert the sonic compressible flow conditions to subsonic expanded flow conditions due to the Mach number constraint of these codes. Then, the flame-geometry descriptors of vertical subsonic jet fires of methane in normal- and sub-atmospheric pressures are estimated by using the same codes (Section 5.2). Lately, the flame shape and the emissive power of vertical and horizontal subsonic jet fires of propane are predicted in FDS (Section 5.3). The main strengths and weaknesses of each fire code are identified and recommendations on the most suitable cell size ranges are provided according to the different jet fire scenarios assessed. Fragments of this chapter have been presented in the *9th International Seminar on Fire and Explosions Hazards* (Rengel et al., 2019a) and are planned to be published in the paper entitled *Experimental and computational analysis of vertical jet fires in normal- and sub- atmospheric pressures* (Rengel et al., 2019b).

5.1. Vertical sonic jet fires of propane

For most gases, the sonic velocity ($M_a = 1$) is reached when the gas exit source pressure exceeds 1.9 bar, which is common in many storage tanks and pipelines (Palacios et al., 2008). Sonic jet fires are usually divided into three zones related to different Mach numbers: (i) the nearfield or under-expanded zone ($M_a \geq 1.0$), (ii) the transition zone ($0.3 < M_a < 1.0$) and (iii) the farfield or expanded zone ($M_a \leq 0.3$) (Franquet et al., 2015). Within the nearfield zone, the sonic velocity can be found at the nozzle exit ($M_a = 1.0$) with a gas pressure greater than the ambient. The released flow undergoes rapid expansion and quickly accelerates to supersonic expansion ($M_a \gg 1.0$) with the decrease in pressure and density.

Consequently, the outflowing gas is governed by compressible and viscous effects, which prevents its mixture with the ambient flow. As the supersonic flow crosses the Mach disk, which is perpendicular to the jet flux where flows produce a normal shock (Fu et al., 2014), better mixing occurs in the transition zone, due to an abrupt decrease in velocity to subsonic speeds and to an increase in pressure and density. Figure 5.1 shows the schematic representation of the under-expanded structure of sonic jet fires and the Mach number distribution (Dulov and Lukyanov, 1984). As the distance from the gas release orifice increases, the velocity of the flow and the Mach number decrease progressively, until the air-fuel mixture is completed and the jet flame occurs. At this point, at the farfield zone, the jet is totally expanded, the subsonic regime is achieved and the flow becomes incompressible.

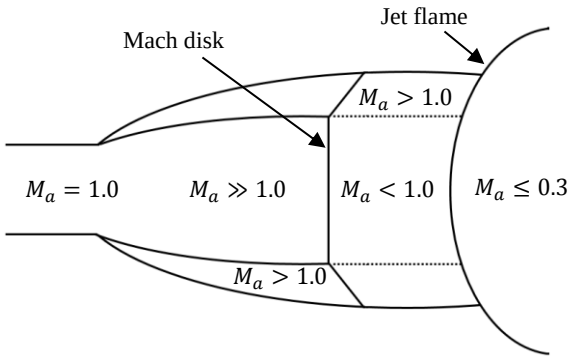

Figure 5.1. Schematic representation of the under-expanded structure of sonic jet fires. Data source come from (Dulov and Lukyanov, 1984).

5.1.1. Mach number constraint

Most CFD fire tools consider the incompressible flow formulation of the Navier-Stokes equations to reduce the number of equations to be solved, hence improving the numerical stability and reducing the computational times. Therefore, these codes are only able to simulate the farfield zones, where the jet flow is in pressure equilibrium with the ambient fluid.

Given the Mach number constraint of computational codes, the pseudo-diameter approach is used in the present analysis to scale the compressible initial conditions of the sonic jet fires at the exit orifice to the equivalent ones in the expanded zone (Figure 5.2) (Birch et al., 1984). The method relies on mass conservation and prevents the air entrainment within the compressible region. The equivalent pressures and temperatures are assumed to be the same as the ambient fluid:

$$\dot{m}_{eq} = \dot{m}_{or} \tag{5.1}$$

$$T_{eq} = T_{\infty} \tag{5.2}$$

$$P_{eq} = P_{\infty} \tag{5.3}$$

Considering $u_{eq} = M_a c$, where c is the sound velocity of the fluid, the equivalent nozzle diameter, $D_{eq,n}$, of the sonic jet fires can be determined as a function of M_a:

$$D_{eq,n} = \sqrt{\frac{4\dot{m}_{eq}}{\pi \rho_{eq} M_a c}} \tag{5.4}$$

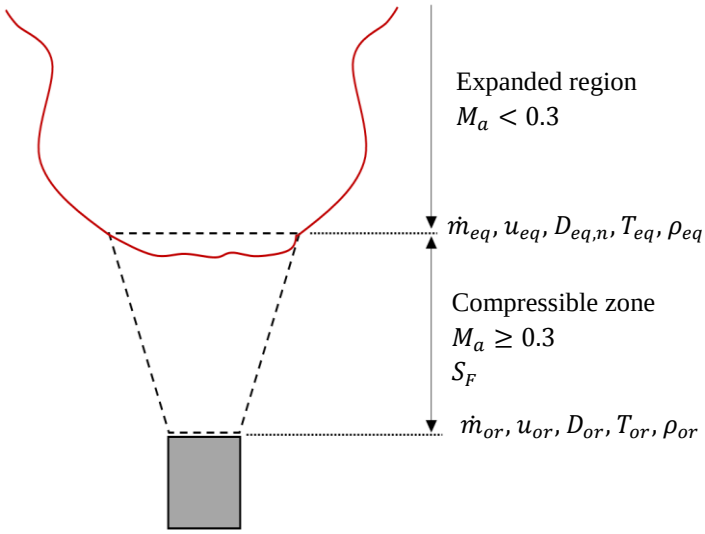

Figure 5.2. Sketch of the pseudo-diameter approach used to scale the initial conditions of the sonic jet fires. Data source come from (Birch et al., 1984).

It is worth noting that the pseudo-diameter approach proposed for analysis clearly neglects some of the real physical effects of sonic jet fires that could disturb the predictions obtained. First, the amount of ambient air entrained into the base of the flame that mixes with the fuel is not considered. Also, the flameless distance between the exit orifice and the flame base is not estimated. Instead, an equivalent nozzle diameter of the flame base is directly assumed as a function of a Mach number.

This section presents simulations of the expanded regions of vertical sonic jet fires of propane performed in FDS, FireFOAM and FLACS-Fire. For that purpose, five different Mach numbers are suggested for each jet fire scenario with values lower than 0.3, which represents the threshold accounting for compressibility flow: 0.01, 0.025, 0.05, 0.10 and 0.20. More details about the experimental data can be found in Section 2.2.

5.1.2. Numerical modelling

Table 5.1 gathers the 5 different equivalent nozzle diameters determined for each vertical jet fire of propane as a function of the Mach number proposed. As it can be seen, the greater the Mach number, the smaller the equivalent nozzle diameter of the jet fire after the expanded region. Greater Mach numbers would lead to thinner cells; however, the compressibility threshold ($M_a < 0.3$) would be largely exceeded. Predictions of the mean flame temperature, mean heat flux, mean flame length and mean flame areas are compared against those measured in the experiments. Virtual sensors are located as described in the experimental set-up to estimate the flame temperatures and heat fluxes received, while the flame shapes are calculated by means of a slice file that recorded the temperatures evolution in the centreline plane of the jet fires. Pixels with apparent temperatures greater than 800 K are considered as flame, while the rest are considered as background.

Table 5.1. Equivalent nozzle diameters of the sonic jet fire experiments as a function of the Mach numbers. See Table 2.2 for main experimental features.

M_a	-		0.01	0.025	0.05	0.10	0.20
Experiment	D_{or} **(mm)**	U^*	$D_{eq,n}$ **(mm)**				
D10_0.09	10	142.6	140	90	60	40	30
D12.75_0.13	12.75	129.4	160	100	70	50	40
D15_0.18	15	121.2	190	120	90	60	40
D20_0.27	20	108.1	240	150	110	70	50
D25.5_0.34	25.5	98.1	260	170	120	80	60

The whole set of sonic jet fires are featured with U^* values higher than 80 and thus, the cell size cannot be determined based on the D^*/δ_x expression (see Section 3.3). Alternatively, the maximum cell size of the sonic jet fire scenarios is based on the only geometrical constraint: the equivalent nozzle diameters. Accordingly, the cell size of each jet fire scenario (in m^3) will have a side equal to $D_{eq,n}$ (in m). For example, the D10_0.09 ($M_a = 0.01$) scenario is modelled with a cell size of 0.14 x 0.14 x 0.14 m^3 and the D12.75_0.13 ($M_a = 0.05$) with a cell size of 0.07 x 0.07 x 0.07 m^3. A sensitivity analysis of the mesh resolution is indirectly performed as for each Mach number proposed, there is a cell size equal to the equivalent diameter calculated.

The ambient temperature and the mass flow rate are prescribed according to the experimental data. A soot fraction of 0.09 kg/kg is considered for the combustion of propane (Kent, 1986) and the lateral and the upper boundaries are open to the outside. Simulations are run for 30 s to achieve long-duration steady states. Table

5.2 summarizes the sub-models solved in FDS, FLACS-Fire and FireFOAM. More details about the mathematical correlations and models constants applied can be found in Section 3.2.

Table 5.2. Sub-models solved in the CFD codes used to simulate the expanded zones of vertical sonic jet fires of propane.

CFD Sub-models	FDS	FLACS-Fire	FireFOAM
Turbulence	**LES** $\mu_t = \rho C_d \Delta \sqrt{k_{sgs}}$	**RANS** $\mu_t = \rho C_\mu \frac{k^2}{\varepsilon}$	**LES** $\mu_t = \rho (C_s \Delta)^2 \lvert S \rvert$
Combustion	**EDC** $\tau_{mix} = max\left[\tau_c, min\left(\tau_d, \tau_a, \tau_g\right)\right]$	**EDC** $\tau_{mix} = \frac{2.433 \left(\frac{\varepsilon}{\nu}\right)^{1/2} \gamma^3 \chi}{1 - \gamma^3 \chi}$	**EDC** $\tau_{mix} = 4.192 \frac{{k_{sgs}}^{1/2}}{\Delta}$
Radiation	**DOM** $\dot{q}_r'' = \kappa(4I_b - G)$ $I_b = C_r \sigma T^4$	**DTM** $\dot{q}_r'' = (1 - \varepsilon)G + \varepsilon \sigma T^4$	**DOM** $\dot{q}_r'' = \kappa(4I_b - G)$ $I_b = \sigma T^4$

5.1.3. Assessment of the predictions

Prior to the analysis, it is worth noting that FLACS-Fire could not run with cell sizes smaller than 0.06 m, which occurred in those tests with Mach numbers of 0.10 and 0.20. The use of very thin grids under RANS turbulence model creates convergence problems in the near boundary surfaces of the domain, hence leading to numerical instabilities. Therefore, FLACS-Fire simulations are run under Mach numbers comprised between 0.01 and 0.05. On the other hand, when FireFOAM simulations are run with cell sizes greater than 0.15 m (Mach numbers of 0.01 and 0.025), jet flames are represented as 'columns of fire' ranging from their bases to the upper boundary layer. In that case, the coarse grids cannot accurately resolve the rate of fuel/oxidant mixing. Consequently, FireFOAM simulations are run under Mach numbers of 0.05, 0.10 and 0.20.

Table 5.3 summarizes the FB and $NMSE$ statistical measurements obtained for the expanded regions simulated in FDS, FireFOAM and FLACS-Fire of vertical sonic jet fires. Italic blue values indicate that the measurement is within the performance criteria established.

Table 5.3. FB and NMSE measurements of the main variables obtained in the CFD codes used for the vertical sonic jet fires as a function of the Mach number. Italic blue values indicate that the measurement is within the established performance criteria established.

CFD	M_a	T_F		$\dot{q}_r''$		L_F		A_F	
		FB	***NMSE***	***FB***	***NMSE***	***FB***	***NMSE***	***FB***	***NMSE***
FDS	0.01	0.32	*0.14*	-0.42	*0.30*	*0.06*	*0.01*	*0.18*	*0.13*
	0.025	0.47	*0.25*	*0.05*	*0.15*	*0.02*	*0.01*	*0.10*	*0.13*
	0.05	0.63	*0.49*	*0.26*	*0.39*	*-0.15*	*0.03*	*0.04*	*0.14*
	0.10	0.61	*0.46*	*0.30*	*0.23*	*-0.04*	*0.00*	*-0.21*	*0.20*
	0.20	0.57	*0.40*	*-0.03*	*0.10*	*0.00*	*0.01*	-0.63	1.09
FireFOAM	0.05	0.70	0.60	-0.96	1.33	*-0.03*	*0.08*	0.67	0.62
	0.10	0.71	0.65	-1.01	1.44	0.32	*0.47*	1.05	5.56
	0.20	0.71	0.64	-1.07	1.65	0.36	*0.28*	1.12	3.06
FLACS-Fire	0.01	0.33	0.62	*0.27*	*0.38*	-0.47	*0.26*	0.49	1.02
	0.025	*0.27*	*0.13*	*0.06*	*0.13*	-0.60	*0.39*	0.63	0.62
	0.05	*0.28*	*0.14*	*-0.28*	*0.40*	-0.65	*0.32*	0.57	0.51

Flame temperature

The mean flame temperature are often under-predicted in the CFD codes used (Figure 5.3). FDS estimations lead to an error estimation ranged between 25% and 50%. Better agreement is often found when jet fires are modelled at smaller Mach numbers and thus, thinner cell sizes. Although the qualitative comparison may reveal reasonable agreement, the *FB* statistical values of FDS are higher than 0.3, hence showing evidence of the discrepancies regarding the mean flame temperature.

The disagreement is more noticeable in FireFOAM as the qualitative error estimation observed is higher than 50% in most cases. The maximum simulated mean temperatures are of 650 ºC, while the measured ones notably exceeded 1000 ºC. None of the estimations agree with the quantitative performance criteria. In general, lower result's accuracy are obtained in FireFOAM than in FDS, which may be due to the model constants implemented within the combustion approach, as well as the simplicity of the mixing scale time calculation method.

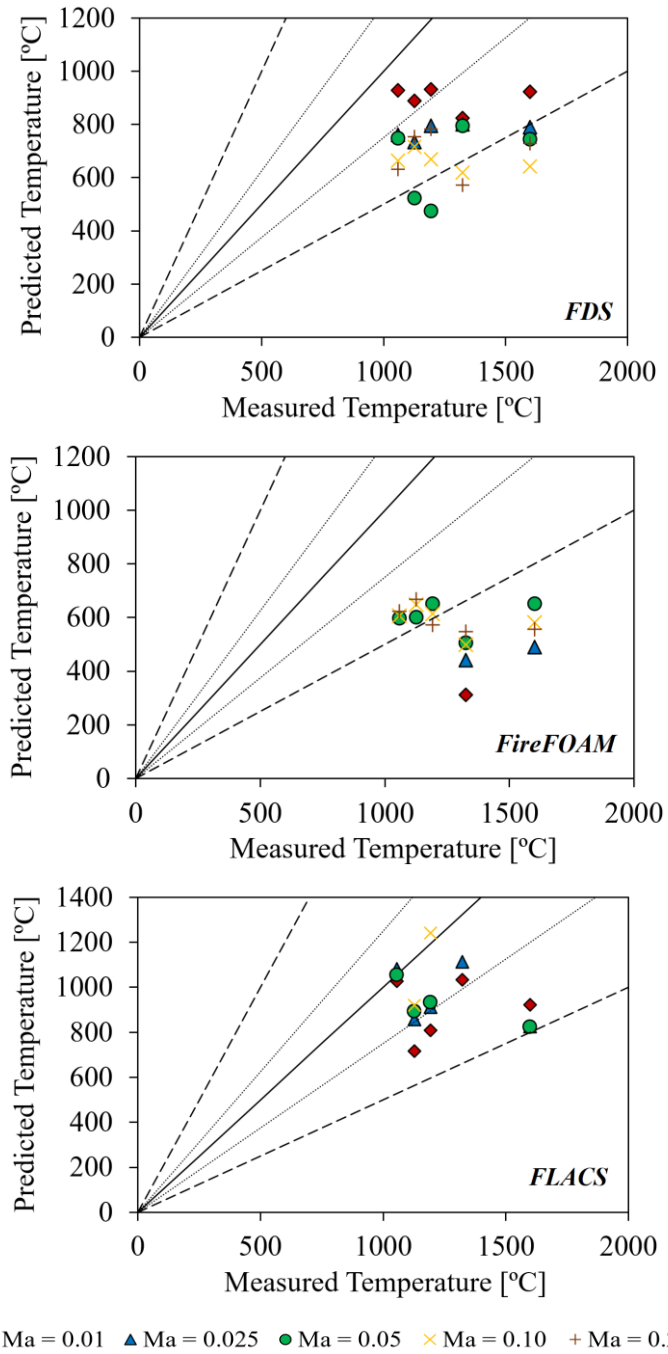

Figure 5.3. Mean jet flame temperature obtained for the vertical sonic jet fires simulated in FDS (up), FireFOAM (centre) and in FLACS-Fire (down).

On the other hand, FLACS-Fire appears to be the most precise CFD model to predict mean flame temperature, as most of the values lead to an error estimation

lower than 35%. In particular, the quantitative statistical methods show good performance when the Mach number defined is of 0.025 and 0.05. This fact highlights the suitability of the $k-\varepsilon$ turbulence model and the methodology used to compute the mixing scale times within the EDC approach.

Heat flux

Each code behaves differently when predicting the mean heat flux received at a certain distance from the nozzle (Figure 5.4). For example, over/under estimations are obtained in FDS and in FLACS-Fire with an error estimation often lower than 50%, while these are largely over-estimated in FireFOAM with an averaged error estimation greater than 50%. Specifically, the FB and $NMSE$ measurements are in agreement in FDS for Mach numbers comprised between 0.025 to 0.20. Very coarse grids corresponding to smaller Mach numbers, may lead to significant error predictions in FDS. On the other hand, the good estimations obtained in FLACS-Fire highlight the suitability of the DTM model to solve the radiant heat flux distribution throughout the computational domain regardless of the mesh resolution.

In contrast, noticeable over-predictions of the mean heat fluxes are determined in FireFOAM for the whole cell sizes modelled. Consequently, none of the statistical methods agree with the performance criteria. FDS and FireFOAM used the DOM approach for solving the RTE equation; however, the heat flux predictions are considerably less accurate in FireFOAM. This fact demonstrates that the model constant implemented in FDS, C_r, is able to correct the emission term in the DOM equation, hence leading to more precise estimations.

Flame length

Figure 5.5 shows the mean flame lengths estimated by the CFD codes. As it can be seen, very good agreement is found in FDS with error estimations always lower than 25%, which leads to a quantitative agreement of the statistical methods for the whole simulations performed. Regardless of the Mach number defined and thus, the cell size modelled, less accurate estimations are obtained in FireFOAM and FLACS-Fire. In both codes the $NMSE$ values are always in accordance with the performance criteria; however, discrepancies are often achieved when assessing the FB statistical measures.

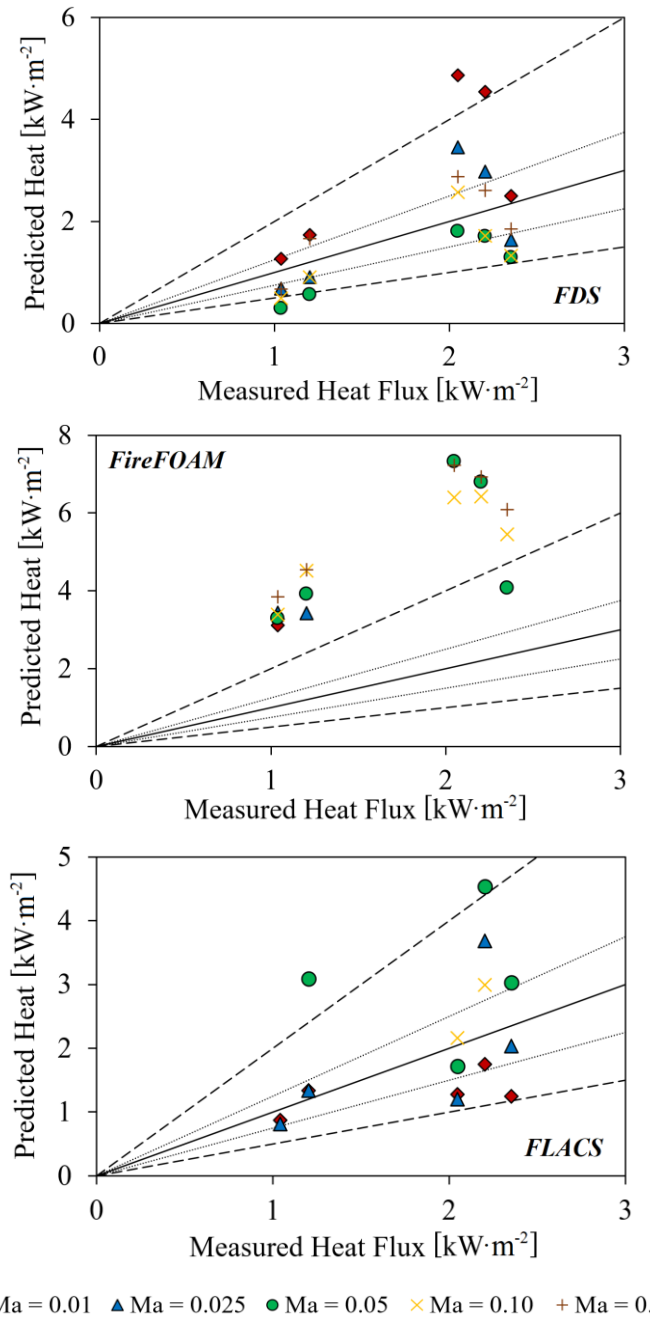

Figure 5.4. Mean radiative heat flux obtained for the vertical sonic jet fires simulated in FDS (up), FireFOAM (centre) and in FLACS-Fire (down).

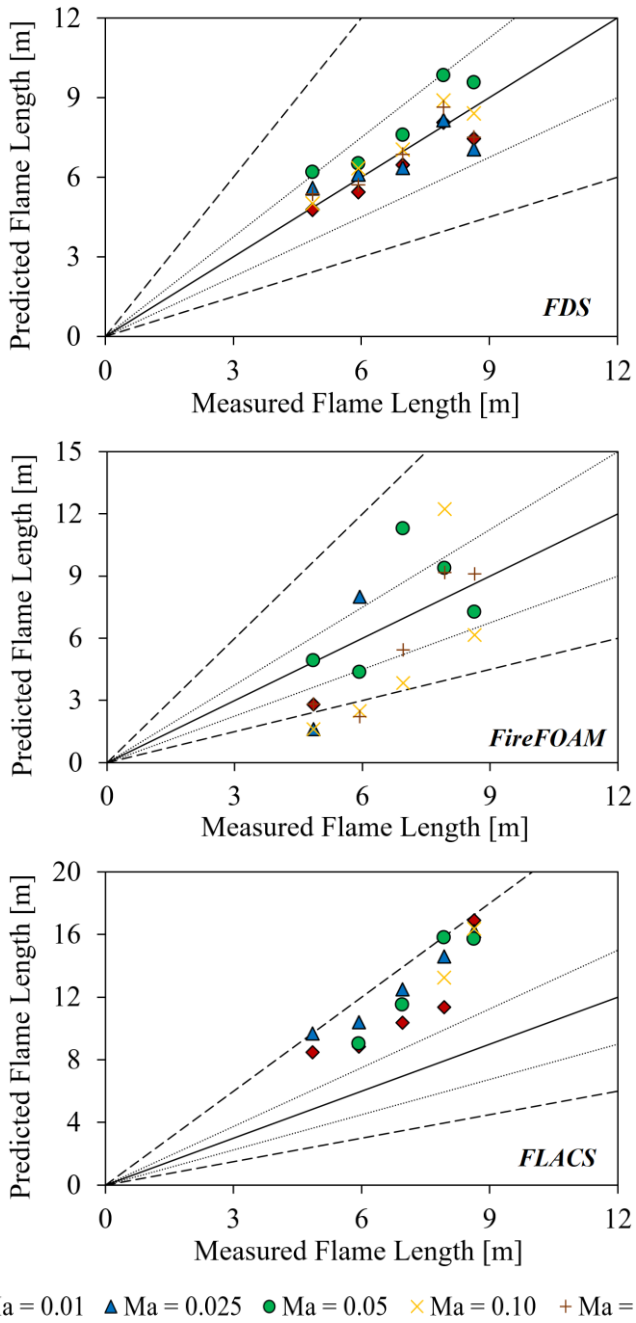

Figure 5.5. Mean flame length obtained for the vertical sonic jet fires simulated in FDS (up), FireFOAM (centre) and in FLACS-Fire (down).

Flame area

The mean flame areas are reasonably estimated in FDS, with better agreement obtained under smaller cells (Figure 5.6). Apart from simulations carried out with a Mach number of 0.20, the rest of the simulations performed agree with both statistical measurements. Considering the previous flame length predictions obtained in FDS, it is noted that the thinner the cell size defined in the code, the wider the surface occupied by the flame. In contrast, these are remarkably under-estimated in FireFOAM and in FLACS-Fire for any cell size defined. Therefore, both codes simulate very thin flames, hence demonstrating that the air entrained into the domain mixes with the released fuel much faster than in reality.

5.1.4. Concluding remarks

FDS, FireFOAM and FLACS-Fire codes were used to predict flame temperature, the heat flux and flame-geometry descriptors of five propane jet fire experiments in an open environment. Due to the low Mach number formulation implemented in the CFD codes, the pseudo-diameter approach was used to determine the conditions of the jets after the expansion of the released gas. The equivalent properties of these (temperature, velocity and diameter) were simulated as a function of five Mach numbers proposed for analysis for each jet fire experiment.

According to the different levels of agreement reached in the CFD codes when varying the Mach number, it is deduced that the equivalent nozzle diameter calculated by means of the pseudo-diameter approach and thus, the cell sizes modelled, have a strong impact on the estimated variables. Even though some discrepancies have been observed in FDS, it arises as the most suitable code to predict the related-fire effects of vertical sonic jet fires of propane. Excepting flame temperature, the rest of the variables estimated are in accordance with the defined performance criteria. In contrast, significant error predictions are found in FireFOAM, hence highlighting the need for further improvement of the mathematical models and the numerical schemes solved. It is highly recommended to carry out *a posteriori* sensitivity analysis of the modelling parameters previously discussed (i.e. models constants, mixing scale times, number of solid angles, etc.) before its use in real applications involving sonic jet fires. Furthermore, the flame temperatures and the heat fluxes can be reasonably predicted in FLACS-Fire. However, neither the flame lengths nor the flame surfaces can be accurately calculated.

Table 5.4 summarizes the suitable Mach number intervals at which the variables assessed in the present analysis can be reasonably estimated in each CFD code used. The last row of the table includes recommended Mach number intervals to predict most of these. Based on the suggested Mach number interval, the precise

cell size for a given sonic jet fire scenario, which coincides with the equivalent nozzle diameter, can be determined from Eq. 5.4.

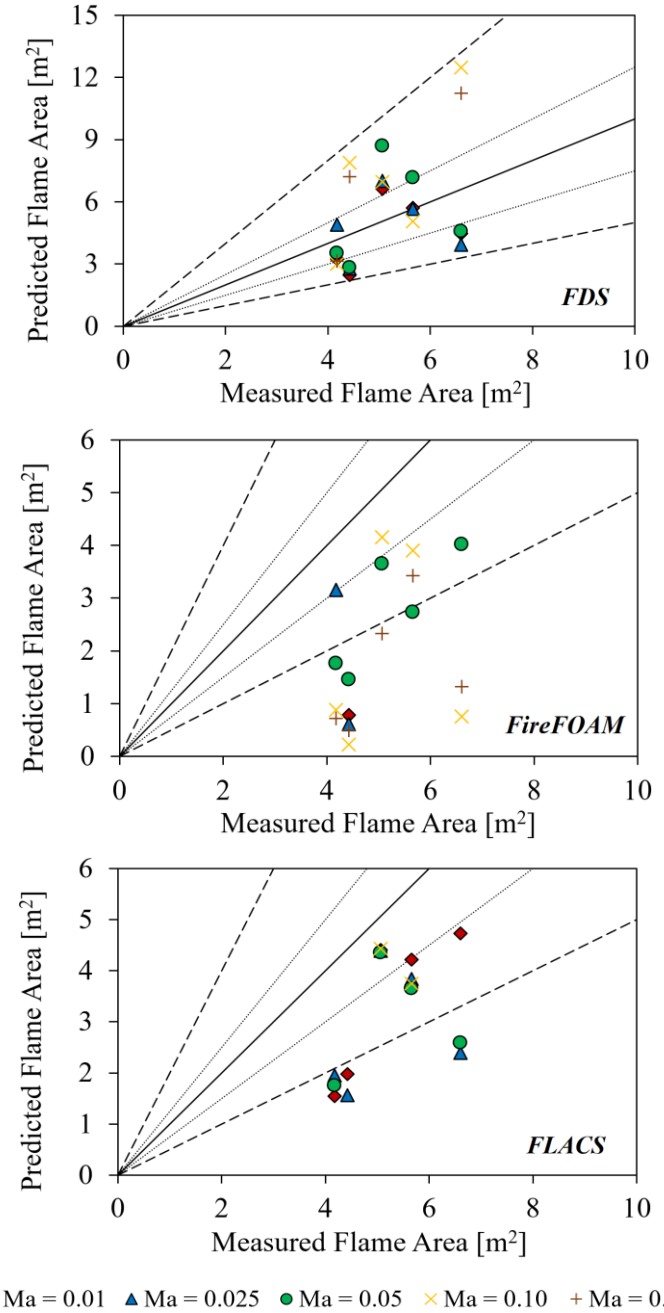

Figure 5.6. Mean flame area obtained for the vertical sonic jet fires simulated in FDS (up), FireFOAM (centre) and in FLACS-Fire (down).

Table 5.4. Recommended Mach number intervals at which FDS, FireFOAM and FLACS-Fire should be set-up to reasonably predict the flame temperature, the radiative heat flux and the flame shape.

Variables	FDS	FireFOAM	FLACS-Fire
T_F	n.a	n.a	$0.025 \leq M_a \leq 0.05$
$\dot{q}_r{}''$	$0.025 \leq M_a \leq 0.20$	n.a	$0.01 \leq M_a \leq 0.05$
L_F	$0.01 \leq M_a \leq 0.20$	$0.05 \leq M_a < 0.10$	n.a
A_F	$0.01 \leq M_a \leq 0.10$	n.a	n.a
Any	$\mathbf{0.025 \leq M_a \leq 0.10}$	$\mathbf{0.05 \leq M_a < 0.10}$	$\mathbf{0.025 \leq M_a \leq 0.05}$

Although the examined sonic jet flames are momentum-dominated, acceptable cell size can be also given in the form of D^*/δ_x for each fire scenario (Table 5.5). The last row includes recommended intervals that can be applied when modelling the expanded regions, which can be determined through the pseudo-diameter approach, of vertical sonic jet fires involving hydrocarbon fuels.

Table 5.5. Recommended D^*/δ_x intervals from which suitable cell sizes can be defined to simulate the expanded regions of vertical sonic jet fires in FDS, FireFOAM and FLACS-Fire.

Fire scenario	D^*	FDS	FireFOAM	FLACS-Fire
D10_0.09	1.44	$18 \leq D^*/\delta_x \leq 35$	$25 \leq D^*/\delta_x \leq 35$	$18 \leq D^*/\delta_x \leq 25$
D12.75_0.13	1.66	$17 \leq D^*/\delta_x \leq 34$	$24 \leq D^*/\delta_x \leq 34$	$17 \leq D^*/\delta_x \leq 24$
D15_0.18	1.89	$16 \leq D^*/\delta_x \leq 33$	$23 \leq D^*/\delta_x \leq 33$	$16 \leq D^*/\delta_x \leq 23$
D20_0.27	2.23	$16 \leq D^*/\delta_x \leq 32$	$22 \leq D^*/\delta_x \leq 32$	$16 \leq D^*/\delta_x \leq 22$
D25.5_0.34	2.44	$15 \leq D^*/\delta_x \leq 31$	$22 \leq D^*/\delta_x \leq 31$	$15 \leq D^*/\delta_x \leq 22$
Any	-	$\mathbf{16 \leq D^*/\delta_x \leq 33}$	$\mathbf{23 \leq D^*/\delta_x \leq 33}$	$\mathbf{16 \leq D^*/\delta_x \leq 23}$

5.2. Vertical subsonic jet fires of methane in normal- and sub- atmospheric pressures

Minor jet fire accidents involving subsonic gas releases may also occur in industrial facilities. Their consequences are less severe than sonic jet fires; however, they are more likely events that may cause accident propagation (Cozzani and Zanelli, 2001). As shown in Appendix A (see Table A.1), most of the subsonic jet fire experiments performed by researchers considered a wide variety of hydrocarbon fuels and nozzle diameters. In contrast, most of these were undertaken in an atmospheric pressure of 1.0 atm, which could be useful to

determine the hazardous jet fire effects in offshore platforms (i.e. Troll A platform, Norway (Structurae. International Database and Gallery of Structures, n.d.)), in marine gas and oil fields (i.e. Blake oil field, UK (Hydrocarbons Technology, n.d.)) and in liquefied natural gas terminals (i.e. LNG terminal on Maasvlakte, The Netherlands (Industry About, 2016)). However, gas power plants, oil and gas refineries and aerial pipelines, which are the most economical transportation mode of large hydrocarbon quantities on land (Bolonkin, 2010), can be located at high altitude regions: Permian Basin oil field at 800 m a.s.l. (USA) (Industry About, 2017), F'Krina gas power plant at 947 m a.s.l. (Algeria) (Industry About, 2014) and A13 oil pipeline at 2892 m a.s.l. (Iran). Thus, fire behaviour research has to be addressed to check fire protection requirements under sub-atmospheric pressures.

Variations in the ambient pressure directly affect the fuel density, hence affecting the heat release rate, defined as one of the most important parameters governing the fire behaviour. Reduced atmospheres also alter the chemical reaction of combustion due to the changes on the effective amount of oxygen available in the ambient air. Although the percentage of oxygen in air is constant at different altitudes (20.9%), at reduced atmospheres the air is less compressed and lighter (Peacock, 1998). Consequently, fewer molecules of oxygen are present in a volume of air to be mixed with the released fuel.

An historical survey revealed that most of the fire incidents involving natural gas occurred in pipelines, closely followed by process plants (Montiel et al., 1999). Actually, natural gas is one of the most processed, transported and used hydrocarbon fuels these days (Varahrami and Haghighat, 2018), whose worldwide production has continuously increased since 1990 as reported by the US Energy Information Administration (EIA) (U.S. Energy Information Administration (EIA), 2018).

Nevertheless, studies on the behaviour of methane jet fires are still very limited at reduced atmospheric pressures. This fact has hindered the assessment of the predictive capabilities of CFD codes when modelling jet fire accidents at high altitudes. This section is aimed at filling this gap by presenting CFD simulations of vertical subsonic jet fires of methane in normal- and sub- atmospheric pressures. Specifically, FDS, FireFOAM and FLACS-Fire codes are used to estimate the flame-geometry descriptors of these type of fires at 0.6 atm, 0.7 atm, 0.8 atm, 0.9 atm and 1.0 atm. More details about the experimental data can be found in Section 2.3.

5.2.1. Numerical modelling

The U^* values obtained for the experiments analysed are ranged between 10.6 (for 1 atm) to 12.5 (for 0.6 atm) and thus, the jet flames are at the beginning of the transition regime from buoyant to momentum-dominated flames. This fact allows the application of the D^*/δ_x correlation to define the most suitable mesh resolution. According to the values commonly recommended (see Section 3.3), four different cell sizes are proposed for each jet fire experiment: 32 mm-cell for D^*/δ_x of 4, 24 mm-cell for D^*/δ_x of 8, 16 mm-cell for D^*/δ_x of 12 and 8 mm-cell for D^*/δ_x of 16. Therefore, a total of 20 fire simulations are performed in each fire code.

As it can be observed, the cell sizes calculated are larger than the original exit orifices (3 mm-diameter). Because of that, equivalent nozzle diameters are defined with the same size than the calculated cell. For example, a vertical subsonic jet fire modelled with a $D^*/\delta_x = 12$ is modelled with an equivalent nozzle diameter of 0.016 m and a cell volume of 0.016 x 0.016 x 0.016 m^3. As a consequence, an equivalent mass flow rate, $\dot{m}_{eq} = 0.25\rho_f u_f \pi {D_{eq,n}}^2$, is calculated for each cell size defined and prescribed within the computational simulation.

The lift-off distance, flame length and equivalent flame diameter of the flames are determined via a slice file that recorded the temperature's evolution in the centreline axis of the jet fires. Pixels with apparent temperatures greater than 600 K are considered as flame, while the rest are considered as background. The turbulence and combustion sub-models described in Table 5.2 are the ones used in the present study for FDS, FireFOAM and FLACS-Fire. Radiation is not accounted in any code due to its negligible influence on the flame shapes. Simulations lasted 30 s to achieve long-duration steady states. A soot fraction of 0.007 kg/kg is assumed as the fraction of carbon from methane fuel converted to soot (Kent, 1986) and the lateral and the upper boundaries are open to the outside. The volume domain modelled in the CFD codes is of 0.6 (L) x 0.6 (W) x 1.0 (H) m^3 for all simulations.

5.2.2. Assessment of the predictions

Regardless of the atmospheric pressure modelled and the geometrical flame feature analysed, it is noted that the cell size is generally the most decisive parameter determining the estimation's accuracy. Also, it is worth noting that neither FLACS-Fire nor FireFOAM are able to predict flame temperatures higher than 600 K under cells of 32 mm. Therefore, both codes are unable to solve the reaction of combustion between the fuel and the oxidant for subsonic flows under coarse grids. Table 5.6 summarizes the FB and $NMSE$ statistical measurements obtained for the vertical subsonic jet fires simulated in FDS, FireFOAM and FLACS-Fire as a function of the different cell sizes and atmospheric pressures set-

up. Italic blue values indicate that the metric is within the performance criteria established.

Table 5.6. FB and NMSE measurements of the flame-geometry descriptors obtained in the CFD codes used for the vertical subsonic jet fires as a function of the cell sizes and atmospheric pressures. Italic blue values indicate that the metric is within the established performance criteria.

CFD Code	P_∞ (atm)	δ_x (mm)	S_F		L_F		D_{eq}		A_F	
			FB	***NMSE***	***FB***	***NMSE***	***FB***	***NMSE***	***FB***	***NMSE***
FDS	0.6	8	2.00	1.00	*-0.02*	*0.00*	-0.39	0.16	*-0.29*	*0.18*
		16	1.06	1.59	*0.08*	*0.00*	*-0.28*	*0.08*	*-0.20*	*0.04*
		24	0.49	*0.25*	*0.28*	*0.00*	*0.14*	*0.02*	0.41	*0.18*
		32	*-0.11*	*0.01*	0.84	0.87	*0.13*	*0.02*	0.95	1.15
	0.7	8	2.00	1.00	*0.06*	*0.00*	-0.38	*0.15*	*-0.30*	*0.11*
		16	0.93	1.11	*0.24*	*0.06*	*-0.18*	*0.03*	*0.06*	*0.00*
		24	*0.20*	*0.04*	*0.30*	*0.11*	*0.13*	*0.02*	0.46	*0.22*
		32	*-0.29*	*0.08*	0.83	0.83	*0.10*	*0.01*	0.91	1.06
	0.8	8	2.00	1.00	*0.11*	*0.01*	-0.47	*0.23*	*-0.28*	*0.12*
		16	0.69	0.55	*0.26*	*0.14*	*-0.20*	*0.04*	*0.18*	*0.03*
		24	*-0.19*	*0.04*	0.42	*0.18*	*0.02*	*0.00*	0.46	*0.22*
		32	-0.56	*0.34*	0.91	1.03	*0.02*	*0.00*	0.94	1.14
	0.9	8	2.00	1.00	*0.16*	*0.03*	-0.51	*0.28*	*-0.26*	*0.13*
		16	*0.22*	*0.05*	*0.30*	*0.13*	-0.46	*0.22*	*-0.11*	*0.01*
		24	-0.67	*0.50*	0.51	*0.28*	*0.00*	*0.00*	0.50	*0.27*
		32	-0.98	1.28	1.03	1.44	*-0.03*	*0.00*	1.00	1.34
	1.0	8	2.00	1.00	*0.22*	*0.09*	-0.54	*0.31*	*-0.25*	*0.07*
		16	2.00	1.00	*0.29*	*0.20*	-0.41	*0.18*	*0.04*	*0.00*
		24	2.00	1.00	0.57	*0.35*	*-0.05*	*0.00*	0.52	*0.29*
		32	2.00	1.00	1.07	1.63	*-0.06*	*0.00*	1.03	1.44
FireFOAM	0.6	8	1.47	4.73	0.73	0.61	0.35	*0.13*	1.02	1.39
		16	0.74	0.65	0.59	0.38	*0.11*	*0.01*	0.69	0.54
		24	*0.09*	*0.01*	*0.30*	*0.11*	*-0.06*	*0.00*	*0.26*	*0.07*
	0.7	8	1.38	3.68	0.85	0.88	*0.21*	*0.05*	1.02	1.40
		16	0.59	*0.38*	0.52	*0.28*	*0.01*	*0.00*	0.53	*0.30*
		24	*-0.29*	*0.10*	*0.29*	*0.09*	*0.01*	*0.00*	*0.30*	*0.09*

Table 5.6. Cont.

CFD Code	P_∞ (atm)	δ_x (mm)	S_F		L_F		D_{eq}		A_F	
			FB	*NMSE*	*FB*	*NMSE*	*FB*	*NMSE*	*FB*	*NMSE*
FireFOAM	0.8	8	1.22	2.36	0.98	1.27	*-0.09*	*0.01*	0.93	*1.11*
		16	0.31	*0.10*	0.82	0.82	*-0.19*	*0.04*	0.68	*0.43*
		24	-0.58	*0.37*	*0.23*	*0.12*	*-0.17*	*0.03*	*0.19*	*0.04*
	0.9	8	*0.22*	*0.05*	0.74	0.63	0.50	*0.27*	1.14	1.91
		16	*-0.18*	*0.03*	0.65	*0.47*	*-0.05*	*0.00*	0.60	*0.40*
		24	-0.82	0.82	*0.28*	*0.36*	*-0.27*	*0.10*	*0.28*	*0.08*
	1.0	8	2.00	1.00	0.76	*0.67*	*0.18*	*0.03*	0.91	1.04
		16	2.00	1.00	0.49	*0.25*	*-0.07*	*0.01*	0.42	*0.18*
		24	2.00	1.00	*0.30*	*0.14*	*-0.18*	*0.03*	*0.20*	*0.04*
FLACS-Fire	0.6	8	1.23	2.45	*-0.18*	*0.03*	-1.68	9.66	-1.73	12.01
		16	*0.23*	*0.06*	0.53	*0.31*	-1.08	1.64	-0.63	0.45
		24	*0,30*	*0.12*	0.58	*0.36*	-1.02	1.42	-0.52	0.29
	0.7	8	1.11	1.80	*-0.20*	*0.04*	-1.70	10.22	-1.75	12.89
		16	0.43	*0.20*	*0.25*	*0.06*	-1.33	3.13	-1.17	2.08
		24	*0.28*	*0.29*	0.47	*0.24*	-1.03	1.44	-0.63	0.44
	0.8	8	1.19	2.21	*-0.16*	*0.03*	-1.70	10.24	-1.73	12.03
		16	0.95	1.18	*-0.02*	*0.00*	-1.39	3.74	-1.39	3.74
		24	*0.15*	*0.02*	0.57	*0.36*	-1.06	1.55	-0.55	0.33
	0.9	8	1.10	1.72	*-0.12*	*0.01*	-1.71	10.78	-1.74	12.41
		16	0.53	*0.30*	*0.11*	*0.01*	-1.46	4.58	-1.41	3.97
		24	*-0.29*	*0.08*	0.59	*0.39*	-1.10	1.74	-0.61	*0.41*
	1.0	8	2.00	1.00	*-0.05*	*0.00*	-1.71	11.11	-1.73	11.83
		16	2.00	1.00	*0.16*	*0.03*	-1.47	4.64	-1.39	3.71
		24	2.00	1.00	0.68	0.52	-1.11	1.78	-0.53	*0.30*

Lift-off distance

Figure 5.7 shows the mean predicted values of the lift-off distance estimated for different pressures and cell sizes with FDS, FireFOAM and FLACS-Fire. None of the codes is able to capture the influence of the ambient pressure on the lift-off distance (i.e. a constant trend is generally obtained) and, according to the cell sizes

modelled, the greater the grid, the larger the lift-off distance. This fact may be probably due to the 'mixed is burnt' assumption considered in the EDC combustion model, which immediately ignites the gas fuel entering into the domain simulated. (Favrin et al., 2018) also pointed out the limitations of computational combustion models to simulate jet fires.

Flame length

Reasonable mean flame length predictions are found in FDS with an error estimation lower than 50% only when simulations are performed with cells thinner than 32 mm (Figure 5.8). In particular, the 8 mm and 16 mm-cell sizes are always in agreement with the statistical measurements. In contrast, the 24 mm-cell match the performance criteria under atmospheric pressures of 0.6 atm and 0.7 atm. In this sense, the pressure solver in FDS is affected by variations on the atmospheric pressure defined within the domain.

Otherwise, notorious under-estimations can be reached in FireFOAM under thin cells. Specifically, the error estimation is around 25% when the cells are of 24 mm, whereas thinner cells lead to higher discrepancies. Indeed, the performance criteria of the statistical measurements are met under 24 mm-cell regardless of the atmospheric pressure. Therefore, the size of the cell has a greater impact than the pressure defined. Compared to FDS, the notable differences on the result's accuracy can be from the model constants adopted by default to solve the turbulent viscosity and the mixing scale times. More complex models, as those implemented in FDS, may contribute to provide higher precision on the estimation of flame length.

The mean flame lengths are also acceptably predicted in FLACS-Fire for different atmospheric pressures. In particular, cell sizes of 8 mm lead to an over-estimation of the measured values, while greater cells lead to under-estimations. Although the qualitative error estimation observed is lower than 50%, the performance criteria is not met under cells of 24 mm. Therefore, lower cell sizes (i.e. 8 mm to 16 mm) must be defined to provide accurate estimations of the flame length.

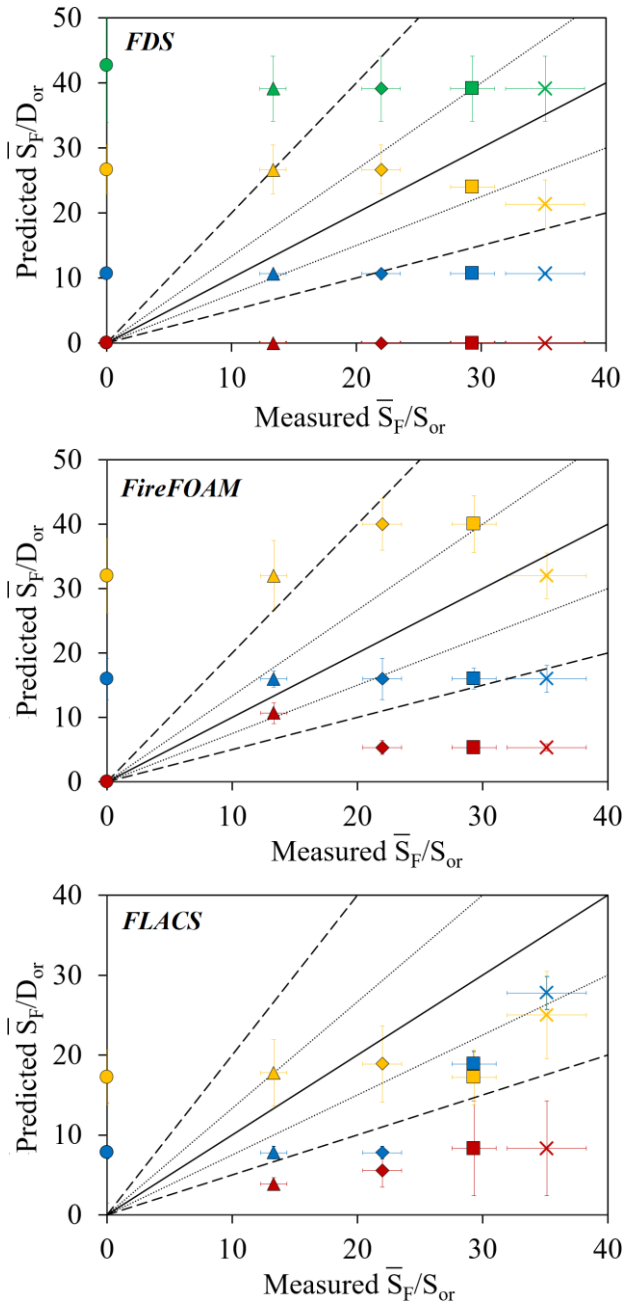

Atmospheric Pressure (Symbols): ○ 0.6 atm △ 0.7 atm ◇ 0.8 atm + 0.9 atm ×1.0 atm

Cell Size (Colours): ● 8 mm ▲ 16 mm ◆ 24 mm × 32 mm

Figure 5.7. Mean dimensionless lift-off distance obtained for the vertical subsonic jet fires simulated in FDS (up), FireFOAM (centre) and in FLACS-Fire (down) as a function of the different atmospheric pressures and cell sizes modelled.

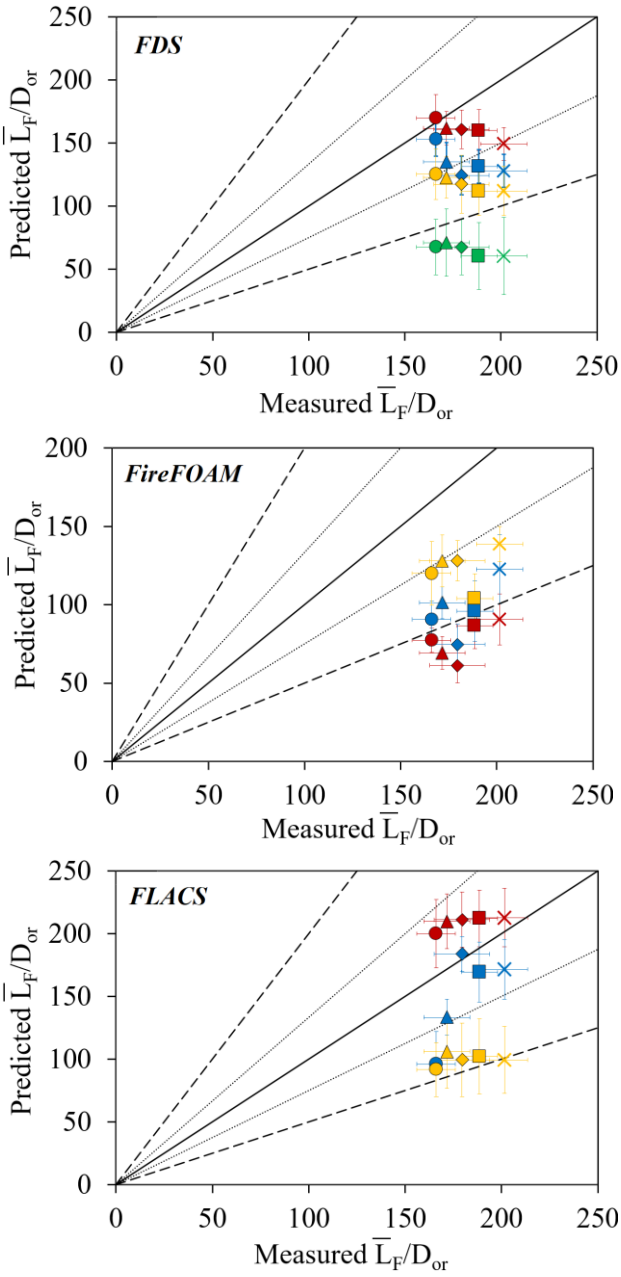

Figure 5.8. Mean dimensionless flame length obtained for the vertical subsonic jet fires simulated in FDS (up), FireFOAM (centre) and in FLACS-Fire (down) as a function of the different atmospheric pressures and cell sizes modelled.

Equivalent flame diameter

Figure 5.9 depicts the mean equivalent flame diameter predicted by the CFD codes, which correspond to the mean width of the flames, for the different pressures and cell sizes. These are often over-predicted in FDS with reasonable agreement between estimation and experimental measurements. The error estimation is lower than 25% when the cells are of 24 mm or higher, whereas it is comprised between 25% and 50% under smaller cells. The performance criteria is always met when simulations are performed with cells of 16 mm, 24 mm and 32 mm.

Similarly, mean equivalent diameters calculated by FireFOAM provide an average error estimation of 30% with subtle differences among cell sizes. In this sense, the atmospheric pressure defined has a negligible influence on the equivalent diameter. Only some simulations under 8 mm-cell lead to disagreements when assess by means of the statistical measurements. In contrast, significant over-estimations of the mean equivalent flame diameters are found in FLACS-Fire regardless of the cell size and atmospheric pressure. The error estimations observed are much higher than 50% and thus, none of the statistical measurements are in agreement with the performance criteria established. Meaning that, the flames predicted in FLACS-Fire are much wider than in reality.

Flame area

According to the grid sizes defined, different levels of accuracy are obtained on the mean flame areas predicted by the CFD codes (Figure 5.10). For example, the error prediction observed in FDS is of 25% or lower when simulations are performed with cells of 8 mm and 16 mm; however, greater cells lead to notable under-predictions of the experimental results. In particular, the performance criteria is only met with simulations with cells of 8 mm and 16 mm. The estimations obtained in FireFOAM always under-estimate the measured flame areas with lower accuracy than FDS. In particular, the highest agreements occur with cells of 24 mm, which is in accordance with the flame length predictions. On the other hand, the flame areas calculated in FLACS-Fire are significantly over-estimated, with error estimations greater than 50%. This lack of agreement arises as a result of the large equivalent flame diameters previously found.

Figure 5.11 shows instant captures and the corresponding segmented images of jet flames at 0.6 atm and 1.0 atm obtained from the slice files of temperatures set in the CFD codes with a cell size of 16 mm. These images depict the tendency of the estimated flame shape obtained with the different computational codes. Regardless of the ambient pressure, more reasonable predictions (lengths and diameters) are obtained with FDS and FireFOAM, while large flames are found with FLACS-Fire.

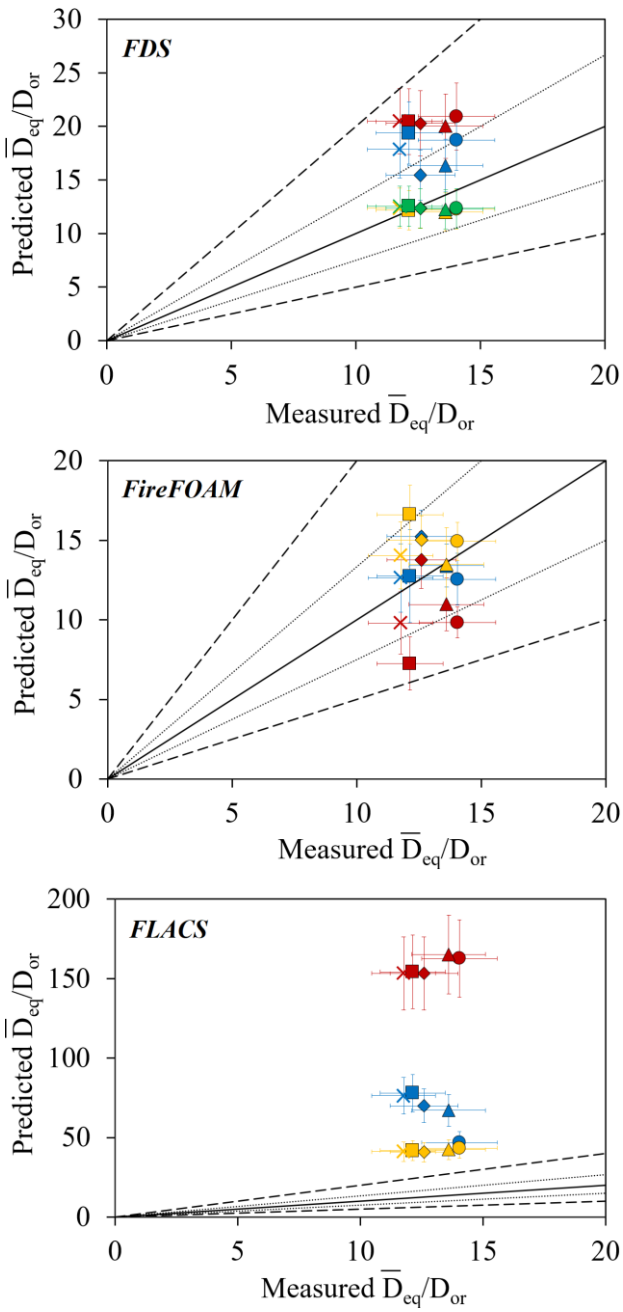

Atmospheric Pressure (Symbols): ○ 0.6 atm △ 0.7 atm ◇ 0.8 atm + 0.9 atm ×1.0 atm

Cell Size (Colours): ● 8 mm ▲ 16 mm ◆ 24 mm × 32 mm

Figure 5.9. Mean dimensionless equivalent diameter obtained for the vertical subsonic jet fires simulated in FDS (up), FireFOAM (centre) and in FLACS-Fire (down) as a function of the different atmospheric pressures and cell sizes modelled.

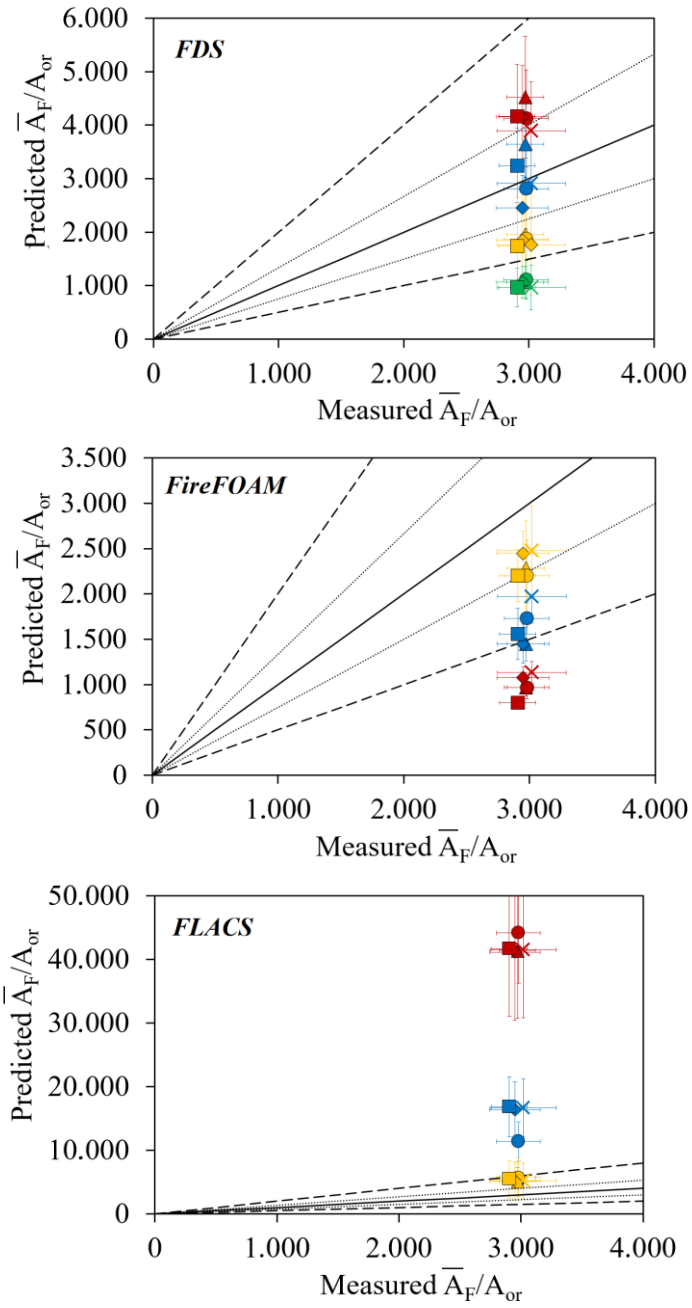

Atmospheric Pressure (Symbols): ○ 0.6 atm △ 0.7 atm ◇ 0.8 atm + 0.9 atm ×1.0 atm

Cell Size (Colours): ● 8 mm ▲ 16 mm ◆ 24 mm × 32 mm

Figure 5.10. Mean dimensionless flame area obtained for the vertical subsonic jet fires simulated in FDS (up), FireFOAM (centre) and in FLACS-Fire (down) as a function of the different atmospheric pressures and cell sizes modelled.

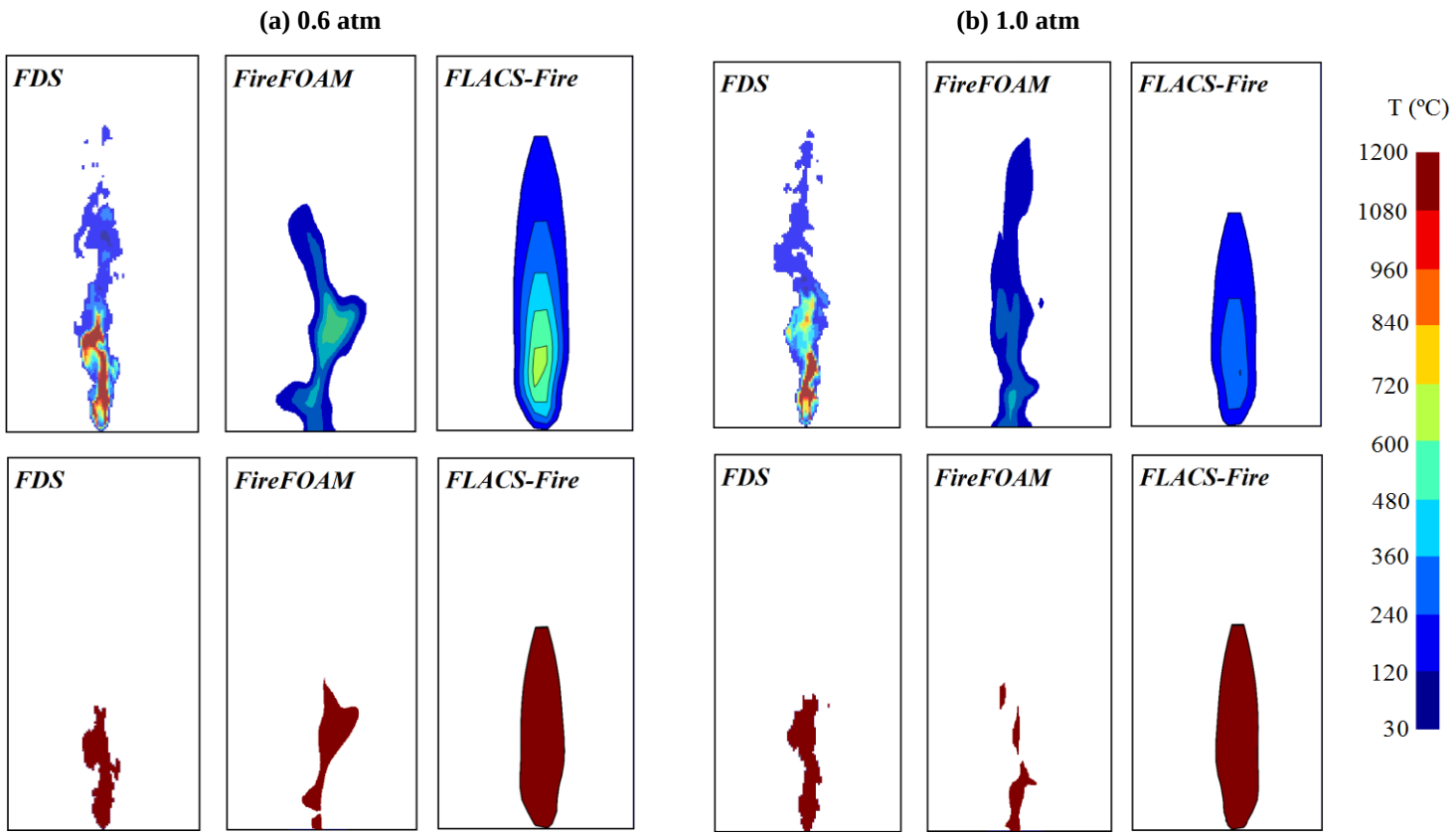

Figure 5.11. Instant captures (up) and segmented images (down) of the slice file of temperatures corresponding to the fire scenarios at (a) 0.6 atm and at (b) 1.0 atm obtained with FDS, FireFOAM and FLACS-Fire.

5.2.3. Soot yield influence

Experiments have shown that different flame colours and shapes can be observed depending on the ambient pressure (see Figure 2.13). This may be due to differences in combustion efficiency. In this regard, the soot yield fraction prescribed in CFD codes for methane (0.7 %) (very low compared to other hydrocarbon fuels, such as propane (9.0 %) or heptane (12.9 %)), which directly affects the products of combustion, may have a direct influence on the estimated flame shapes. In order to assess the influence of this parameter on flame shape, six simulations have been run in FDS with cell sizes of 16 mm (as it was previously observed that it is a good cell size for most of the geometry descriptors). Specifically, different soot yield fractions have been tested in jet flames at 0.7 atm and 1.0 atm: 0.7 %, 0.5 %, 0.3 % and no soot at all.

Table 5.7 shows the estimations of flame length, equivalent diameter and flame surface obtained with FDS for different soot yield fractions and ambient pressures of 0.7 atm and 1.0 atm. As it can be observed, the estimated flame shape is very similar regardless of the soot yield fraction and the ambient pressure defined. Thus, its influence on the flame shape predictions is negligible.

Table 5.7. Mean geometrical features of the jet fires predicted in FDS with cell sizes of 16 mm and different soot yield fractions.

Soot yield fractions	$\overline{P}_{\infty}$ (atm)	$\overline{L}_F$ (m)	$\overline{D}_{eq}$ (m)	$\overline{A}_F$ (m^2)
0.7 %	0.7	0.41	0.047	0.018
	1.0	0.42	0.050	0.021
0.5 %	0.7	0.41	0.048	0.020
	1.0	0.42	0.050	0.022
0.3 %	0.7	0.44	0.052	0.023
	1.0	0.44	0.051	0.022
0.0 %	0.7	0.45	0.051	0.023
	1.0	0.42	0.047	0.019

5.2.4. Concluding remarks

The geometrical parameters of vertical subsonic jet fires of methane in normal- and sub- atmospheric pressures were predicted by FDS, FireFOAM and FLACS-Fire. Four different grids were selected for each methane jet fire experiment: 8 mm, 16 mm, 24 mm and 32 mm.

The lift-off distances could not be predicted in any of the CFD codes used by means of the EDC combustion approach. Reasonable predictions of flame length, equivalent flame diameter and flame area were usually found in FDS and FireFOAM. Nevertheless, more precise outcomes were obtained in FDS due to the more detailed mixing scale time based on the fastest physical process of the local state of the flow field. On the other hand, a considerable lack of agreement of the equivalent diameter and flame area was obtained in FLACS-Fire in spite of the reasonable flame length estimations.

Table 5.8 summarizes the suitable D^*/δ_x correlation values suggested to estimate the flame shape (except the lift-off distances) of vertical subsonic jet fires of propane at reduced atmospheres in CFD codes. The last row includes recommended D^*/δ_x values from which suitable cell sizes can be calculated to accurately determine the flame shapes of these type of fires in FDS, FireFOAM and FLACS-Fire. Taking into account the above-mentioned points, FDS is noted as the most suitable code to correctly estimate the flame shape of vertical methane jet fires in reduced atmospheres. FireFOAM could also be used for assessing the hazardous effects of subsonic jet fires; however, the results are less accurate than those found in FDS. In addition, the soot yield fraction had a negligible influence on the flame shape predictions.

Table 5.8. Recommended D^*/δ_x intervals suggested to predict the flame shape of vertical subsonic jet fires of propane at reduced atmospheres in FDS, FireFOAM and FLACS-Fire.

Variables	FDS	FireFOAM	FLACS-Fire
L_F	$12 \leq D^*/\delta_x \leq 16$	$D^*/\delta_x = 8$	$D^*/\delta_x = 16$
D_{eq}	$4 \leq D^*/\delta_x \leq 12$	$8 \leq D^*/\delta_x \leq 12$	n.a
A_F	$12 \leq D^*/\delta_x \leq 16$	$D^*/\delta_x = 8$	n.a
Any	$\boldsymbol{D^*/\delta_x = 12}$	$\boldsymbol{D^*/\delta_x = 8}$	$\boldsymbol{D^*/\delta_x = 16}$

5.3. Vertical and horizontal subsonic jet fires of propane

In previous sections, the predictive capabilities of CFD codes were assessed when modelling vertical sonic and subsonic jet fires involving hydrocarbon gas releases. Nevertheless, high-pressurized gas leaks leading to jet fire accidents can also occur in horizontal or inclined orientations (Casal et al., 2012). Particularly, the jet fire orientation is of special interest as it will directly affect the flame shape, its size and the intensity of thermal fluxes emitted. (Gopalaswami et al., 2016) observed that the number of horizontal jet fire experiments reported in literature was minimal compared to vertical jet fires. Consequently, there are very few CFD

simulation analysis of non-vertical jet flames involving hydrocarbon gases (Bennett et al., 1991; Chakrabarty and Aloqaily, 2011; Huang et al., 2018, 2017; Osenbroch, 2006; Zhao and Magenes, 2016).

Given the lack simulation studies of horizontal jet fires, the present chapter presents CFD simulations of vertical and horizontal jet flames. Unlike the sections described above, FDS is the only CFD code used to perform the complete set of simulations. Up until now, FDS has been revealed as the most appropriate code able to reasonably predict the related-fire effects of different types of hydrocarbon fires: from large-scale pool fires, to sonic and subsonic jet fires in normal- and sub- atmospheric pressures. Firstly, predictions of the flame-geometry descriptors are compared against experimental measurements. Based on quantitative statistical measurements, the most appropriate cell size range is defined. Then, the surface emissive power is estimated and compared against experiments by modelling jet fire scenarios with the proposed cell size. To that end, different number of solid angles are also assessed. More details about the experimental data can be found in Section 2.4.

5.3.1. Numerical modelling

Both sets of experiments, vertical and horizontal jet fires of propane, are featured with $U^* < 12$ and thus, the D^*/δ_x correlation can be used to provide a good balance between low grid resolution and computational cost. In this regard, a sensitivity analysis of the mesh resolution is also carried out in this study given the differences of the gas fuels and jet flame orientations. In general, a minimum and a maximum values of 4 and 16 are suggested to resolve the proposed correlation (see Section 3.3). Nevertheless, in previous sections a minimum D^*/δ_x value of 8 was always recommended to reasonably estimate the related-fire effects. Given that, four different D^*/δ_x values are suggested for analysis: 8, 12, 16 and 32.

Table 5.9 summarizes the cell sizes calculated for each fire scenario according to the D^*/δ_x values proposed. A total of 40 fire simulations are performed in FDS. As it can be seen, the sizes of the cells determined are always greater than the original nozzle diameters. Consequently, and as done in section 5.2.1., equivalent nozzle diameters are defined with the same size than the calculated cell. For example, the V12.75_0.007 ($D^*/\delta_x = 8$) scenario is modelled with an equivalent nozzle diameter of 0.08 m and a cell size of 0.08 x 0.08 x 0.08 m^3 and the H19.05_0.042 ($D^*/\delta_x = 32$) with an equivalent nozzle diameter of 0.04 m and a cell size of 0.04 x 0.04 x 0.04 m^3.

Flame length, equivalent flame diameter and flame area are determined via a slice files that recorded the temperatures evolution in the centreline axis of the jet fires. Pixels with apparent temperatures greater than 600 K are considered as flame, while the rest are considered as background. Figure 5.12 shows instant captures of

horizontal and vertical jet fires modelled in FDS during the steady state of the fires. The white contours represent the flame surfaces obtained in both scenarios after having applied the temperature threshold. The lift-off distances are not accounted in this case due to the 'mixed is burnt' assumption considered in the EDC combustion model. More details about the model limitation can be found in Section 5.2.2.

Table 5.9. Cell sizes obtained for the different subsonic jet fires as a function of the D^*/δ_x recommended values.

D^*/δ_x		-		8	12	16	32
Experiment	D_{or} **(mm)**	D^*	$\dot{Q}^{*2/5}$	δ_x **(mm)**			
V12.75_0.007	12.75	0.51	40.1	80	50	40	20
V12.75_0.016	12.75	0.72	55.7	120	80	60	30
V20_0.02	20	0.78	38.8	120	80	60	30
V43.1_0.066	43.1	1.26	29.1	200	120	100	50
V43.1_0.142	43.1	1.72	39.5	260	180	130	75
H19.05_0.015	19.05	0.70	36.3	120	80	60	30
H19.05_0.016	19.05	0.72	37.3	110	70	50	30
H19.05_0.025	19.05	0.56	44.6	120	90	60	30
H19.05_0.040	19.05	1.03	53.8	160	100	80	40
H19.05_0.042	19.05	1.05	54.9	160	100	80	40

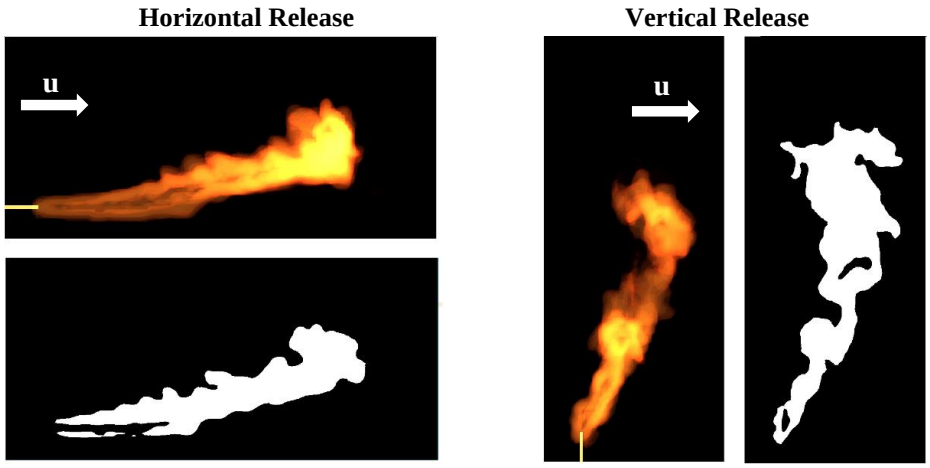

Figure 5.12. Examples of horizontal (left) and vertical (right) releases of the jet fires simulated in FDS. The white contour indicates the area of the flame obtained from a temperature slice file.

Moreover, the surface emissive power is calculated with a wide-angle radiometer located perpendicular to the predominant wind direction facing the flames. Its radial distance from the exit orifice varied from 1.7 m to 3.7 m depending on the jet fire scenario to avoid the direct contact with the resulting flames.

The turbulence, combustion and radiation sub-models described in Table 5.2 belonging to FDS are the ones used in the present study. When performing these simulations, a newer FDS version incorporated by default the Monin-Obukhov (MO) approximation to represent the lateral wind velocity. Therefore, the MO method is used to simulate the presence of wind in the horizontal jet fire scenarios. Simulations are run for 30 s to achieve long-duration steady states. The mass flow rate and the ambient temperature are prescribed according to the experimental data. A soot fraction of 0.09 kg/kg is assumed as the fraction of carbon from propane fuel converted to soot (Kent, 1986) and the lateral and the upper boundaries are open to the outside.

5.3.2. Assessment of the predictions

Cell size

Table 5.10 shows the statistical measurements of the flame-geometry descriptors obtained in FDS for horizontal and vertical subsonic jet fires of propane as a function of the cell size and the geometrical variable. Italic blue values indicate that the metric is within the performance criteria established.

Table 5.10. FB and NMSE measurements of the flame-geometry descriptors obtained in FDS for the vertical and horizontal subsonic jet fires of propane. Italic blue values indicate that the metric is within the established performance criteria.

Jet Release	D^*/δ_x	L_F		D_{eq}		A_F	
		FB	***NMSE***	***FB***	***NMSE***	***FB***	***NMSE***
Vertical	8	*-0.05*	*0.15*	*-0.30*	*0.42*	-0.34	0.92
	12	*-0.02*	*0.11*	*-0.28*	*0.39*	-0.30	0.64
	16	*-0.16*	*0.20*	-0.33	0.62	-0.45	1.47
	32	-0.34	0.51	-0.34	0.63	-0.62	2.42
Horizontal	8	*-0.19*	*0.16*	*0.17*	*0.17*	*-0.02*	*0.29*
	12	*-0.22*	*0.14*	*0.29*	*0.22*	*0.07*	*0.04*
	16	*-0.22*	*0.15*	0.51	0.63	*0.30*	*0.26*
	32	*-0.24*	*0.12*	0.55	0.68	*0.26*	*0.23*

For vertical jet fires, the mean flame lengths are well predicted with D^*/δ_x values ranged from 8 to 16, while these should be of 8 and 12 to provide acceptable estimations of the equivalent flame diameters. On the other hand, none of the cell sizes examined are able to provide reasonable estimations of the mean flame area. This is due to the slight over estimations achieved in the flame length and equivalent diameter. Differently, the mean flame length and area of horizontal jet fires are in accordance with the performance criteria for the whole cell sizes. In particular, the predicted flames are longer and narrower than those measured. The mean equivalent flame diameters can only be reasonably calculated under D^*/δ_x values of 8 and 12. Moreover, the reasonable results obtained demonstrate the suitability of the wind approach used in these simulations.

Despite the discrepancies achieved in the flame areas predicted in vertical jet fires, it is noted that $8 \leq D^*/\delta_x \leq 12$ is the most convenient correlation range to estimate the flame shapes in both jet fire orientations. Recent works involving turbulent heptane flames suggested a D^*/δ_x value of 13 to deliver reasonable estimations of the flame lengths (Ferng and Lin, 2010; Lin et al., 2009), which is in accordance with the main findings highlighted in the present study.

Number of solid angles

Surface emissive power of the jet fire experiments predicted in FDS are summarized in Table 5.9. The cell sizes of the simulations are determined by considering $D^*/\delta_x = 12$, which is the recommended value previously found. Also, four different number of solid angles are defined to assess its influence on the emissive power predicted by FDS: 100, 200, 400 and 800.

Table 5.11 shows the FB and $NMSE$ measurements of the mean surface emissive powers obtained in FDS for both types of jet fire releases according to the number of rays fired. As it can be seen, the greater the number of solid angles, the more accurate the predictions. Emissive power of vertical jet fires is always in accordance within the performance criteria defined, while the horizontal ones met the criteria only under 400 and 800 solid angles. In addition, emissive power is over-estimated in vertical releases, while under-predictions are found in horizontal jet fires. These differences are derived from the geometrical parameters estimated by FDS. The vertical jets are featured with greater flame areas than those measured and thus, greater surface emissive power is obtained. In contrast, the narrower and smaller flames predicted from horizontal releases lead to lower estimations of the emissive power. Based on the present assessment, a minimum number of solid angles of 400 is recommended to provide reasonable predictions of the radiative heat fluxes and thus, of the emissive power of the flames for both types of jet releases. The results found are also in agreement with those presented in previous researches (Ferng and Lin, 2010; Lin et al., 2009).

Table 5.11. FB and NMSE measurements of the surface emissive power obtained in FDS for the vertical and horizontal subsonic jet fires of propane as a function of the number of solid angles. Italic blue values indicate that the metric is within the established performance criteria.

Jet Release	Statistical Measurements	Nº of Solid Angles			
		100	200	400	800
Vertical	FB	*-0.06*	*-0.07*	*-0.08*	*-0.09*
	$NMSE$	*0.22*	*0.20*	*0.18*	*0.15*
Horizontal	FB	0.53	0.33	*0.30*	*0.28*
	$NMSE$	0.68	0.50	*0.45*	*0.44*

5.3.3. Concluding remarks

Flame-geometry descriptors and surface emissive power of vertical and horizontal subsonic jet fires of propane were estimated in FDS. An assessment of different cell sizes revealed that the most suitable D^*/δ_x values should be comprised between 8 and 12 for both type of jet releases. In particular, more precise estimations of the flame shapes were achieved in horizontal jet fires than in vertical ones. Also, a minimum number of 400 solid angles is recommended to accurately estimate the radiative heat fluxes and thus, the emissive powers of the flames.

CHAPTER 6

BEST PRACTICE GUIDELINES IN CFD MODELLING OF ACCIDENTAL HYDROCARBON FIRES IN OPEN ENVIRONMENTS

This section provides a complete set of Best Practice Guidelines (BPG) focused on the practical needs of engineers and Authorities Having Jurisdiction (AHJ) to (i) validate and to (ii) perform computational simulations involving large-scale pool fires and jet fires in open environments. The reader of this BPG document is firstly introduced to a methodology developed for carrying out CFD validation analysis, which details the main steps required to state a code as 'valid' or not to perform real computational fire simulations. Secondly, recommendations on the most appropriate CFD numerical settings are provided to reasonably predict the hazardous effects of accidental hydrocarbon fires. The suggestions noted are based on the main findings of the Chapter 4 and Chapter 5. The suggestions noted must be used with caution, especially for scenarios in which the flow characteristics and code versions could be very different from the examined ones. This work represents a key first step towards a better understanding on the application and use of computational fluid dynamics on accidental hydrocarbon fires in open environments for risk analysis purposes.

6.1. The need of BPG in CFD fire modelling

Since CFD modelling has entered into the research and industrial community, it has become a very useful and promising tool to predict many phenomena of practical interest in different engineering fields (Tolias et al., 2018). This is partly due to the lower costs of computational simulations compared to experiments and to the capabilities of assessing many parameters of the same problem without significant extra cost. Within the fire safety sector, CFD codes are routinely used as analysis tools able to handle complex geometries and significant amount of fire characteristics (Dayanandan et al., 2015). Nowadays, the growth on the number of performance-based designs (PBD) as an alternative approach to prescriptive fire codes has contributed to increase the number of computational fire simulations performed (Chow, 2015). Particularly, PBD codes are being developed to regulate its application given the higher flexibility and innovation capacity that may lead

to lower construction costs without lowering the level of safety (Zalok and Hadjisophocleous, 2011).

The raising trend of CFD simulations has arisen the concern of AHJ about the possible lack of full appreciation of the users concerning the complex modelling parameters required and thus, their impact on the solutions reached (Hadjisophocleous and McCartney, 2005). The development of graphical user interfaces (GUI) and the growth in high performance computing (i.e. from PC-cluster systems to massively parallel supercomputers) allow users without any knowledge of the mathematical models solved nor the fire physics involved, to easily run simulations with good-looking and defendable outcomes. As a result, the predictions obtained could be lacking reliability, hence leading to under- or over- fire protection measures. If the equipment remains under-protected, more severe consequences will be originated in an accidental fire event. In contrast, over-protective measures able to diminish the fire impact will imply excessively and/or unaffordable high costs.

In order to provide reliable estimations of the phenomena of interest through computational simulations, it is essential to firstly address the crucial aspects of the numerical modelling. For that purpose, Best Practice Guidelines (BPG) have been developed to provide guidance on the use of CFD in numerous engineering fields: for reactor safety analysis (Menter et al., 2002; Nuclear Energy Agency, 2015), for marine applications (WS Atkins Consultants, 2002), for dispersion flows in urban environments (Franke et al., 2007; INERIS, 2015), for the design and assessment of ventilation and gas dispersion in gas turbine enclosures (Ivings et al., 2003), for smoke control and management system designs in complex enclosed spaces (Gobeau and Zhou, 2004; Hadjisophocleous and McCartney, 2005) and for hydrogen safety applications (Tolias et al., 2018). Despite the considerable number of BPG documents available, there is no one developed to provide guidance on CFD simulations of accidental hydrocarbon fires occurring in chemical and process industries. Consequently, there are no guidelines bringing support to engineers and AHJ when assessing the predictive capabilities of CFD codes or when performing simulations involving large-scale pool fires and jet fires in open environments.

6.2. BPG in CFD validation analysis

CFD validation analysis examines whether the physical models used in computer simulations agree with real world observations. The basic validation strategy is to identify and quantify both error and uncertainty through comparison of simulation predictions with experimental data.

Validation analysis is increasingly been performed and reported in technical documents to reveal the model's uncertainties in a way that is useful for the end users (McGrattan and Hostikka, 2012). However, CFD validation analysis may be worthless in a high percentage given the large number of possible fire scenarios occurring in real accidents and the continuous development and release of new code's versions. Consequently, it is almost preferable to conduct CFD validation analysis according to the user's interests than considering out-of-date validation exercises or those involving different fire scenarios than those required.

Figure 6.1 presents a detailed description of an in-house methodology developed to carry out CFD validation analysis of accidental hydrocarbon fires in open environments. It provides guidance on the assessment of the predictive capabilities of any computational code when modelling these types of fires. The proposed procedure could be adopted for future CFD validation analysis involving similar fire scenarios as there is no need for implementing extensive statistical methods. In addition, it may be of great interest for AHJ and end users to better define the appropriateness of a CFD code to simulate or not certain fire scenarios.

1. Experimental Data	
Fire experiments description	Hydrocarbon fuel
	Fire area/diameter geometry
	Mass flow rate/Burning rate
	Measuring devices
	Experimental results
2. *A Priori* Validation Analysis	
Code selection	Previous validation analysis
	License costs
	Graphical user interfaces
	Computational resources
Numerical parameters	Simulation time
	Default modelling options
	Computational domain
	Mesh resolution
Computational measurements	Virtual sensors
	Slice files
	Data processing
Results comparison	Statistical measures
	Performance criteria
3. *A Posteriori* Sensitivity Analysis	
Numerical adjustments	Sub-models and models constants
Quantitative results comparison	Statistical measures
	Performance criteria
4. Reporting Conclusions	
Technical document	Validity of the code
	Recommendations

Figure 6.1. Methodology developed to perform CFD validation analysis of computational simulations involving accidental hydrocarbon fires in open environments.

6.2.1. Experimental data

The first task of the CFD validation analysis consists on describing the fire experiments willing to be compared against simulation results. These can be either obtained from previous investigations or from in-house tests, which should at least contain the following information:

- Chemical composition of the hydrocarbon fuel used. Additional information such as the heat of combustion, the heat of reaction, the kinematic/dynamic viscosity of the fuel and its density is highly valuable.

- Geometry and dimensions of the fire base (area, diameter or radius) from which the fuel flow is released or burnt. The possible inclination and the orientation (horizontal or vertical) must be given.

- Mass flow rate or gas velocity in the case of jet fires and burning rates for liquid pool fires. Alternatively, dimensionless numbers, such as the Froude number or the Reynolds number, may be given. Mach numbers are highly valuable to detail the flow regime of gas fuel releases.

- Description of the type, location and number of devices set-up and cameras used to measure the different variables of interest, as well as the time step at which the variables are registered. Special attention must be given to the environmental conditions: ambient temperature, wind velocity and direction, terrain description and altitude above the sea level. Description of other equipment and apparatus involved on the fire experimentation are highly valuable, such as obstacles and structures. The segmentation processes performed from the video recordings determining the flame-geometry descriptors must be completely detailed.

- Spreadsheets containing the variables evolutions as a function of time. Instead, the averaged values and the standard deviations can be provided for specific fire states. The steady state is the one commonly reported; however, the growth or the extinction states could also be considered if required. Complementarily, graphical scatter plots of the variables measured as a function of time can be shown: thermocouples temperature, heat fluxes and boundary conditions.

6.2.2. *A priori* validation analysis

After having described the experimental set-up, the second task of the CFD validation analysis entails *a priori* computational simulations. These are basically intended to represent the fire phenomenon of interest by setting up the default

numerical options of a CFD code. Following there is a description of the most important features of *a priori* fire simulations.

Code selection

Sometimes the user must perform computational simulations with a specific code according to regulations or to the stakeholder's requests. In these cases, there is no choice for selecting a different CFD tool and the *a priori* validation analysis must be carried out with the enforced code. Otherwise, the user is responsible for selecting the most appropriate code, which can be based on the following recommendations:

- Previous validation exercises reported in technical documents. Possibly, similar scenarios as those of interest have been previously validated against certain CFD tools. Therefore, no further validation analysis is required only if the code version is the same and similar modelling options have been assessed (i.e. combustible, fire size, burning/mass loss rates and boundary conditions).

- Licence costs. Open-source codes, such as FDS and FireFOAM, are more likely to be selected because these can be freely downloaded and used. Nevertheless, commercial codes can be of great interest depending on the case study. For example, if the impact of flash fires must be evaluated in an offshore platform, FLACS-Fire is more adequate than the previous ones because of the greater number of studies made involving this type of fires as summarized in the user's guide.

- Graphical user interface (GUI). The existence of GUI's can facilitate the definition of the input numerical parameters and the design of complex geometries. Consequently, the time needed to build fire scenarios is considerably reduced. Nevertheless, certain GUI possess limitations that should be checked in advance such as the use of specific sub-models.

- Computational resources. The time required to complete simulations is of crucial importance when selecting a CFD tool. In general, the number of cells modelled is the parameter that dictates the computational simulation time; however, there are other factors that must also be considered. For example, the code capability for splitting multiple meshes into different PC cores can significantly reduce the computational time. The sub-models defined to solve the turbulence, combustion, radiation and soot phenomena may also affect the times needed to complete simulations. CFD user's guides generally contain more information on the computational costs associated to the sub-models solved.

Numerical parameters

Default modelling options must be maintained with no modification at all as these are based in a wide range of validation exercises and numerical assessments performed by the code developers. Either for pool fires and jet fires, the amount of combustible burnt per unit of time should be always prescribed as a flow entering through a vent located according to the experimental set-up rather than predicting its value via pyrolysis sub-models. The soot yield fraction should be also prescribed to facilitate the conversion of combustion products into soot to avoid long and complex mathematical calculations. Table 6.1 provide details on the burning rates and soot yield fractions of most common hydrocarbon fuels used in industrial facilities.

Table 6.1. Burning rate, soot yield fraction and heat of combustion of the most common hydrocarbon fuels used in industrial facilities. Data sources come from (Babrauskas, 1983; Kent, 1986).

Fuel	Chemical formula	$\dot{m}''$ (kg·s^{-1}·m^{-2})	Soot yield (%)	ΔH_c (MJ·kg^{-1})
Methane	CH_4	0.078	0.7	50
Propane	C_3H_8	0.099	9.0	46
Heptane	C_7H_{16}	0.101	12.0	44.6
Gasoline	C_6H_{14}	0.083	10.0	44.7
Diesel	$C_{12}H_{26}$	0.062	12.0	42.4
Butane	C_4H_{10}	0.078	10.0	45.7

Computational domains must be defined according to the obstacles restrictions, the measuring devices, or to the flame length estimated in the experiments. Apart from the ground, the rest of the lateral boundaries of the volume modelled must be left open unless otherwise specified. Wind velocity and direction must be prescribed in windy fire scenarios as described in the experiments.

A preliminary mesh sensitivity analysis must be undertaken for buoyancy-dominated plumes based on the D^*/δ_x correlation, whose values should be ranged between 4 and 16 (Sally and Kassawara, 2007). The most suitable cell sizes can be determined in two different ways: (i) when there is reasonable agreement between simulation results and measurements, or (ii) when the estimations found are very similar for different D^*/δ_x values. The exit orifices of jet fires can be smaller than the proposed cell sizes. In those cases and when the jet fires are subsonic, equivalent nozzle diameters must be calculated, whose values are the same as the cell sizes determined. Otherwise, when the jet fires are sonic, the pseudo-diameter approach must be applied, which determines an equivalent nozzle diameter as a function of the Mach number. Then, the cell size is defined with the

same value of the resulting equivalent nozzle diameter. In either case, equivalent mass flow rates must be calculated and defined within the computational simulation. Depending on the computational resources available and the CFD code used, multiple meshes may be configured to reduce the computational times required. The split grids should approximately contain the same number of cells to improve the computer performance.

CFD simulations must be lasted for at least 60 s to obtain reasonable steady state predictions of the different parameters. Longer simulation times can be considered if there are conditions that vary over time (i.e. mass of fuel burnt, ambient temperature or the wind velocity/direction), or if proposed by the AHJ.

Computational measurements

The time step for registering variables should be equal that the one used in the experimental dataset. If this was not reported, a time step of 0.25 s or 0.50 s is suggested. Virtual sensors can be used to directly determine the temperature registered for thermocouples and the heat flux received at a certain distance from the fire origin by radiometers or radiant panels. On the other hand, slice files recording the temperature contour must be placed in the centreline axis of the fire and parallel to the wind direction (only if wind is present) to determine the geometrical features of the flames (i.e. flame length, flame area, flame height, or tilted angle). It is worth noting that lift-off distance of jet fires cannot be predicted under the 'mixed is burnt' assumption used by the EDC combustion model.

The surface emissive power of the flames cannot be directly measured from CFD simulations. Instead, these can be determined by means of alternative methods such as the solid flame model. To that end, virtual sensors that capture the heat flux received must be placed facing the fire at a maximum radial distance of 5 m from its origin and perpendicular to the wind direction. In addition, the flame shapes of the fire must also be measured by means of slice files as previously explained. An atmospheric transmissivity of 1 should be assumed given the short distance between the sensor and the fire, and the view factor between the sensor and the fire flames must be determined.

Comparison of results

Qualitative scatter plots are suggested to rapidly offer an overview of the code capabilities to estimate the variables of interest. If so, vertical and horizontal bars of the mean values predicted should be added to depict the standard deviations of the simulation results and the experimental data, respectively. However, these are not mandatory as there is no quantification of the computational uncertainties nor of the agreement reached over time (Oberkampf and Barone, 2006). Instead, at least two quantitative statistical measurements must be undertaken simultaneously to compare computational predictions against experimental measurements and

thus, to determine the possible uncertainties derived from simulation predictions. To that end, a performance criterion must be defined for each quantitative comparison method applied, by which a code can be stated as valid or not. In the present document, the Fractional Bias (FB) and the Normalised Mean Squared Error ($NMSE$) are the statistical measures suggested (Rew and Deaves, 1995). These must comply with the following performance criteria: the mean bias must be within ± 30 % of the mean ($-0.3 \leq FB \leq 0.3$) and the random scatter about a factor of 2 of the mean ($NMSE \leq 0.5$) (Hanna et al., 2004). If the predictions are within the performance criteria defined, the code is declared 'valid' for carrying out computational simulations of the fire scenarios investigated. If not, *a posteriori* sensitivity analysis offers a second-modelling change to meet the criteria by modifying some numerical parameters within the CFD tool used.

6.2.3. *A posteriori* sensitivity analysis

Computational simulations are highly sensitive to the uncertainties in the input data, to the level of rigor used in modelling the relevant physics and chemistry of the fire phenomenon and to the use of inadequate numerical models (*ISO 16730-1:2015(E) Fire safety engineering - Procedures and requirements for verification and validation of calculation methods - Part 1: General*, 2015). Therefore, it could be possible that the *a priori* validation analysis do not meet the minimum level of agreement expected. In these cases, further adjustments are necessary to improve the accuracy of results, which can be accomplished through *a posteriori* sensitivity analysis. These mainly consists on performing new CFD simulations by modifying certain parameters of the code in order to reasonably estimate the fire scenario of interest. As occurred with the *a priori* validation analysis, the new predictions must be compared against more than one quantitative statistical measures, such as the FB and $NMSE$ and must meet the performance criteria. The adjustments envisaged are related with the sub-models solved and the model constants implemented.

In the case of windy fire scenarios, different wind sub-models may be firstly evaluated only if more than one are available within the fire code. Complementarily, the wind sub-models constants user-defined, such as the ground roughness and the reference heights, could also be modified to find out the most appropriate ones. If the lack of agreement remains, whatever the ambient conditions are, additional modelling changes are necessary. The variables leading to disagreements act as indicators of where the modifications should be made. For example, if the heat fluxes registered by the virtual radiometer are not accurate enough, adjustments must be performed to the approach used to solve the RTE. For instance, other radiation sub-models may be used to estimate the radiative heat fluxes or the number of solid angles should be progressively increased until convergence on the radiative fluxes predictions is achieved. If this does not occur,

radiation sub-model constants, such as the correction factor, may be varied in last instance.

On the other hand, modifications on the turbulence and combustion sub-models should be undertaken if discrepancies are observed in the temperatures measured. In this sense, different turbulence approaches intended to closure the RANS or LES equations may be assessed. Likewise, some models constants, such as the Smagorinsky constant or similar ones, may be varied until the agreement is reached. Secondly, variations on the constants defined to determine the mixing time scales could be performed only if previous modifications do not improve the accuracy of estimations. It is worth noting that adjustments on the model's constants may lead to numerical instabilities and modelling errors when modelling different types of fire scenarios. Because of that it is suggested to avoid when possible their modifications.

6.2.4. Concluding remarks

When AHJ review engineering projects involving computational fire simulations, or when users are seeking for an appropriate CFD tool to perform simulations, they typically begin by reviewing validation analysis reports. These are essentially focused on notifying if a code is 'valid' or not to estimate the fire-related effects for certain fire scenarios based on quantitative comparisons. Possibly, the performance criteria are met under some variables, whereas there are others that do not agree with the experimental results. In these cases, the CFD tool can be noted as 'valid' for estimating certain variables even if there are others that cannot be accurately predicted.

It is essential to provide well-documented validation reports in order to avoid misunderstandings that might arise and to facilitate the understanding of the modelling options defined. For that purpose, the technical document must contain at least all the details corresponding to the different phases previously described. In addition, a summary document is suggested to highlight the main findings obtained through the CFD validation analysis performed. The final report can also include recommendations on further modelling adjustments that may improve the results accuracy, or that may reduce the computational times required, as well as comments about the user-tool friendliness. Lastly, the written reports could be sent to the code developers to discuss about the pros and cons found, hence contributing to its development and improvement.

6.3. BPG in CFD modelling for fire hazard assessments

Assessing the hazards of possible accidental hydrocarbon fires occurring in industrial facilities is extremely useful to determine the safety design and the safety measures required to minimize their impact in equipment and personnel. To that end, semi-empirical methods can provide reasonable predictions of the related-fire effects; however, there are certain cases where computational simulations are highly recommended because of its modelling advantages (more details can be found in Section 1.2.) or when required by AHJ or stakeholders. In these cases, the selected CFD code must be validated prior to perform CFD simulations. Previous section brings details to undertake a CFD validation analysis. Nevertheless, validation analysis of CFD codes cannot be always carried out given the lack of experimental data or the complicated access to the databases. In consequence, the level of accuracy of the estimations obtained rest unknown, hence hindering its use in real engineering problems.

The present section provides BPG in CFD for fire hazard assessments involving a wide range of possible hydrocarbon fire accidents that can occur in chemical and process industries (Table 6.2). It provides guidance on the numerical parameters that should be set-up within the CFD tool used to maximize the reliability of the estimations. The recommendations provided are based on the main findings obtained in Chapter 4 and Chapter 5 as a result of the good agreement commonly found between predictions and experimental measurements, especially in FDS. The presented document should be valuable for a broad audience, from unexperienced to expert CFD users. Any interested user in performing computational simulations related to large-scale pool fires or jet fires should be able to accomplish it with acceptable results. The presented suggestions are valid for different CFD tools; however, caution must always be taken as these can contain different sub-models and numerical schemes.

The main sub-models solved (i.e. the turbulence, combustion, radiation, soot and wind) are the same regardless of the type of hydrocarbon fire. Consequently, there is no numerical modelling difference between simulations involving pool fires of kerosene of 6 m-diameter and for subsonic jet fires of methane with nozzle diameters of 10 mm. Mass loss rates must be prescribed rather than predicted via pyrolysis models. The minimum number of solid angles must be of 400 to provide reasonable estimations of the radiative heat fluxes. Additional values of the ground roughness used for solving the wind sub-model can be found in (Stull, 2000), while soot fraction values for different hydrocarbon fuels can be found in (Kent, 1986).

The maximum numerical time step should be of 0.8 to avoid numerical instabilities and the minimum simulation time must be of 60 s under steady ambient conditions. Longer simulation times can be set-up if desired, or if some modelling conditions

vary over time. The minimum length of vertical axis only depends on the fire diameter. In contrast, the minimum length of lateral axis depends on the fire diameter and the wind conditions.

On the other hand, the mesh resolution is defined according to the resulting Mach number, M_a, and the fire diameter, D. The dimensionless expression of the characteristic diameter of the fire, D^*/δ_x, is calculated when the Mach number is equal or lower than 0.3. The cell size, δ_x, is then determined by considering the recommended ranges for the expression, which should vary from 8 to 16 approximately. If the calculated cell size is higher than the fire diameter ($D < \delta_x$), an equivalent nozzle diameter should be considered, $D_{eq,n}$, whose value must be the same as the cell size ($D_{eq,n} = \delta_x$). An equivalent mass flow rate is determined as a function of the equivalent nozzle diameter found. For fuel flows with Mach numbers higher than 0.3, the pseudo-diameter approach must be applied. Taking into account the initial ambient and flow release conditions, an equivalent nozzle diameter is obtained by considering a Mach number equal or lower than 0.10. The cell size defined is of the same value as the equivalent diameter found. In average, a mean error estimation of ± 22 % can be achieved when following the stated BPG to perform computational simulations of hydrocarbon fires in open environments.

Table 6.2. Numerical parameters suggested to perform computational simulations involving turbulent hydrocarbon fires in open environments.

Numerical Parameters	Recommendations
Numerical Time Step	• CFL ≤ 0.8
Simulation Time	• $\geq 60\ s$
Computational Domain	• Min. length vertical axis: $8D^{(1)}$ • Min. length lateral axis in windless scenarios: $2D^{(1)}$ • Min. length lateral axis in windy scenarios: $\geq 6D^{(1)}$
Mesh Resolution	• If $M_a \leq 0.3$ and $D^{(1)} > \delta_x$: $16 \geq D^*/\delta_x \geq 8.0$ • If $M_a \leq 0.3$ and $D^{(1)} < \delta_x$: $12 \geq D^*/\delta_x \geq 8.0$ $D_{eq,n} = \delta_x$ $\dot{m}_{eq} = 0.25\rho_f u_f \pi {D_{eq,n}}^2$ • $M_a \geq 0.3$: Pseudo-diameter approach $D_{eq,n} = \sqrt{4\dot{m}_f/\pi c \rho_f M_a}$, with $M_a \leq 0.10$ $D_{eq,n} = \delta_x$
Fuel Evaporation	• Prescribed mass flow rate
Turbulence	• LES: Deardorff model
Combustion	• EDC: Complex mixing time scales
Radiation	• DOM: Minimum number of solid angles: ≥ 400
Wind	• Monin-Obukhov Similarity:(2) Recommended values: $\eta = 0.03$ and $L = 100$
Soot	• Conversion Factor Model(3)
Measurements	• Measuring time step: $\geq 0.25\ s$ • Temperatures and radiative fluxes: Virtual sensors • Flame-geometry descriptors(4): temperature SF

(1) Pool diameter in the case of pool fires and equivalent diameter in the case of jet fires.

(2) Reference height depends on the experimental data. More values of the ground roughness can be found in (Stull, 2000).

(3) Soot fraction values for several hydrocarbon fuels can be found in (Kent, 1986).

(4) Lift-off distances cannot be predicted in the case of jet fires.

CHAPTER 7

CASE STUDY: COMPUTATIONAL FIRE HAZARD ASSESSMENT IN STORAGE TANKS IN THE PORT OF BARCELONA

This section presents a case study on the use of CFD simulations when performing a fire hazard assessment (FHA) in an oil storage farm. Specifically, FDS is the CFD code selected to carry out simulations of fires involving real oil storage tanks located at the Port of Barcelona. The main objective is to evaluate the impact of the possible accidental fires that may occur on the surrounding structures and people. For that purpose, different fire scenarios are proposed for analysis according to the distribution and number of storage tanks, as well as the ambient conditions (i.e. temperature and wind). Simulation results are compared with predictions obtained by means of semi-empirical correlations in order to examine the advantages and drawbacks of both modelling methods. Fire protection measures and safety recommendations are provided based on the related-fire effects estimated in the present study.

7.1. Fire hazard assessment in oil storage tanks

Liquid storage tanks are commonly used in chemical and process industries for storage of combustible and flammable liquids (Argyropoulos et al., 2012). The loss of containment of hazardous material may lead to accidental events with severe results: injuries, fatalities, business interruption, loss of a facility and environmental impact (Liu et al., 2017). A literature survey on storage tank accidents that occurred in industries from 1960 to 2003 revealed that fire was the most common cause (Chang and Lin, 2006). The 33 % of these were caused by lightning, the other 30 % by human errors, while the rest were originated by causes such as equipment failure, sabotage, leak and line rupture, static electricity, and radiant heat.

Within this framework, the appropriate prevention and control measures must be determined to reduce the occurrence and effects of accidental fires. In this regard, fire hazard assessments (FHA) are convenient methods to identify possible fire hazards without consideration of the likelihood of occurrence (Meacham et al., 2016). Consequently, fire protection procedures and management policies required to ensure safety can be implemented, hence minimising the impact of

accidental fires in oil storage farms. FHA's typically involve surveys on the potential ignition sources, fuel sources, arrangements and configurations of fuel packages, boundary conditions, as well as the existence of fire safety features (John, 2016). Based on this information, different fire scenarios are then proposed to assess the related-fire effects in the affected area. It is worth noting that FHA's can be used during design phase, as part of an approval process, or as part of an inspection and maintenance program.

There exist different tools and methods to perform FHA's in industrial facilities. International standards and regulations have been typically used to assess the fire hazards and the possible consequences triggered. Nevertheless, CFD simulations are increasingly being used to that end (more details on CFD modelling can be found in Section 1.2.). Recently, different authors performed fire simulations in FDS and Fluent codes involving oil storage tanks from 12 to 50 m-diameters containing hydrocarbon fuels such as kerosene, butane, and gasoline under different wind conditions (Ahmadi et al., 2019; Benucci and Uguccioni, 2010; Liu et al., 2017; Sun et al., 2014). Their main concern was to determine the heat fluxes received in the equipment and obstacles sited near the fire sources. These works essentially highlight the usefulness of CFD codes to provide insight into the possible consequences triggered by accidental fires. Following sub-sections show a computational FHA performed in a real oil storage farm located in the Port of Barcelona.

7.2. The Port of Barcelona

7.2.1. Situation

The Port of Barcelona covers a total land area of over one thousand hectares, with wharves and berths totalling 20.3 kilometres with alongside depths up to 16 meters (World Port Source, 2019). Figure 7.1 shows the aerial view of the Port of Barcelona limited with the rest of the city by a straight dark and continuous line. The port area is divided into eight different terminals according to the activities performed in each one. Among these, the liquid bulk terminal (marked in orange) stores the hazardous materials arrived on cargoes prior to its distribution through the national road, rail and pipeline networks.

In 2016, the port handled a total of almost 10.8 million tons of liquid bulk cargoes, including almost 9.0 million tons of hydrocarbons distributed as follows: 4.1 million tons of natural gas, almost 2.4 million tons of diesel oils, over 1.5 million tons of gasoline, nearly 865.6 thousand tons of fuel oil, and almost 36 thousand tons of other liquid bulk cargo (i.e. petroleum products, fuel oil, coal, petroleum fuel gases, and crude oil). The other liquid bulk cargoes moving through the Port

of Barcelona included almost 1.2 million tons of chemical products and nearly 473 thousand tons of oils and fats.

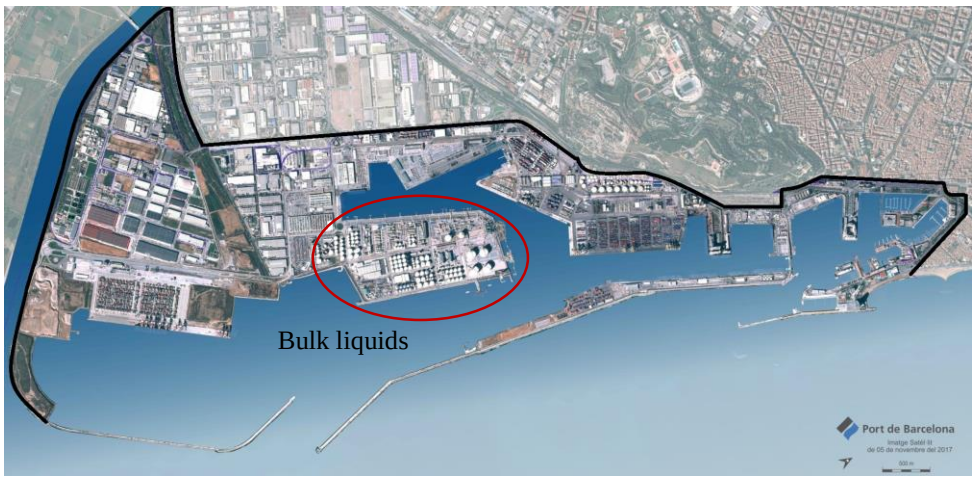

Figure 7.1. Aerial view of the Port of Barcelona (Port of Barcelona, 2019). The continuous dark line separates the Port from the rest of the city. The red circle indicates the bulk liquids area.

Table 7.1 summarizes the storage tanks information of the operating companies in the liquid bulk terminal. The largest ones correspond to Enagas, whose tanks have a storage capacity of 840,000 m^3. Enagas is a common carrier for the high-pressure natural gas network and the technical manager for Spain's gas system. In a lower amount, Relisa receives, handles, and forwards bulk liquids that include chemical and biofuel products in an area of 2.7 hectares that is able to store up to 200,000 m^3 along 127 tanks. TEPSA is a leader for receiving, storage, and forwarding bulk liquid petroleum products, biofuels, and chemicals. It has the largest number of tanks in the Port of Barcelona (244) with a total capacity for almost 350,800 m^3. Similar fuels are stored in Vopak Terquimsa's tanks, with a higher capacity per tank that could achieve 39,000 m^3. The company provides logistic access to Spain, Southern Europe, and North Africa. Koalagas, a joint venture of Decal España, supplies, stores, and handles liquefied petroleum gas (LPG). It is the first company in Spain to use TEXSOL® protection for LPG spheres. Its facility has a total capacity for 4,000 m^3 divided in two spheres. Meroil and Tradebe store and distribute a wide range of petroleum products such as gasoline, diesel, and kerosene, with tank capacities that could achieve 30,000 m^3.

Most of the tanks sited in the Port of Barcelona are fixed-roof with cone-shaped welded to the top edge of the tank shells. These are especially conceived for the storage of liquid fuels with vapour pressures close to atmospheric pressure. The design prevents water accumulation and permits a vapour space between the liquid surface and the roof underside (Shelley, 2008). This allows the roof to be separated from the tank shell and prevents it from propelling upwards in case of an internal

overpressure (Nwabueze, 2016). The diameters, the heights and the separation distances between tanks vary according to the operating companies and their capacities. Although there are no details on the materials composing the vertical cylinders, it is assumed that the tanks are in carbon steel with epoxy paint as thermal insulator (American Petroleum Institution, 2018).

Table 7.1. Storage tanks information of the operating companies in the Port of Barcelona.

Company	Ref.	Stored fuels	Nº of tanks	Tank capacity ($\cdot 10^3$ m^3)	Total storage capacity ($\cdot 10^5$ m^3)
Enagas	(Enagas SA, 2015)	LNG	8	840	67.2
Relisa	(Receptora de Liquidos SA (Relisa), 2019)	Miscellaneous(2) Biofuel	127	0.1 to 7.5	2.0
TEPSA	(Terminales Portuarias SL (TEPSA), 2019)	Petroleum(1) Miscellaneous(2) Biofuel	244	0.05 to 18	3.5
Vopak Terquimsa	(Vopak Terquimsa, 2019)	Petroleum(1) Miscellaneous (2) Lubricant/Vegetal	44	0.18 to 39	1.95
Decal & Koalagas	(Decal España SA, 2019)	LPG	25	15 to 20	4.45
Meroil	(Meroil SA, 2019)	Petroleum(1)	32	3 to 30	6.4
Tradebe	(Tradebe Port Services, 2019)	Petroleum(1)	29	5 to 24	3.75

(1) Combustibles such as fuel oil, diesel, gasoline, jet fuel, and kerosene among others.

(2) Chemicals such as fertilizers, organic/inorganic acids, and alcohols among others.

7.2.2. Fire accidents in fixed-roof tanks

Fires are likely to occur when vapours or liquids are released from a controlled environment to areas where there may be an ignition source, or alternatively, when an ignition source is introduced into a controlled environment. There exist different accidental fires that can occur in fixed-roof tanks: overfill ground fires, vent fires, and full surface fires (Crippa et al., 2009). The overfill ground fires, also called dike fires, are considered the least severe type of fire incidents in fixed-roof tanks. These commonly result from piping or tank leakages, and operator error or equipment malfunction. Provided that the dikes are correctly designed, the liquid combustible released will be confined within the dikes and the fire would be treated as a pool fire. However, if the dike walls are compromised, the burning fuel could escape from it, which could lead to a possible escalation of the fire.

Vent fires are mainly caused by lightning strikes that ignite combustible vapours on the top of the roof. These are small fires that can usually be extinguished with a dry chemical fire extinguisher or by reducing the pressure in the tank. On the

other hand, overpressures inside the tanks often provoke internal explosions above the liquid fuel layer, which propel upwards the shell of the roof. Immediately, the combustible is ignited and a full surface fire is originated. These are the most severe and challenging fire accidents in fixed-roof storage tanks because of the large burning areas and the considerable amount of resources needed to control and extinguish the fire. During full surface fires, the boilover event, which causes burning fuel to be ejected outside the tank area and increases the turbulence of the fire, may arise as a result of the fire-fighting extinction attempts such as the filling of the tanks with fresh water or foams (Koseki et al., 2003). In consequence, the combustible particles expelled from the liquid surface may present a hazardous situation for personnel and firefighters sited near the tank in fire, and may also be the initiating event for an additional fire or explosion (Hemmatian et al., 2014).

7.2.3. Fire hazards and consequences

The main hazardous effects of oil storage tank fires affecting the personnel and the structure equipment are the radiative heat fluxes, the heat stress, and the toxicity of the products of combustion (Nwabueze, 2016). Among these, the thermal fluxes equally pose a significant hazard for both, people and facilities. Depending on the amount of heat released, the distance from the fire to the targets affected, and the ambient conditions, the thermal radiation on people can range from first degree burn injury to fatality (Table 7.2). Unprotected general public is considered to be safe under maximum heat fluxes of 1.5 $kW \cdot m^{-2}$, while severe pain may be caused with values equal or higher than 2.5 $kW \cdot m^{-2}$ (British Standards Institution, 2004; LaChance et al., 2010). Protected fire responders may tolerate threshold values up to 5 $kW \cdot m^{-2}$. Greater heat flux may cause significant injuries and fatalities. On the other hand, structures can be also notably impacted by thermal fluxes (Table 7.3). Threshold values of 5 $kW \cdot m^{-2}$ or lower may cause light damages, such as windows breakage. Thermal fluxes ranged between 10 and 20 $kW \cdot m^{-2}$ imply moderate damages on structures as these are being heated up, and heat flux values of 100 $kW \cdot m^{-2}$ or higher provoke the failure of the structure and the total loss of containment.

Table 7.2. Impact of radiant heat flux on people. Data sources come from (British Standards Institution, 2004; LaChance et al., 2010).

Heat Flux ($kW \cdot m^{-2}$)	Effects on People
1.5	• No harm. • Safe for the general public and for the stationery personnel.
2.5	• Intensity tolerable for 5 min. • Severe pain above 5 min exposure.
3	• Intensity tolerable for non-frequent emergency personnel for 30 min.
5	• Pain for 20 s exposure. • 1st degree burn. • Intensity tolerable for frequent emergency personnel.
9.5	• 2nd degree burn after 20 s.
12.5 - 15	• 1st degree burn after 10 s. • 1 % fatality in 1 min.
25	• Significant injury in 10 s. • 100 % fatality in 1 min.
35 - 37.5	• 1 % fatality in 10 s.

Table 7.3. Impact of radiant heat flux on structures and equipment. Data sources come from (Lees, 1996).

Heat Flux ($kW \cdot m^{-2}$)	Effects on Structures and Equipment
5	• Glass breakage (30 min exposure).
8 - 12	• Radiation intensity threshold capable to cause domino effects (> 30 min exposure). • Ignition vegetation (10 min exposure)..
10 - 20	• Ignition of hydrocarbon fuels (1 min exposure). • Melting of plastics (30 min exposure). • Failure of structures except concrete (20 min exposure). • Cable insulation degradation (> 30 min exposure).
25 - 32	• Steel deformation (> 30 min exposure). • Ignition of wood (15 min exposure)..
35 - 37.5	• Process equipment and structural damage (> 30 min exposure).
100	• Steel structure collapse (> 30 min exposure).
200	• Concrete structure failure (30 min exposure).

The air temperature is another hazardous factor that only affects people. Under high ambient temperatures, the body's natural cooling efficiency could be impeded, hence causing heat stress that may result in severe pathological effects and possible fatal outcomes (Table 7.4). Under temperatures lower than 70 ºC there is an uncomfortable feeling, while between 70 ºC and 150 ºC the impact on people is often dominated by difficulty to breathe. Particularly, 149 ºC is the maximum survivable air temperature threshold defined.

Table 7.4. Impact of air temperature on people. Data sources come from (DNV Technica, 2001; "NORSOK STANDARD - Risk and emergency preparedness assessment," 2010).

Temperature (ºC)	Effects on People
70	• Uncomfortable situation
127	• Difficult breathing.
140	• 5 min tolerance limit for escape
149	• Temperature limit for escape.

Smoke and the products of combustion originated may also pose a critical situation for people. The species released from hydrocarbon fires notably vary according to the type of fuel and materials involved: carbon dioxide, carbon monoxide, nitrogen oxides, sulphur dioxide, volatile organic compounds, polycyclic aromatic hydrocarbons, hydrogen sulphide, aerosols and soot. These are of special concern in enclosed compartments due to the accumulation of toxic particles affecting people. Nevertheless, in open environments, the CO component is known to cause the majority of deaths by reducing the visibility and exposing people for unacceptable long periods of time (Ramsdale et al., 2003). Specifically, the minimum visibility levels that should be maintained in the escape routes must be at least of 10 m (British Standards Institution, 2019).

7.3. Methodology

7.3.1. Fire scenarios

Figure 7.2 depicts an aerial (up) and a perspective (down) view of the oil storage tanks located in the Port of Barcelona proposed for analysis (limited with a straight red and continuous line). These belong to Tradebe company and are used to store petroleum products.

Figure 7.2. Aerial (up) and perspective view (down) of the oil storage tanks located in the Port of Barcelona considered for analysis. Both images obtained with Google Earth®.

Figure 7.3 shows the location and separation distances of the oil storage tanks considered. Due to the lack of technical documentation, the dimensions noted have been measured with Google Earth®. In addition, Table 7.5 provides complete details of these: diameters, heights, and capacities.

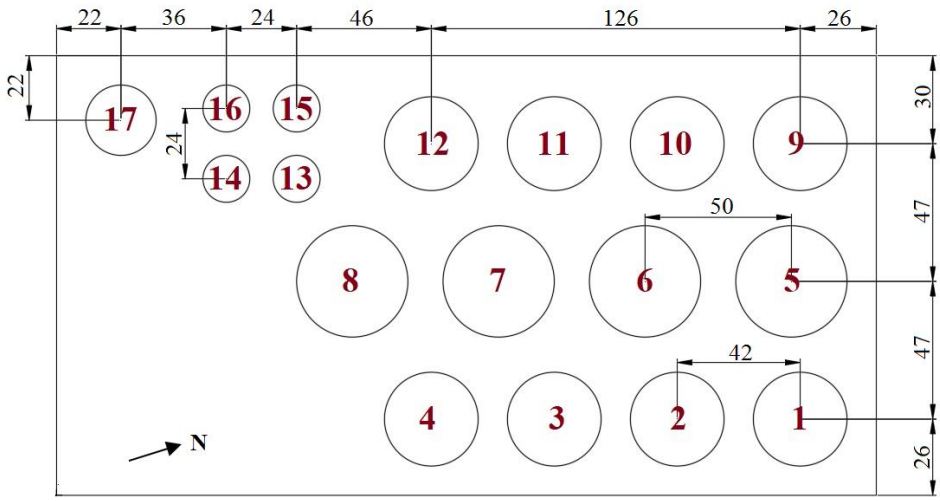

Figure 7.3. Dimensions (in meters) of the oil storage tanks located in the Port of Barcelona considered in the present case study. Tanks are designated in red bold numbers.

Table 7.5. Diameters, heights and capacities of the different tanks located in the Port of Barcelona area, considered in the present case study.

Number	Capacity (m^3)	Diameter (m)	Height (m)
1 to 4	18,000	32	22
5 to 8	25,000	38	22
9 to 12	18,000	32	22
13 to 16	3,600	16	18
17	8,600	24	19

Wind and ambient temperatures are key elements that directly affect the development of port operations. In order to continuously obtain reliable and updated information on the weather conditions at any given time the Port of Barcelona has 8 meteorological stations scattered around the whole area and located at 10 m-height over the ground (Figure 7.4). These are equipped with sensors able to measure different variables such as wind velocity/direction, atmospheric pressure, ambient temperature, relative humidity, and solar radiation.

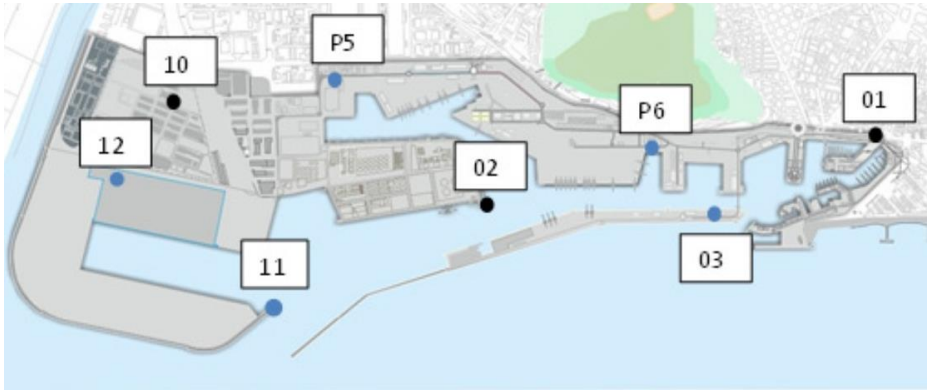

Figure 7.4. Location of the meteorological stations scattered around the Port of Barcelona.

The meteorological station 2 brings the most precise weather conditions of the liquid bulk terminal, where the oil storage tanks considered for the current analysis are located. Table 7.6 summarizes the averaged statistical values of the wind velocities and ambient temperatures measured on it from 2008 to 2015 according to the seasons of the year (Port of Barcelona, 2015). Standard deviations are not included as these were not reported. As it can be observed, mean wind speeds remain constant during the whole year. The predominant direction of the wind in cold seasons (i.e. winter and autumn) is from the east, while the coastal breezes having a northerly component predominate warm seasons (i.e. spring and summer). In contrast, averaged minimum and maximum ambient temperatures clearly vary during the periods of the year: minimum ones of 7 ºC are achieved in winter, whereas maximum ones of 27 ºC are obtained in summer.

Table 7.6. Mean statistical values of the wind velocities and directions and the ambient temperature measured from 2008 to 2015 by the meteorological station 2. Data sources come from (Port of Barcelona, 2015).

Season	Wind Velocity			Ambient Temperature		
	Mean ($m \cdot s^{-1}$)	Max. ($m \cdot s^{-1}$)	Direction(1)	Min. (ºC)	Mean (ºC)	Max. (ºC)
Spring	3.5	18.8	North	13	15	17
Summer	3.4	17.0	North	23	25	27
Autumn	3.2	20.4	East	11	14	16
Winter	3.2	22.1	East	7	11	14

(1) The direction indicates where the wind comes from. For example, a northerly wind indicates that the wind blows from the north to the south.

Table 7.7 shows the 12 fire scenarios proposed for the present computational FHA. All these involve full surface fires occurring in the roof tanks due to its severity and difficulties for its extinction. Tanks are supposed to be completely filled with gasoline, which is used as the main hydrocarbon fuel in the all fire scenarios. As

it can be seen, different burning tanks and weather conditions are examined to assess the related-fire effects that could occur at different seasons of the year in the Port of Barcelona. Specifically, the first four fire scenarios have the fire origin in the tank number 6, which is completely surrounded by others. Thus, the fire effects can affect different adjacent tanks depending on the wind speed and direction. The rest of the fire scenarios proposed have the fire origin in the tank number 9 and number 1 under a fixed wind direction for each of them. By this, the hazardous effects at remote tanks from the burning ones can be assessed.

Table 7.7. Fire scenarios proposed for the computational FHA involving gasoline storage tanks located in the Port of Barcelona.

Fire Scenario	Burning Tank	Ambient Temperature (ºC)	Wind Velocity ($m \cdot s^{-1}$)	Wind Direction
1	6	27	3.4	North
2	6	7	3.2	East
3	6	27	17.0	North
4	6	7	22.1	East
5	9	27	3.5	North
6	9	13	3.4	North
7	9	27	17.0	North
8	9	13	18.8	North
9	1	16	3.2	East
10	1	7	3.2	East
11	1	16	20.4	East
12	1	7	22.1	East

All the tanks surfaces are recovered with an epoxy paint film to protect them against the high radiative fluxes that could receive (Chiguma et al., 2013), whose thermal properties are summarized in Table 7.8. Active fire protection measures are often implemented in storage farms given the difficulties to achieve adequate separation distances in limited industrial areas. In the case of fixed-roof tanks, foam and water systems are designed to be applied through the tank wall and into the burning fuel area to minimise the effect of radiated heat (National Fire Protection Association, 2016). Nevertheless, both systems can fail while working or can be much less efficient than expected and thus, none of these are represented in the simulations performed. Consequently, the worst-case fire scenario can be determined without the influence of external agents.

Table 7.8. Thermal properties of the epoxy paint considered in FDS. Data sources come from (Chiguma et al., 2013).

Thermal Property	Units	Value
Diffusivity	$m^2 \cdot s^{-1}$	$1.60 \cdot 10^{-7}$
Specific heat	$J \cdot kg^{-1} \cdot K^{-1}$	1,284.0
Conductivity	$W \cdot m^{-1} \cdot K^{-1}$	1.78
Density	$Kg \cdot m^{-3}$	8,664.3

7.3.2. CFD modelling

FDS v6.7.0 is the CFD tool used to simulate the fire scenarios proposed. The numerical parameters defined within the code are selected according to the BPG in CFD modelling for fire hazard assessments exposed in Section 6.3:

- The numerical time step is of 0.8.
- The computational domain composed by rectangular and isotropic grid cells is defined according to the obstacles dimensions: 150 m x 280 m x 120 m.
- The Deardorff turbulence model is used to close the LES equations.
- The EDC model is used to solve the combustion phenomena.
- The DOM model is used to solve the RTE under 400 solid angles.
- The Monin- Obukhov Similarity model is used to represent the wind conditions with $\eta = 0.03$, $h_{ref} = 10\ m$, and $L = 100$.
- The CFM model is used to convert the gasoline products of combustion into soot (the soot yield is of 0.10 $kg \cdot kg^{-1}$, and the carbon monoxide yield is of 0.010 $kg \cdot kg^{-1}$ (Koseki, 1999)).

Simulations are run for 15 minutes to obtain long duration of the fire in an Intel® Xeon® E5 2.20 GHz with 256 GB RAM. Apart from the ground, the rest of the boundary layers are open to the outside given the nature of the fire scenarios. The following values have been assumed for the determination of the heat release rate, $\dot{Q}$, which is used for the calculation of the characteristic diameter of the fire: a heat of combustion, Δh_c, of 44.4 $MJ \cdot kg^{-1}$, and a mass loss rate per unit area, $\dot{m}''$, of 0.083 $kg \cdot s^{-1} \cdot m^{-2}$ (Muñoz et al., 2004). According to the maximum recommended values for buoyancy-dominated flows ($D^*/\delta_x = 16$), a cell size of 1.50 m is obtained and set-up for the computational simulations performed. The mesh volume is divided into 4 CPU cores to speed up the simulation times.

Given the diverse harmful effects of storage tank fires on people and structures, different computational measurements are performed. Boundary files are used to calculate the heat flux received at the tanks surfaces. In addition, slice files at 1.8

m over the ground are used to determine the temperatures, and visibility levels and the thermal flux that may harm people sited in the vicinity of the fire area (National Fire Protection Association, 2018). All variables are registered each 0.25 s. The fds2ascii software is used to convert the boundary and slice files into spreadsheets containing the mean values of the measurements obtained at each cell.

The fire scenarios and the modelling parameters defined are built in Pyrosim®, which acts as a graphical user interface for FDS. The rounded tanks are built in Autocad®, and lately imported in Pyrosim® in the appropriate location. Figure 7.5 shows the storage farm design drawn in Pyrosim® used to perform the fire simulations proposed for analysis.

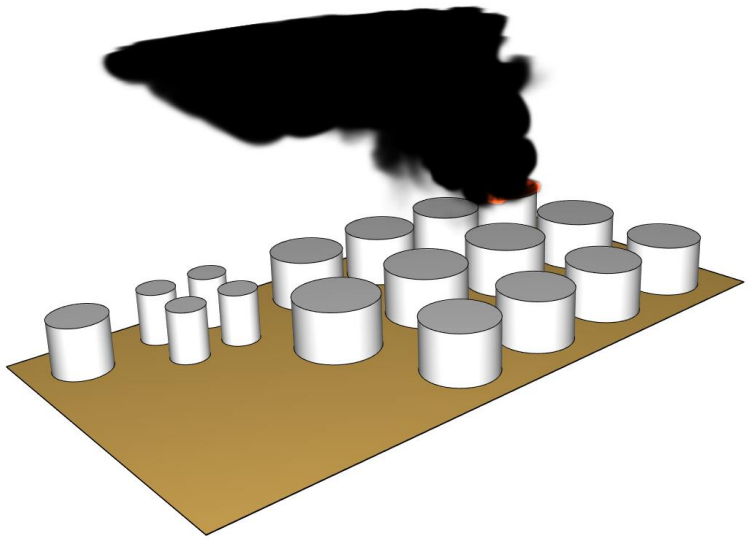

Figure 7.5. Instant capture of the fire scenario 6 showing the geometry created in Pyrosim® and used for the present FHA performed in FDS.

7.3.3. Semi-empirical correlations

There are a considerable number of semi-empirical correlations developed from specific sets of well-defined experiments that can predict the geometrical features and thermal fluxes emitted by hydrocarbon fires (Cowley and Johnson, 1992). Particularly, the heat flux received at a given distance from the fire origin, $\dot{q}_r''$, can be calculated by means of the point source model (Drysdale, 1999):

$$\dot{q}_r'' = \frac{\chi_r \dot{Q}}{4\pi {d_R}^2} \tag{7.1}$$

where χ_r is the radiative fraction (~ 0.35 for large-scale pool fires (Koseki, 1999)), which determines the amount of energy that is transmitted by radiation in a fire, $\dot{Q}$

represents the heat release rate and d_R is the distance from the flame centre to the target location. Specifically, the flame shape is needed to determine the separation distance between the fire origin and the tank's surfaces. Muñoz et al. 2004 developed a correlation that predicts the dimensionless flame length, L_F/D, of large-scale pool fires, which was obtained from numerous diesel and gasoline pool fire experiments ranged from 1.5 to 6 m-diameters:

$$\frac{L_F}{D} = 7.74(m^*)^{0.375}(u^*)^{-0.096} \tag{7.2}$$

where m^* and u^* are the dimensionless mass flow rates and wind velocities expressed as follows:

$$m^* = \frac{\dot{m}''}{\rho_\infty \sqrt{gD}} \tag{7.3a}$$

$$u^* = \begin{cases} {u_w}/{u_c} & if\ u_w \geq u_c \\ 1 & if\ u_w < u_c \end{cases} \tag{7.3b}$$

where $\dot{m}''$ is the mass flow rate per unit area of the pool, ρ_∞ is the ambient density, g is the gravitational acceleration, u_w is the wind velocity, and u_c is the characteristic wind speed determined as:

$$u_c = \left({g\dot{m}''D}/{\rho_\infty}\right)^{1/3} \tag{7.4}$$

In addition, the same authors also provided an equation to estimate the tilted angle of the flame, θ, which often occurs in the presence of high wind speeds:

$$\cos\theta = \begin{cases} 0.96{u^*}^{-0.26} & for\ u^* \geq 1 \\ 1 & u^* < 1 \end{cases} \tag{7.5}$$

7.4. Results and Discussion

7.4.1. Computational estimations

Figure 7.6 shows the mean maximum temperatures registered 1.8 m above the ground affecting personnel on the storage farm area due to the heat stress. The 4th fire scenario is the only one at which the temperature threshold beyond which an uncomfortable situation is originated is reached. Other fire scenarios, such as the 3th, the 7th, the 8th, the 11th and the 12th also achieve considerable temperature values above the ground (i.e. ~60 ºC). Therefore, it is deduced that the highest temperature conditions are originated when the tank fire occurs under wind speeds equal or higher than 17.0 m·s^{-1} regardless of the ambient temperature.

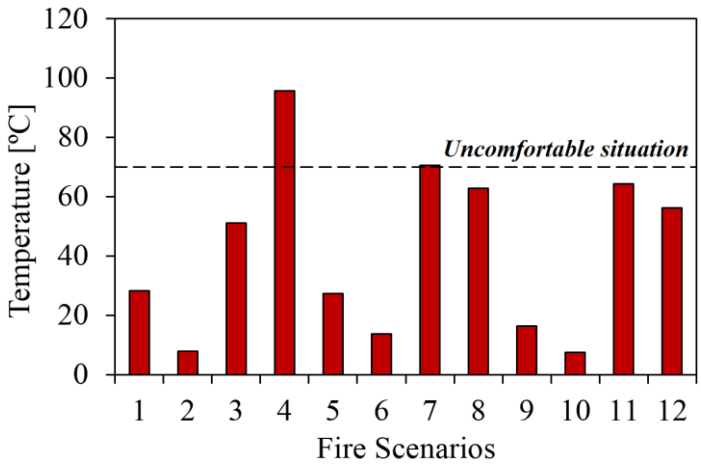

Figure 7.6. Mean maximum temperature values predicted 1.8 m above the ground within the storage farm according to the different fire scenarios modelled in FDS. Long-dashed line represents the performance criteria beyond which uncomfortable conditions for people are originated.

On the other hand, the higher the wind velocity, the lower the height above the ground at which the smoke and products of combustion travel throughout the storage farm. In consequence, the visibility levels are notably reduced as observed in Figure 7.7. The minimum visibility criteria is largely exceeded in highly windy scenarios, whose values may be even lower than 5 m distance in certain areas within the storage farm. Therefore, the possible lack of visibility represents a more hazardous situation than the high temperatures reached if an accidental fire occurs under high wind speeds.

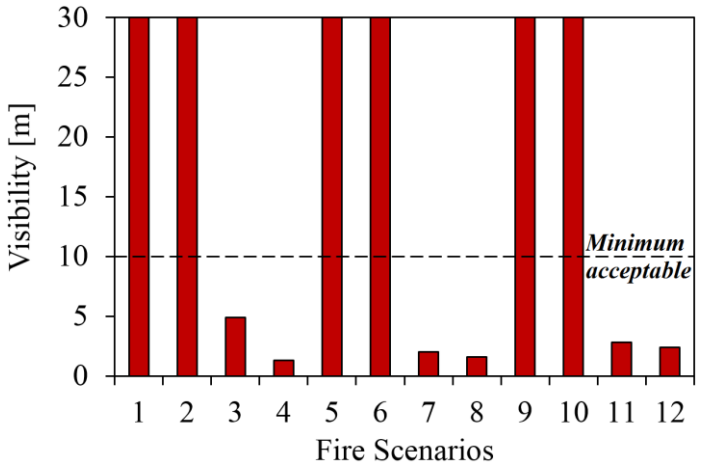

Figure 7.7. Mean minimum visibility levels predicted 1.8 m above the ground within the storage farm according to the different fire scenarios modelled in FDS. Long-dashed line represents the performance criteria below which unacceptable visibility conditions for people are reached.

The locations at which the highest temperatures can lead to uncomfortable situations and where the visibility levels are significantly reduced mainly depend on the burning tank location and the wind direction. Figure 7.8 and Figure 7.9 show the temperature and visibility values, respectively, of two fire scenarios having different fires location and wind direction. As it can be seen, the most hazardous areas are those located far away from the fire origin in the same direction of the wind.

Figure 7.10 shows the maximum radiative heat fluxes registered 1.8 m above the ground for the different fire scenarios modelled. As before, windy scenarios are more dangerous than windless ones, especially those with wind speeds equal or higher than 17.0 $m \cdot s^{-1}$. In these cases, the heat flux values calculated always pose a critical situation for un-protected people, while some of them also represent a risky scenario for protected personnel as the thermal fluxes may exceed the 5 $kW \cdot m^{-2}$ in certain areas of the storage farm.

Based on the results found, it is highly recommended that personnel positioned in the tank's dikes, which are continuously exposed to the potential fire hazards, should wear protective clothing and masks, especially in windy days. They should also be informed about the wind direction in advance. By this, the evacuees, which are supposed to be familiar with the facility, may avoid escape routes directly affected by the smoke and the other products of combustion in case of an accidental tank fire. In addition, when facility workers are performing maintenance or other tasks in the storage farm, firefighters should firstly intervene in areas far away from the burning tank. All these are suggestions aimed at preventing fatalities in oil storage farms.

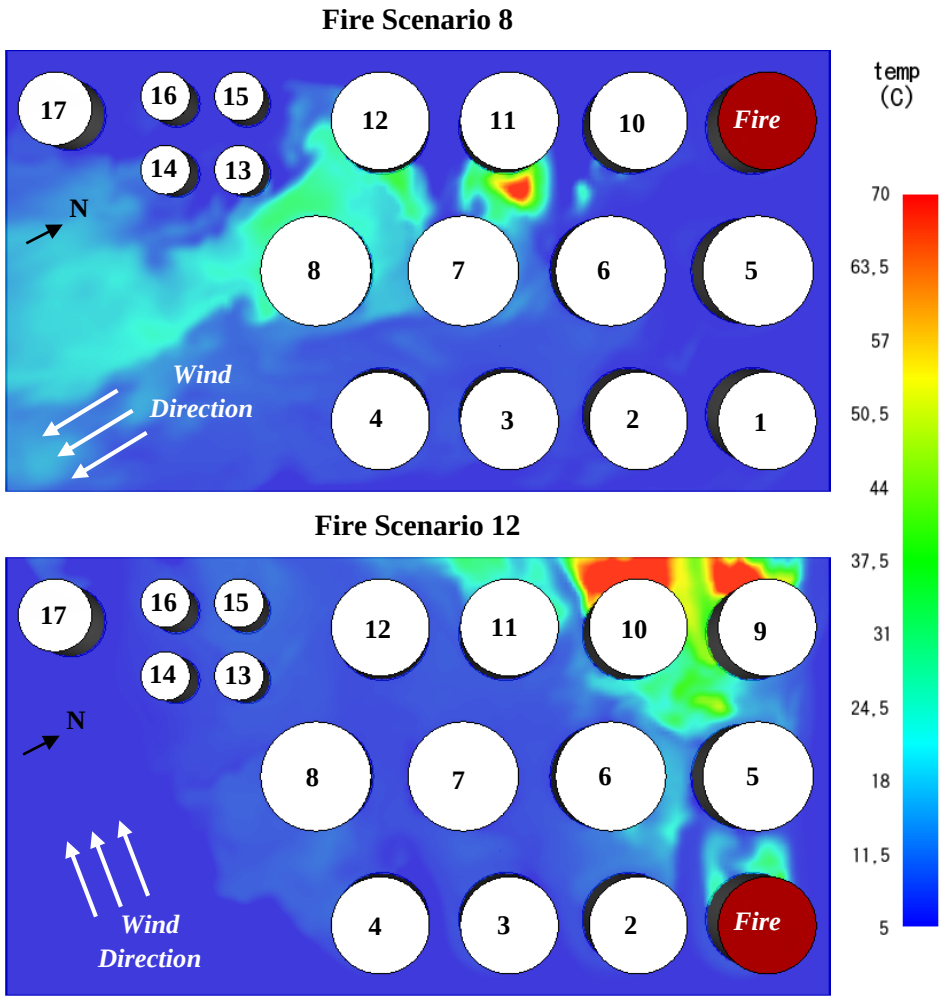

Figure 7.8. Instant capture of the temperature level at 1.8 m above the ground during the steady state of the fire scenario 8 (up) and the fire scenario 12 (down) that demonstrates temperature dependency on the fire location and the wind direction.

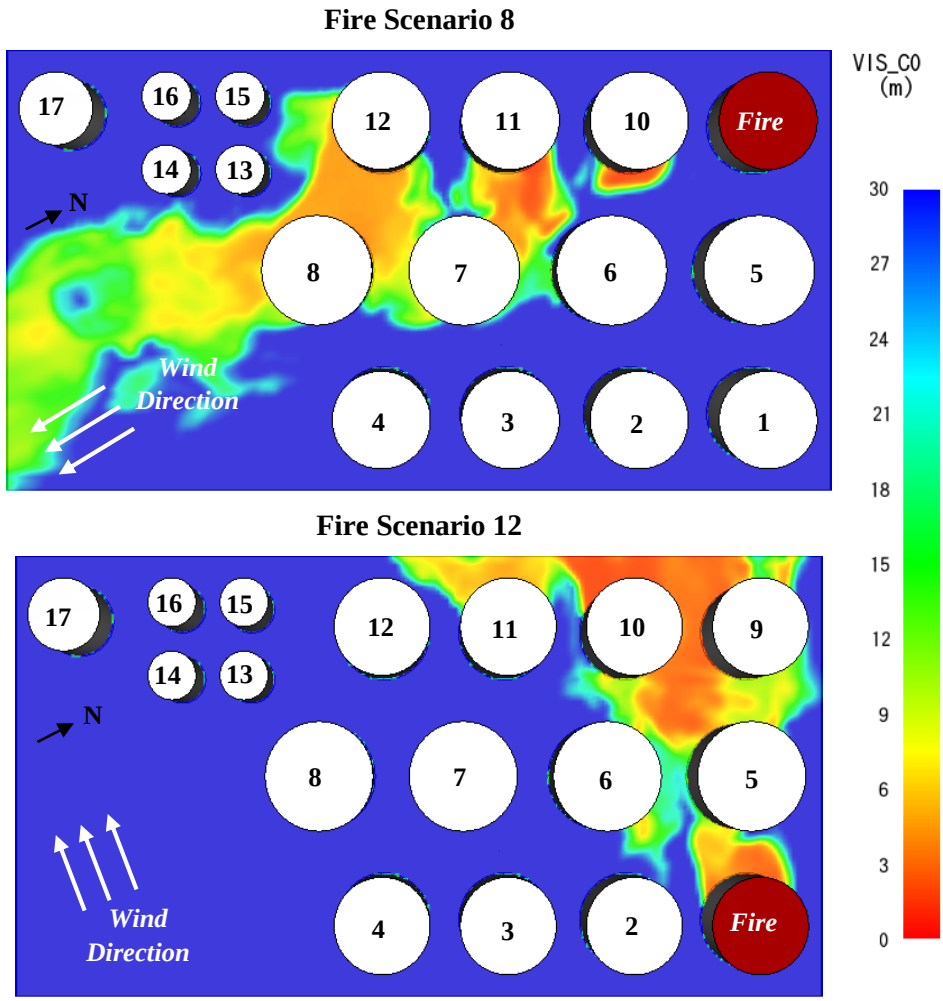

Figure 7.9. Instant capture of the visibility level at 1.8 m above the ground during the steady state of the fire scenario 8 (up) and the fire scenario 12 (down) that demonstrates visibility dependency on the fire location and the wind direction.

Apart from the harmful fire effects on people, the plant equipment could be also highly damaged by the fire. Figure 7.11 depicts the mean maximum heat flux received at the surfaces of the tanks for those scenarios where at least one tank received more than 5 $kW \cdot m^{-2}$ (i.e. threshold beyond which the structures start suffering the thermal effects). Thus, the scenarios where the whole tanks composing the storage farm received less than 5 $kW \cdot m^{-2}$ have been not included, which correspond to fire scenarios with mean wind speeds of ~3.5 $m \cdot s^{-1}$. Particularly, the most affected tanks are the ones closest to the burning tank in the wind direction. For example, the fire scenario 3, which is featured with a fire in the tank number 6 and a northerly wind of 17 $m \cdot s^{-1}$, will mostly affect the tank number 7 (121.3 $kW \cdot m^{-2}$), the tank number 3 (38.1 $kW \cdot m^{-2}$) and the tank number

2 (9.4 kW·m^{-2}). Therefore, the most affected structures are the closest ones to the fire origin in the same wind direction, while the most hazardous areas for people in windy scenarios are those remotely located from the burning tank.

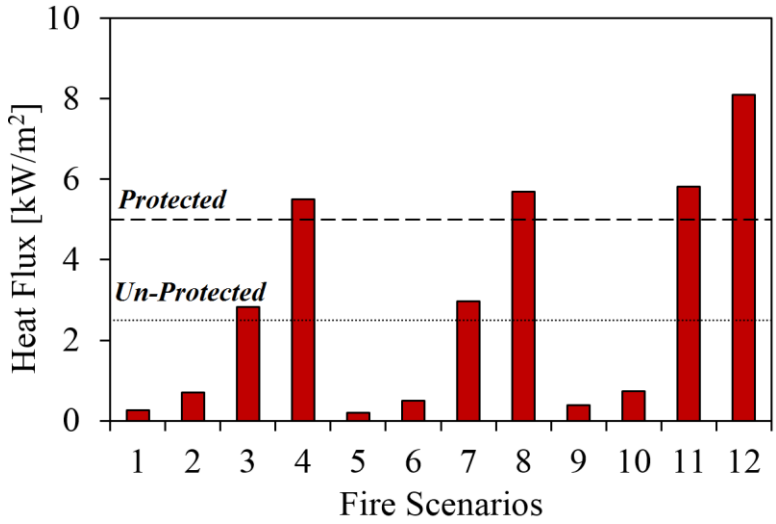

Figure 7.10. Mean maximum heat flux predicted 1.8 m above the ground within the storage farm according to the different fire scenarios modelled in FDS. Short and long-dashed lines represent the performance criteria above which unacceptable heat flux values are reached for unprotected and protected personnel, respectively.

In certain cases, the estimated mean heat flux have been more than 100 kW·m^{-2} and thus, the steel structure may collapse if the exposure time is of 30 minutes or longer. On the other hand, other tanks could receive lower heat fluxes than 100 kW·m^{-2}. Although simulated thermal values do not indicate structure failure, some equipment may stop working, and electric materials (i.e. cables, cabinets, etc.) and other hydrocarbon fuels may be ignited, hence leading to an escalation of the initial fire event. This fact highlights the importance of fireproofing the tanks and pipelines surfaces, and to properly isolate the possible combustible leaks that may form fuel pools on the ground. In short, it is observed that the consequences of a full surface fire occurring in an oil storage tank mainly depend on the geometry of the site, the wind speed and its direction, as well as the tank location.

Figure 7.11. Mean maximum heat flux received at the tanks surfaces for those fire scenarios simulated in FDS where at least one of the tanks received more than 5 kW·m^{-2}. Heat flux are expressed in kW·m^{-2}.

7.4.2. Heat flux predictions with semi-empirical correlations

The fire scenarios 3, 4, 7 and 12 are considered in this section given the significant heat flux received in adjacent tanks as previously observed through FDS simulations. Table 7.9 presents the flame lengths (ranged between 25 and 30 m) and tilted angles (around 50º) calculated by means of the semi-empirical correlations for these fire scenarios.

According to the geometrical features of the flames calculated, Figure 7.12 shows the heat flux received at the tanks surfaces determined by means of the point source model. As it can be seen, the radiative heat fluxes are considerably higher than those predicted in CFD simulations. This may be partly due to the noticeable inclination of the flames, which shorten the separation distances between the fire

and the tank's surfaces, hence leading to higher heat flux values. In this analysis, at least two adjacent tanks can collapse as these receive more than 100 kW·m^{-2}, while the rest can suffer steel deformation as the heat flux often exceed the threshold of 25 kW· m^{-2}.

Table 7.9. Flame shapes of the burning tank's flames determined by means of the semi-empirical correlations for the fire scenarios considered.

Fire Scenario	Burning Tank	u_w (m·s^{-1})	Wind Direction	$\dot{Q}$ (MW)	L_F (m)	θ (º)
3	6	17.0	North	4,179.4	30.3	52.4
4	6	22.1	East	4,179.4	28.8	55.5
7	9	17.0	North	2,963.8	26.2	53.1
12	1	22.1	East	2,963.8	24.9	56.1

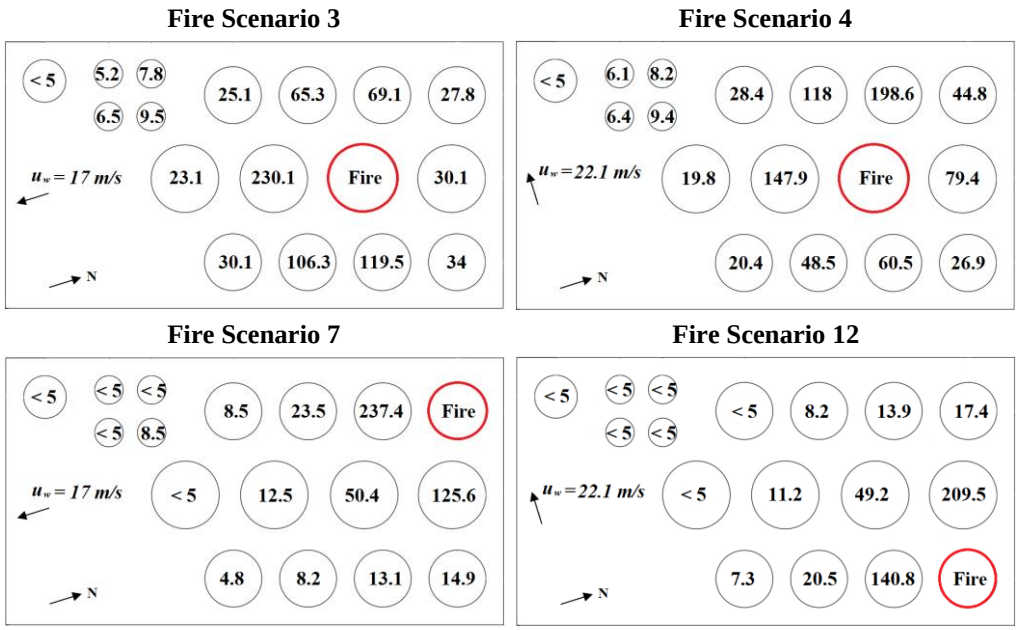

Figure 7.12. Heat flux received at the tanks surfaces determined through semi-empirical correlations for those fire scenarios simulated considered. Heat flux are expressed in kW·m^{-2}.

The heat flux calculated with semi-empirical correlations are more conservative than with computational simulations as the values are considerably greater. Thus, the safety measures proposed based on correlation's results would be more restrictive and costly. These methods, which are daily used to assess the fire risk in chemical and process industries, cannot examine the temperatures nor the visibility affecting people.

Semi-empirical methods can provide estimations of the heat flux received at the tank's surfaces facing the flames; however, these cannot determine the heat flux values at the tank's shadows. For example, in the Figure 7.8 (down), we observe that the highest temperatures of the fire scenario 12 are found in the tank number 10 (~70 ºC), which is located far away from the fire origin. These high temperatures, which cannot be determined with semi-empirical correlations, can lead to considerable high heat fluxes affecting the tank structure.

On the other hand, computational simulations can provide estimations of the fire effects that can threat personnel and the tank's surfaces. In addition, CFD modelling provides more realistic predictions of the related-fire effects in industrial facilities than semi-empirical correlations. Nevertheless, the appropriate numerical settings should be set-up to obtain reasonable results and the computational times required to complete simulations must be taken into account. In the current case study, the average computational time to run each fire scenario was of 228 hours (9.5 days) approximately, which was obtained by dividing the mesh volume into 4 CPU cores. A greater number of CPU cores would significantly reduce the mean simulation time. Although the noticeable times required to complete simulations may difficult its use in real applications, it is demonstrated that CFD modelling is a more appropriate calculation method than semi-empirical correlations when performing detailed FHA. The precise estimations and the considerable amount of data obtained can contribute to implement safety measures in chemical and process industries.

CHAPTER 8

CONCLUSIONS

The aim of this thesis was to assess the predictive capabilities of different CFD when determining the related-fire effects of accidental hydrocarbon fires that can occur in processing environments.

The flame shape and thermal flux hazards of large-scale pool fires of 1.5, 3, 4, 5 and 6 m-diameter were estimated with FDS and FLACS-Fire. A preliminary sensitivity analysis revealed that the maximum cell size and the minimum domain height in both codes should be of 0.2 m and 8D m, respectively. Accurate predictions of the flame shape and the surface emissive power were obtained in *a priori* simulations in both CFD codes. *A posteriori* sensitivity analysis outlined that better estimations of the flame temperature and heat flux are found in FDS and FLACS-Fire when the mass loss rates are prescribed instead of predicted. The MO wind sub-model defined in FDS also contributed to improve the agreement between simulation results and experimental measurements. The minimum number of rays recommended was of 300 for FLACS-Fire and of 400 for FDS to reasonably solve the RTE equation.

The flame temperature, heat flux and the flame-geometry descriptors of vertical sonic jet fires of propane were predicted in FDS, FireFOAM and FLACS-Fire. The expansion conditions of the jet fire were simulated in the CFD codes due to the low Mach number formulation. Accurate estimations of the flame shape and heat flux were found in FDS, while noticeable disagreements were reached in FireFOAM. On the other hand, the flame temperature and the heat flux were well predicted in FLACS-Fire. The dimensionless fire characteristic diameter, D^*/δ_x, should be of 16 for FDS and FLACS-Fire to determine the most suitable cell size.

The flame-geometry descriptors of vertical subsonic jet fires of methane in normal- and sub- atmospheric pressures were predicted in FDS, FireFOAM and FLACS-Fire. The lift-off distance could not be estimated in any of the CFD codes used by means of the EDC combustion approach. The other geometrical parameters were well predicted in FDS and FireFOAM; however, a considerable lack of agreement was obtained in FLACS-Fire. The soot yield fraction had a negligible influence on the flame shape. The dimensionless fire characteristic

diameter, D^*/δ_x, should be of 12 for FDS and of 8 for FireFOAM to determine the most suitable cell size

Furthermore, the flame shape and surface emissive power of vertical and horizontal subsonic jet fires of propane were estimated in FDS. An assessment of different cell sizes revealed that the most suitable D^*/δ_x values should be of 12 for both type of jet releases. Particularly, more precise estimations were achieved in horizontal jet fires than in vertical ones.

The results presented in this thesis show the great potential of CFD codes to estimate the hazardous effects of large-scale pool fires and jet fires under different release and ambient conditions. Specifically, FDS is noted as the most suitable code to perform risk analysis in chemical and process industries when applying the appropriate numerical settings. Thus, computational fire simulations may contribute to prevent major fire accidents in facilities, hence providing safer plants. It would be of great interest to expand the current study to different fuels, ambient conditions (i.e. wind and temperature), and additional measurements.

Best Practice Guidelines (BPG) in CFD modelling of accidental hydrocarbon fires were developed based on the numerous computational simulations of different fire scenarios performed. These indicate the main steps required to determine a code as 'valid' or not, and provide guidance on the most suitable modelling settings able to accurately predict the hazards derived from accidental hydrocarbon fires. The BPG developed were used in a case study involving CFD simulations intended to assess the fire hazards derived from large pool fires in an oil storage farm located in the Port of Barcelona. Too conservative and unrealistic predictions were obtained with semi-empirical correlations. Therefore, CFD modelling is the most appropriate calculation method to perform detailed FHA in chemical and process industries only if the appropriate numerical parameters are defined within the computational simulations.

APPENDIX A

SEMI-EMPIRICAL CORRELATIONS FOR THE FLAME SHAPE ESTIMATION OF JET FIRES AND POOL FIRES

Table A.1 gathers the semi-empirical correlations developed to determine flame length, L_F, lift-off distance, S_F, and equivalent diameter, D_{eq}, of hydrocarbon jet fires developed from real fire experiments. These variables can be obtained as a function of the gas velocity leaving through the exit orifice, u_{or}, or by means of dimensionless numbers such as Froude number, Fr, the Reynolds number, Re, or the non-dimensional heat release rate, $\dot{Q}^*$, which is expressed as (Zukoski et al., 1980):

$$\dot{Q}^* = \frac{\dot{Q}}{\rho_\infty c_p T_\infty {D_{or}}^2 \sqrt{g D_{or}}} \tag{A.1}$$

where $\dot{Q}$ is the heat release rate of the fire, c_p is the specific heat, D_{or} is the exit orifice diameter and T_∞ is the ambient temperature.

Table A.1. Experimental studies involving vertical hydrocarbon jet fires under different conditions and the correlations developed to predict some geometrical parameters.

Ref.	D_{or} (mm)	P_∞ (atm)	Flow Regime	Fuel	Correlation
(Peter and Williams, 1983)	4.0 - 12.0	1.0	Subsonic	CH_4	$\frac{S_F}{D_{or}} = 3.6 \cdot 10^{-3} \frac{u_{or}}{D_{or}}$
(Sonju and Hustad, 1984)	10 - 80	1.0	Subsonic	CH_4	$\frac{L_F}{D_{or}} = 21 Fr^{0.2}$
				C_3H_8	$\frac{L_F}{D_{or}} = 28 Fr^{0.2}$
(McCaffrey, 1989)	38 - 102	1.0	Subsonic Sonic	CH_4	$\frac{L_F}{D_{or}} = 28 Fr^{0.2}$
(Rokke et al., 1994)	0.84 - 2.58	1.0	Subsonic	C_3H_8	$\frac{L_F}{D_{or}} = 33 Fr^{0.2}$ $\frac{S_F}{D_{or}} = 2.1 \cdot 10^{-3} \frac{u_{or}}{D_{or}}$

Table A.1. Cont.

Ref.	D_{or} (mm)	P_∞ (atm)	Flow Regime	Fuel	Correlation
(Sugawa and Sakai, 1995)	6.5 - 27.6	1.0	Subsonic	C_3H_8	$\frac{L_F}{D_{or}} = 8.14Q^{*1/3}$ $\frac{S_F}{D_{or}} = 1.39 \cdot 10^{-2}Q^{*3/5}$ $\frac{D_{eq}}{D_{or}} = 1.92Q^{*1/3}$
(Costa et al., 2004; Santos and Costa, 2005)	5 - 8	1.0	Subsonic	CH_4	$\frac{L_F}{D_{or}} = 23Fr^{0.2}$ $\frac{S_F}{D_{or}} = 3.1 \cdot 10^{-3}\frac{u_{or}}{D_{or}}$
				C_3H_8	$\frac{L_F}{D_{or}} = 36Fr^{0.2}$ $\frac{S_F}{D_{or}} = 2.6 \cdot 10^{-3}\frac{u_{or}}{D_{or}}$
				C_2H_4	$\frac{L_F}{D_{or}} = 24Fr^{0.2}$ $\frac{S_F}{D_{or}} = 8.0 \cdot 10^{-4}\frac{u_{or}}{D_{or}}$
(Kiran and Mishra, 2007)	2.2	1.0	Subsonic	C_4H_{10}	$\frac{L_F}{D_{or}} = 30Fr^{0.2}$ $\frac{S_F}{D_{or}} = 1.8 \cdot 10^{-3}\frac{u_{or}}{D_{or}}$
(Gómez-Mares et al., 2009; Palacios et al., 2012; Palacios and Casal, 2011)	10 - 43.1	1.0	Subsonic Sonic	C_3H_8	$\frac{L_F}{D_{or}} = Re^{0.4}$ $S_F = 6 \cdot 10^{-4}Re^{0.5}$ $\frac{D_{eq}}{D_{or}} = 0.14Re^{0.4}$
(Hu et al., 2015, 2014; L. Hu et al., 2013; L. H. Hu et al., 2013)	4 - 10	0.64	Subsonic	C_3H_8	$\frac{S_F}{D_{or}} = 1.36u_{or} - 5.88$
		1.0	Subsonic	C_3H_8	$\frac{S_F}{D_{or}} = 0.6u_{or} - 5.33$

Then, the total flame height of the jet flames, H_F, can be calculated as:

$$H_F = L_F \cos \Omega_F + S_F \tag{A.2}$$

where Ω_F represents the flame tilt angle formed in the presence of wind:

$$cos(\Omega_F) = \begin{cases} a(u^*)^b & if\ u^* \geq 1 \\ 1 & if\ u^* < 1 \end{cases} \tag{A.3}$$

where a and b are experimental coefficients, and u^* is the dimensionless wind velocity determined as:

$$u^* = \begin{cases} {u_w}/{u_c} & if\ u_w \geq u_c \\ 1 & if\ u_w < u_c \end{cases} \tag{A.4}$$

where u_w is the wind velocity, and u_c is the characteristic wind speed:

$$u_c = \left({g\dot{m}'' D_{or}}/{\rho_\infty}\right)^{1/3} \tag{A.5}$$

where $\dot{m}''$ is the mass flow rate per unit area, ρ_∞ is the ambient air density and g is the gravitational acceleration.

On the other hand, Table A.2 summarizes the most widely known equations for determining the dimensionless flame lengths of hydrocarbon pool fires. These are often obtained from the following correlation:

$$\frac{L_F}{D} = a(m^*)^b (u^*)^c \tag{A.6}$$

where m^* is the dimensionless mass flow rate of the pool fire:

$$m^* = \frac{\dot{m}''}{\rho_\infty \sqrt{gD}} \tag{A.7}$$

Alternatively, the flame length of pool fires may be also calculated as a function of the dimensionless heat release rate.

Table A.2. Experimental studies involving hydrocarbon pool fires under different conditions and the correlations developed to predict the dimensionless flame length.

Ref.	D (m)	Fuel	Correlation
(Moorhouse, 1982)	~ 15	CH_4	$\frac{L_F}{D} = 6.2(m^*)^{0.254}(u^*)^{-0.044}$
(Pritchard and Binding, 1992)	6.0 - 22.0	CH_4	$\frac{L_F}{D} = 10.615(m^*)^{0.305}(u^*)^{-0.03}$
(Mangialavori and Rubino, 1992)	1.0 - 6.0	C_xH_y (2)	$\frac{L_F}{D} = 31.6(m^*)^{0.58}$
(Heskestad, 1999)	(1)	C_xH_y (2)	$\frac{L_F}{D} = -1.02 + 3.7\dot{Q}^{*\,2/5}$
(Muñoz et al., 2004)	1.5 - 6.0	$C_{12}H_{26}$ C_6H_{14}	$\frac{L_F}{D} = 7.74(m^*)^{0.375}(u^*)^{-0.096}$

(1) Laboratory scale experiments

(2) Wide range of hydrocarbon fuels

APPENDIX B
LITERATURE REVIEW

Table B.1. Summary of the main features regarding CFD simulation studies of hydrocarbon fires published in literature.

Year	Ref.	Fire Type	Fuel	Fire Size (1)	CFD Code (2)	Measurements (3)				Validation Simulation	Comparison Method
						G_F	T_F	$\dot{q}_r''$	Others		
1995	(Barker et al., 1995)	Jet	Methane	L	CFX	×	✓	✓	✓	✓	Qualitative
	(Sinai and Owens, 1995)	Pool	Kerosene	L	CFX	✓	✓	×	×	✓	Qualitative
1996	(Tieszen et al., 1996)	Pool	Jet Fuel	L	VULCAN	✓	✓	×	×	✓	Qualitative
		Pool	Methane	L	VULCAN	✓	✓	×	×	✓	Qualitative
1997	(Cook et al., 1997)	Jet	Methane	L	In-house	✓	✓	✓	✓	✓	Qualitative
		Jet	Methane	MF	In-house	✓	✓	✓	✓	✓	Qualitative
		Jet	Methane	L	In-house	✓	✓	✓	✓	✓	Qualitative
	(Johnson et al., 1997)	Jet	Propane	M	CFX	✓	✓	✓	×	✓	Qualitative
		Jet	Methane	M	CFX	✓	✓	✓	×	✓	Qualitative

Table B.2. Cont.

Year	Ref.	Fire Type	Fuel	Fire Size (1)	CFD Code (2)	Measurements (3)				Validation Simulation	Comparison Method
						G_F	T_F	$\dot{q}_r''$	Others		
1999	(Johnson et al., 1999)	Jet	Propane	M	CFX	✓	✓	×	✓	✓	Qualitative
		Jet	Methane	L	CFX	✓	✓	×	✓	✓	Qualitative
2000	(Baum and McGrattan, 2000)	Pool	Diesel	L	In-house	✓	×	✓	×	×	-
	(Sinai, 2000)	Pool	Kerosene	L	CFX	✓	×	×	✓	×	-
2002	(Rawat et al., 2002)	Pool	Methane	L	In-house	×	×	×	✓	✓	Qualitative
2003	(Cleaver et al., 2003)	Jet	Methane	M	In-house	✓	✓	✓	✓	✓	Qualitative
		Jet	Methane	L	In-house	✓	✓	✓	✓	✓	Qualitative
		Jet	Methane	L	In-house	✓	✓	✓	✓	✓	Qualitative
		Jet	Methane	MF	In-house	✓	✓	✓	✓	✓	Qualitative
		Jet	Methane	MF	In-house	✓	✓	✓	✓	✓	Qualitative
2004	(Greiner and Suo-Anttila, 2004)	Pool	Jet Fuel	L	Isis-3D	×	✓	×	×	✓	Qualitative
		Pool	Jet Fuel	L	Isis-3D	×	✓	×	×	✓	Qualitative
	(Are et al., 2004)	Pool	Jet Fuel	L	CAFE-3D	×	✓	×	✓	✓	Qualitative
2005	(Krishnamoorthy et al., 2005)	Pool	Methane	M	In-house	×	✓	✓	×	✓	Qualitative

Table B.3. Cont.

Year	Ref.	Fire Type	Fuel	Fire Size (1)	CFD Code (2)	Measurements (3)				Validation Simulation	Comparison Method
						G_F	T_F	$\dot{q}_r''$	Others		
2006	(Cumber and Spearpoint, 2006)	Jet	Propane	M	GENMIX	✓	✓	×	✓	✓	Qualitative
		Jet	Propane	L	GENMIX	✓	✓	×	✓	✓	Qualitative
		Jet	Propane	L	GENMIX	✓	✓	×	✓	✓	Qualitative
	(Osenbroch, 2006)	Jet	Methane	L	FLEXSIM	✓	✓	✓	✓	✓	Qualitative
		Jet	Methane	L	FLEXSIM	✓	✓	✓	✓	✓	Qualitative
		Jet	Methane	L	FLEXSIM	✓	✓	✓	✓	✓	Qualitative
	(Rigas and Sklavounos, 2006)	Flash	Methane	-	CFX	×	✓	✓	×	✓	Quantitative
		Flash	Methane	-	CFX	×	✓	✓	×	✓	Quantitative
		Flash	Methane	-	CFX	×	✓	✓	×	✓	Quantitative
		Flash	Methane	-	CFX	×	✓	✓	×	✓	Quantitative
2007	(Pierce and Moss, 2007)	Pool	Heptane	M	SOFIE	×	✓	✓	✓	✓	Qualitative
	(del Valle et al., 2007)	Pool	Jet Fuel	L	CAFE-3D	×	✓	×	×	✓	Qualitative
2008	(Trouvé, 2008)	Pool	Propylene	L	FDS	×	×	×	✓	×	-
2009	(Chen et al., 2009)	Pool	Methane	L	FDS	×	✓	✓	✓	✓	Qualitative

Table B.4. Cont.

Year	Ref.	Fire Type	Fuel	Fire Size (1)	CFD Code (2)	Measurements (3)				Validation Simulation	Comparison Method
						G_F	T_F	$\dot{q}_r''$	Others		
2009	(Vela, 2009)	Pool	Jet Fuel	L	Fluent	✓	✓	✓	×	✓	Quantitative
		Pool	Jet Fuel	L	Fluent	✓	✓	✓	×	✓	Quantitative
		Pool	Jet Fuel	L	Fluent	✓	✓	✓	×	✓	Quantitative
		Pool	Jet Fuel	L	Fluent	✓	✓	✓	×	✓	Quantitative
2010	(Aloqaily, 2010)	Jet	Methane	M	PHOENICS	✓	✓	✓	×	✓	Quantitative
		Jet	Methane	M	PHOENICS	✓	✓	✓	×	✓	Quantitative
		Jet	Methane	L	PHOENICS	✓	✓	✓	×	✓	Quantitative
		Jet	Methane	L	PHOENICS	✓	✓	✓	×	✓	Quantitative
		Jet	Methane	L	PHOENICS	✓	✓	✓	×	✓	Quantitative
		Jet	Methane	L	PHOENICS	✓	✓	✓	×	✓	Quantitative
		Jet	Methane	L	PHOENICS	✓	✓	✓	×	✓	Quantitative
	(Ferng and Lin, 2010)	Pool	Heptane	M	FDS	✓	×	✓	×	✓	Qualitative
		Pool	Heptane	M	FDS	✓	×	✓	×	✓	Qualitative
	(Lopez and Figueroa, 2010)	Pool	Jet Fuel	L	CAFE-3D	×	✓	×	×	✓	Qualitative

Table B.5. Cont.

Year	Ref.	Fire Type	Fuel	Fire Size (1)	CFD Code (2)	Measurements (3)				Validation Simulation	Comparison Method
						G_F	T_F	$\dot{q}_r''$	Others		
2010	(Benucci and Uguccioni, 2010)	Pool	Kerosene	L	FDS	×	×	✓	×	×	-
		Pool	Kerosene	L	FDS	×	×	✓	×	×	-
2011	(Gavelli et al., 2011)	Flash	Methane	-	FLACS	×	×	×	✓	×	-
	(Chakrabarty and Aloqaily, 2011)	Jet	Methane	L	PHOENICS	×	✓	✓	✓	×	-
	(Satoh et al., 2011)	Pool	Diesel	L	FDS	✓	×	✓	×	×	-
	(Eldredge et al., 2011)	Pool	Heptane	M	ARCHES	✓	✓	✓	×	✓	Qualitative
2012	(Ilic et al., 2012)	Jet	Methane	M	Fluent	×	✓	✓	✓	×	-
	(Chen et al., 2012)	Pool	Crude Oil	L	FDS	✓	×	✓	×	×	-
	(Mansour, 2012)	Pool	Gasoline	L	FDS	×	×	✓	×	✓	Quantitative
		Pool	Gasoline	L	FDS	×	×	✓	×	✓	Quantitative
2013	(Li et al., 2013)	Pool	Propane	L	FDS	✓	×	✓	×	×	-
	(Vasanth et al., 2013)	Pool	Diesel	L	Fluent	×	✓	✓	✓	✓	Qualitative
	(Sudheer et al., 2013)	Pool	Gasoline	M	FDS	×	✓	✓	×	✓	Qualitative
		Pool	Gasoline	M	FDS	×	✓	✓	×	✓	Qualitative
		Pool	Gasoline	M	FDS	×	✓	✓	×	✓	Qualitative

Table B.6. Cont.

Year	Ref.	Fire Type	Fuel	Fire Size (1)	CFD Code (2)	Measurements (3)				Validation Simulation	Comparison Method
						G_F	T_F	$\dot{q}_r''$	Others		
2014	(Sun et al., 2014)	Pool	Methane	L	Fluent	✓	✓	✓	×	✓	Quantitative
		Pool	Methane	L	Fluent	✓	✓	✓	×	✓	Quantitative
		Pool	Methane	L	Fluent	✓	✓	✓	×	✓	Quantitative
		Pool	Methane	L	Fluent	×	×	✓	×	×	-
	(Kelsey et al., 2014)	Pool	Methane	L	FDS	✓	×	×	✓	✓	Quantitative
	(Vasanth et al., 2014)	Pool	Gasoline	S	Fluent	×	✓	✓	✓	✓	Qualitative
		Pool	Gasoline	S	Fluent	×	✓	✓	✓	✓	Qualitative
		Pool	Gasoline	S	Fluent	×	✓	✓	✓	✓	Qualitative
2015	(Muthusamy and Wingerden, 2015)	Flash	Propane	-	FLACS	×	✓	✓	×	✓	Qualitative
		Flash	Propane	-	FLACS	×	✓	✓	×	✓	Qualitative
	(Malkeson et al., 2015)	Jet	Propane	M	KFK	✓	✓	×	×	✓	Qualitative
		Jet	Propane	M	FLACS	✓	✓	×	×	✓	Qualitative
		Jet	Propane	M	CFX	✓	✓	×	×	✓	Qualitative
	(Rajendram et al., 2015)	Jet	Methane	MF	FDS	×	×	✓	×	×	-
	(Masum et al., 2015)	Pool	Methane	L	CFX	✓	✓	×	×	✓	Qualitative

Table B.7. Cont.

Year	Ref.	Fire Type	Fuel	Fire Size (1)	CFD Code (2)	Measurements (3)				Validation Simulation	Comparison Method
						G_F	T_F	$\dot{q}_r''$	Others		
2015	(Peris-Sayol et al., 2015)	Pool	Gasoline	L	FDS	×	✓	×	×	×	-
		Pool	Gasoline	L	FDS	×	✓	×	×	×	-
	(Chatterjee et al., 2015)	Pool	Heptane	M	FireFOAM	×	✓	✓	✓	✓	Qualitative
2016	(Sakamoto et al., 2016)	Pool	Gasoline	L	Fluent	✓	×	×	×	×	-
	(Sikanen and Hostikka, 2016)	Pool	Acetone	L	FDS	✓	×	×	✓	✓	Qualitative
		Pool	Benzene	L	FDS	✓	×	×	✓	✓	Qualitative
		Pool	Butane	L	FDS	✓	×	×	✓	✓	Qualitative
		Pool	Heptane	L	FDS	✓	×	×	✓	✓	Qualitative
2017	(Jang and Choi, 2017)	Jet	Methane	M	KFK	✓	✓	✓	×	×	-
	(Huang et al., 2017)	Jet	Methane	S	FDS	✓	×	×	×	✓	Qualitative
		Jet	Methane	S	FDS	✓	×	×	×	✓	Qualitative
		Jet	Methane	S	FDS	✓	×	×	×	✓	Qualitative
		Jet	Methane	S	FDS	✓	×	×	×	✓	Qualitative
		Jet	Methane	S	FDS	✓	×	×	×	✓	Qualitative
		Jet	Methane	S	FDS	✓	×	×	×	✓	Qualitative

Table B.8. Cont.

Year	Ref.	Fire Type	Fuel	Fire Size (1)	CFD Code (2)	Measurements (3)				Validation Simulation	Comparison Method
						G_F	T_F	$\dot{q}_r''$	Others		
2017	(Huang et al., 2017)	Jet	Methane	S	FDS	✓	×	×	×	✓	Qualitative
		Jet	Methane	S	FDS	✓	×	×	×	✓	Qualitative
		Jet	Methane	S	FDS	✓	×	×	×	✓	Qualitative
		Jet	Methane	S	FDS	✓	×	×	×	✓	Qualitative
		Jet	Methane	S	FDS	✓	×	×	×	✓	Qualitative
		Jet	Methane	S	FDS	✓	×	×	×	✓	Qualitative
		Jet	Methane	S	FDS	✓	×	×	×	✓	Qualitative
	(Sun et al., 2017)	Jet	Methane	M	FDS	✓	✓	×	×	×	-
		Jet	Methane	M	FDS	✓	✓	×	×	×	-
		Jet	Methane	M	FDS	✓	✓	×	×	×	-
		Jet	Methane	M	FDS	✓	✓	×	×	×	-
		Jet	Methane	M	FDS	✓	✓	×	×	×	-
		Jet	Methane	M	FDS	✓	✓	×	×	×	-
		Jet	Methane	M	FDS	✓	✓	×	×	×	-
		Jet	Methane	M	FDS	✓	✓	×	×	×	-

Table B.9. Cont.

Year	Ref.	Fire Type	Fuel	Fire Size (1)	CFD Code (2)	Measurements (3)				Validation Simulation	Comparison Method
						G_F	T_F	$\dot{q}_r''$	Others		
2017	(Baalisampang et al., 2017)	Jet	Methane	M	FDS	✓	×	✓	×	×	-
2018	(Rengel et al., 2018)	Pool	Diesel	L	FDS	✓	✓	✓	✓	✓	Quantitative
		Pool	Gasoline	L	FDS	✓	✓	✓	✓	✓	Quantitative
		Pool	Diesel	L	FDS	✓	✓	✓	✓	✓	Quantitative
		Pool	Gasoline	L	FDS	✓	✓	✓	✓	✓	Quantitative
		Pool	Diesel	L	FDS	✓	✓	✓	✓	✓	Quantitative
		Pool	Gasoline	L	FDS	✓	✓	✓	✓	✓	Quantitative
		Pool	Diesel	L	FDS	✓	✓	✓	✓	✓	Quantitative
		Pool	Gasoline	L	FDS	✓	✓	✓	✓	✓	Quantitative
		Pool	Diesel	L	FDS	✓	✓	✓	✓	✓	Quantitative
		Pool	Gasoline	L	FDS	✓	✓	✓	✓	✓	Quantitative
		Pool	Diesel	L	FLACS	✓	✓	✓	✓	✓	Quantitative
		Pool	Gasoline	L	FLACS	✓	✓	✓	✓	✓	Quantitative
		Pool	Diesel	L	FLACS	✓	✓	✓	✓	✓	Quantitative
		Pool	Gasoline	L	FLACS	✓	✓	✓	✓	✓	Quantitative

Table B.10. Cont.

Year	Ref.	Fire Type	Fuel	Fire Size (1)	CFD Code (2)	Measurements (3)				Validation Simulation	Comparison Method
						G_F	T_F	$\dot{q}_r''$	Others		
2018	(Rengel et al., 2018)	Pool	Diesel	L	FLACS	✓	✓	✓	✓	✓	Quantitative
		Pool	Gasoline	L	FLACS	✓	✓	✓	✓	✓	Quantitative
		Pool	Diesel	L	FLACS	✓	✓	✓	✓	✓	Quantitative
		Pool	Gasoline	L	FLACS	✓	✓	✓	✓	✓	Quantitative
		Pool	Diesel	L	FLACS	✓	✓	✓	✓	✓	Quantitative
		Pool	Gasoline	L	FLACS	✓	✓	✓	✓	✓	Quantitative
	(Davidy, 2018)	Jet	Heptane	M	FDS	×	×	✓	×	×	-
	(Shen et al., 2018)	Pool	Propane	S	FDS	×	✓	✓	×	✓	Qualitative
		Pool	Propane	S	FDS	×	✓	✓	×	✓	Qualitative
		Pool	Propane	S	FDS	×	✓	✓	×	✓	Qualitative
		Pool	Propane	S	FDS	×	✓	✓	×	✓	Qualitative
		Pool	Propane	S	FDS	×	✓	✓	×	✓	Qualitative
		Pool	Propane	S	FDS	×	✓	✓	×	✓	Qualitative
		Pool	Propane	S	FDS	×	✓	✓	×	✓	Qualitative

Table B.11. Cont.

Year	Ref.	Fire Type	Fuel	Fire Size [1]	CFD Code [2]	Measurements [3]				Validation Simulation	Comparison Method
						G_F	T_F	$\dot{q}_r''$	Others		
2018	(Bolek and Ergin, 2018)	Pool	Methane	L	FDS	✓	✓	✓	✓	×	-
		Pool	Methane	L	FDS	✓	✓	✓	✓	×	-
		Pool	Methane	L	FDS	✓	✓	✓	✓	×	-
		Pool	Methane	L	FDS	✓	✓	✓	✓	×	-
		Pool	Methane	L	FDS	✓	✓	✓	✓	×	-
	(Wang and Wen, 2018)	Pool	Heptane	S	FireFOAM	✓	✓	✓	✓	✓	Qualitative
		Pool	Heptane	S	FireFOAM	✓	✓	✓	✓	✓	Qualitative
		Pool	Heptane	S	FireFOAM	✓	✓	✓	✓	✓	Qualitative
		Pool	Heptane	S	FireFOAM	✓	✓	✓	✓	✓	Qualitative
		Pool	Heptane	S	FireFOAM	✓	✓	✓	✓	✓	Qualitative
	(Y. B. Huang et al., 2018)(Y. Huang et al., 2018)	Jet	Methane	S	FDS	×	✓	✓	×	×	-
		Jet	Methane	S	FDS	×	✓	✓	×	×	-
		Jet	Methane	S	FDS	×	✓	✓	×	×	-
		Jet	Methane	S	FDS	×	✓	✓	×	×	-

Table B.12. Cont.

Year	Ref.	Fire Type	Fuel	Fire Size (1)	CFD Code (2)	Measurements (3)				Validation Simulation	Comparison Method
						G_F	T_F	$\dot{q}_r''$	Others		
2018	(Y. B. Huang et al., 2018)(Y. Huang et al., 2018)	Jet	Methane	S	FDS	×	✓	✓	×	×	-
		Jet	Methane	S	FDS	×	✓	✓	×	×	-
		Jet	Methane	S	FDS	×	✓	✓	×	×	-
		Jet	Methane	S	FDS	×	✓	✓	×	×	-
		Jet	Methane	S	FDS	×	✓	✓	×	×	-
		Jet	Methane	S	FDS	×	✓	✓	×	×	-
		Jet	Methane	S	FDS	×	✓	✓	×	×	-
		Jet	Methane	S	FDS	×	✓	✓	×	×	-
		Jet	Methane	S	FDS	×	✓	✓	×	×	-
2019	(Pio et al., 2019)	Pool	Methane	L	FDS	✓	✓	✓	×	✓	Qualitative
		Pool	Methane	L	FDS	✓	✓	✓	×	✓	Qualitative
		Pool	Methane	L	FDS	✓	✓	✓	×	✓	Qualitative
		Pool	Methane	L	FDS	✓	✓	✓	×	✓	Qualitative
	(Lyu et al., 2019)	Jet	Methane	M	FDS	×	✓	✓	✓	×	-
		Jet	Methane	M	FDS	×	✓	✓	✓	×	-

Table B.13. Cont.

Year	Ref.	Fire Type	Fuel	Fire Size (1)	CFD Code (2)	Measurements (3)				Validation Simulation	Comparison Method
						G_F	T_F	$\dot{q}_r''$	Others		
2019	(Ahmadi et al., 2019)	Pool	Kerosene	M	FDS	×	×	✓	×	×	-
		Pool	Kerosene	L	FDS	×	×	✓	×	×	-
		Pool	Kerosene	L	FDS	×	×	✓	×	×	-

(1) S: Small; M: Medium; L: Large; and MF: Major Failure

(2) Codes versions are not included

(3) G_F: Flame-geometry descriptors; T_F: Flame Temperature; $\dot{q}_r''$: radiative heat flux

APPENDIX C
EXPERIMENTAL DATA

Large-scale pool fires

Table C.1. Mean measurements registered with the experimental devices and determined through the IR image analysis performed in the large-scale pool fire tests. Data sources come from (Ferrero et al., 2007, 2006; Muñoz et al., 2007, 2004).

Experiment	$\dot{m}''$ (kg·s^{-1}·m^{-2})	$\dot{q}_r{}''$ (kW·m^{-2})	$\overline{A}_F$ (m^{-2})	$\overline{H}_F$ (m)	$\overline{E}$ (kW·m^{-2})
D1.5_1.33	0.08 ± 0.00	1.83 ± 0.3	4.97 ± 1.3	2.96 ± 0.7	42.90 ± 8.5
G1.5_0.44	0.10 ± 0.00	3.02 ± 0.5	6.53 ± 1.6	3.26 ± 0.7	42.33 ± 8.5
D3_0.00	0.30 ± 0.01	0.98 ± 0.08	n.a	n.a	n.a
G3_0.00	0.49 ± 0.01	1.71 ± 0.1	n.a	n.a	n.a
D3_2.39	0.38 ± 0.00	6.12 ± 1.9	12.22 ± 1.9	5.40 ± 1.3	50.66 ± 7.8
G3_1.14	0.60 ± 0.00	5.47 ± 1.0	25.06 ± 3.9	7.07 ± 1.5	51.32 ± 9.9
D4_0.43	0.62 ±0.00	3.22 ± 0.4	34.60 ± 5.3	8.28 ± 1.7	47.79 ± 7.6
G4_0.52	1.03 ± 0.00	4.89 ± 0.8	41.85 ± 4.8	11.60 ± 1.7	61.07 ± 8.7
D5_1.02	1.40 ± 0.00	3.30 ± 0.8	37.67 ± 9.5	8.09 ± 2.3	37.51 ± 7.9
G5_0.00	1.82 ± 0.06	4.87 ± 0.4	47.37 ± 4.2	12.08 ± 1.5	66.56 ± 9.4
D6_1.10	1.14 ± 0.00	2.06 ± 0.4	59.57 ± 7.4	12.76 ± 2.7	61.21 ± 7.9
G6_0.00	1.93 ± 0.09	2.80 ± 0.5	58.32 ± 7.2	14.76 ± 1.6	61.95 ± 8.9
D1.5_1.33	0.08 ± 0.00	1.83 ± 0.3	4.97 ± 1.3	2.96 ± 0.7	42.90 ± 8.5
G1.5_0.44	0.10 ± 0.00	3.02 ± 0.5	6.53 ± 1.6	3.26 ± 0.7	42.33 ± 8.5

Table C.2. Mean temperatures registered with the thermocouples set-up in the large-scale pool fire tests. Data sources come from (Ferrero et al., 2007, 2006; Muñoz et al., 2007, 2004).

Experiment	$\overline{T}_{B1}$ (ºC)	$\overline{T}_{B2}$ (ºC)	$\overline{T}_{B3}$ (ºC)	$\overline{T}_{B4}$ (ºC)	$\overline{T}_{B5}$ (ºC)
22_D15	55.7 ± 1.0	35.5 ± 0.4	32.2 ± 0.1	32.9 ± 0.2	24.5 ± 0.1
21_G15	194.5 ± 40.2	91.1 ± 16.5	70.6 ± 10.5	70.3 ± 9.4	39.4 ± 5.4
01_D3	727.4 ± 117.4	423.9 ± 110.7	297.2 ± 81.8	174.3 ± 34.7	115.5 ± 18.5
17_G3	889.6 ± 36.5	752.3 ± 28.9	576.8 ± 39.0	369.0 ± 25.2	233.3 ± 12.7
04_D3	31.3 ± 1.3	28.9 ± 1.2	26.5 ± 1.6	16.1 ± 0.4	14.4 ± 0.2
03_G3	196.2 ± 25.7	111.0 ± 10.9	87.9 ± 8.5	39.1 ± 2.6	29.8 ± 2.3
14_D4	241.4 ± 29.9	164.6 ± 17.5	136.1 ± 14.3	77.7 ± 9.3	57.6 ± 4.8
13_G4	545.6 ± 137.9	408.8 ± 82.2	351.3 ± 49.4	224.3 ± 29.8	139.7 ± 18.0
10_D5	82.2 ± 5.5	74.5 ± 3.0	63.2 ± 1.6	41.1 ± 0.6	34.4 ± 0.3
08_G5	532.2 ± 44.9	370.3 ± 43.9	345.5 ± 40.8	253.8 ± 39.9	151.8 ± 23.5
07_D6	275.2 ± 67.5	189.2 ± 56.3	143.5 ± 59.1	101.3 ± 46.1	70.0 ± 30.3
06_G6	1144.7 ± 51.6	1108.7 ± 82.2	1036.5 ± 104.9	909.0 ± 144.5	782.3 ± 155.7

Vertical sonic jet fires of propane

Table C.3 Mean measurements registered with the experimental devices and determined through the IR image analysis performed in the vertical sonic jet fire tests of propane. Data sources come from (Gómez-Mares et al., 2010, 2009; Palacios et al., 2012, 2008; Palacios and Casal, 2011).

Experiment	$\overline{T}_T$ (ºC)	$\dot{q}_r''$ (kW·m^{-2})	$\overline{H}_F$ (m)	$\overline{A}_F$ (m^2)
D10_0.09	1324.2 ± 119.3	1.04 ± 0.21	4.85 ± 0.60	4.42 ± 1.14
D12.75_0.13	1600 ± 15.8	1.20 ± 0.08	4.93 ± 0.62	4.18 ± 0.47
D15_0.18	1058.12 ± 145.7	2.35 ± 1.03	5.96 ± 1.55	6.60 ± 2.94
D20_0.27	1126.9 ± 72.64	2.20 ± 0.13	5.63 ± 0.59	5.66 ± 0.78
D25.5_0.34	1193.9 ± 66.5	2.05 ± 0.05	4.93 ± 0.42	5.07 ± 0.85

Vertical subsonic jet fires of methane at normal- and sub-atmospheric pressures

Table C.4. Mean measurements determined through the VHS image analysis performed in the vertical subsonic jet fire tests of methane at normal- and sub- atmospheric pressures.

Exp.	P_{atm} (atm)	$\overline{S}_F$ (m)	$\overline{L}_F$ (m)	$\overline{H}_F$ (m)	$\overline{A}_F$ (m^2)	$\overline{D}_{eq}$ (m)
D3_0.6	0.6	0.11 ± 0.009	0.50 ± 0.03	0.60 ± 0.04	0.02 ± 0.0	0.04 ± 0.0
D3_0.7	0.7	0.09 ± 0.005	0.52 ± 0.04	0.60 ± 0.04	0.02 ± 0.0	0.04 ± 0.0
D3_0.8	0.8	0.07 ± 0.004	0.54 ± 0.04	0.60 ± 0.05	0.02 ± 0.0	0.04 ± 0.0
D3_0.9	0.9	0.04 ± 0.003	0.57 ± 0.03	0.60 ± 0.03	0.02 ± 0.0	0.04 ± 0.0
D3_1.0	1.0	0.00 ± 0.00	0.60 ± 0.04	0.60 ± 0.04	0.02 ± 0.0	0.04 ± 0.0

Vertical and horizontal jet fires of propane

Table C.5. Mean measurements determined through the VHS image analysis performed in the vertical (Palacios et al., 2012, 2008) and horizontal (Gopalaswami et al., 2016; Laboureur et al., 2016; Zhang et al., 2015) subsonic jet fire tests of propane.

Orientation	Experiment	$\overline{S}_F$ (m)	$\overline{L}_F$ (m)	$\overline{D}_{eq}$ (m)	$\overline{A}_F$ (m^2)	$\overline{E}$ (kW·m^{-2})
Vertical	V12.75_0.007	0.13	0.80	0.24	0.19	55.00
	V12.75_0.016	0.19	1.51	0.26	0.39	38.03
	V20_0.020	0.12	2.18	0.35	0.76	33.63
	V43.1_0.066	0.29	7.60	1.18	8.97	45.30
	V43.1_0.142	0.46	9.27	1.34	12.42	80.00
Horizontal	H19.05_0.015	0.37	2.08	0.58	1.21	19.20
	H19.05_0.016	0.51	2.76	0.65	1.79	46.00
	H19.05_0.025	0.77	3.46	0.66	2.28	61.00
	H19.05_0.040	0.98	3.67	0.69	2.53	69.00
	H19.05_0.042	0.76	3.19	0.73	2.33	53.00
	H19.05_0.110	1.81	4.41	0.76	3.35	77.0
	H19.05_0.109	2.11	4.27	0.68	2.90	58.0

Articles published in journals and proceedings

- Rengel B, Mata C, Palacios A, Pastor E, Casal J, Planas E (2019) CFD modelling of vertical sònic jet fires, 9th International Seminar on Fire and Explosions Hazards, Saint Petersburg.
- Rengel B, Mata C, Pastor E, Casal J, Planas E (2018) A priori validation of CFD modelling of hydrocarbon pool fires, Journal of Loss Prevention in the Process Industries, doi: 10.1016/j.jlp.2018.08.002.
- Mata C, Pastor E, Rengel B, Valero M, Planas E, Palacios A, Casal J (2018) Infrared Imaging Software for Jet Fire Analysis, Chemical Engineering Transactions, doi:10.3303/CET1867147.
- Rengel B, Pastor E, Rios O., Mata C, Bartolomé A, Planas E (2017) Assessment of the predictive capabilities of diferent modelling tools to forecast fire effects in residential compartments. Conference Proceedings of Research and Advanced Technology in Fire Safety.
- Rengel B, Pastor E, Hermida D, Gómez E, Molinelli L, Planas E (2017) Computational Analysis of Fire Dynamics Inside a Wind Turbine, Fire Technology, doi: 10.1007/s10694-017-0664-0.

Publications in preparation

- Rengel B, Palacios A, Hu L, Wang Q, Agueda A, Pastor E, Casal J, Planas E. Experimental and computational analysis of vertical jet fires in normal- and sub- atmospheric pressures, Fuel, already submitted.

Oral presentations

- Rengel B, Mata C, Palacios A, Pastor E, Casal J, Planas E (April 2019) CFD Modelling of Vertical Sonic Jet Fires, 9th International Seminar on Fire and Explosion Hazards (Saint Petersburg, Russia).
- Rengel B, Mata C, Pastor E, Casal J, Planas E (2018) Assessment of the predictive capabilities of computational modelling tools to forecast hydrocarbon pool fire effects, 2nd SFPE Europe Fire Safety Engineering Conference & Expo (Rotterdam, Netherlands).
- Rengel B, Mata C, Pastor E, Casal J, Planas E. (2017) Validation of CFD Modelling of Hydrocarbon Pool Fires, 10th World Congress of Chemical Engineering (Barcelona, Spain).

- Rengel B, Pastor E, Rios O, Mata C, Bartolomé A, Planas E (2017) Assessment of the predictive capabilities of diferent modelling tools to forecast fire effects in residential compartments, Research and Advanced Technology in Fire Safety (Santander, Spain).

REFERENCES

Adamek, T., 2006. Using contour information and segmentation for object registration modeling and retrieval. Dubin City University.

Ahmadi, O., Mortazavi, S.B., Pasdarshahri, H., Mohabadi, H.A., 2019. Consequence analysis of large-scale pool fire in oil storage terminal based on computational fluid dynamic (CFD). Process Saf. Environ. Prot. 123, 379–389. https://doi.org/10.1016/j.psep.2019.01.006

Aloqaily, A., 2010. Jet Flame Length and Thermal Radiation: Evaluation with CFD Simulations, in: GCPS.

American Petroleum Institution, 2018. API Standard 650 - Welded Tanks for Oil Storage.

ANSYS CFX-Pre User's Guide, 2017.

ANSYS FLUENT User's Guide, 2017.

Are, N., Greiner, M., Suo-Anttila, A., 2004. CAFE-3D: A fast running computational tool for analysis of radioactive material packages in fire environments. Am. Soc. Mech. Eng. Press. Vessel. Pip. Div. PVP 483, 165–173. https://doi.org/10.1115/PVP2004-2797

Argyropoulos, C.D., Christolis, M.N., Nivolianitou, Z., Markatos, N.C., 2012. A hazards assessment methodology for large liquid hydrocarbon fuel tanks. J. Loss Prev. Process Ind. 329–335. https://doi.org/10.1016/j.jlp.2011.12.003

Audouin, L., Chandra, L., Consalvi, J.L., Gay, L., Gorza, E., Hohm, V., Hostikka, S., Ito, T., Klein-Hessling, W., Lallemand, C., Magnusson, T., Noterman, N., Park, J.S., Peco, J., Rigollet, L., Suard, S., Van-Hees, P., 2011. Quantifying differences between computational results and measurements in the case of a large-scale well-confined fire scenario. Nucl. Eng. Des. 241, 18–31. https://doi.org/10.1016/j.nucengdes.2010.10.027

Audouin, L., Kolb, G., Torero, J.L., Most, J.M., 1995. Average Centreline Temperatures of a Buoyant Pool Fire Obtained by Image Processing of Video Recordings. Fire Saf. J. 24, 167–187.

Azzi, C., Rogstadkjenet, L., 2016. Use of CFD in the performance-based design for fire safety in the oil and gas sector, in: 11th Conference on Performance-Based Codes and Fire Safety Design Methods.

Baalisampang, T., Abbassi, R., Garaniya, V., Khan, F., Dadashzadeh, M., 2017. Modelling the Impacts of Fire in a Typical FLNG Processing Facility, in: International Conference on Safety and Fire Engineering.

Babrauskas, V., 1983. Estimating large pool fire burning rates. Fire Technol. 19, 251–261. https://doi.org/10.1007/BF02380810

Barker, P.W., Johnson, A.D., Goto, N., 1995. CFD calculation of the combustion and radiation properties of large-scale natural gas jet flames, in: Proceedings of the 2nd

1995 Symposium on Major Hazards Onshore and Offshore. pp. 195–211.

Baum, H.R., McGrattan, K.B., 2000. Simulation of large industrial outdoor fires. Fire Saf. Sci. 611–622.

Bennett, J., Cowley, L., Davenport, J., Dowson, J., 1991. Large-scale natural gas and LPG jet fires final report to the cec. Technical report, CEC research program: Majo Technological Hazards.

Benucci, S., Uguccioni, G., 2010. Fire hazard calculations for hydrocarbon pool fires - application of "Fire Dynamics Simulator - FDS" to the risk assessment of an Oil Extraction Platform, in: 4th International Conference on Safety and Environment in Process Industry. pp. 291–296. https://doi.org/10.3303/CET1019048

Beyler, C.L., 2016. Fire hazard calculations for large, Open hydrocarbon fires, in: SFPE Handbook of Fire Protection Engineering. pp. 2591–2663. https://doi.org/10.1007/978-1-4939-2565-0

Birch, A.D., Brown, D.R., Dodson, M.G., 1984. The Structure and Concentration Decay of High Pressure Jets of Natural Gas. Combust. Sci. Technol. 5, 249–261.

Bolek, A., Ergin, S., 2018. A Large Eddy Simulation of LNG Pool Fire on Board a Chemical/Oil Tanker. J. Phys. Conf. Ser. 1107. https://doi.org/10.1088/1742-6596/1107/4/042006

Bolonkin, A.A., 2010. Aerial high altitude gas pipeline. J. Nat. Gas Sci. Eng. 2, 114–121. https://doi.org/10.1016/j.jngse.2010.04.003

Bradley, D., Gaskell, P.H., Gu, X., Palacios, A., 2016. Jet flame heights, lift-off distances, and mean flame surface density for extensive ranges of fuels and flow rates. Combust. Flame 164, 400–409. https://doi.org/10.1016/j.combustflame.2015.09.009

British Standards Institution, 2019. BS 7974:2019 - Application of fire safety engineering principles of the design of buildings. Code of practice.

British Standards Institution, 2004. Published Document PD 7974-6:2004. The application of fire safety engineering principles to fire safety design of buildings - Part 6: Human factors: Life safety strategies - Occupants evacuation, behaviour and condition.

Brzustowski, T.A., Sommer, E.C., 1973. Predicting radiant heating from flares, in: Proceedings-Division of Refining. pp. 865–893.

Casal, J., 2017. Evaluation of the effects and consequences of major accidents in industrial plants. 2nd ed. Elsevier, Amsterdam.

Casal, J., Gómez-Mares, M., Muñoz, M., Palacios, A., 2012. Jet fires: a "minor" fire hazard? Chem. Eng. Trans. 26, 13–20. https://doi.org/10.3303/CET1226003

Chai, T., Draxler, R.R., Prediction, C., 2014. Root mean square error (RMSE) or mean absolute error (MAE)? – Arguments against avoiding RMSE in the literature 1247–1250. https://doi.org/10.5194/gmd-7-1247-2014

Chakrabarty, A., Aloqaily, A., 2011. Using CFD to assist facilities comply with thermal hazard regulations such as new API RP-752 recommendations. pp. 205–212.

Chang, J.I., Lin, C., 2006. A study of storage tank accidents. J. Loss Prev. Process Ind.

19, 51–59. https://doi.org/10.1016/j.jlp.2005.05.015

Chatris, J.M., Quintela, J., Folch, J., Planas, E., Arnaldos, J., Casal, J., 2001. Experimental study of burning rate in hydrocarbon pool fires. Combust. Flame 126, 1373–1383. https://doi.org/10.1016/S0010-2180(01)00262-0

Chatterjee, P., Wang, Y., Meredith, K. V., Dorofeev, S.B., 2015. Application of a subgrid soot-radiation model in the numerical simulation of a heptane pool fire. Proc. Combust. Inst. 35, 2573–2580. https://doi.org/10.1016/j.proci.2014.05.045

Chen, Z., Song, W.H., Lv, L.Y., 2012. Analysis for combustion characteristics of large-scale pool fire with wind, in: 4th International Conference on Multimedia and Security, MINES 2012. pp. 505–508. https://doi.org/10.1109/MINES.2012.73

Chen, Z.B., Dembele, S., Wen, J.X., Tam, V., 2009. Towards Large Eddy Simulation of LNG Pool Fires 326–335.

Chiguma, J., Johnson, E., Shah, P., Gornopolskaya, N., Jr, W.E.J., 2013. Thermal Diffusivity and Thermal Conductivity of Epoxy-Based Nanocomposites by the Laser Flash and Differential Scanning Calorimetry Techniques. Open J. Compos. Mater. 3, 51–62.

Chow, W.K., 2015. Performance-based approach to determining fi re safety provisions for buildings in the Asia-Oceania regions. Build. Environ. 91, 127–137. https://doi.org/10.1016/j.buildenv.2015.04.007

Ciambelli, P., Meo, M.G., Russo, P., Vaccaro, S., 2006. CFD Simulations of Road Tunnel Fires to Estimate the Influence of Ventilation Systems on Safety, in: 3rd International Conference "Tunnel Safety and Ventilation." pp. 324–333.

Cleaver, R.P., Cumber, P.S., Fairweather, M., 2003. Predictions of free jet fires from high pressure, sonic releases. Combust. Flame 132, 463–474. https://doi.org/10.1016/S0010-2180(02)00491-1

Cook, D.K., Cumber, P.S., Fairweather, M., Shemirani, F., 1997. Modelling free and impacting underexpanded jet fires, in: Icheme Symposium Series.

Costa, M., Parente, C., Santos, A., 2004. Nitrogen oxides emissions from buoyancy and momentum controlled turbulent methane jet diffusion flames. Exp. Therm. Fluid Sci. 28, 729–734. https://doi.org/10.1016/j.expthermflusci.2003.12.010

Cowley, L.T., Johnson, A.D., 1992. Oil and gas fires: characteristics and Impact, OTI 92 596.

Cox, G., Chitty, R., 1980. A Study of the Deterministic Properties of Unbounded Fire Plumes. Combust. Flame 39, 191–209.

Cozzani, V., Zanelli, S., 2001. An Approach to the Assessment of Domino Accidents Hazard in Quantitative Area Risk Analysis, in: Loss Prevention and Safety Promotion in the Process Industries. pp. 1263–1274. https://doi.org/10.1016/b978-044450699-3/50040-9

Crippa, C., Fiorentini, L., Rossini, V., Stefanelli, R., Tafaro, S., Marchi, M., 2009. Fire risk management system for safe operation of large atmospheric storage tanks. J. Loss Prev. Process Ind. 22, 574–581. https://doi.org/10.1016/j.jlp.2009.05.003

Cumber, P.S., Spearpoint, M., 2006. A computational flame length methodology for

propane jet fires. Fire Saf. J. 41, 215–228. https://doi.org/10.1016/j.firesaf.2006.01.003

Davidy, A., 2018. CFD Simulation and Mitigation with Boiling Liquid Expanding Vapor Explosion (BLEVE) Caused by Jet Fire. ChemEngineering 3, 1. https://doi.org/10.3390/chemengineering3010001

Dayanandan, S., Chin, B., Liew, Z., Hoe, L.K., Ho, H., Wong, R., Ho, V., Khiank, Y.W., Yuan, C.K., Ng, J., Magrabi, A., 2015. Singapore Fire Safety Engineering Guidelines 2015.

Deardorff, J.W., 1980. Stratocumulus-capped mixed layers derived from a three-dimensional model. Boundary-Layer Meteorol. 18, 495–527.

Decal España SA, 2019. Storage and handling services for LPG in Spain [WWW Document]. URL https://www.decalstorage.com/terminals/spain/koalagas.html (accessed 6.28.19).

del Valle, M., Kramer, M.A., Greiner, M., Lopez, C., Suo-anttila, A., 2007. Temperature Response of a Rail-Cask-Size Pipe Calorimeter in Large-Scale Pool Fires 1–10.

DesJardin, P.E., Gritzo, L.A., Tieszen, S.R., 2000. Modeling the Effect of Water Spray Suppression of Large Scale Pool Fires, in: Halon Options Technical Working Conference. pp. 262–273.

DNV Technica, 2001. Human resistance against thermal effects, explosion effects, toxic effects and obscuration of vision.

Drysdale, D., 2011. An Introduction to Fire Dynamics. John Wiley & Sons.

Drysdale, D., 1999. An introduction to fire dynamics. Chichester, UK.

Dulov, V.G., Lukyanov, G.A., 1984. Gas Dynamics of the Outflow Processes. Novosibirsk (Russia).

EDF R&D, 2018. Code_Saturne 5.2.0 Practical User's Guide.

Eldredge, W.M., Thornock, J.N., Smith, P.J., 2011. Development , Verification , and Validation of the Responsive Boundary Model for Pool Fire Simulations. Am. Inst. Aeronaut. Astronaut. 1–29.

Enagas SA, 2015. Transmission, storage and regasification services and infrastructure. Madrid.

Favrin, S., Busini, V., Rota, R., Derudi, M., 2018. Practical LES modelling of jet fires: Issues and challenges. Chem. Eng. Trans. 67, 259–264. https://doi.org/10.3303/CET1867044

Ferng, Y.M., Lin, C.H., 2010a. Investigation of appropriate mesh size and solid angle number for CFD simulating the characteristics of pool fires with experiments assessment. Nucl. Eng. Des. 240, 816–822. https://doi.org/10.1016/j.nucengdes.2009.12.001

Ferng, Y.M., Lin, C.H., 2010b. Investigation of appropriate mesh size and solid angle number for CFD simulating the characteristics of pool fires with experiments assessment. Nucl. Eng. Des. 240, 816–822. https://doi.org/10.1016/j.nucengdes.2009.12.001

Ferreira, T., Rasband, W., 2012. ImageJ user guide, IJ 1.46r. https://doi.org/10.1038/nmeth.2019

Ferrero, F., Muñoz, M., Arnaldos, J., 2007. Effects of thin-layer boilover on flame geometry and dynamics in large hydrocarbon pool fires. Fuel Process. Technol. 88, 227–235. https://doi.org/10.1016/j.fuproc.2006.09.005

Ferrero, F., Muñoz, M., Kozanoglu, B., Casal, J., Arnaldos, J., 2006. Experimental study of thin-layer boilover in large-scale pool fires. J. Hazard. Mater. 137, 1293–1302. https://doi.org/10.1016/j.jhazmat.2006.04.050

Fiveland, W.A., 1984. Discrete-Ordinates Solutions of Radiative Transport Equation for Rectangular Enclosures. J. Heat Transfer 106, 699–706.

Flower, W.L., Bowman, C.T., 1988. Soot production in axisymmetric laminar diffusion flames at pressures from one to ten atmospheres. Symp. Combust. 21, 1115–1124. https://doi.org/10.1016/S0082-0784(88)80342-4

Franke, B., Hellsten, J., Schlünzen, A., Carissimo, H., 2007. Best practice guidelines for the CFD simulation of flows in the urban environment. COST Action 732 Quality Assurance and Improvement of Microscale Meteorological Models.

Franquet, E., Perrier, V., Gibout, S., Bruel, P., 2015. Free underexpanded jets in a quiescent medium: A review. Prog. Aerosp. Sci. 77, 25–53. https://doi.org/10.1016/j.paerosci.2015.06.006

Fu, D., Yu, Y., Niu, Q., 2014. Simulation of underexpanded supersonic jet flows with chemical reactions. Chinese J. Aeronaut. 27, 505–513. https://doi.org/10.1016/j.cja.2014.04.003

Fu, S., Yan, X., Zhang, D., Li, C., Zio, E., 2016. Framework for the quantitative assessment of the risk of leakage from LNG-fueled vessels by an event tree-CFD. J. Loss Prev. Process Ind. 43, 42–52. https://doi.org/10.1016/j.jlp.2016.04.008

Fureby, C., Tabor, G., Weller, H.G., Gosman, D., 1997. A comparative study of subgrid scale models in homoeneous isotropic turbulence. Phys. Fluids 9, 1416–1429.

Gavelli, F., Davis, S., Hansen, O.R., 2011. A Unified Model for LNG Pool Spread and Vapor Dispersion: Is Wind Scooping Really A Factor? 12.

Gexcon AS, 2017. FLACS v10.7 User's Manual.

Gobeau, N., Zhou, X.X., 2004. Evaluation of CFD to predict smoke movement in complex enclosed spaces. Application to three real scenarios: an underground station, an offshore accomodation module and a building under contruction.

Gómez-Mares, M., Muñoz, M., Casal, J., 2010. Radiant heat from propane jet fires. Exp. Therm. Fluid Sci. 34, 323–329. https://doi.org/10.1016/j.expthermflusci.2009.10.024

Gómez-Mares, M., Muñoz, M., Casal, J., 2009. Axial temperature distribution in vertical jet fires. J. Hazard. Mater. 172, 54–60. https://doi.org/10.1016/j.jhazmat.2009.06.136

Gómez-Mares, M., Zárate, L., Casal, J., 2008. Jet fires and the domino effect. Fire Saf. J. 43, 583–588. https://doi.org/10.1016/j.firesaf.2008.01.002

Gopalaswami, N., Liu, Y., Laboureur, D.M., Zhang, B., Mannan, M.S., 2016.

Experimental study on propane jet fire hazards: Comparison of main geometrical features with empirical models. J. Loss Prev. Process Ind. 41, 365–375. https://doi.org/10.1016/j.jlp.2016.02.003

Gore, J.P., 1986. A Theoretical and Experimental Study of Turbulent Jet Flame Radiation. The Pennsylvania State University, University Park.

Greenshields, C.J., 2017. OpenFOAM User Guide.

Greiner, M., Suo-Anttila, A., 2004. Validation of the Isis-3D computer code for simulating large pool fires under a variety of wind conditions. Am. Soc. Mech. Eng. Press. Vessel. Pip. Div. PVP 467, 101–112. https://doi.org/10.1115/1.1767173

Guilkey, J., Harman, T., Luitjens, J., Schmidt, J., Thornock, J., de St. Germain, J., Shankar, S., Peterson, J., Brownlee, C., 2009. Uintah User Guide Version 1.1, SCI Institute, University of Utah.

Hadjisophocleous, G., McCartney, C.J., 2005. Guidelines for the use of CFD simulations for fire and smoke modeling. NRCC-47740.

Hanna, S.R., Hansen, O.R., Dharmavaram, S., 2004. FLACS CFD air quality model performance evaluation with Kit Fox, MUST, Prairie Grass, and EMU observations. Atmos. Environ. 38, 4675–4687. https://doi.org/10.1016/j.atmosenv.2004.05.041

Hasofer, A.M., 2009. Modern sensitivity analysis of the CESARE-Risk computer fire model. Fire Saf. J. 44, 330–338. https://doi.org/10.1016/j.firesaf.2008.07.007

Health and Safety Executive, 2006. Guidance on risk assessment for offshore installations.

Hemmatian, B., Abdolhamidzadeh, B., Darbra, R.M., Casal, J., 2014. The significance of domino effect in chemical accidents. J. Loss Prev. Process Ind. 29, 30–38. https://doi.org/10.1016/j.jlp.2014.01.003

Heskestad, G., 1999. Turbulent Jet Diffusion Flames, Consolidation of Flame. Combust. Flame 118, 51–60.

Hu, L., Wang, Q., Delichatsios, M., Lu, S., Tang, F., 2014. Flame radiation fraction behaviors of sooty buoyant turbulent jet diffusion flames in reduced- and normal atmospheric pressures and a global correlation with Reynolds number. Fuel 116, 781–786. https://doi.org/10.1016/j.fuel.2013.08.059

Hu, L., Wang, Q., Delichatsios, M., Tang, F., Zhang, X., Lu, S., 2013. Flame height and lift-off of turbulent buoyant jet diffusion flames in a reduced pressure atmosphere. Fuel 109, 234–240. https://doi.org/10.1016/j.fuel.2012.12.050

Hu, L., Zhang, X., Wang, Q., Palacios, A., 2015. Flame size and volumetric heat release rate of turbulent buoyant jet diffusion flames in normal- and a sub-atmospheric pressure. Fuel 150, 278–287. https://doi.org/10.1016/j.fuel.2015.01.081

Hu, L.H., Wang, Q., Tang, F., Delichatsios, M., Zhang, X.C., 2013. Axial temperature profile in vertical buoyant turbulent jet fire in a reduced pressure atmosphere. Fuel 106, 779–786. https://doi.org/10.1016/j.fuel.2012.10.051

Huang, Y., Li, Y., Dong, B., 2018. Radiant Heat Flux Profile of Horizontally Oriented Rectangular Source Fuel Jet Fires. Ind. Eng. Chem. Res. 57, 1078–1088.

https://doi.org/10.1021/acs.iecr.7b03977

Huang, Y., Li, Y., Dong, B., Li, J., 2017. Predicting the main geometrical features of horizontal rectangular source fuel jet fires. J. Energy Inst. 91, 1153–1163. https://doi.org/10.1016/j.joei.2017.06.008

Huang, Y.B., Li, Y.F., Dong, B.Y., 2018. The Temperature Profile of Rectangular Fuel Source Jet Fire with Different Aspect Ratio. Procedia Eng. 211, 280–287. https://doi.org/10.1016/j.proeng.2017.12.014

Hydrocarbons Technology, n.d. Blake Oil Field Exploitation [WWW Document]. URL https://www.hydrocarbons-technology.com/projects/blake/ (accessed 5.23.19).

Ilic, M., Stefanovic, V., Ilic, G., Pavlovic, S., Kustrimovic, D., 2012. Numerical simulation of wall temperature on gas pipeline due to radiation of natural gas during combustion. Therm. Sci. 16, 567–576. https://doi.org/10.2298/TSCI120503192I

Industry About, 2017. Permian Basin Oil Field [WWW Document]. URL https://www.industryabout.com/country-territories-3/1057-usa/oil-and-gas/41280-permian-basin-oil-field (accessed 5.23.19).

Industry About, 2016. Gate - Maasvlakte LNG Plant [WWW Document]. URL https://www.industryabout.com/country-territories-3/1643-netherlands/oil-and-gas/24083-gate-maasvlakte-lng-plant (accessed 5.23.19).

Industry About, 2014. F'Kirina Gas Power Plant [WWW Document]. URL https://www.industryabout.com/country-territories-3/1181-algeria/fossil-fuels-energy/15909-f-kirina-gas-power-plant

INERIS, 2015. Guide de Bonnes Pratiques pour la réalisatio de modélisations 3D pour des scénarios de dispersion atmosphérique en situation accidentelle.

IRSN, 2018. ISIS 5.1.3 - Tutorial.

ISO 16730-1:2015(E) Fire safety engineering - Procedures and requirements for verification and validation of calculation methods - Part 1: General, 2015.

Ivings, M.J., Lea, C.J., Ledin, H.S., 2003. Outstanding safety questions concerning the analysis of ventilation and gas dispersion in gas turbine enclosures: Best Practice Guidelines for CFD.

Jahn, W., Rein, G., Torero, J., 2008. The Effect of Model Parameters on the Simulation of Fire Dynamics. Fire Saf. Sci. 9, 1341–1352. https://doi.org/10.3801/IAFSS.FSS.9-1341

Jahn, W., Rein, G., Torero, J.L., 2011. A posteriori modelling of the growth phase of Dalmarnock Fire Test One. Build. Environ. 46, 1065–1073. https://doi.org/10.1016/j.buildenv.2010.11.001

Jang, C.B., Choi, S.W., 2017. Simulation and Damage Analysis of an Accidental Jet Fire in a High-Pressure Compressed Pump Shelter. Saf. Health Work 8, 42–48. https://doi.org/10.1016/j.shaw.2016.06.005

John, R.H., 2016. Product Fire Risk Analysis, in: Hurley, M. (Ed.), SFPE Handbook of Fire Protection Engineering, Fifth Edition. pp. 3211–3225. https://doi.org/0.1007/978-1-4939-2565-0

Johnson, A., Shirvill, L., Ungut, A., 1999. CFD calculation of impinging gas jet flames, Health & Safety Executive.

Johnson, A.D., Ebbinghaus, A., Imanari, T., Lennon, S.P., Marie, N., 1997. Large-Scale Free and Impinging Turbulent Jet Flames: Numerical Modelling and Experiments. Process Saf. Environ. Prot. 75, 145–151. https://doi.org/10.1205/095758297528977

Jones, W.P., Launder, B.., 1972. The prediction of laminarization with a two-equation model of turbulence. Int. J. Heat Mass Transf. 15, 301–314. https://doi.org/10.1016/0017-9310(72)90076-2

Joo, P.H., Charest, M.R.J., Groth, C.P.T., Gülder, Ö.L., 2013. Comparison of structures of laminar methane-oxygen and methane-air diffusion flames from atmospheric to 60atm. Combust. Flame 160, 1990–1998. https://doi.org/10.1016/j.combustflame.2013.04.030

Kelsey, A., Gant, S., McNally, K., Hill, H., Betteridge, S., Technology, S., Thornton, C., Box, P.O., 2014. Application of global sensitivity analysis to FDS simulations of large LNG fire plumes, in: Symposium Series No 159. pp. 1–11.

Kent, J.H., 1986. A quantitative relationship between soot yield and smoke point measurements. Combust. Flame 63, 349–358.

Kent, J.H., Honnery, D., 1987. Soot and Mixture Fraction in Turbulent Diffusion Flames. Combust. Sci. Technol. 54. https://doi.org/10.1080/00102208708947062

Khan, F.I., Abbasi, S.A., 1999. Major accidents in process industries and an analysis of causes and consequences. J. Loss Prev. Process Ind. 12, 361–378. https://doi.org/10.1016/S0950-4230(98)00062-X

Kiran, D.Y., Mishra, D.P., 2007. Experimental studies of flame stability and emission characteristics of simple LPG jet diffusion flame. Fuel 86, 1545–1551. https://doi.org/10.1016/j.fuel.2006.10.027

Koseki, H., 1999. Large Scale Pool Fires: Results of Recent Experiments, in: Fire Safety Science - Proceedings of the Sixth International Symposium. pp. 115–132.

Koseki, H., 1989. Combustion Properties of Large Liquid Pool Fires. Fire Technol. 25, 241–255.

Koseki, H., Natsume, Y., Iwata, Y., Takahashi, T., Hirano, T., 2003. A study on large-scale boilover using crude oil containing emulsified water. Fire Saf. J. 38, 665–677. https://doi.org/10.1016/j.firesaf.2003.07.003

Koylu, U.O., Faeth, G.M., 1992. Structure of Overfire Soot in Buoyant Turbulent Diffusion Flames at Long Residence Times. Combust. Flame 89, 140–156. https://doi.org/10.1016/0010-2180(92)90024-J

Krishnamoorthy, G., Borodai, S., Rawat, R., Spinti, J., Smith, P.J., Asme, 2005. Numerical modeling of radiative heat transfer in pool fire simulations, in: Proceedings of the ASME Heat Transfer Division 2005, Vol 1. pp. 327–337. https://doi.org/10.1115/IMECE2005-81095

Laboureur, D.M., Gopalaswami, N., Zhang, B., Liu, Y., Mannan, M.S., 2016. Experimental study on propane jet fire hazards: Assessment of the main geometrical features of horizontal jet flames. J. Loss Prev. Process Ind. 41, 355–364. https://doi.org/10.1016/j.jlp.2016.02.003

LaChance, J., Tchouvelev, A., Engebo, A., 2010. Development of uniform harm criteria for use in quantitative risk analysis of the hydrogen infrastructure. Int. J. Hydrogen Energy 36, 2381–2388. https://doi.org/10.1016/j.ijhydene.2010.03.139

Lam, C.S., Weckman, E.J., 2015. Wind-blown pool fire, Part II: Comparison of measured flame geometry with semi-empirical correlations. Fire Saf. J. 78, 130–141. https://doi.org/10.1016/j.firesaf.2015.08.004

Launder, B.E., Spalding, D.P., 1974. The numerical computation of turbulent flows. Comput. Methods Appl. Mech. Eng. 3, 269–289.

Lazaro, M., Boehmer, H., Alvear, D., Capote, J.A., Trouve, A., 2008. Numerical simulation of fire growth, transition to flashover, and post-flashover dynamics in the dalmarnock fire test. Fire Saf. Sci. 1, 1377–1388. https://doi.org/10.3801/IAFSS.FSS.9-1377

Lee, K.O., Megaridis, C.M., Zelepouga, S., Saveliev, A. V, Kennedy, L.A., Charon, O., Ammouri, F., 2000. Soot formation effects of oxygen concentration in the oxidizer stream of laminar coannular nonpremixed methane air flames. Combust. Flame 121, 323–333.

Lees, F.P., 1996. Loss Prevention in the Process Industries - Hazard Identification, Assessment and Control.

Li, Q.G., Song, W.H., Zhang, M., Lei, Y., 2013. Numerical Simulation of Liquefied Propane Gas Storage Tanks Full-Size Pool Fire Based on FDS. Appl. Mech. Mater. 353–356, 2419–2423. https://doi.org/10.4028/www.scientific.net/AMM.353-356.2419

Lilly, D.K., 1967. The representation of small-scale turbulence in numerical simulation experiment, in: Proceedings of the IBM Scientific Computing Symposium on Environmental Science.

Lin, C., Ferng, Y., Hsu, W., Hua, N.T., 2010. Investigations on the Characteristics of Radiative Heat Transfer in Liquid Pool Fires. Fire Technol. 46, 321–345. https://doi.org/10.1007/s10694-008-0071-7

Lin, C.H., Ferng, Y.M., Hsu, W.S., 2009. Investigating the effect of computational grid sizes on the predicted characteristics of thermal radiation for a fire. Appl. Therm. Eng. 29, 2243–2250. https://doi.org/10.1016/j.applthermaleng.2008.11.010

Liu, Q., Chen, Z., Liu, H., Yin, W., Yang, Y., 2017. CFD simulation of fire dike overtopping from catastrophic ruptured tank at oil depot. J. Loss Prev. Process Ind. 49, 427–436. https://doi.org/10.1016/j.jlp.2017.06.005

Lopez, C., Figueroa, V., 2010. Fire Tests and Analyses of a Rail Cask-Sized Calorimeter, in: 16th International Symposium on the Packaging and Transportation of Radioactive Materials.

Lowesmith, B.J., Hankinson, G., Acton, M.R., Chamberlain, G., 2007. An Overview of the Nature of Hydrocarbon Jet Fire Hazards in the Oil and Gas Industry and a Simplified Approach to Assessing the Hazards. Process Saf. Environ. Prot. 85, 207–220. https://doi.org/10.1205/psep06038

Ludwing, J.C., Mortimore, S., 2013. PHOENICS-VR Reference Guide, TR 326.

Lyu, S., Zhang, Y., Wang, W., Ma, S., Huang, Y., 2019. Simulation Study on Influence

of Natural Gas Pipeline Pressure on Jet Fire. IOP Conf. Ser. Earth Environ. Sci. 242. https://doi.org/10.1088/1755-1315/242/2/022041

Magnussen, B., Hjertager, B., 1977. On mathematical modeling of turbulent combustion with special emphasis on soot formation and combustion. Symp. Combust. 16, 719–729. https://doi.org/10.1016/S0082-0784(77)80366-4

Magnussen, B.F., Sintef, N., Thermodynamics, A., Dynamics, F., Evanger, T., Vembe, B.E., Lilleheie, N.I., 2000. Kameleon FireEx in Safety Applications, in: SPE International Conference on Health, ,Safety, and the Environment in Oil and Gas Exploration and Production.

Malkeson, S.P., Jones, T., English, R., 2015. Jet Fire Computational Fluid Dynamics Simulations : Validation from an Industrial and Consultancy Perspective, in: 25th Symposium Colloquim on the Dynamics of Explosions and Reactive Systems.

Mangialavori, G., Rubino, F., 1992. Experimental tests on large hydrocarbon pool fires, in: 7th International Symposium on Loss Prevention and Safety Promotion in the Process Industry.

Mansour, K., 2012. Fires in large atmospheric storage tanks and their effect on adjacent tanks. Loughborough University.

Maragkos, B., Merci, B., 2017. Large Eddy Simulations of CH4 Fire Plumes. Flow Turbul. Combust. 239–278. https://doi.org/10.1007/s10494-017-9803-4

Maragkos, G., Beji, T., Merci, B., 2017. Advances in modelling in CFD simulations of turbulent gaseous pool fires. Combust. Flame 181, 22–38. https://doi.org/10.1016/j.combustflame.2017.03.012

Masum, M., Rahman, A., Ahmed, S., Khan, F., 2015. LNG pool fire simulation for domino effect analysis. Reliab. Eng. Syst. Saf. 143, 19–29. https://doi.org/10.1016/j.ress.2015.02.010

Mata, C., Pastor, E., Rengel, B., Valero, M., Planas, E., Palacios, A., Casal, J., 2018. Infrared Imaging Software for Jet Fire Analysis. Chem. Eng. Trans. 67, 877–882. https://doi.org/10.3303/CET1867147

McCaffrey, B.J., 1989. Momentum diffusion flame characteristics and the effects of water spray. Combust. Sci. Technol. 63, 315–335. https://doi.org/10.1080/00102208908947134

McCaffrey, B.J., 1981. Some measurements of the radiative power output of diffusion flames, in: WSS Combustion Meeting Paper No. WSS/CI 81-15.

McGrattan, K., Hostikka, S., 2012. Verification and Validation Process of a Fire Model, in: Probabilistic Safety Assessment and Management. Helsinki.

McGrattan, K., Hostikka, S., McDermott, R., Floyd, J., Vanella, M., Weinschenk, C., Overholt, K., 2017. Fire Dynamics Simulator User's Guide. https://doi.org/10.6028/NIST.SP.1019

McGrattan, K., Miles, S., 2016. Modeling Fires Using Computational Fluid Dynamics (CFD), in: Hurley, M. (Ed.), SFPE Handbook of Fire Protection Engineering. pp. 1034–1065. https://doi.org/10.1007/978-1-4939-2565-0

McGuinness, K., O'Connor, N.E., 2010. A comparative evaluation of interactive

segmentation algorithms. Pattern Recognit. 43, 434–444. https://doi.org/10.1016/j.patcog.2009.03.008

Meacham, B.J., Charters, D., Johnson, P., Salisbury, M., 2016. Building Fire Risk Analysis, in: SFPE Handbook of Fire Protection Engineering, Fifth Edition. MJ Hurely (ed.), pp. 2941–2991. https://doi.org/10.1007/978-1-4939-2565-0

Menter, F., Hemstrom, B., Henriksson, M., Karlsson, R., Latrobe, A., Martin, A., Muhlbauer, P., Rep, C., Scheuerer, M., Smith, B., Takacs, T., 2002. CFD Best Practice Guidelines for CFD Code Validation for Reactor-Safety Applications.

Meroil SA, 2019. Meroil Port of Barcelona [WWW Document]. URL http://www.meroil.es/logistica/terminal-de-barcelona (accessed 6.28.19).

Mihailidou, E.K., Antoniadis, K.D., Assael, M.J., 2012. The 319 major industrial accidents since 1917. Int. Rev. Chem. Eng. 4, 529–540.

Miralles, A., Ramos, M., Pastor, E., Planas, E., 2014. The Effect of the Computational Grid Size on the Prediction of a Flammable Cloud, in: Proceedings of the ASME 2014 33rd International Conference on Ocean, Offshore and Arctic Engineering. pp. 1–8. https://doi.org/10.1115/OMAE2014-24587

Mishra, K.B., 2010. Experimental investigation and CFD simulation of organic peroxide pool fi res (TBPB and TBPEH). Universität Duisburg-Essen.

Mok, W.K., Chow, W.K., Kong, H., 2004. "Verification and Validation" Computational Fluid Dynamics in Fire. Int. J. Archit. Sci. 5, 58–67.

Möller, F., 1973. Einführung in die Meteorologie. Mannheim, Germany.

Monin, A., Obukhov, A., 1959. Basic laws of turbulent mixing in the surface layer of the atmosphere. Tr. Akad. Nauk SSSR Geophiz. Inst. 24, 163–187.

Montiel, H., Vílchez, J.., Arnaldos, J., Casal, J., 1999. Historical Analysis of Natural Gas Accidents. J. Hazard. Mater. 51, 77–92.

Moorhouse, J., 1982. Scaling criteria for pool fires derived from large-scale experiments, in: Institution of Chemical Engineers Symposium. pp. 165–179.

Mudan, K.S., 1984. Thermal radiation hazards from hydrocarbon fires. Prog. Energy Combust. Sci. 10, 59–80.

Muñoz, M., Arnaldos, J., Casal, J., Planas, E., 2004. Analysis of the geometric and radiative characteristics of hydrocarbon pool fires. Combust. Flame 139, 263–277. https://doi.org/10.1016/j.combustflame.2004.09.001

Muñoz, M., Planas, E., Ferrero, F., Casal, J., 2007. Predicting the emissive power of hydrocarbon pool fires. J. Hazard. Mater. 144, 725–729. https://doi.org/10.1016/j.jhazmat.2007.01.121

Muthusamy, D., Wingerden, K. Van, 2015. Numerical simulation of vapour cloud fires using FLACS-Fire, in: International Fire Safety Symposium.

National Fire Protection Association, 2018. NFPA 101 - Life Safety Code.

National Fire Protection Association, 2016. NFPA 11 - Standard for Low-, Medium-, and High-Expansion Foam.

Nilsen, A.R., Log, T., 2009. Results from three models compared to full-scale tunnel

fires tests. Fire Saf. J. 44, 33–49. https://doi.org/10.1016/j.firesaf.2008.03.001

NORSOK STANDARD - Risk and emergency preparedness assessment, 2010.

Nuclear Energy Agency, 2015. Best Practice Guidelines for the Use of CFD in Nuclear Reactor Safety Applications – Revision.

Nwabueze, D.O., 2016. Liquid Hydrocarbon Storage Tank Fires – How Prepared is your Facility? Chem. Eng. Trans. 48, 301–306. https://doi.org/10.3303/CET1648051

Oberkampf, W.L., Barone, M.F., 2006. Measures of agreement between computation and experiment: Validation metrics. J. Comput. Phys. 217, 5–36. https://doi.org/10.1016/j.jcp.2006.03.037

Osenbroch, J., 2006. CFD study of gas dispersion and jet fires in complex geometries. Esbjerg Institute of Technology, Aalborg University.

Palacios, A., Casal, J., 2011. Assessment of the shape of vertical jet fires. Fuel 90, 824–833. https://doi.org/10.1016/j.fuel.2010.09.048

Palacios, A., Muñoz, A., Casal, J., 2008. Jet fires: An experimental study of the main geometrical features of the flame in subsonic and sonic regimes. AlChE J. 55, 256–263. https://doi.org/10.1002/aic

Palacios, A., Muñoz, M., Darbra, R.M., Casal, J., 2012. Thermal radiation from vertical jet fires. Fire Saf. J. 51, 93–101. https://doi.org/10.1016/j.firesaf.2012.03.006

Palazzi, E., Fabiano, B., 2012. Analytical modelling of hydrocarbon pool fires: Conservative evaluation of flame temperature and thermal power. Process Saf. Environ. Prot. 90, 121–128. https://doi.org/10.1016/j.psep.2011.06.009

Peacock, A.J., 1998. Oxygen at High Altitude. Br. Med. J. 317, 1063–1066.

Peris-Sayol, G., Paya-Zaforteza, I., Alos-Moya, J., Hospitaler, A., 2015. Analysis of the influence of geometric, modeling and environmental parameters on the fire response of steel bridges subjected to realistic fire scenarios. Comput. Struct. 158, 333–345. https://doi.org/10.1016/j.compstruc.2015.06.003

Peter, N., Williams, F.A., 1983. Lift-off characteristics of turbulent jet diffusion flames. Am. Inst. Aeronaut. Astronaut. J. 21, 423–429.

Pierce, J.B.M., Moss, J.B., 2007. Smoke production, radiation heat transfer and fire growth in a liquid-fuelled compartment fire. Fire Saf. J. 42, 310–320. https://doi.org/10.1016/j.firesaf.2006.11.006

Pio, G., Carboni, M., Iannaccone, T., Cozzani, V., Salzano, E., 2019. Numerical simulation of small-scale pool fires of LNG. J. Loss Prev. Process Ind. 61, 82–88. https://doi.org/10.1016/j.jlp.2019.06.002

Planas-Cuchi, E., Chatris, J., López, C., Arnaldos, J., 2003. Determination of flame emissivity in hydrocarbon pool fires using infrared thermography. Fire Technol. 39, 261–273. https://doi.org/10.1023/A:1024193515227

Planas-Cuchi, E., Montiel, H., Casal, J., 1997. A survey of the origin, type and consequences of fire accidents in process plants and in the transportation of hazardous materials. Process Saf. Environ. Prot. 75, 3–8. https://doi.org/10.1205/095758297528706

Pope, S.B., 2012. Turbulent Flows. Cambridge University Press, New York. https://doi.org/10.1017/CBO9780511840531

Port of Barcelona, 2019. Mapa guía [WWW Document]. URL http://www.portdebarcelona.cat/es_ES/web/el-port/mapa-guia (accessed 6.28.19).

Port of Barcelona, 2015. Medio atmosférico [WWW Document]. https://doi.org/http://www.portdebarcelona.cat/es_ES/web/el-port/medi-atmosferic

Pritchard, M.J., Binding, T.M., 1992. FIRE2: A new approach for predicting thermal radiation levels from hydrocarbon pool fires, in: Symposium on Major Hazards Onshore and Offshore. pp. 491–505.

Pula, R., Khan, F.I., Veitch, B., Amyotte, P.R., 2005. Revised fire consequence models for offshore quantitative risk assessment. J. Loss Prev. Process Ind. 18, 443–454. https://doi.org/10.1016/j.jlp.2005.07.014

Rajendram, A., Khan, F., Garaniya, V., 2015. Modelling of fire risks in an offshore facility. Fire Saf. J. 71, 79–85. https://doi.org/10.1016/j.firesaf.2014.11.019

Ramsdale, S.A., Cropper, M., Tickle, G.A., Watt, J., 2003. Final Report of AEA Technology's Contribution to the Safety First Project.

Rawat, R., Pitsch, H., Ripoll, J., 2002. Large-eddy simulation of pool fires with detailed chemistry using an unsteady flamelet model, in: Center of Turbulence Research - Proceedings of the Summer Program.

Ray, A., Chander, S., Ray, A., 2014. Flame impingement heat transfer : A review Flame impingement heat transfer : A review. https://doi.org/10.1016/j.enconman.2005.01.011

Receptora de Liquidos SA (Relisa), 2019. Facilities [WWW Document]. URL http://www.relisa.com/ (accessed 6.28.19).

Rengel, B., Mata, C., Palacios, A., Pastor, E., Casal, J., Planas, E., 2019a. CFD Modelling of Vertical Sonic Jet Fires, in: 9th International Seminar on Fire and Explosion Hazards. Saint Petersburg, pp. 819–830.

Rengel, B., Mata, C., Pastor, E., Casal, J., Planas, E., 2018. A priori validation of CFD modelling of hydrocarbon pool fires. J. Loss Prev. Process Ind. 56, 18–31. https://doi.org/10.1016/j.jlp.2018.08.002

Rengel, B., Palacios, A., Hu, L., Wang, Q., Agueda, A., Pastor, E., Casal, J., Planas, E., 2019b. Experimental and computational analysis of vertical jet fires in normal- and sub- atmospheric pressures. Unpubl. Manuscr.

Rew, P., Deaves, D., 1995. The validation and application of pool fire models, in: Safety Engineering and Risk Analysis. pp. 57–65.

Rew, P.J., Spencer, H., Maddison, T., 1998. The sensitivity of risk assessment of flash fire events to modelling assumption, in: Icheme Symposium Series. pp. 265–278.

Rigas, F., Sklavounos, S., 2006. Simulation of Coyote series trials - Part II: A computational approach to ignition and combustion of flammable vapor clouds. Chem. Eng. Sci. 61, 1444–1452. https://doi.org/10.1016/j.ces.2005.09.005

Rigas, F., Sklavounos, S., 2005. Simulation of Coyote series trials - Part II: A computational approach to ignition and combustion of flammable vapor clouds.

Chem. Eng. Sci. 61, 1444–1452. https://doi.org/10.1016/j.ces.2005.09.005

Rokke, N.A., Hustad, J.E., Sonju, O.K., 1994. A study of partially premixed unconfined propane flames. Combust. Flame 97, 88–106. https://doi.org/10.1016/0010-2180(94)90118-X

Sakamoto, J., Nakayama, J., Nakarai, T., Kasai, N., Shibutani, T., Miyake, A., 2016. Effect of gasoline pool fire on liquid hydrogen storage tank in hybrid hydrogen-gasoline fueling station. Int. J. Hydrogen Energy 41, 2096–2104. https://doi.org/10.1016/j.ijhydene.2015.11.039

Sally, M., Kassawara, R., 2007. NUREG-1824. Verification and Validation of Selected Fire Models for Nuclear Power Plant Applications.

Santos, A., Costa, M., 2005. Reexamination of the scaling laws for NOxemissions from hydrocarbon turbulent jet diffusion flames. Combust. Flame 142, 160–169. https://doi.org/10.1016/j.combustflame.2005.03.004

Satoh, K., Liu, N., Xie, X., Zhou, K., Chen, H.C., Wu, J., Lei, J., Lozano, J., 2011. CFD Study of Huge Oil Depot Fires - Generation of Fire Merging and Fire Whirl in (7x7) Arrayed Oil Tanks. Fire Saf. Sci. 10, 693–705. https://doi.org/10.1561/1500000016

Sedano, C.A., López, O.D., Ladino, A., Muñoz, F., 2017. Prediction of a Small-Scale Pool Fire with FireFoam. Int. J. Chem. Eng. 2017, 1–12. https://doi.org/10.1155/2017/4934956

Shah, N., 1979. A new method of computation of radiation heat transfer in combustion chambers. Imperial College, University of London.

Shelley, C.H., 2008. Storage Tank Fires: Is Your Department Prepared? [WWW Document]. Fire Eng. URL https://www.fireengineering.com/articles/print/volume-161/issue-11/features/storage-tank-fires-is-your-department-prepared.html (accessed 6.28.19).

Shen, G., Zhou, K., Wu, F., Jiang, J., Dou, Z., 2018. A model considering the flame volume for prediction of thermal radiation from pool fire. Fire Technol. https://doi.org/10.1007/s10694-018-0779-y

Shen, G.S., Jiang, J.C., Zhou, K. Bin, Zhang, S.J., Wu, F., Zou, M.Y., 2018. Analysis for Fire Plume Temperature in Developing Area and Radiation Heat Flux Distribution in Small-scale Pool Fire. Procedia Eng. 211, 606–613. https://doi.org/10.1016/j.proeng.2017.12.054

Sikanen, T., Hostikka, S., 2017. Predicting the heat release rates of liquid pool fires in mechanically ventilated compartments. Fire Saf. J. 0–1. https://doi.org/10.1016/j.firesaf.2017.03.060

Sikanen, Topi, Hostikka, S., 2016. Modeling and simulation of liquid pool fires with in-depth radiation absorption and heat transfer. Fire Saf. J. 80, 95–109. https://doi.org/10.1016/j.firesaf.2016.01.002

Sikanen, T., Hostikka, S., 2016. Modeling and simulation of liquid pool fires with in-depth radiation absorption and heat transfer. Fire Saf. J. 80, 95–109. https://doi.org/10.1016/j.firesaf.2016.01.002

Sinai, Y.L., 2000. Exploratory CFD modelling of pool fire instabilities without cross-

wind. Fire Saf. J. 35, 51–61. https://doi.org/10.1016/S0379-7112(00)00011-4

Sinai, Y.L., Owens, M.P., 1995. Validation of CFD modeling of unconfined pool fire with cross-wind: Flame geometry. Fire Saf. J. 24, 1–34.

Smagorinsky, J., 1963. General circulation experiments with the primitive equations. I: The basic experiment. Mon. Weather Rev. 91, 99–165.

Sonju, O.K., Hustad, J., 1984. An experimental study of turblent jet diffusion flames, Norwegian Maritime Research.

Spalding, D.B., 2013. GENMIX: A General Computar Program for Two-Dimensional Parabolic Phenomena, Journal of Chemical Information and Modeling. https://doi.org/10.1017/CBO9781107415324.004

Steinhaus, T., Welch, S., Carvel, R.O., Torero, J.L., 2007. Large-scale pool fires. Therm. Sci. 11, 101–118. https://doi.org/10.2298/TSCI0702101S

Structurae. International Database and Gallery of Structures, n.d. Troll A Platform [WWW Document]. URL https://structurae.net/structures/troll-a-platform (accessed 5.23.19).

Stull, R.B., 2000. Meteorology for Scientists and Engineers, 2nd Editio. ed. California.

Sudheer, S., 2013. Characterization of Open Pool Fires and Study of Heat Transfer in Bodies Engulfed in Pool Fires.

Sudheer, S., Saumil, D., Prabhu, S.V., 2013. Physical experiments and Fire Dynamics Simulator simulations on gasoline pool fires. J. fire Sci. 31, 309–329.

Sugawa, O., Sakai, K., 1995. Flame Length and Width Produced by Ejected Propane Gas Fuel From a Pipe. Fire Saf. Sci. 2, 411–421. https://doi.org/10.3210/fst.17.55

Sun, B., Guo, K., Pareek, V.K., 2014. Computational fluid dynamics simulation of LNG pool fire radiation for hazard analysis. J. Loss Prev. Process Ind. 29, 92–102. https://doi.org/10.1016/j.jlp.2014.02.003

Sun, L., Yan, H., Liu, S., Bai, Y., 2017. Load characteristics in process modules of offshore platforms under jet fire: The numerical study. J. Loss Prev. Process Ind. 47, 29–40. https://doi.org/10.1016/j.jlp.2017.02.018

Suo-anttila, A., Lopez, C., Khalil, I., 2005. Users Manual for CAFE-3D : A Computational Fluid Dynamics Fire Code.

T., G., 1984. Lift-off Heights and Visible Lengths of Vertical Turbulent Jet Diffusion Flames in Still Air. Combust. Sci. Technol. 41, 17–29. https://doi.org/10.1080/00102208408923819

Tan, S.H., 1967. Flare sytem design simplified, in: Hydrocarbon Processing. pp. 172–176.

Terminales Portuarias SL (TEPSA), 2019. Barcelona Terminal [WWW Document]. https://doi.org/https://www.tepsa.es/barcelona/

Tieszen, S.R., Nicolette, V.F., Gritzo, L.A., Holen, J.K., Murray, D., Moya, J.L., 1996. Vortical Structures In Pool Fires : Observation, Speculation, and Simulation.

Tolias, I.C., Giannissi, S.G., Venetsanos, A.G., Keenan, J., Shentsov, V., Makarov, D., Coldrick, S., Kotchourko, A., Ren, K., Jedicke, O., Melideo, D., Baraldi, D., Slater,

S., Duclos, A., Verbecke, F., Molkov, V., 2018. Best practice guidelines in numerical simulations and CFD benchmarking for hydrogen safety applications. Int. J. Hydrogen Energy 1–13. https://doi.org/10.1016/j.ijhydene.2018.06.005

Torero, L., Jahn, W., Stern-gottfried, J., Ryder, N.L., Rein, G., Mowrer, F., Coles, A., Joyeux, D., Desanghere, S., La, M., Alvear, D., Capote, J.A., Jowsey, A., Abecassis-empis, C., Reszka, P., 2009. Round-robin study of a priori modelling predictions of the Dalmarnock Fire Test One. Fire Saf. J. 44, 590–602. https://doi.org/10.1016/j.firesaf.2008.12.008

Tradebe Port Services, 2019. Capacity [WWW Document]. https://doi.org/https://www.tradebeportservices.com/capacity

Trouvé, A., 2008. CFD Modeling of Large-Scale Pool Fires, in: The Second International Energy 2030 Conference. pp. 413–422.

U.S. Energy Information Administration (EIA), 2018. Natural Gas Production/Consumption - 2015 [WWW Document]. URL https://www.eia.gov/beta/international/

U.S. Energy Information Administration (EIA), 2016. International Energy Outlook 2016 Liquid fuels, DOE/EIA-0484(2016). https://doi.org/www.eia.gov/forecasts/ieo/pdf/0484(2016).pdf

Varahrami, V., Haghighat, M.S., 2018. The assessment of liquefied natural gas (LNG) demand reversibility in selected OECD countries. Energy Reports 4, 370–375. https://doi.org/10.1016/j.egyr.2018.05.006

Vasanth, S., Tauseef, S.M., Abbasi, T., Abbasi, S.A., 2013. Assessment of four turbulence models in simulation of large-scale pool fires in the presence of wind using computational fluid dynamics (CFD). J. Loss Prev. Process Ind. 26, 1071–1084. https://doi.org/10.1016/j.jlp.2013.04.001

Vasanth, S., Tauseef, S.M., Abbasi, T., Rangwala, A.S., Abbasi, S.A., 2014. Assessment of the effect of pool size on burning rates of multiple pool fires using CFD. J. Loss Prev. Process Ind. 30, 86–94. https://doi.org/10.1016/j.jlp.2014.04.011

Vela, I., 2009. CFD prediction of thermal radiation of large, sooty, hydrocarbon pool fires.

Villafañe, D., Darbra, R., Casal, J., 2011. Flash fire: historical analysis and modeling. Chem. Eng. Trans. 24, 1111–1116. https://doi.org/10.3303/CET1124186

Vopak Terquimsa, 2019. Terminal in Barcelona [WWW Document]. https://doi.org/http://www.vopakterquimsa.com/terminal-barcelona.html

Wang, C.J., Wen, J., 2018. Numerical Study of Heptane Pool Fires on a Hollow Square Pan. Procedia Eng. 211, 689–698. https://doi.org/10.1016/j.proeng.2017.12.065

World Port Source, 2019. Port of Barcelona - Port Commerce [WWW Document]. https://doi.org/http://www.worldportsource.com/ports/commerce/ESP_Port_of_Barcelona_1207.php

WS Atkins Consultants, 2002. Best Practices Guidelines for Marine Applications of CFD.

Zalok, E., Hadjisophocleous, G. V, 2011. Assessment of the Use of Fire Dynamics

Simulator in Performance-Based Design. Fire Technol. 47, 1081–1100. https://doi.org/10.1007/s10694-009-0117-5

Zhang, B., Liu, Y., Laboureur, D., Mannan, M.S., 2015. Experimental study on propane jet fire hazards: thermal radiation. Ind. Eng. Chem. Res. 54, 9251–9256. https://doi.org/10.1021/acs.iecr.5b02064

Zhao, J., Magenes, L., 2016. CFD Modeling of Jet Fires of Different Configurations, in: 12th Global Congress on Process Safety.

Zukoski, E.E., Kubota, T., Cetegen, B., 1980. Entrainment in fire plumes. Fire Saf. J. 107–121.